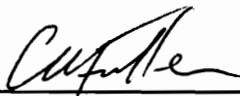# ACTIVE CONTROL OF COUPLED WAVE PROPAGATION IN FLUID-FILLED ELASTIC CYLINDRICAL SHELLS

by

Bertrand J. Brévart

Dissertation submitted to the Faculty of the

Virginia Polytechnic Institute and State University

in partial fulfillment of the requirements for the degree of

Doctor of Philosophy

in

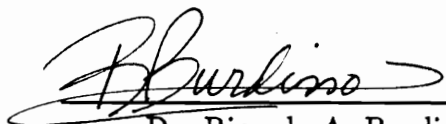Mechanical Engineering

APPROVED:

_____

Dr. Chris R. Fuller, Chairman

_____   _____

Dr. Mahendra P. Singh   Dr. Harry H. Robertshaw

_____   _____

Dr. Ricardo A. Burdisso   Dr. William R. Saunders

December, 1994

Blacksburg, Virginia

ACTIVE CONTROL OF COUPLED WAVE PROPAGATION
IN FLUID-FILLED ELASTIC CYLINDRICAL SHELLS

by

Bertrand J. Brévart

Committee Chairman: Chris R. Fuller

Mechanical Engineering

(ABSTRACT)

The vibrational energy propagating in straight fluid-filled elastic pipes is carried by the structure as well as by the internal fluid. Part of the energy in the system may also transfer from one medium to the other as propagation occurs. For various types of harmonic disturbance, this study demonstrates that, whether the propagating energy is predominantly conveyed in the shell or in the fluid, large attenuations of the total power flow may be achieved by using an active control approach. As the shell and fluid motions are fully coupled, the implementation of intrusive sources/sensors in the acoustic field can be also avoided. The approach is based on using radial control forces applied to the outer shell wall and error sensors observing the structural motion.

A broad analytical study gives insight into the control mechanisms. The cylindrical shell is assumed to be infinite, *in vacuo* or filled with water. The first disturbance source investigated is a propagating free wave of circumferential order n=0 or n=1. The control forces are appropriate harmonic line forces radially applied to the structure. The radial displacement of the shell wall at discrete locations downstream of the control forces is minimized using linear quadratic optimal control theory. The attenuation of the total power flow in the system after control is used to

study the impact of the fluid on the performance of the control approach. Results for the shell *in vacuo* are presented for comparison. Considering the breathing mode (n=0), the fluid decreases the control performance when the disturbance is a structural-type incident wave. Significant reductions of the transmitted power flow can be achieved when the disturbance is a fluid-type of wave. Regarding the beam mode (n=1), the fluid increases the control performance below the first acoustic cut-off frequency and decreases it above this frequency.

The analytical study is then extended to the active control of the pipe vibrations induced by more realistic disturbances such as a point force or an internal monopole source. The point force disturbance addresses the problem of mechanical excitation whereas the internal monopole source directs the attention towards the acoustic excitation of the piping system. The modal radial displacements of the shell, corresponding to the first three circumferential modes (n=0,1,2), are individually minimized at one axial location, using linear quadratic optimal control theory. The control inputs are two radial point forces and one ring force. At low frequencies, the active control approach results in large attenuations of the total power flow beyond the error sensors whether the propagating energy is predominantly carried in the shell or in the fluid before control.

The results of experiments conducted on a plexiglass shell in air or filled with water are then presented and analyzed. The first set of experiments deals with the active control of an axisymmetric radial line force disturbance. The actuators and sensors were implemented using polyvinylidene fluoride (PVDF) cables wrapped around the shell. The chosen control algorithm was the filtered-x version of the adaptive LMS algorithm. Good control of the axisymmetric wave propagation is

demonstrated except at frequencies associated with waves cutting on. The active control of of the pipe vibrations due to a radial point force disturbance (shaker) was also investigated. The modal radial displacements of the shell (n=0,1,2) were observed by sensors made of PVDF cable and shaped PVDF film. The design and the implementation of these sensors is reviewed. For excitation frequencies below 150 Hz, large attenuations of the total power flow (> 10 dB) were obtained. The experimental study corroborates the high potential for active control of total energy flow in fluid-filled piping systems. The limitations of the approach are discussed.

Acknowledgements

I would like to thank all the people who contributed to the achievement of this work. First of all, I would like to thank my dissertation advisor, Dr. Chris Fuller, for giving me the opportunity to work in the interesting and dynamic field of active control. His technical expertise and physical insight into complex problems proved very educational. I sincerely thank him for his help, guidance and advice. Secondly, I would like to thank Dr. Mahendra Singh, Dr. Harry Robertshaw, Dr. Ricardo Burdisso and Dr. William Saunders for serving on my advisory committee.

I would like to recognize all my friends in the Vibration and Acoustics Laboratories for their moral or technical support. Thanks are due to Dawn Williams for helping me a countless number of times with the paper work.

I would like to thank my entire family and all my friends in France for their continual support from overseas. My parents, Jean and Monique Brévart, have always been there when I needed them. I can never possibly thank them enough or repay them for all that they have given. Last and most important, my wonderful wife, Ramiria. Thank you for providing encouragement and support, you are my true inspiration. Your unconditional love has helped me complete this work.

To my wife, with Deepest Love.

Contents

List of Figures

List of Tables

Nomenclature

a	shell mean radius
c_f	fluid acoustic free wave speed
c_L	shell extension phase speed
D	shell membrane stiffness
E	Young's modulus
E'	complex Young's modulus
E_c	control effort
f	frequency
f_r	ring frequency
F_{sjn}	fluid power factor
$F_c^0,\ F_c^1,\ F_c^2$	control forces
FL	fluid loading term
F_0	amplitude of the input force
h	shell wall thickness
I_x^f	axial component of the time-averaged acoustic intensity in the fluid
I_x^s	axial component of the instantaneous structural intensity in the shell wall
I_π	control performance parameter

IL	power insertion loss
J	cost function
$J_n(\ )$	first kind Bessel function of order n
k_f	wavenumber of the acoustic free wave in the fluid
k_n	axial wavenumber
k_{ns}	axial wavenumber of the branch s
k_{ns}^d	axial wavenumber of the incident wave
k^r	radial wavenumber
k_s^r	radial wavenumber of the branch s
D	shell bending stiffness
n	circumferential mode order
N_x	axial force resultant in the shell wall
$N_{x\theta}$	in-plane shear force resultant in the shell wall
M_x	bending moment of a shell element
$M_{x\theta}$	twisting moment of a shell element
p	pressure
p_a	pressure fluid loading
p_p^f	free field pressure due to a monopole source
p_m	free field amplitude of the monopole source
$p_0^x,\ p_0^\theta,\ p_0^r$	axial, tangential and radial components of the forcing load p_0
P_{ns}	pressure amplitude
$\bar{P}_n$	spectral pressure amplitude
Q_x	transverse shear force resultant in the shell wall
$r,\ x,\ \theta$	cylindrical co-ordinates
r_p	radial position of the monopole source

R_a	ratio of axial to radial amplitude
s	branch number
S_n	number of propagating branches for a given cicumferential mode n
S_{sjn}	shell power factor
$u,\ v,\ w$	shell displacements
$U_{ns},\ V_{ns},\ W_{ns}$	shell displacement amplitudes
$\bar{U}_n,\ \bar{V}_n,\ \bar{W}_n$	shell spectral displacement amplitudes
w_n	modal radial displacement of the shell
w_{ns}^d	disturbance wave displacement
$\dot{w}_x$	angular rotation of the shell element in the x-direction
$\dot{w}_\theta$	angular rotation of the shell element about the x-axis
W_{ns}^d	disturbance wave amplitude
$x_c^0,\ x_c^1,\ x_c^2$	positions of control forces F_c^0, F_c^1 and F_c^2
$x_e^0,\ x_e^1,\ x_e^2$	positions of the error sensors
x_0	position of the radial line force F_0
v_x	axial component of the particle velocity in the fluid
β	thickness factor
δ	Dirac delta function
δ_{mn}	Kronecker delta function
∂	partial derivative
Δx_c	distance between the control line forces
Δx_e	distance between the error points
ε_n	=2 if n=0, =1 if n≠0
ϵ_n	=1 if n=0, =2 if n≠0
η	damping coefficient

ν	Poisson's ratio
ρ_f	specific mass of the fluid
ρ_s	specific mass of the shell material
ω	circular frequency
Ω	non-dimensional frequency, $\Omega = \omega a / c_L$
Ω_{n0}	non-dimensional cut-on frequency of the circumferential mode n
Π_f	power flow in the fluid
Π_s	power flow in the shell wall
Π_t	total power flow
Π_t^n	total power flow due to the circumferential mode n
θ_n	polarization angle of the circumferential mode shape n with respect to $\theta = 0$.

Chapter 1

Introduction

Piping systems appear as load-carrying elements in various industrial and military applications. The vibrations induced by these loads can cause major problems such as mechanical fatigue or undesirable radiated noise fields. Fatigue may result in damage to vital parts of installations. For this reason, engineers have been particularly concerned with these vibrations in power plants and petrochemical refineries. The noise radiated from pipes is believed to contribute significantly to the noise signature of military ships and submarines. Therefore, the detection and the identification of these naval vessels would be more difficult if the transmission of noise along pipes was minimized. Piping systems are also responsible for the propagation of domestic noise in apartment buildings. Despite stricter regulations concerning the noise transmission through the walls, pipes in kitchens and bathrooms transmit unwanted noise from one apartment to the other.

Piping systems can be excited by a large number of sources related to the structural path or to the internal fluid path. The presence of a discontinuity in the flow for example, such as a valve or a bend, generally creates a local turbulence, i.e.

a noise source in the fluid. Large amounts of vibrational energy may be delivered to the system by pumps and compressors. Other vibrational sources may first reach some equipment attached to the piping system which ultimately transmit vibrational energy to the pipe itself. Reciprocally, as vibrational energy propagates along the piping system, it can excite other equipment attached to the structure, often at distances far from the source. Part of the propagating energy may also result in noise radiation from the pipe surface.

Because of the mixed nature of the energy transmission path, control of the total energy flow conveyed through fluid-filled piping systems can be a difficult task to achieve by passive methods. The present study investigates an active control approach to reduce the vibrations and hopefully the total power flow through infinite fluid-filled elastic cylindrical shells. In spite of the extensive application of active vibration control in recent years, it is the first time that analytical and experimental studies on active control of coupled wave propagation in fluid-filled cylindrical elastic shells are presented.

1.1 Vibrations of fluid-filled cylindrical elastic shells

A thorough understanding of the dynamic behaviour of fluid-filled cylindrical shells is critical to an investigation on active control applied to such systems. In order to understand the effect of an internal fluid loading on the response of a pipe shell, a brief literature review on the simplified problem of a cylindrical shell vibrating *in vacuo* has first been carried out.

2

Most of the theoretical studies of *in vacuo* shell systems were based upon approximate shell equations which are only valid in limited ranges of wall thickness and frequency. A detailed discussion of these numerous shell theories has been given by Kraus [1] and Leissa [2]. Using the Flügge shell equations for example, Fuller [3] fully described the free vibrations of infinite thin cylindrical shells *in vacuo*, including the motion associated with complex wavenumbers. In the same paper, he presented an analytical study of the effects of axisymmetric discontinuities in the shell wall on the propagation of flexural waves. Heckl [4] was the first to derive a solution to the vibration problem of infinitely long shells driven by a point force. By using a simple shell model, Heckl obtained formulae for the resonant frequencies and the modal density of the simply supported shell as well as the point impedance of the infinite shell. Using more accurate shell equations (Donnell-Mushtari), Junger and Feit [5] studied the forced vibrations of a simply supported shell *in vacuo*. They presented solutions for the natural frequencies and the mobility of the finite shell driven by a point force.

The characteristic equation of a cylindrical elastic shell *in vacuo* derived using the exact three-dimensional equations of linear elasticity is valid for all ranges of wall thickness and frequency. However, this derivation involves several complexities and the analysis thereof has not been completed. The equation has been investigated to some extent by Hermann and Mirsky [6, 7, 8], Gazis [9], Greenspon [10], Bird, Hart and McClure [11] and Armenakas, Gazis and Hermann [12]. More recently, Borgiotti and Rosen [13, 14] presented a state vector approach to the exact three-dimensional analysis of the forced vibrations of infinite and finite thin cylindrical shells *in vacuo*. The state vector technique, although relatively complex, provides a systematic approach to the formulation and the solution of various cylindrical shell

problems such as the determination of dispersion curves and the forced vibrational response to a point force or to a localized couple.

While the *in vacuo* solution may be applicable with reasonable accuracy to instances where the characteristic impedance of the internal medium is very small compared to that of the shell, as for shells in air for example, it can not be used when the shell is filled with liquid. On the other hand, the solution of the fully coupled system has been extensively studied by various authors. Kumar [15, 16], Del Grosso and McGill [17] and Del Grosso [18] first investigated the characteristic equation of a fluid-filled cylindrical elastic shell. These studies were based on the exact three-dimensional equations of linear elasticity. However, they were restricted to the finding of real wavenumber solutions of the characteristic equation. Then, Kumar [19] presented the complete dispersion of axisymmetric waves, i.e. including complex wavenumber solutions. Using approximate shell equations (Donnell-Mushtari), Fuller and Fahy [20] extended the investigation to higher order circumferential modes. They gave extensive physical interpretations of all the eigenvalues of the infinite system. They also determined whether the vibrational energy associated with each propagating free wave was located in the pipe wall or in the contained fluid. The theoretical dispersion curves for fluid-filled cylindrical shells were experimentally validated by Esparcieux [21] on an oil-filled pipe and by Plona *et al.* [22] on a water-filled pipe. Recently, Leyrat [23], using the same shell equations as Fuller *et al.* [20], went one step further and investigated the effect of an internal flow on the vibrations of thin cylindrical elastic shells. He derived the characteristic equation of the system and, like Fuller *et al.*, analyzed the pipe behaviour in terms of propagation of free waves. Leyrat also presented a solution for the mobility of infinite and finite cylindrical shell systems subjected to a radial point force,

4

including the effect of a uniform internal flow. He experimentally verified some of his analytical results such as the transfer response of an infinite cylindrical shell filled with a static fluid. Following this work, Brévart and Fuller [24] evaluated the effect of a uniform internal flow on the distribution of vibrational energy in the coupled system. Their results were consistent with Leyrat's and revealed that the effect of fluid convection principally appears near cut-on and coincidence frequencies, for high values of Mach number ($M > 0.01$).

The forced response of infinite fluid-filled cylindrical elastic shells was briefly studied by Merkulov et $al.$ [25, 26]. For both point force excitation [25] and internal monopole excitation [26] of the coupled system, their analysis of the system response was limited to an evaluation of the relative amplitudes of propagating waves with varying branch and circumferential mode number. James [27, 28] evaluated the acoustic radiated power, the vibrational response of the shell wall and the pressure amplitudes of the exterior and interior fluids of an infinite water-filled shell immersed in air, for a monopole source and a mechanical point force excitation. James used numerical integration and the stationary phase method to evaluate the response functions and, while his investigation has revealed many important behavioral characteristics of the coupled system, information on the wave propagation mechanisms did not appear through his work. Fuller used a different approach to consider the problem of point force and internal monopole excitation of fluid-filled cylindrical shells [29, 30]. He computed the response functions by using the residue theorem so that the system behavior could be explained in terms of free wave propagation characteristics. Along with the derivation of the input mobility [29], Fuller studied the wave transmission through a radial ring constraint and the distribution of vibrational energy between the fluid and the shell wall for driving line and

point forces. He evaluated the distribution of vibrational energy in the coupled system for an internal monopole excitation as well [30]. As the Donnell-Mushtari shell equations exclude the effects of rotary inertia and transverse shear stresses, all of Fuller's analyses were restricted to less than mid-high frequency ranges. A recent study by Brévart, Journeau and Fuller [31] included the response of an infinite fluid-filled cylindrical shell to a point force excitation at very high frequencies. The investigation was based on the state vector formalism developed by Borgiotti and Rosen [13] using the exact three-dimensional equations of linear elasticity. Along with the analysis of the point force response of the system, Brévart *et al.* presented the dispersion solution of waves with very high circumferential mode orders in a very large frequency range.

All of the above studies focussed on the harmonic vibrations of a cylindrical elastic shell *in vacuo* or filled with liquid. In other words, they provided information on the system response in the time-average sense. Recently, Brévart and Fuller [32] have investigated the wave propagation paths in a fluid-filled elastic cylindrical shell excited by a radial impulsive line force applied to the shell wall. The impulse response of the shell wall was obtained by performing a discrete Fourier transform of the system frequency response. This investigation was followed by another time domain study concerning the energy exchange between the coupled media of impulsively excited fluid-filled shells [33]. This last study revealed that the net amount of energy delivered to the fluid medium at the impact location was much smaller for a beam type excitation (n=1) than for an axisymmetric excitation (n=0). Furthermore, for both types of excitation, it appeared that nearly half of the energy delivered to the fluid medium at the impact eventually returned to the shell wall. The impulse response of an infinite fluid-filled steel pipe was experimentally inves-

tigated by Möser, Heckl and Ginters [34]. They noticed that the impulsive source generated signals of long duration even in the absence of reflections at the pipe ends. This behaviour was due to the frequency components associated with waves cutting on.

1.2   Objective and approach

The ultimate objective of this work is to control, by active means, the energy transfer, or total power flow, in infinite fluid-filled cylindrical shells. Any type of vibrational wave propagating in the system carries a certain amount of energy in either or both of the fluid and shell media. Ideally, it is thus desired to keep all the vibrational waves in the system from propagating beyond a certain position on the pipe.

A similar goal has been achieved by Gibbs [35] for finite thin beams. The two different motions of the beam, i.e. flexure and extension, were individually observed by paired piezoelectric sensors. Using the wavenumber information obtained from a beam model, Gibbs designed digital filters yielding real time estimates of positive and negative traveling flexural and extensional waves. The outputs of the filters, used as error signals, were then minimized using a feedforward adaptive controller. It must be noted that the technique relies on the accuracy of the beam model and, consequently, defects in the beam cross section are likely to affect the control performance. This problem could be solved by implementing wavenumber filtering capabilities of the adaptive system.

In order to control the total power flow in fluid-filled pipes, real-time estima-

tion of the amplitude of the propagating waves is the optimal solution. However, the characteristic equation of a fluid-filled cylindrical shell is fairly more complex than that of a beam. The solutions of the equation may first be decomposed into mutually independent circumferential modes (n=0,1,2,...). For each circumferential mode, multiple propagating wave types with dispersion laws of varying complexity may exist. The number of propagating wave types increases with frequency. At very low frequencies, i.e. well below the ring frequency of the pipe, four different types of wave can simultaneously propagate energy in the system. Three of them are associated with the axisymmetric shell motion (n=0) and the fourth one corresponds to the beam type motion of the shell (n=1). Waves of higher circumferential order (n=2,3,...) are evanescent in the very low frequency range, i.e. their contribution to the system response is negligible away from the cross section where they are excited. At higher frequencies however, the propagation of these lobar waves, along with the propagation of higher order wave types, must be accounted for.

The wave decomposition problem in fluid-filled pipes of finite length was first investigated by Pavić [36] with application to acoustic and structural intensity measurement methods. Pavić restricted his analysis to frequencies below the cut-on frequency of the circumferential mode n=2, i.e. well below the ring frequency of the pipe. In order to extract the wave amplitudes, he briefly described a configuration of accelerometers and strain gauges. The measurements suggested by Pavić included radial motion, tangential velocity and displacement, axial displacement, axial strain and two axial strain derivatives. Very recently, de Jong [37] presented other wave decomposition techniques for fluid-filled pipes which were based on the use of accelerometers and flush-mounted pressure transducers. From the work of Pavić and de Jong, it appears that accurate measurements of the wave contribu-

tions in fluid-filled pipes are difficult to achieve and require very large arrays of sensors with matched sensitivities. In addition, the wave decomposition relies on the accuracy of the model providing the wavenumber information. Defects in the pipe cross section or bubbles at the interface between the shell and the fluid may adversely affect the decomposition. An experimental determination of the wavenumbers is the solution to this problem. The array processing requirements to achieve wavenumber filtering in fluid-filled pipes have been recently investigated by Corrado and Clifton [38]. They have shown that particularly long arrays, i.e. a large number of sensors with matched sensitivities, are necessary to maintain a high resolution of the beamforming process.

Due to the implementation complexity, real time estimation and minimization of the total power flow, as performed by Gibbs for beams, is not attempted in the present study. The control approach investigated is more straightforward. Given a disturbance and a practical configuration of error sensors and control forces, it is desired to determine whether large attenuations of the total power flow can be achieved by using active control. Even though the objective may be to minimize the structural power flow, the fluid power flow or the sum of both, the most convenient location to apply the control forces is directly to the shell wall. The error information to be minimized would be best given by sensors observing the structural motion. Sources or sensors in the acoustic field could obstruct the flow of the internal fluid. Control of the fluid power flow may be achieved by using radial control forces which provide good coupling between the shell wall and the fluid field.

9

1.3 Scope of the work

The primary purpose of this research is to demonstrate that large reductions of the total power flow through infinite straight fluid-filled pipes can be actively achieved by means of radial control forces applied to the shell wall for various types of disturbance.

A broad analytical study giving insight into the control mechanisms has been conducted. The first disturbances considered are individual harmonic propagating free waves of circumferential order n=0 and n=1. These two circumferential modes illustrate the system typical behaviour and are thus studied separately in detail. The control forces are radial line forces with the same circumferential distribution as the disturbance. The radial displacement of the shell wall at discrete locations downstream of the control forces is minimized using linear quadratic optimal control theory. The difference of total power flow through the system before and after control is then used to evaluate the impact of the fluid on the performance of the control approach. The total power flow through the system is evaluated by integrating the structural intensity in the shell wall and the acoustic intensity in the fluid field over a pipe cross section. Results for fluid-filled shells are presented in comparison to the performance of the control approach performed on the same shell *in vacuo*.

After demonstrating the controllability of certain waves in certain frequency ranges, the analytical work is extended to more complex disturbances such as point forces and internal monopole sources. The control forces are point forces as well as ring forces. It is assumed that one can minimize the radial wall motion associated with various circumferential modes using modal sensors, i.e. distributed sensors

with spatial filtering capabilities. For various excitation frequencies of the disturbances, the modal decomposition of the total power flow, before and after control, is evaluated and analyzed.

In order to validate the analytical investigations, the results of various experiments performed on a plexiglass cylindrical shell are presented. Typical properties of the shell systems, i.e. the air-filled shell and the water-filled shell, are determined and compared to analytical predictions.

The active control of an axisymmetric disturbance is investigated. The axisymmetric excitation is implemented by using a piezoelectric polymer cable (PVDF cable) wrapped an exact number of turns around the shell and excited through a high voltage power amplifier. Axisymmetric control forces and error sensors are also implemented by means of PVDF cable. Using a feedforward adaptive controller, the axisymmetric radial displacement of the shell wall is minimized at discrete locations. The effect of the discontinuity created by the active control arrangement is evaluated from the residual vibrations of the shell beyond the error sensors as well as from the attenuation of the pressure in the fluid field.

The active control of a point force disturbance, implemented using an electromechanical shaker, is experimentally investigated. A set of point and ring forces (shakers and PVDF cables) are used to control the radial wall motion associated with various circumferential modes. The modes are observed by modal error sensors made of PVDF film and cable. The performance of the control arrangement is determined from the modal radial motion of the shell beyond the error sensors as well as from the attenuation of the pressure in the fluid field.

1.4 Organization

A comprehensive review of the theory of wave propagation in fluid-filled cylindrical shells is presented in Chapter 2. The characteristic equation of the coupled fluid-shell system is derived and the free wave characteristics are discussed. In Chapter 3, an active approach to control the propagation of a single free wave by means of radial line forces is analytically investigated. The chapter includes the derivation of the forced response of a fluid-filled cylindrical shell to a radial line force as well as the derivation of an expression for the total power flow in the coupled system. The linear quadratic optimal control theory is also introduced in Chapter 3. The control problem associated with more realistic disturbances, i.e. disturbances yielding the simultaneous presence of several propagating wave types, is addressed in Chapter 4. An active control approach to minimize the total power flow generated by a point force or an internal monopole source at low frequency is presented. Experiments have been performed in order to validate the analytical models. The arrangement and the characterization of the experimental apparatus are discussed in Chapter 5. The results of the active control experiments are presented in Chapter 6. Based upon the results of the investigations presented in the previous chapters, some conclusions are given in Chapter 7. Recommendations are also made for future work.

Chapter 2

Free Wave Propagation in Cylindrical Shell Systems

A thorough characterization of the free wave propagation in infinite cylindrical elastic shells, whether they are *in vacuo* or filled with a fluid, is a key step to the understanding of the dynamic behaviour of shell systems subjected to any type of disturbance. In this chapter, the characteristic equation of a cylindrical elastic shell filled with fluid is derived. The dispersion curves of two different shells, *in vacuo* or filled with water, are presented. The behaviour of each individual branch, or free wave, is explained in physical terms.

2.1   Equations of motion of the coupled system

The cylindrical coordinate system used in the analysis is shown in Figure 2.1 . Different formulations of the equations of motion for cylindrical shells are available in the literature. Most of them can be found in Leissa's monograph [2]. The Donnell-Mushtari shell equations [5] were proved to be particularly convenient
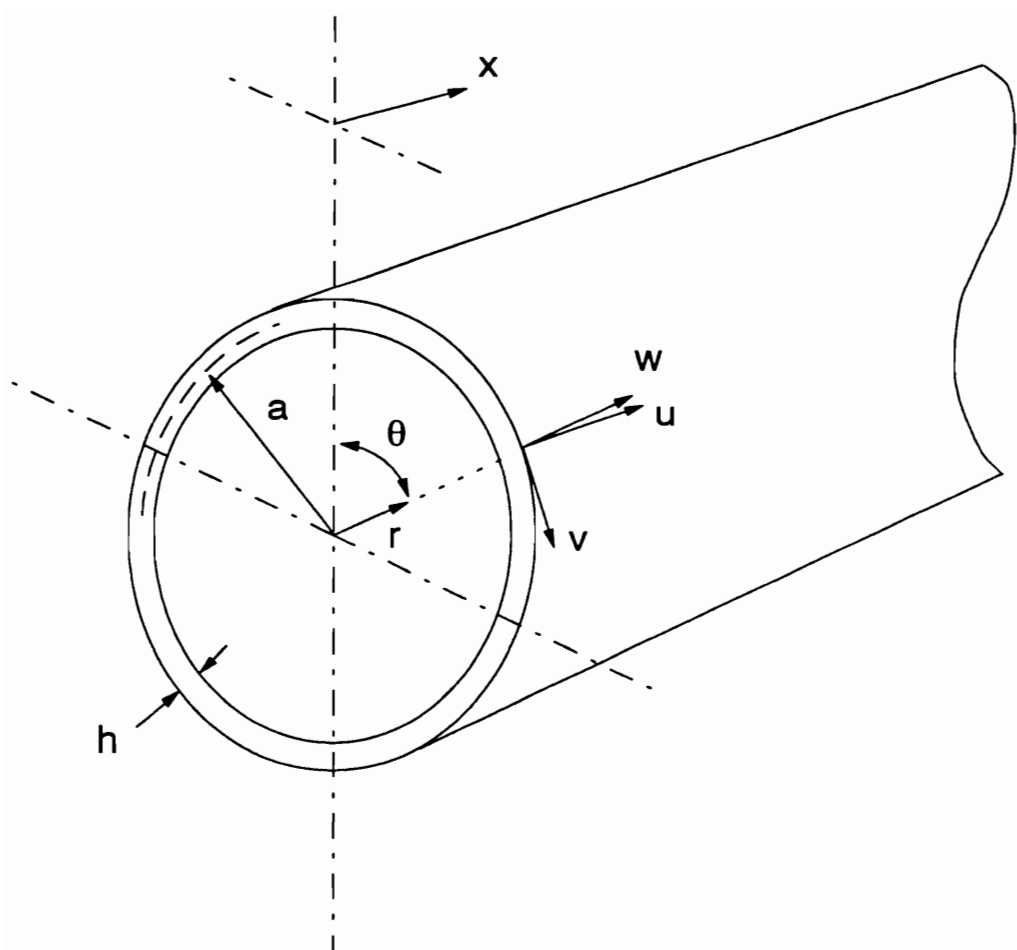
Figure 2.1: Coordinate system.

in describing the harmonic motion of thin-walled cylindrical shells containing an acoustic field. They were extensively used by several authors, such as Junger and Feit [5], Fuller [20, 29, 30, 39], Leyrat [23] or Brévart [24], in a great number of books and papers. The Donnell-Mushtari equations, which are a simplified version of Kennard's differential equations [40], were recently found to give unsatisfactory results at very low frequencies. On the other hand, Kennard's shell equations give reliable results at very low frequencies and are thus preferred to describe the shell motion in this investigation. Kennard's shell equations are only valid for thin-walled shells and exclude the effects of rotary inertia and transverse shear stresses. Thus, they can only be used for analysis in the low frequency range, i.e. below and just above the ring frequency of the shell, as it the case in the present investigation on active control. For high frequency analysis of cylindrical shells, it is recommended to use a "thick" shell theory that includes the effects of both rotary inertia and transverse shear deformations, such as the one presented by Borgiotti and Rosen [13] for example. The validity of the Donnell-Mushtari and Kennard's shell equations, with respect to the exact three dimensional equations of linear elasticity [13], will be assessed in Section 2.2.2 by looking at the dispersion curves of an *in vacuo* shell.

The inhomogeneous form of Kennard's shell equations [40], including a pressure fluid loading, $p_a(\theta, x)$, and an external pressure load $\mathbf{p_0}$ with axial, tangential and radial components p_0^x, p_0^θ and p_0^r respectively, is written as:

$$\frac{\partial^2 u}{\partial x^2} + \frac{1-\nu}{2a^2}\frac{\partial^2 u}{\partial \theta^2} + \frac{1+\nu}{2a}\frac{\partial^2 v}{\partial x \partial \theta} + \frac{\nu}{a}\frac{\partial w}{\partial x} - \frac{\ddot{u}}{c_L^2} = \frac{p_0^x(1-\nu^2)}{Eh}, \qquad (2.1)$$

$$\frac{1+\nu}{2a}\frac{\partial^2 u}{\partial x \partial \theta} + \frac{1-\nu}{2}\frac{\partial^2 v}{\partial x^2} + \frac{1}{a^2}\frac{\partial^2 v}{\partial \theta^2} + \frac{1}{a^2}\frac{\partial w}{\partial \theta} + \frac{h^2}{8a^4}\frac{\nu}{1-\nu}\left(\frac{\partial^3 w}{\partial \theta^3} + \frac{\partial w}{\partial \theta}\right)$$

15

$$-\frac{\ddot{v}}{c_L^2} = \frac{p_0^\theta(1-\nu^2)}{Eh}, \qquad (2.2)$$

$$\frac{\nu}{a}\frac{\partial u}{\partial x} + \frac{1}{a^2}\frac{\partial v}{\partial \theta} + \frac{w}{a^2} + \beta^2\left(a^2\frac{\partial^4 w}{\partial x^4} + 2\frac{\partial^4 w}{\partial x^2 \partial \theta^2} + \frac{1}{a^2}\frac{\partial^4 w}{\partial \theta^4} + \frac{4-\nu}{2(1-\nu)}\frac{1}{a^2}\frac{\partial^2 w}{\partial \theta^2}\right.$$

$$\left. + \frac{2+\nu}{2(1-\nu)}\frac{w}{a^2}\right) + \frac{\ddot{w}}{c_L^2} - \frac{p_a(1-\nu^2)}{Eh} = \frac{p_0^r(1-\nu^2)}{Eh}, \qquad (2.3)$$

where β is the shell thickness parameter given by $\beta^2 = h^2/12a^2$, a is the mean radius of the shell and h is the shell thickness. The extensional phase speed in the shell material is defined as $c_L = \sqrt{E/\rho_s(1-\nu)^2}$, where E, ν and ρ_s are the Young's modulus, the Poisson's ratio and the specific mass of the shell material, respectively. Note that the pressure fluid loading, $p_a(\theta, x)$, acts normally to the cylindrical surface of the shell and thus only appears in the third equation.

The assumed solution for the displacement of the shell wall, associated with an axial wavenumber k_{ns}, consists of standing waves in the circumferential direction

$$u = \sum_{n=0}^{\infty}\sum_{s=1}^{\infty} U_{ns}\cos(n\theta)e^{i(k_{ns}x-\omega t-\pi/2)}, \qquad (2.4)$$

$$v = \sum_{n=0}^{\infty}\sum_{s=1}^{\infty} V_{ns}\sin(n\theta)e^{i(k_{ns}x-\omega t)}, \qquad (2.5)$$

$$w = \sum_{n=0}^{\infty}\sum_{s=1}^{\infty} W_{ns}\cos(n\theta)e^{i(k_{ns}x-\omega t)}. \qquad (2.6)$$

The subscript "ns" refers to a particular wave s of circumferential order n. The circumferential mode shapes are illustrated in Figure 2.2.

The acoustic wave equation for the internal fluid in the cylindrical co-ordinate
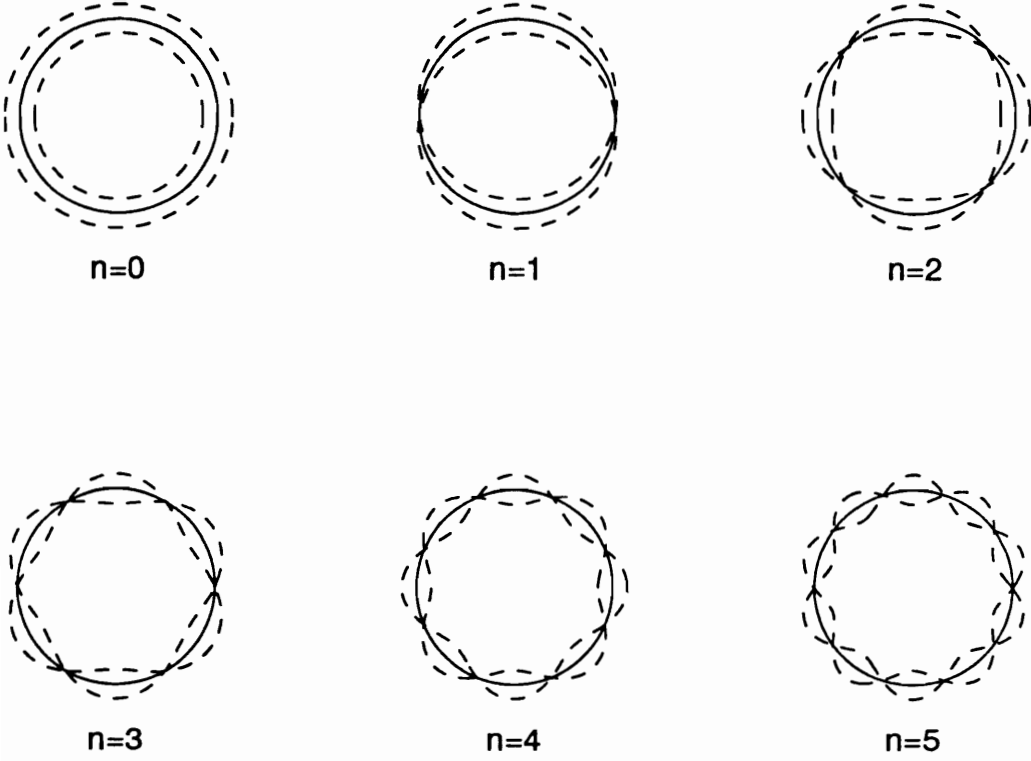
Figure 2.2: Circumferential mode shapes.

system is [41]

$$\frac{\partial^2 p}{\partial x^2} + \frac{1}{r}\frac{\partial}{\partial r}(r\frac{\partial p}{\partial r}) + \frac{1}{r^2}\frac{\partial^2 p}{\partial \theta^2} - \frac{1}{c_f^2}\frac{\partial^2 p}{\partial t^2} = 0, \tag{2.7}$$

where c_f denotes the speed of the acoustic free wave in the fluid.

An assumed form of the pressure field in the contained fluid which satisfies this equation is:

$$p = \sum_{n=0}^{\infty}\sum_{s=0}^{\infty} P_{ns}\cos(n\theta)J_n(k_s^r r)e^{i(k_{ns}x-\omega t)}, \tag{2.8}$$

where k_s^r is given by the vector relation

$$(k_s^r)^2 = k_f^2 - k_{ns}^2. \tag{2.9}$$

k_f in Equation (2.9) is defined as ω/c_f.

At the shell-fluid interface, the radial displacement of the fluid must equal the radial displacement of the shell. Using Euler's equation [41] in the fluid field,

$$-\frac{\partial p}{\partial r} = \rho_f \frac{\partial^2 w}{\partial t^2}, \tag{2.10}$$

where ρ_f is the specific mass of the fluid, and Equations (2.6) and (2.8), we obtain the following relation between pressure and shell radial displacement amplitudes

$$P_{ns} = \frac{\rho_f\omega^2}{k_s^r J_n'(k_s^r a)}W_{ns}. \tag{2.11}$$

The pressure fluid loading at the shell wall can thus be expressed in terms of the shell radial vibration as

$$p_a(\theta, x) = \sum_{n=0}^{\infty}\sum_{s=0}^{\infty} W_{ns}\frac{\rho_f\omega^2 J_n(k_s^r a)}{k_s^r J_n'(k_s^r a)}\cos(n\theta)e^{i(k_{ns}x-\omega t)}. \tag{2.12}$$

In order to study the free vibrations of the system, the forcing function, $\mathbf{p_0}$, whose components p_0^x, p_0^θ and p_0^r appear in the right hand side of Equations 2.1, 2.2 and 2.3, is set equal to zero. Substituting Equations (2.4), (2.5), (2.6) and (2.12) into Equations (2.1), (2.2) and (2.3), the free vibrations of the coupled system can be represented in matrix form as

$$
\begin{bmatrix} L_{11} & L_{12} & L_{13} \\ L_{21} & L_{22} & L_{23} \\ L_{31} & L_{32} & L_{33} \end{bmatrix} \begin{bmatrix} U_{ns} \\ V_{ns} \\ W_{ns} \end{bmatrix} = \begin{bmatrix} 0 \\ 0 \\ 0 \end{bmatrix}, \tag{2.13}
$$

$$
L_{11} = -\Omega^2 + (k_{ns}a)^2 + \frac{1}{2}(1-\nu)n^2, \quad L_{12} = \tfrac{1}{2}(1+\nu)n(k_{ns}a), \quad L_{13} = \nu(k_{ns}a),
$$

$$
L_{21} = L_{12}, \quad L_{22} = -\Omega^2 + \tfrac{1}{2}(1-\nu)(k_{ns}a)^2 + n^2, \quad L_{23} = n - \frac{h^2}{8a^2}\frac{\nu}{1-\nu}n(n^2-1),
$$

$$
L_{31} = L_{13}, \quad L_{32} = n,
$$

$$
L_{33} = -\Omega^2 + 1 + \beta^2 \left\{ \left[(k_na)^2 + n^2\right]^2 - \frac{4-\nu}{2(1-\nu)}n^2 + \frac{2+\nu}{2(1-\nu)} \right\} - FL,
$$

where Ω is the non-dimensional frequency, defined as $\Omega = \omega a/c_L$. FL is the fluid loading term due to the presence of the fluid acoustic field,

$$
FL = \Omega^2 \frac{\rho_f}{\rho_s}(\frac{h}{a})^{-1}\frac{J_n(k_s^r a)}{(k_s^r a)J_n'(k_s^r a)}. \tag{2.14}
$$

In terms of the shell non-dimensional frequency Ω, the radial fluid wavenumber $k_s^r a$ is related to the axial wavenumber $k_{ns}a$ by the expression

$$
k_s^r a = \pm\sqrt{\Omega^2(c_L/c_f)^2 - (k_{ns}a)^2}. \tag{2.15}
$$

The homogeneous system of equations (2.13) does not have a solution unless

19

the determinant of the matrix $\mathbf{L}$ is zero,

$$|\mathbf{L}| = 0. \tag{2.16}$$

Equation (2.16) provides the characteristic equation of the coupled system. Solving Equation (2.16) for $k_{ns}a$, for various non-dimensional frequencies Ω, yields the so called dispersion curves of the coupled system.

2.2 Dispersion curves

Different numerical techniques which have been used to determine the roots of Equation (2.16) are discussed in this section. Following this, the quality of Kennard's shell equations is appraised by comparing, for a simple shell system, the dispersion plots emanating from various shell theories. Finally, dispersion plots for two different types of shells (*in vacuo* and filled with water) are presented and analyzed.

2.2.1 Root searching procedure

In order to determine the roots of the characteristic equation, it is first assumed that the shell material is undamped. Considering an *in vacuo* shell, i.e. FL=0 in Equation (2.13), the characteristic equation (2.16) is a fourth order polynomial in $(k_{ns}a)^2$ and it can be solved for $(k_{ns}a)^2$ using Laguerre's method for example (IMSL subroutine DZPLRC [42]). The corresponding dispersion curves for one direction of propagation consist of four different waves or branches. With the inclusion of an internal fluid loading, it can be proved that the transcendental Equation (2.16) has

an infinite number of roots; this result is made apparent by expressing the Bessel functions in Equation (2.14) as power series. Several steps are thus necessary to find the most important roots of the characteristic equation. First, similar to Fuller's method [20], an approximate location of the purely real roots and the purely imaginary roots is determined using a stepping procedure and testing the sign of the left-hand term of Equation (2.16). Singularities in the characteristic function are eliminated by noting that these occur when the fluid loading term FL changes sign [20]. The actual roots are then found by using an algorithm that combines linear interpolation, inverse quadratic interpolation and the bisection method (IMSL subroutine DZBREN [42]). The complex roots associated with the near field waves in the system are obtained from an algorithm using Müller's method and the *in vacuo* near field waves as initial guesses (IMSL subroutine DZANLY [42]). Finally, structural damping can be added to the shell material. Then, all the corresponding roots of the system become complex, as will be seen in Section 2.2.4. They are obtained by means of Müller's method and using the pre-determined roots of the characteristic equation as initial guesses. If the damping in the shell material is large, as in the case of rubbers or glassy materials for example (see Section 2.2.4), it is necessary to start with a small value of damping, find the associated roots and iterate the procedure until the desired amount of damping in the shell material is reached.

2.2.2 Validity of Kennard's shell equations

At this point, it is important to assess the quality of the Kennard's shell equations by comparing the dispersion curves (real roots) of an *in vacuo* steel shell
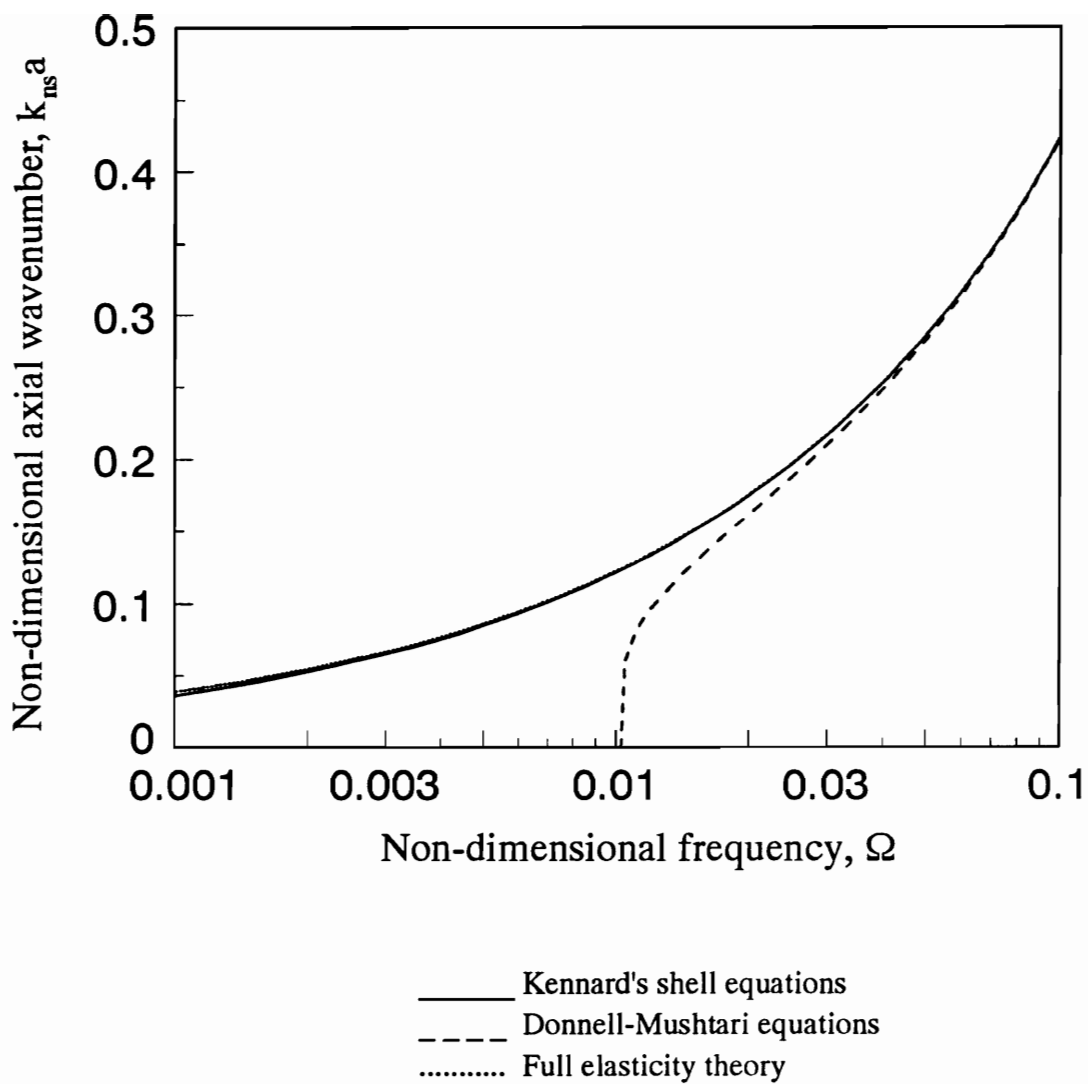
Figure 2.3: Dispersion curves (real roots) obtained from various shell equations, considering a steel shell *in vacuo*, h/a=0.05, n=1, $\Omega \in [0.001; 0.1]$.

22
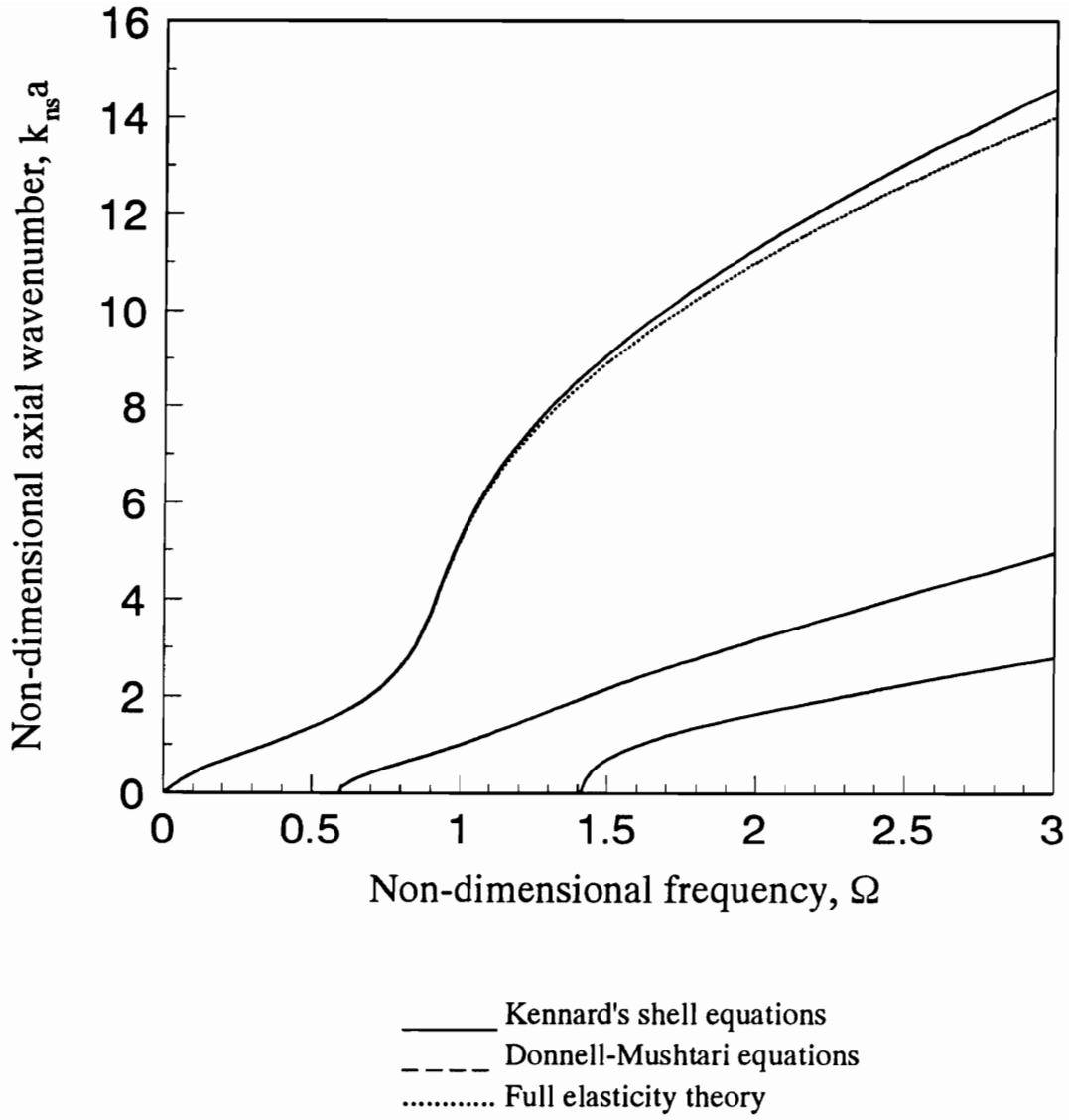
Figure 2.4: Dispersion curves (real roots) obtained from various shell equations, considering a steel shell *in vacuo*, h/a=0.05, n=1, $\Omega \in [0.1; 3]$.

using the Donnell-Mushtari shell equations [20], Kennard's shell equations and the full elasticity theory [13]. Results for the propagating wave of circumferential order n=1 in the very low non-dimensional frequency range [0.001;0.1], using the three different formulations, are shown in Figure 2.3. While the results using Kennard's equations and the full elasticity theory seem to agree very well, the Donnell-Mushtari shell equations predict that there is no wave which can propagate at frequencies below $\Omega = 0.01$. This contradicts experimental observations and contravenes the expectation that flexural vibrations of a pipe are analogous to those of a rod at low frequencies.

Figure 2.4 shows the dispersion curves in the non-dimensional frequency range $\Omega \in [0.1; 3]$. In this range, Kennard's and the Donnell-Mushtari shell equations yield the same dispersion curves. However, the full elasticity theory predicts a slower phase speed of the flexural wave at frequencies above the ring frequency $\Omega = 1$. This gap increases with frequency because the simplified equations neglect rotary inertia and transverse shear forces, whose effects also increase with frequency. However, the error introduced by the simplified shell equations remains relatively small, below 2%, in the frequency range $\Omega \in [0.1; 3]$. Therefore, in the non-dimensional frequency range [0;3], Kennard's shell equations provide a good alternative to the complex shell theory that is based on a full elasticity of the shell material.

2.2.3 Dispersion plots of undamped shell systems

The damping in the shell material is first assumed to be zero and will be considered in the next section. Typical dispersion curves for a steel shell of thickness

24

h/a=0.05 vibrating in the breathing mode (n=0), *in vacuo* and filled with water, are shown in Figures 2.5 and 2.6. The properties of the material used in the calculations are indicated in Table 2.1. Note that, when considering an *in vacuo* shell, the essential nature of each wave, i.e. whether it is flexural, extensional, torsional, etc..., can be determined from the amplitude ratios, U_{ns}/W_{ns} and V_{ns}/W_{ns}, obtained by re-substituting the roots of the characteristic equation into the equations of motion (2.13) [3]. For each waves propagating in a fluid-filled shell, there is a distribution of vibrational energy between the shell wall and the contained fluid. The solution for this energy distribution has been derived by Fuller and Fahy [20]. The degree to which the energy is concentrated in the fluid or in the shell wall provides additional information on the nature of a travelling wave.

Considering an *in vacuo* shell, there are two waves denoted as s=1 and 2 which are purely real and thus propagating at low frequencies. The s=2 wave is a pure torsional shear wave. It is uncoupled from the radial shell motion and it is thus unaffected by a fluid loading, as Figure 2.6 reveals. The s=1 wave is extensional in nature at low frequencies and changes into a flexural wave around the ring frequency $\Omega = 1$, at which its wavelength equals the mean circumference of the shell. At frequencies below $\Omega = 1$, the complex branches s=3 and 4 together represent an attenuated standing wave in the positive x direction. This bending near field changes into an extensional wave and a flexural near field above the ring frequency.

If the shell is now filled with water, two waves, denoted as s=1 and 2, in addition to the torsional shear wave (denoted as s=0), can propagate at all frequencies. The branch s=1 is an "acoustically slow" wave, relatively close in nature

Table 2.1: Shell characteristics and material properties.

Material	Steel	Plexiglass	Water
Thickness ratio h/a	0.05	0.0426	—
Young's modulus (N/m^2)	19.2×10^{10}	1.9175×10^9	—
Poisson's ratio	0.3	0.4	—
Specific mass (kg/m^3)	7800	1109	1000
Free wave speed (m/s)	5200	1435	1500
Damping Ratio η	$5. \times 10^{-4}$	0.036	0
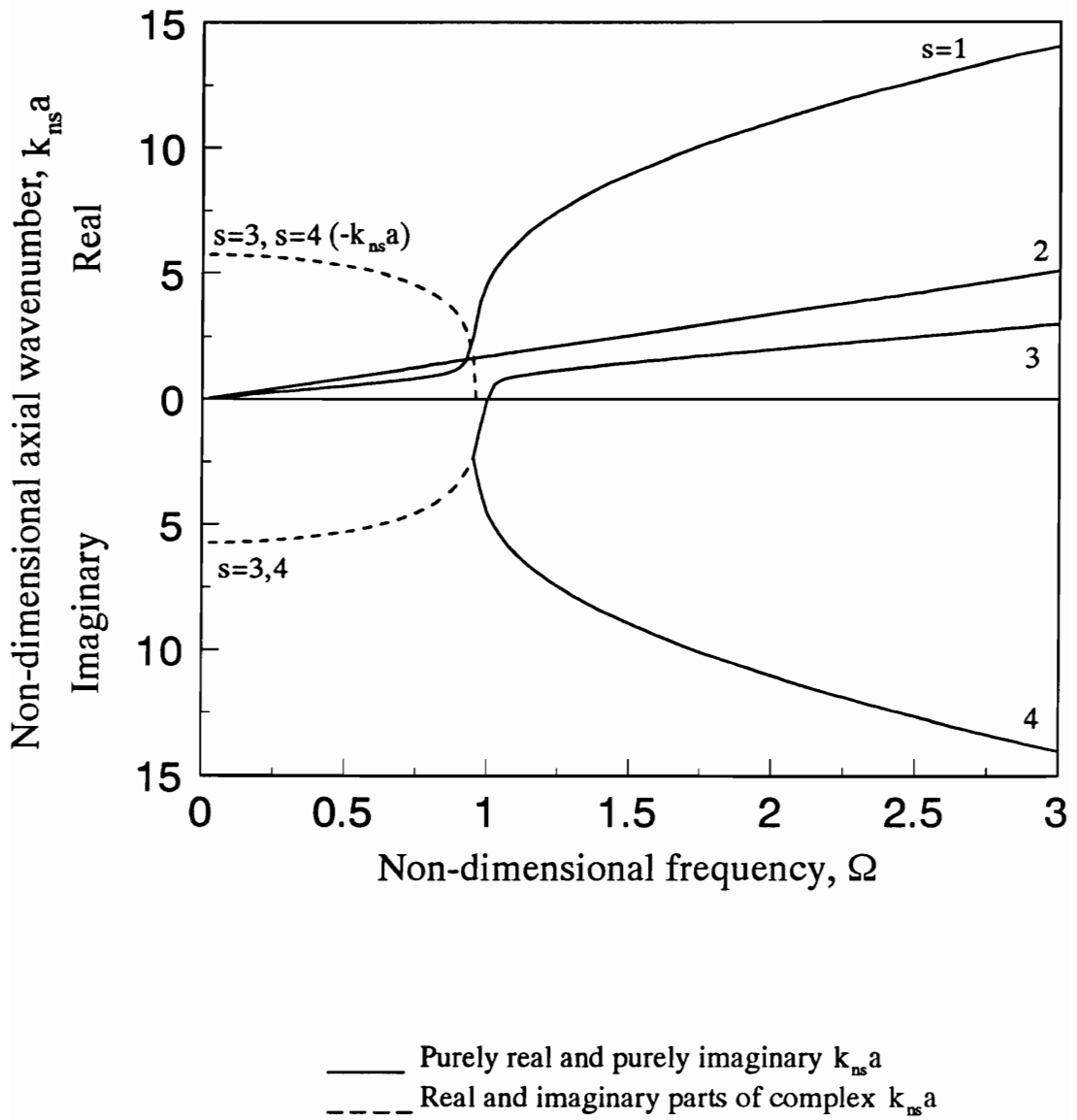
Figure 2.5: Dispersion curves for an *in vacuo* steel shell, h/a=0.05, n=0.
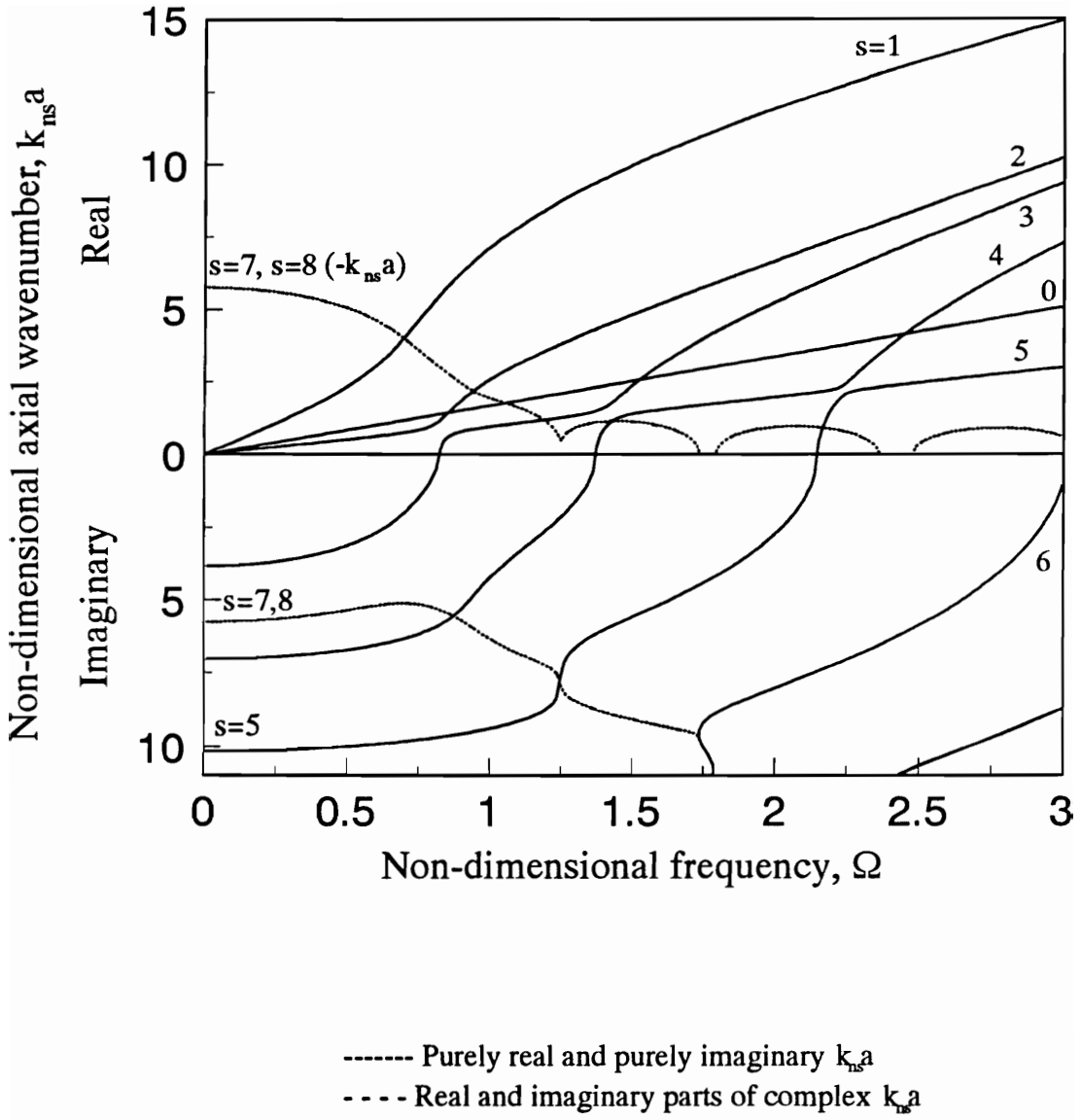
Figure 2.6: Dispersion curves for a water-filled steel shell, h/a=0.05, n=0.

to the acoustic plane wave in a rigid-walled tube at low frequencies. This branch approaches the *in vacuo* flexural solution at very high frequencies. The main characteristic of this wave is that its radial wavenumber is purely imaginary at all frequencies. This implies that, in the fluid field, the nature of the wave consists of a pressure near field located close to the shell wall. In more physical terms, the fluid loading for this particular wave appears as a mass loading added on the inner side of the structure. The branch s=2 is a structural type of wave at low frequencies, close to the *in vacuo* extensional solution. Because of the heavy fluid introduced in the system and the induced coupling phenomenon, this branch turns into a pressure release duct solution above the ring frequency [20]. Around the frequency $\Omega = 0.85$ at which the coupled system strongly resonates as a ring, a fourth branch (s=3) becomes propagative. The frequency at which a branch wavenumber changes from imaginary to real is called the cut-on frequency. The branch s=3 initially follows the *in vacuo* extensional shell solution until it coincides with a fifth branch that cuts on at $\Omega = 1.3$. Around this frequency, the nature of s=3 wave approaches the second rigid walled duct mode. The higher order branches, s=4,5,..., have a behaviour which is very similar to that of the branch s=3, cutting on as fluid waves and changing to extensional shell waves while the preceding shell type branch converts to a fluid wave.

Considering the beam mode (n=1) and an *in vacuo* shell (Figure 2.7), there is only one wave (s=1) that propagates undamped at low frequencies. Fuller has shown that the amplitude ratio V_{ns}/W_{ns} associated with this wave approaches unity below the ring frequency [3]. This implies that the nature of the s=1 wave in this frequency range is neither largely flexural nor largely torsional; in fact, the shell motion approaches that of a simple rod. Past the ring frequency however, the
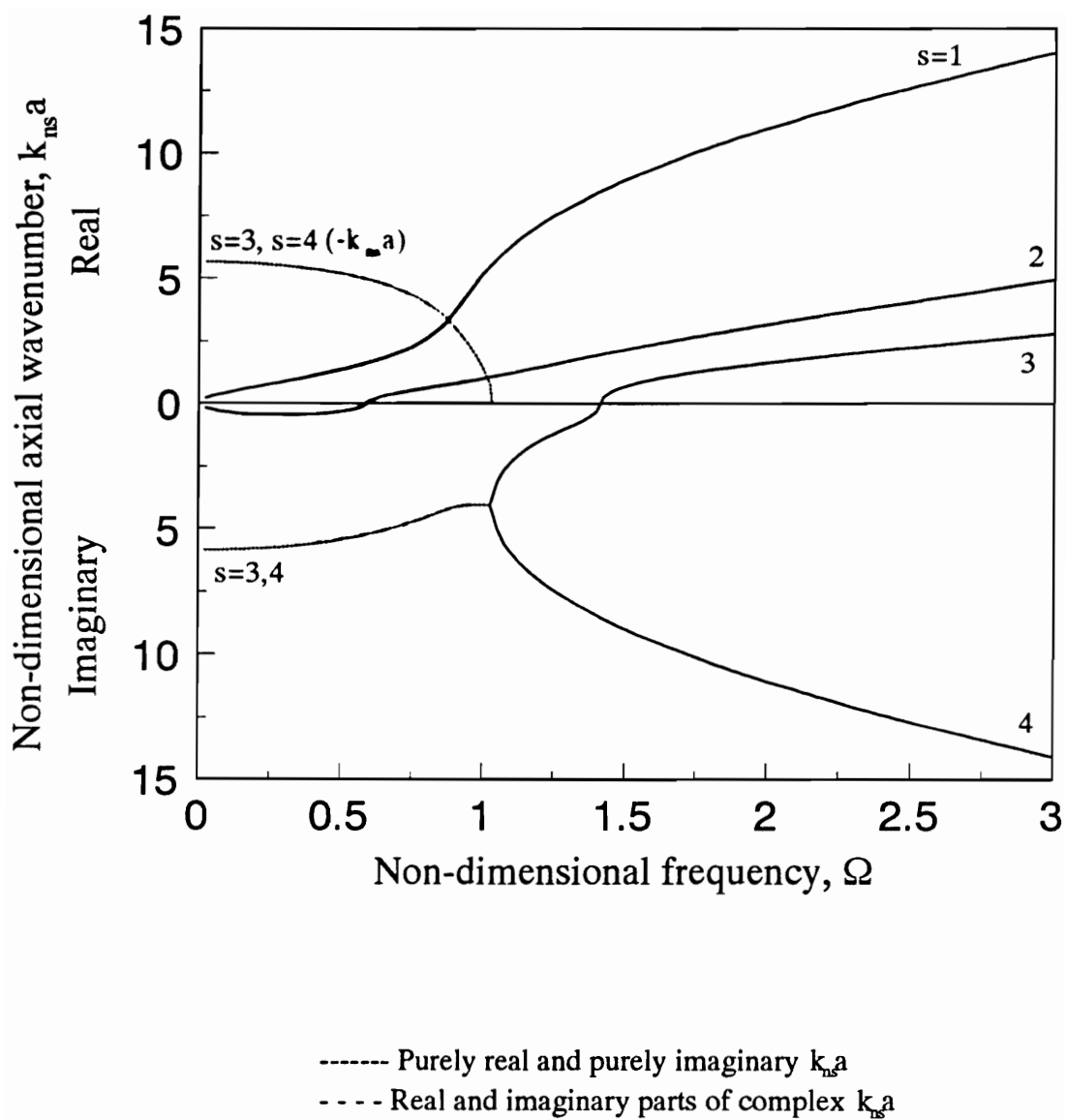
Figure 2.7: Dispersion curves for an *in vacuo* steel shell, h/a=0.05, n=1.

nature of the s=1 wave changes markedly and becomes mostly flexural. The s=2 wave is purely imaginary at low frequencies and can not actually propagate energy. However, because its imaginary part is very small, the bending motion associated with this wave is lightly damped. The s=2 wave can be seen to cut on around $\Omega = 0.6$ and turns rapidly into a torsional shear wave.

Considering the water-filled shell (Figure 2.8), the dispersion curves resemble those of the breathing mode, except for the few differences that appear between the *in vacuo* dispersion plots. Again, only one wave (s=1) propagates energy at low frequencies. The main characteristic of this wave is that its radial wavenumber is imaginary at all frequencies. This means that the fluid simply acts as an added mass on the inner side of the shell for this particular wave. The s=2 wave cuts on as a torsional shear wave and, as it encounters the s=3 wave, quickly reverts its behaviour to approach the first rigid walled duct mode of circumferential order n=1. The s=3 wave cuts on as an extensional shell wave, then changes to a torsional type of wave as the branch s=4 cuts on and finally tends toward the second rigid walled duct mode. Such a behaviour, for circumferential modes $n > 0$, leads to two series of plateaux on the dispersion curves, due to coincidences of both torsional and extensional shell waves with acoustic duct waves. For more details on the dispersion curves of the circumferential modes n=0 and n=1, the reader is referred to Fuller and Fahy [20].

The dispersion curves for higher order circumferential modes $(n > 1)$ are very similar to those of the beam mode (n=1). However, the s=1 wave, which cuts on at $\Omega = 0$ for modes n=0 and n=1, does not propagate at low frequencies. This wave is characterized by a non-zero cut-on frequency which increases with the
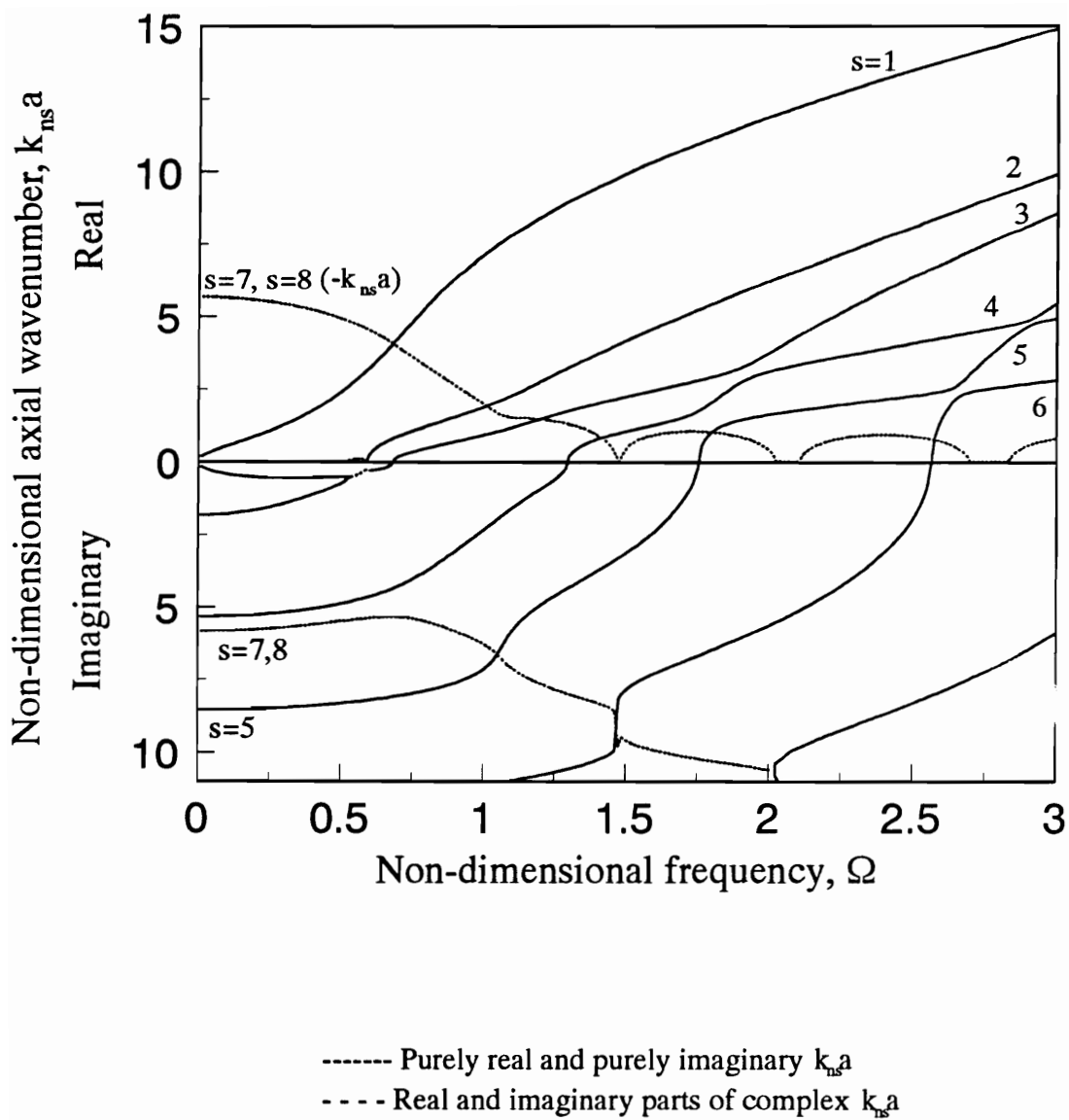
Figure 2.8: Dispersion curves for a water-filled steel shell, h/a=0.05, n=1.

circumferential mode order. Because the s=1 wave is the first wave to cut-on as the frequency is increased, its cut-on frequency is commonly called the cut-on frequency of the circumferential mode. For a shell vibrating *in vacuo*, the cut-on frequency of the high order circumferential modes ($n > 1$) can be evaluated by the following equation [49]:

$$\Omega_{n0} \simeq \frac{\beta(n^2 - 1)n}{\sqrt{1 + n^2 + \beta^2(n^2 - 1)^2}}. \tag{2.17}$$

In Table 2.2 are indicated the cut-on frequencies of the circumferential modes n=2 to 5 for the steel shell *on vacuo*, obtained from the exact characteristic equation (2.16) and from the simplified Flügge equation (2.17). The results reveal the accuracy of Equation (2.17). This equation predicts that the cut-on frequencies of an *in vacuo* shell system are only a function of the shell geometry. The cut-on frequencies of the circumferential modes n=2 to 5 for the steel shell filled with water, obtained from the exact characteristic equation (2.16), appear in Table 2.3. It can be noticed that these frequencies are lower than for the *in vacuo* shell. This behaviour is associated with the overall mass increase of the shell system. At cut-on, the shell motion has infinite axial wavelength and resonates like a single degree of freedom system. If k_n is the shell stiffness associated with a given circumferential mode shape n and m is the mass of the shell per unit length, the natural frequencies of the *in vacuo* shell system can be roughly given by

$$\Omega_n = \frac{a}{c_L}\sqrt{\frac{k_n}{m}}. \tag{2.18}$$

For the fluid-filled shell system, this expression becomes

$$\Omega_n = \frac{a}{c_L}\sqrt{\frac{k_n}{m + m'}}, \tag{2.19}$$

where m' is the mass of the fluid per unit length of shell.

For various reasons, which will be detailed in Chapter 5, the experimental validation of the theory developed in Chapters 3 and 4 was performed on a plexiglass cylindrical shell whose properties are given in Table 2.1. It is thus important to extend the theoretical work and study this shell configuration, in addition to the steel shell which is commonly utilized in industrial applications.

The damping in the shell material is again assumed to be zero and will be considered in Section 2.2.4. Using non-dimensional frequencies $\Omega = \omega a/c_L$ on the x-axis, the dispersion plots (Figures 2.9 and 2.10) for the modes n=0 and n=1 obtained for an *in vacuo* plexiglass shell are very similar to those of the steel shell. However, as the phase speed c_L of the extensional wave in plexiglass is much lower than in steel, the actual frequencies ω considered in the plots are much lower (approximately 3.5 times lower). For this reason, when considering the plexiglass shell filled with water (Figures 2.11 and 2.12), the acoustic modes cut on at much higher values of non-dimensional frequency Ω than with a water-filled steel shell of the same dimensions. The dispersion curves for the plexiglass shell filled with water are thus very different from those obtained previously for the water-filled stell shell.

Figure 2.11 shows the results for a plexiglass shell filled with water and vibrating in the breathing mode (n=0). The s=0 wave is a torsional shear wave uncoupled from any other motion. The s=1 wave is an acoustically slow wave, close to the rigid walled acoustic plane wave at very low frequencies and quickly changing to a shell type of wave as the frequency increases. The s=2 wave is extensional in nature over the entire frequency range $\Omega \in [0; 3]$. The first cut-on of an acoustic type of wave occurs near $\Omega = 2.4$. For $\Omega < 2.4$, the fluid thus appears to have

Table 2.2: Cut-on frequencies of high order circumferential modes for a steel shell *in vacuo.*

Mode order	Exact cut-on frequency obtained from Eq. (2.16)	Cut-on frequency obtained from Flügge Eq. (2.17)
2	0.039	0.039
3	0.110	0.109
4	0.211	0.210
5	0.341	0.339

Table 2.3: Cut-on frequencies of high order circumferential modes for a steel shell filled with water.

Mode order	Cut-on frequency
2	0.028
3	0.083
4	0.166
5	0.279
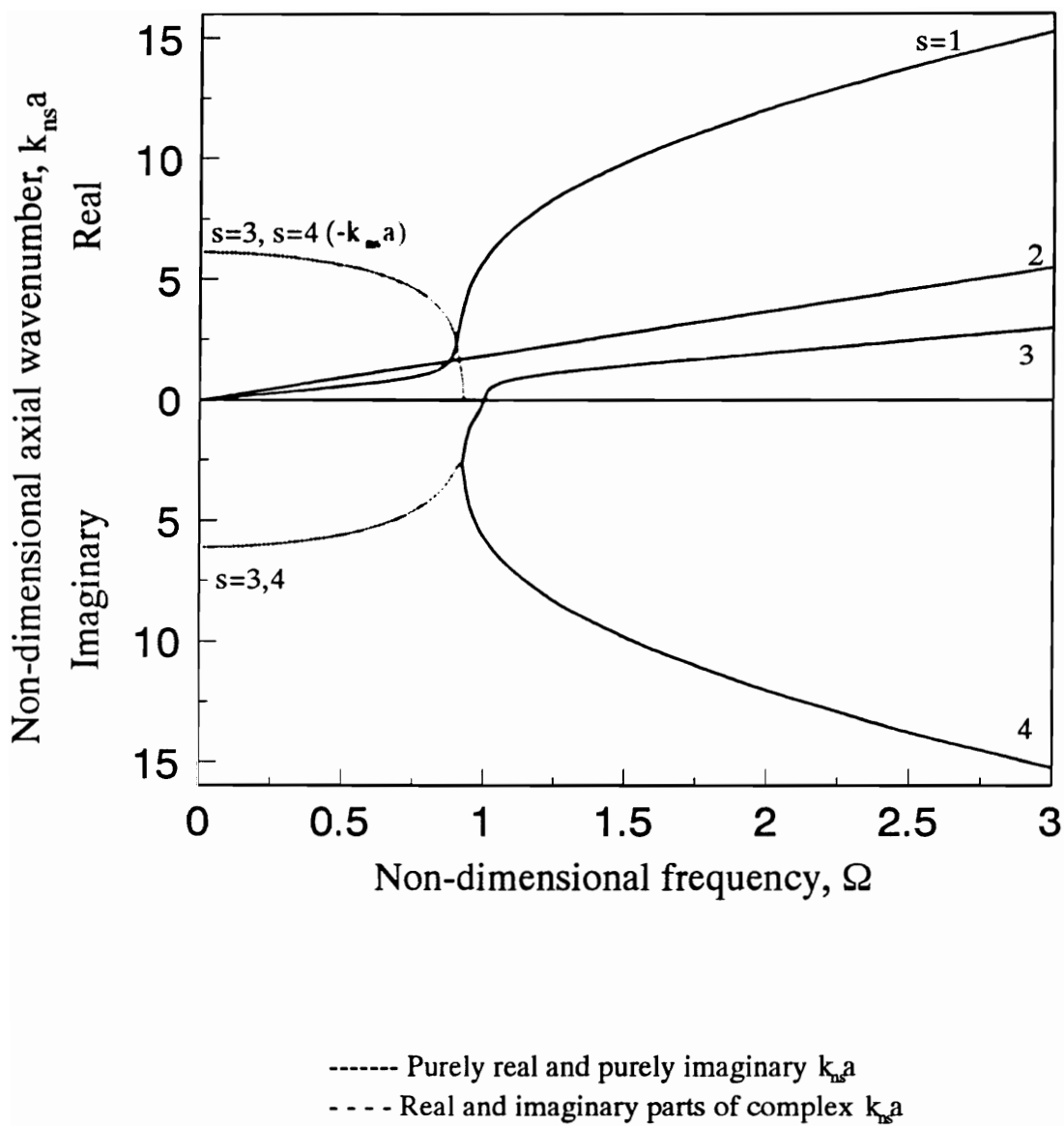
Figure 2.9: Dispersion curves for an *in vacuo* plexiglass shell, h/a=0.05, n=0.
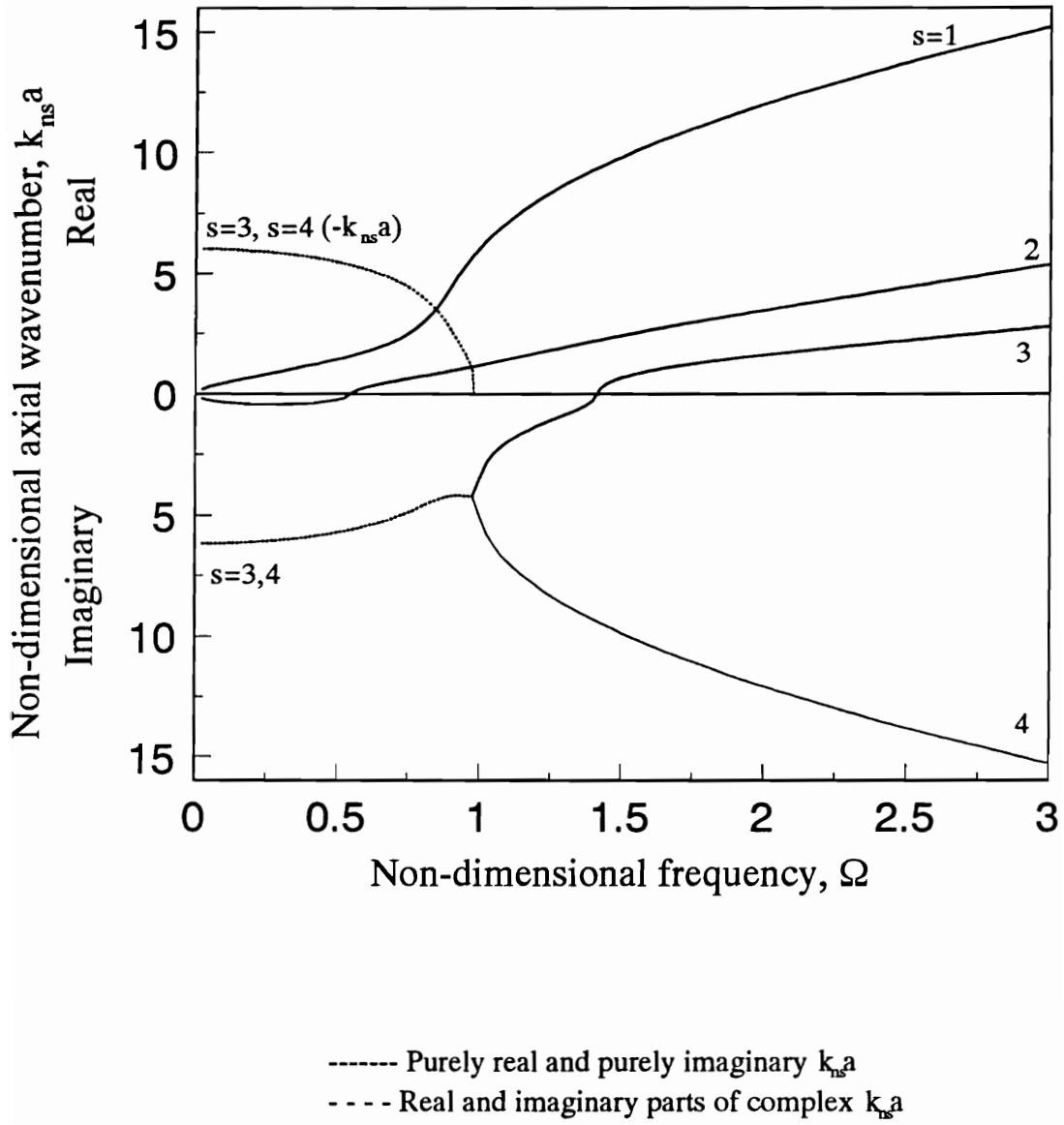
Figure 2.10: Dispersion curves for an *in vacuo* plexiglass shell, h/a=0.05, n=1.

38

a high impedance relative to the shell wall. This has been previously noticed by Fuller *et al.* when studying hard rubber shells with properties approaching those of plexiglass [20].

The dispersion curves for the beam mode (Figure 2.12) reveal similar effects of the change in shell material. The s=2 wave cuts on as a torsional shear wave and remains purely torsional throughout the frequency range. The s=3 wave cuts on as an extensional shell wave and it is unaffected by the fluid in the frequency range studied.

The cut-on frequencies of the circumferential modes n=2 to 5 for *in vacuo* and water-filled plexiglass shells are indicated in Table 2.4. They were obtained from the exact characteristic equation (2.16). The plexiglass shell is slightly thinner than the steel shell and, therefore, the cut-on frequencies for the *in vacuo* plexiglass shell are slightly smaller than for the *in vacuo* steel shell, as expected from Equation (2.17). The differences between the cut-on frequencies for the *in vacuo* shell and those for the water-filled shell appear substantial because of the high impedance of the water relative to the plexiglass shell wall.

2.2.4 Effect of shell hysteretic damping on the dispersion plots

Up to this point, it has been assumed that the shell materials were undamped. However, all real materials dissipate energy, no matter how little, during cyclic deformation [43]. This energy loss is very small in steel but relatively important in glassy materials like plexiglass. The inorganic oxides found in glass form different lattice geometries. Damping arises from the relaxation processes that occurs

39
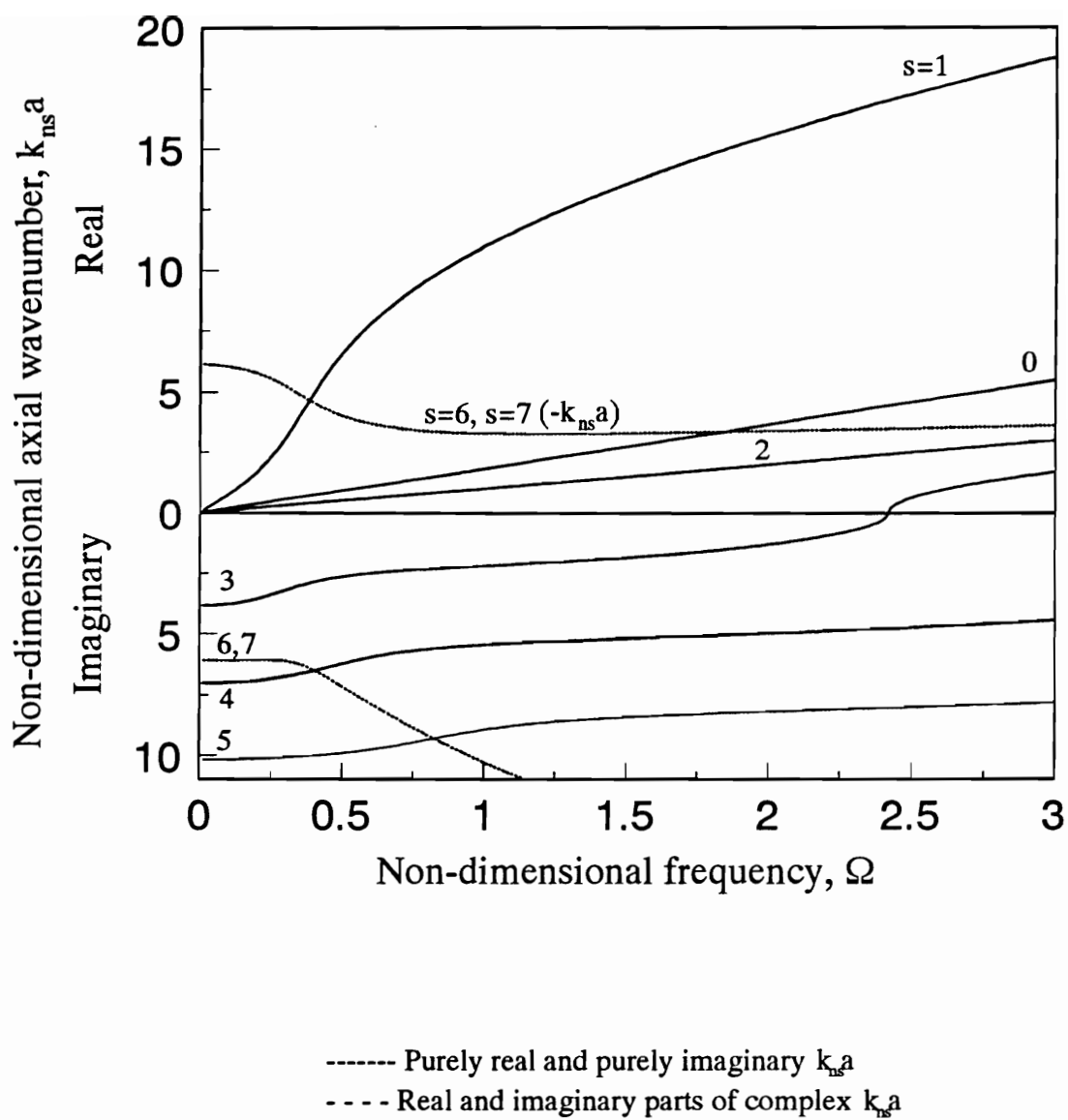
Figure 2.11: Dispersion curves for a water-filled plexiglass shell, h/a=0.05, n=0.

40
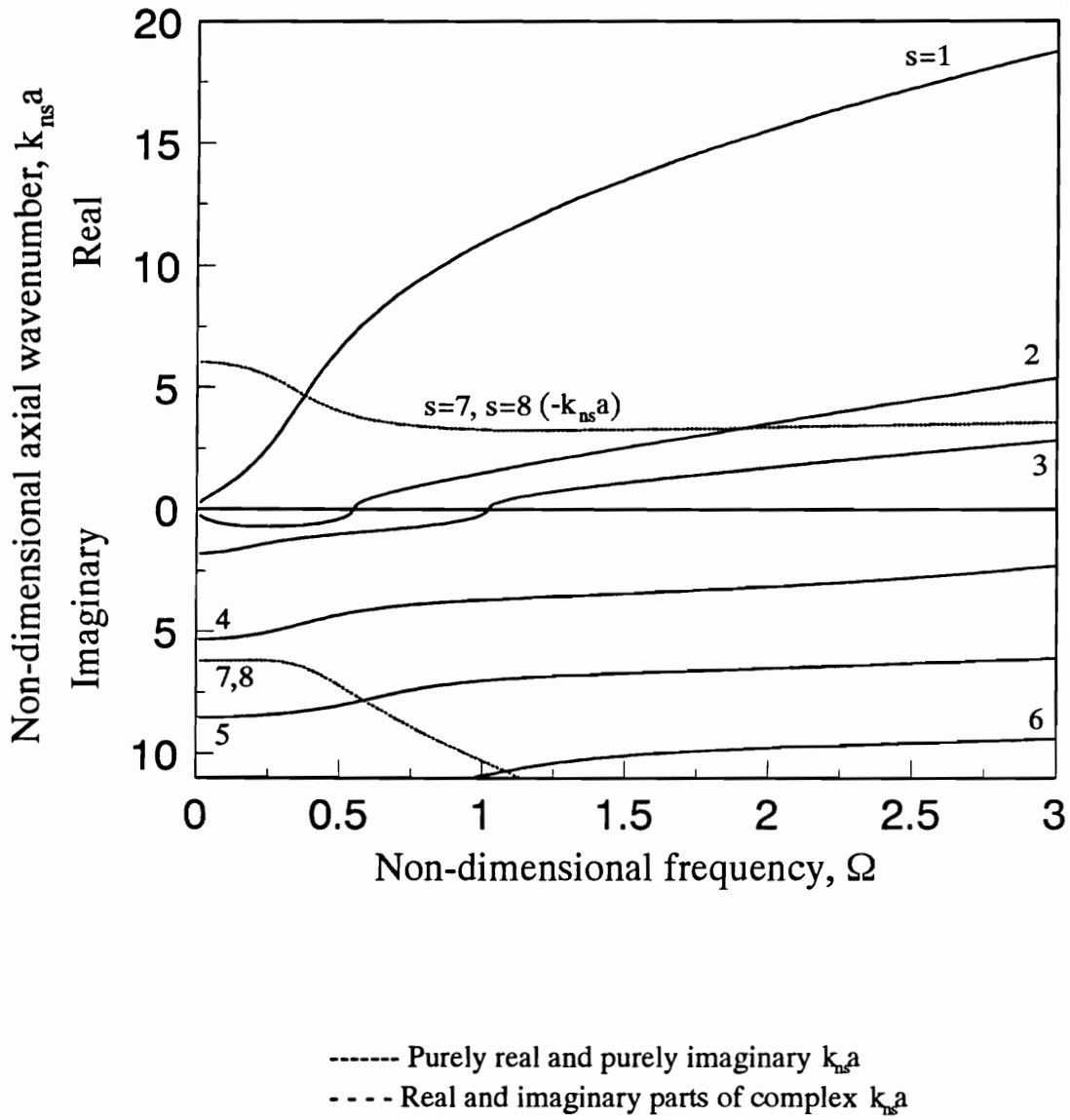
Figure 2.12: Dispersion curves for a water-filled plexiglass shell, $h/a=0.05$, $n=1$.

The plot shows:
- Y-axis: Non-dimensional axial wavenumber, $k_{ns}a$ (Real above, Imaginary below, values 20, 15, 10, 5, 0, 5, 10)
- X-axis: Non-dimensional frequency, Ω (values 0, 0.5, 1, 1.5, 2, 2.5, 3)
- Curve labels: $s=1$, 2, 3, $s=7$, $s=8$ ($-k_{ns}a$), 4, $7,8$, 5, 6

Legend:
------- Purely real and purely imaginary $k_{ns}a$
- - - - Real and imaginary parts of complex $k_{ns}a$

41

Table 2.4: Cut-on frequencies of high order circumferential modes for *in vacuo* and water-filled plexiglass shells.

Mode order	*In vacuo* shell cut-on frequencies	Water-filled shell cut-on frequencies
2	0.033	0.011
3	0.095	0.036
4	0.183	0.074
5	0.294	0.129

after deformation, the recovery being due to various conditions of thermodynamic equilibrium [43]. As explained by Nashif *et al.* [43], the complex Young's modulus approach, $E' = E(1 - j\eta)$, is a valid and convenient way to model the energy dissipation in materials for frequency domain analyses. The sign of the imaginary part of E' was chosen to obtain a decay of the wave amplitudes as propagation occurs. As only steady state harmonic response of the system is of concern in this study, the hysteretic assumption, for which E and η are considered constant over a frequency range at a specific temperature, can be used; note that this assumption leads to causality problems when considering the transient response [43]. In addition, as η is smaller than 0.1 for both shell materials used in this analysis, the constant E, η model can be seen as a good representation of the real system behavior in the frequency range $\Omega \in [0; 3]$. Values for the loss factor η in common materials can be found in [44]. The actual values of η for steel and plexiglass materials used in this analysis appear in Table 1. The value of η for plexiglass was obtained from experimental data, as will be described in Chapter 5.

The addition of 0.05% hysteretic damping in steel has very little effect on the dispersion curves. The main effect appears on the initially purely real roots; they now reveal a very small imaginary part associated with a slight attenuation of the wave amplitude as propagation occurs. Considering the plexiglass shell, the effect of 3.6% damping on the real branches of the dispersion curves becomes relatively important. Figure 2.13 shows the imaginary part of the propagating waves for an *in vacuo* plexiglass shell vibrating in the breathing mode. Note that the real part of the waves is unchanged from the results shown in Figure 2.9. One can notice from Figure 2.13 that damping mainly affects the s=1 branch. The imaginary part of the s=1 wave is particularly large near the ring frequency at which the shell resonates as

a ring. The attenuation is also large on the s=2 branch as it cuts on. The torsional shear wave is lightly affected by the structural damping.

When the shell is filled with water (Figure 2.14), the effect of hysteretic damping on the dynamics of the system is much smaller than when the shell is *in vacuo*. This is again due to the high impedance of the fluid relative to the shell wall. One may notice that the damping effect on the s=1 wave at low frequencies increases sharply between $\Omega = 0$ and 0.4, as the branch characteristics change from those of a rigid walled acoustic plane wave to those of a shell type of wave, near field at the wall. Above $\Omega \simeq 0.4$, the attenuation of the s=1 wave is moderate and relatively constant.
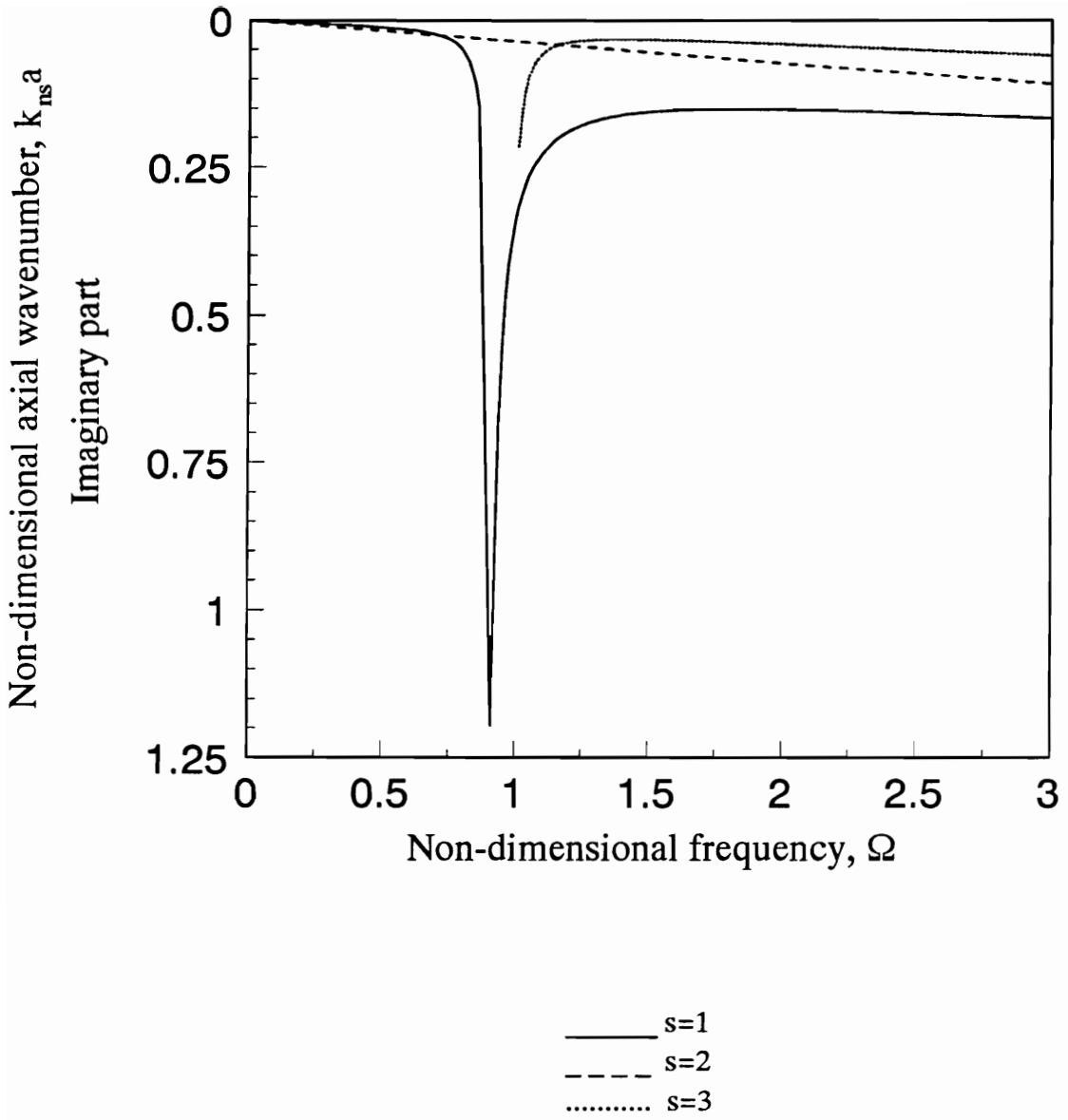
Figure 2.13: Imaginary part of propagating free waves in an *in vacuo* plexiglass shell, $\eta = 3.6\%$, h/a=0.05, n=0.
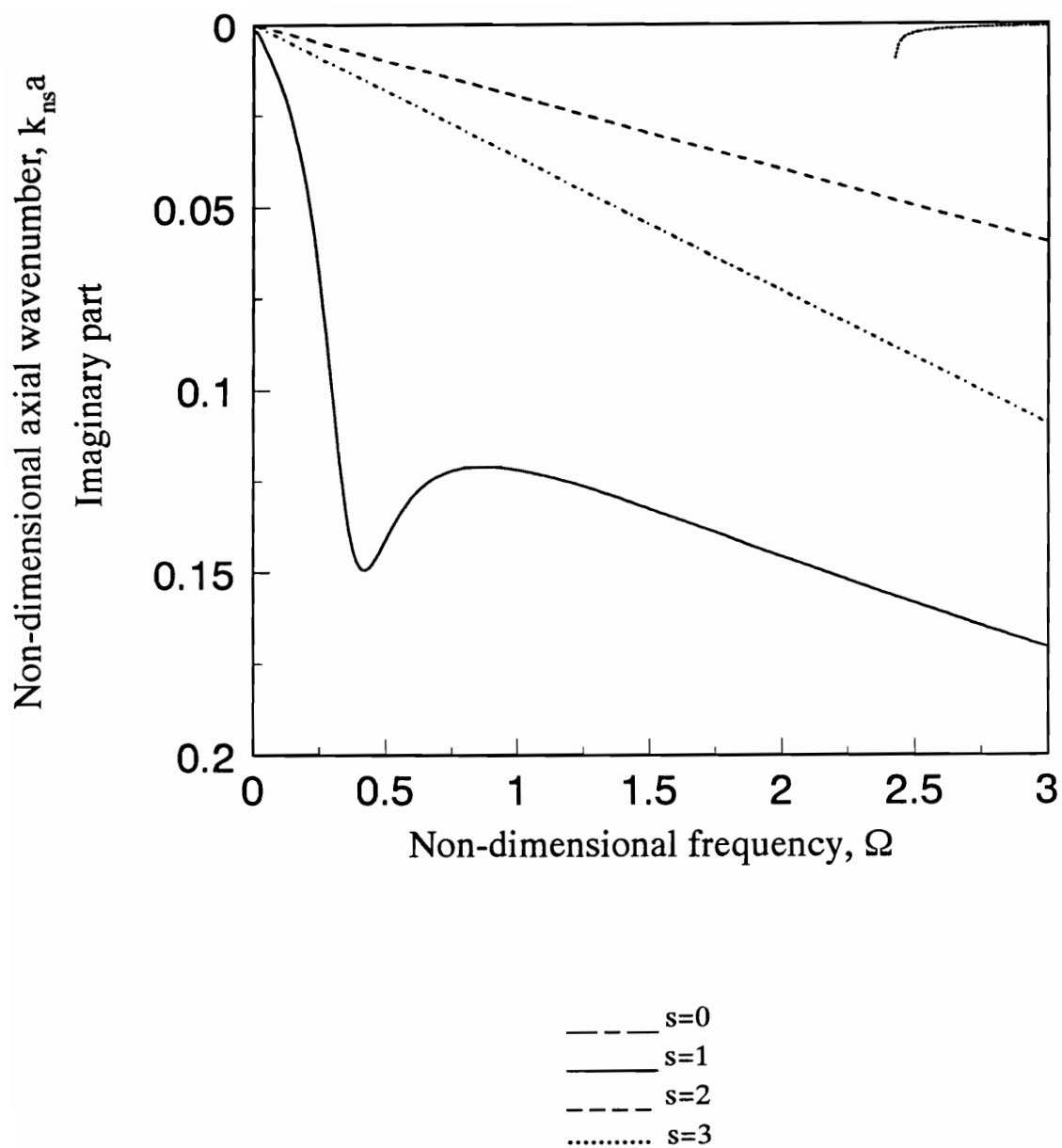
Figure 2.14: Imaginary part of propagating free waves in a water-filled plexiglass shell, $\eta = 3.6\%$, h/a=0.05, n=0.

Chapter 3

Active Control of Wave Propagation

Harmonic disturbances in real piping systems are often complex and sometimes even unknown. However, as long as the piping system is close to being homogeneous, i.e. suiting the model presented in Chapter 2, the vibrational waves generated by these sources are all solutions of the characteristic equation of the infinite shell system, determined in Chapter 2. Then, depending on the driving source, some of these "free" waves are more excited than others.

In this chapter, the disturbance on the infinite shell system is assumed to be a single propagating free wave s of circumferential order $n = 0$ or $n = 1$. The control forces are radial line forces along the shell circumference. Their dependence upon the circumferential angle follows the distribution of the disturbance field. Radial forces were preferred to other type of forces because they provide the best coupling between the shell wall and the fluid field. The radial displacement of the shell wall at discrete locations downstream of the control forces is minimized using linear quadratic optimal theory. The rationale is that the radial displacement of the shell

47

wall can be measured with sensors made of polyvinylidene fluoride material (PVDF). This will be explained in Chapter 5. The difference of total power flow through the system before and after control is then used to evaluate the impact of the fluid on the performance of the control approach.

3.1 Control configuration

The diagrams in Figure 3.1 describe the arrangements of the two control approaches investigated in this chapter. The first approach (case 1 in Figure 3.1) consists in using one radial control line force with the same circumferential distribution as the incident wave, i.e. n=0 or n=1, to minimize the radial displacement of the shell at one axial position along the circumference of the shell. The second approach (case 2 in Figure 3.1) consists in using two control forces spaced a distance Δx_c apart to minimize the radial displacement at two different locations spaced a distance Δx_e apart. As in case 1, the two control line forces follow the distribution of the disturbance field.

3.2 Incident wave disturbance

The disturbance considered in this investigation is a single propagating free wave which, in terms of shell radial displacement, may be written as

$$w_{ns}^d(x) = W_{ns}^d \cos(n\theta) \, e^{i k_{ns}^d x} \tag{3.1}$$

where the axial wavenumber k_{ns}^d is given by the dispersion curves of the shell system for a mode n, investigated in Chapter 2, and W_{ns}^d is the amplitude of the wave at

Case 1

Minimization Position

Control Force

Residual Vibrations

Incident wave

∞

∞

n=0

∞

∞

n=1

Case 2

Minimization Positions

Control Forces

Δx_c

Δx_e

Residual Vibrations

Incident wave

∞

∞
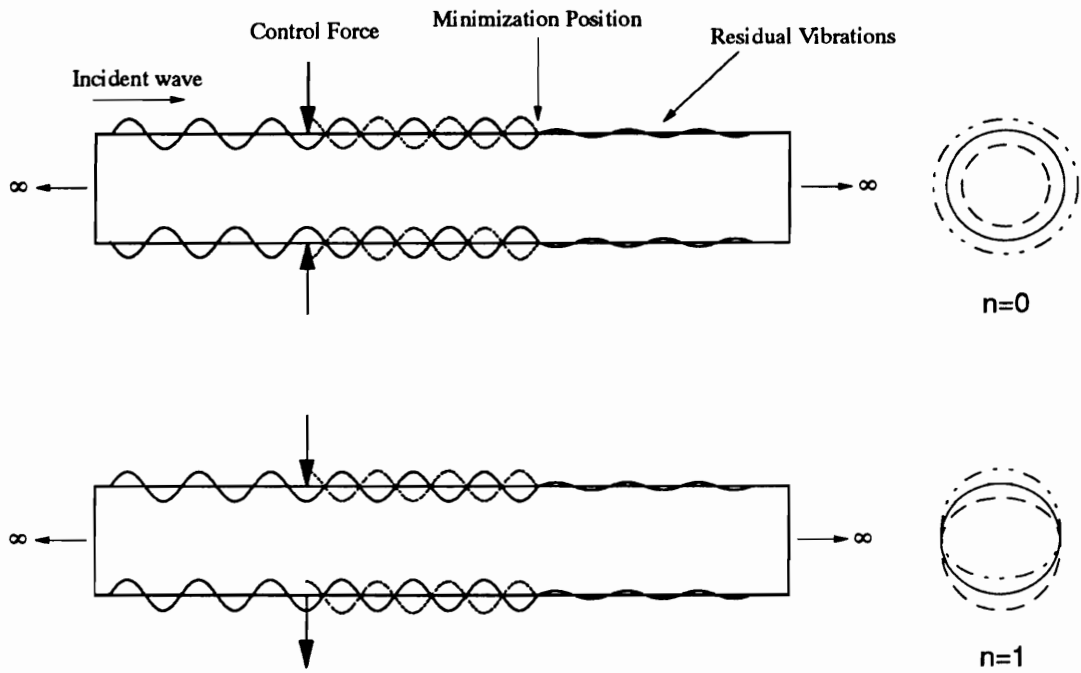
0 x_c^1 x_c^2 x_e^1 x_e^2
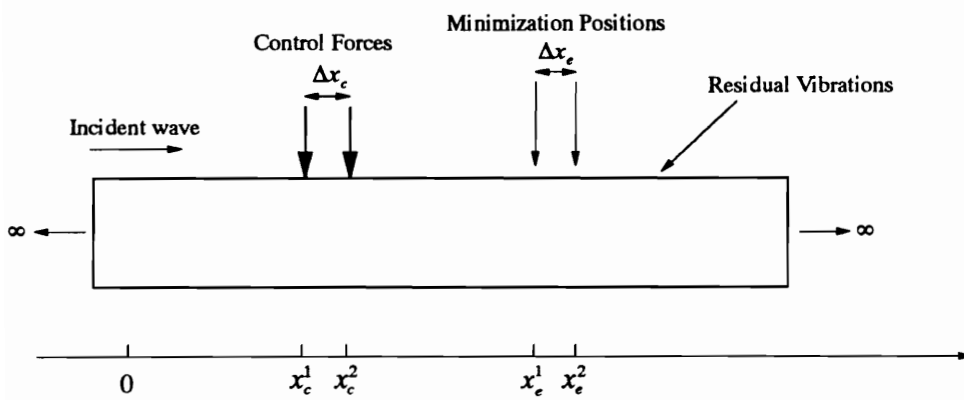
Figure 3.1: Control configurations.

x=0. As discussed previously in Chapter 2, k_{ns}^d is strongly dependent upon the frequency and the type of wave for a given shell system. In addition, due to the added damping in the shell material, the wave amplitude will slightly decay as the wave propagates through the control discontinuity. Finally, as only harmonic vibrations are considered, the time variation $e^{-i\omega t}$ in Equation 3.1 has been omitted.

3.3   Response of a fluid-filled cylindrical shell to a distributed radial line force

As seen in Section 3.1, the control forces considered are radial line forces of the same circumferential distribution as the disturbance. The response of an infinite fluid-filled cylindrical elastic shell to a line force, in terms of shell radial velocity or displacement, has been previously derived by Fuller [29]. For the sake of completeness, Fuller's derivation is included in this section . The solution for the pressure in the fluid field is also presented.

In terms of external pressure loading on the shell wall, a radial line force of circumferential order n applied at x_0 can be written as

$$\mathbf{p_0} = \begin{pmatrix} p_0^x \\ p_0^\theta \\ p_0^r \end{pmatrix} = \begin{pmatrix} 0 \\ 0 \\ F_0 \cos(n\theta)\delta(x - x_0) \end{pmatrix} \tag{3.2}$$

where F_0 has the unit of force per unit length of circumference.

Given a circumferential mode n, the shell displacements, the pressure in the fluid field and the radial component of the forcing function, p_r, are expressed as

inverse wavenumber transforms:

$$u = \frac{1}{2\pi} \int_{-\infty}^{+\infty} \bar{U}_n \cos(n\theta) e^{i(k_n x - \pi/2)} dk_n, \qquad (3.3)$$

$$v = \frac{1}{2\pi} \int_{-\infty}^{+\infty} \bar{V}_n \sin(n\theta) e^{ik_n x} dk_n, \qquad (3.4)$$

$$w = \frac{1}{2\pi} \int_{-\infty}^{+\infty} \bar{W}_n \cos(n\theta) e^{ik_n x} dk_n, \qquad (3.5)$$

$$p = \frac{1}{2\pi} \int_{-\infty}^{+\infty} \bar{P}_n J_n(k^r r) \cos(n\theta) e^{ik_n x} dk_n, \qquad (3.6)$$

$$p_0^r = \frac{1}{2\pi} \int_{-\infty}^{+\infty} F_0 \cos(n\theta) e^{ik_n(x - x_0)} dk_n. \qquad (3.7)$$

The boundary condition at the shell-fluid interface yields the following relation between the spectral amplitudes of the shell radial displacement and the fluid pressure,

$$\bar{P}_n = \frac{\rho_f \omega^2}{k^r J_n'(k^r a)} \bar{W}_n. \qquad (3.8)$$

The pressure fluid loading at the shell wall can thus be expressed as

$$p_a = \frac{1}{2\pi} \int_{-\infty}^{+\infty} \bar{W}_n \frac{\rho_f \omega^2 J_n(k^r a)}{k^r J_n'(k^r a)} \cos(n\theta) e^{ik_n x} dk_n. \qquad (3.9)$$

Substituting Expressions (3.4), (3.5), (3.6) and (3.9) into Kennard's shell equations (Equations (2.1), (2.2) and (2.3) in Chapter 2), one obtains the spectral equations of motion of the forced response of the system in a matrix form:

$$\begin{bmatrix} L_{11} & L_{12} & L_{13} \\ L_{21} & L_{22} & L_{23} \\ L_{31} & L_{32} & L_{33} \end{bmatrix} \begin{bmatrix} \bar{U}_n \\ \bar{V}_n \\ \bar{W}_n \end{bmatrix} = \begin{bmatrix} 0 \\ 0 \\ \frac{a F_0 e^{-ik_n x_0}}{\rho_s c_L^2 h/a} \end{bmatrix}, \qquad (3.10)$$

where the terms of the matrix $\mathbf{L}$ are the same as in Equation 2.13.

Solving for $\bar{W}_n$ and taking the inverse transform, the radial displacement w

51

is given by

$$w(x,\theta) = \frac{F_0 \cos(n\theta)}{2\pi \rho_s c_L^2 h/a} \int_{-\infty}^{+\infty} I_{33} e^{ik_n a\left(\frac{x}{a}-\frac{x_0}{a}\right)} dk_n a, \tag{3.11}$$

where

$$I_{33} = (L_{11}L_{22} - L_{12}L_{21})/|\mathbf{L}|. \tag{3.12}$$

Using Equation (3.8) and the solution for $\bar{W}_n$ given by Equation (3.10), the forced response in terms of pressure in the fluid field may be written as:

$$p(x,\theta) = \frac{F_0 \rho_f \Omega^2 \cos(n\theta)}{2\pi \rho_s h} \int_{-\infty}^{+\infty} \frac{I_{33} J_n(k^r r)}{k^r a J_n'(k^r a)} e^{ik_n a\left(\frac{x}{a}-\frac{x_0}{a}\right)} dk_n a. \tag{3.13}$$

The integrals in Equations (3.11) and (3.13) are computed by using the theorem of residues, as performed by Fuller [29]. Each of the residues are evaluated at the poles of the I_{33} term, i.e. at the zeros k_{ns} of the characteristic equation solved for previously.

The radial displacement can thus be written as

$$w(x,\theta) = \frac{iF_0 \cos(n\theta)}{\rho_s c_L^2 h/a} \sum_{s=1}^{\infty} Res_n^w(s), \tag{3.14}$$

$$Res_n^w(s) = \left. \frac{L_{11}L_{22} - L_{12}L_{21}}{|\mathbf{L}|^\diamond} e^{ik_n a\left(\frac{x}{a}-\frac{x_0}{a}\right)} \right|_{k_n=k_{ns}}. \tag{3.15}$$

The diamond superscript in Equation 3.15 denotes the derivative with respect to $k_n a$. The computation of this derivative is presented in Appendix A.

The forced pressure in the fluid field is derived similarly and is given by:

$$p(x,\theta) = \frac{iF_0 \rho_f \Omega^2 \cos(n\theta)}{\rho_s h/a} \sum_{s=1}^{\infty} Res_n^p(s), \tag{3.16}$$

52

$$Res_n^p(s) = \frac{J_n(k^r r)\,(L_{11}L_{22} - L_{12}L_{21})}{(k^r a J_n'(k^r a)|\mathbf{L}|)^\diamond} e^{ik_n a\left(\frac{x}{a} - \frac{x_0}{a}\right)}\Bigg|_{k_n = k_{n_s}} . \qquad (3.17)$$

As the number of roots of the characteristic equation, for a given circumferential mode n and a given frequency, is infinite when the shell is filled with fluid, the theoretical number of residues required to evaluate the shell radial displacement and the fluid pressure is also infinite, as indicated in Equations (3.14) and (3.16). However, high order branches in the imaginary plane, corresponding to acoustic waves in a rigid walled duct, are nearly uncoupled from the shell motion and yield very small values of residue in the shell response calculation. The number of residues in Equation (3.14) can thus be truncated to a finite number S_n. For all the results in the present analysis, the branch number was truncated to $S_n = 8$. As for the computation of the pressure in the fluid field, the truncation is not so staightforward. The high order acoustic waves discussed above are evanescent at the source plane. Consequently, the residues associated with these waves are only negligible when evaluating the pressure well away from the source plane where higher order wave contributions have decayed to zero.

Figure 3.2 shows the non-dimensional input mobility ($\dot{w}/F_0 \times \rho_s c_L^2 h/a$ at $x = x_0$) of *in vacuo* steel and plexiglass shells vibrating in the breathing mode. At low frequencies ($\Omega < 0.5$), the real part of the input mobility for both shells is very small because the shell motion is largely extensional and radial motion of the shell is only induced by Poisson's coupling. Between $\Omega = 0.5$ and $\Omega = 0.8$, the mobility rises slightly, more markedly for the plexiglass shell as its Poisson's ratio is larger. Above $\Omega \simeq 0.8$, as the nature of the s=1 wave changes from extensional to flexural, the mobility increases dramatically to reach a maximum around the ring
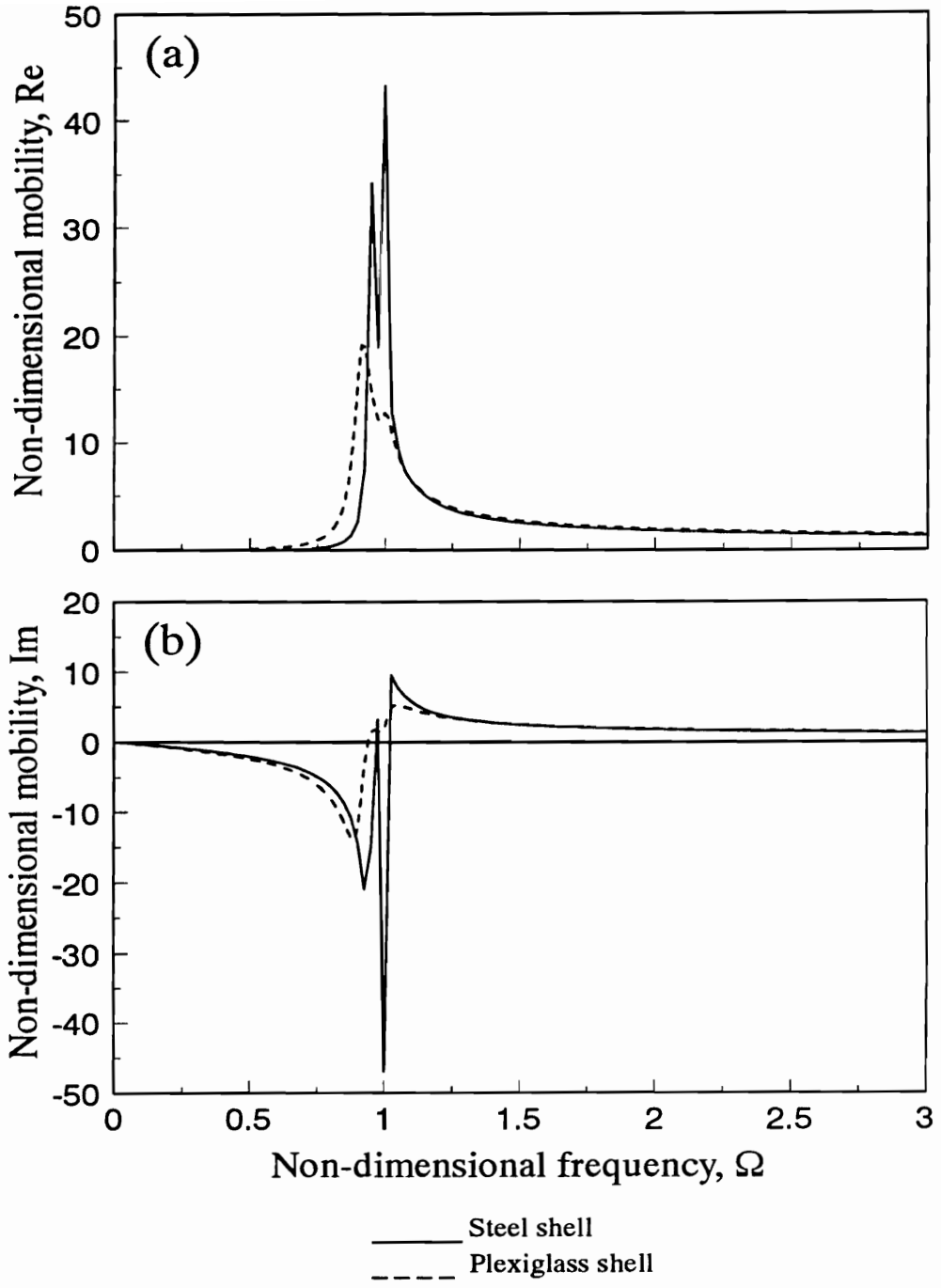
Figure 3.2: Input mobility for steel and plexiglass shells *in vacuo*, n=0; (a) Real part, (b) Imaginary part.

frequency. Whereas the steel shell resonance peak at $\Omega = 1$ is large and sharp, the resonance of the plexiglass shell, near $\Omega \simeq 0.9$, appears strongly damped. As seen in Chapter 2, all the propagating waves in the plexiglass shell system are damped, with the largest damping effect taking place at the system resonance. The reactive mobility (imaginary part) for both shells is small and negative at low frequencies as the system appears very stiff to radial motion. This apparent stiffness of the system decreases slowly as the frequency is increased (more markedly for the plexiglass shell) and drops sharply as the shell resonates radially near $\Omega = 1$. Above the ring frequency, the reactive mobility changes sign indicating that the shell motion, which is almost purely flexural, is sensitive to mass effects.

Figure 3.3 shows the non-dimensional input mobility of water-filled steel and plexiglass shells vibrating in the mode n=0. First, it must be noted that the present results for the water-filled steel shell slightly differ from those obtained by Fuller [29] for the same shell system. This is because the mobility is here evaluated at a larger number of frequencies, using a much smaller value of damping ratio than the one used by Fuller in his analysis. The same remarks also apply to Leyrat's work [23]. For both shells, at frequencies, below $\Omega \simeq 0.6$, the real part of the mobility is larger than the mobility corresponding to the *in vacuo* case. This is due to the s=1 branch behaving like a fluid wave in a compliant tube in this frequency range. Near $\Omega \simeq 0.8$, the steel shell mobility rises dramatically as the branch s=2 approaches the first pressure release duct solution [29] and the coupled media strongly resonate in the radial direction. Near $\Omega \simeq 1.4$, a second resonance of the water-filled steel shell occurs as the branch s=4 cuts on and the s=3 branch approaches the second rigid walled duct solution. Similar behaviour also occurs around $\Omega \simeq 2.2$. The other two resonances of the system near $\Omega \simeq 1.8$ and $\Omega \simeq 2.5$ are related to the
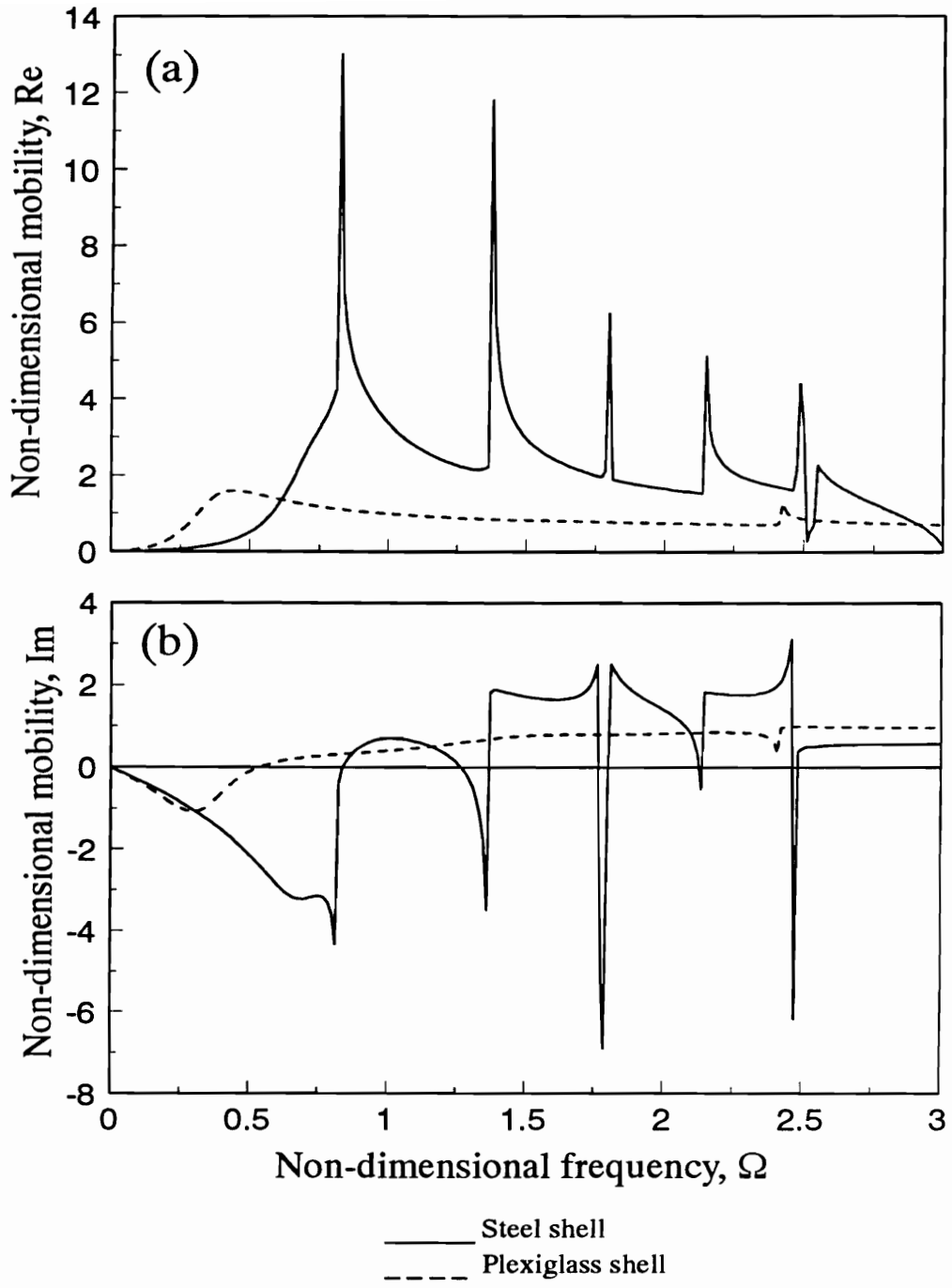
Figure 3.3: Input mobility for steel and plexiglass shells filled with water, n=0; (a) Real part, (b) Imaginary part.

"meander" behaviour of the imaginary branches [20] as these branches coincide with the bending near field. These resonances of the system sharply decay away from the input force location. The reactive mobility of the water-filled steel shell is close to that of the *in vacuo* steel shell at low frequencies. However, the mobility does not fall as dramatically at the system resonance (near $\Omega \simeq 0.8$) because the fluid at this frequency increases the mass type reactance of the system. The reactive mobility remains mostly positive above $\Omega \simeq 0.8$ but reverts to negative as the system resonates and reveals an apparent stiffness loss. Unlike that of the steel shell, the mobility of the water-filled plexiglass shell does not reveal any major peak due to resonances of the system and remains relatively small across the whole frequency range. A small increase of the system response appears near $\Omega \simeq 2.4$ as the branch s=3, corresponding to the first pressure release duct solution, cuts on. The reactive mobility is small and negative at low frequencies but quickly reverts to a mass type reactance above $\Omega \simeq 0.6$.

Figure 3.4 shows the non-dimensional pressure field $(p/iF_0\rho_f\Omega^2 \times \rho_s h/a)$ in the water-filled steel shell ten radii from an axisymmetric radial line force for non-dimensional frequencies between 0 and 3. Because the pressure field is axisymmetric, the results illustrate a single value of circumferential position. It appears that the pressure in the fluid is particularly large when the waves approaching the acoustic duct solution cut on (these waves are denoted as s=3, 4 and 5 in the dispersion plot of Figure 2.6). Near $\Omega \simeq 0.85$, the pressure distribution is close to that of the first pressure release duct mode. Near $\Omega \simeq 1.35$, the pressure distribution approaches that of the second hard walled duct solution. Finally, near $\Omega \simeq 2.1$, the distribution approaches that of the third hard walled duct mode. At low frequencies, the pressure distribution is quasi-uniform in the cross section. This is due to the

s=1 wave behaving like the acoustic plane wave, as explained in Chapter 2.

Figure 3.5 shows the distribution of the pressure field in the water-filled plexiglass shell. The pressure is particularly large near $\Omega \simeq 2.4$ as the wave s=3, behaving like a duct wave, cuts on. At this frequency, the pressure distribution is very close to that of the first pressure release duct mode. At lower frequencies, the pressure is dominant near the shell wall due to the s=1 wave being pressure near-field at the wall. Between $\Omega = 0$ and $\Omega \simeq 0.3$, the pressure distribution is consistent with the fact that the s=1 wave approaches the first rigid walled duct solution, i.e. the plane wave.

3.4 Power flow in the coupled shell system

The total vibrational energy flowing through the coupled shell system is the sum of two quantities: the acoustic axial power flow in the fluid field and the structural axial power flow in the shell wall. Solutions for these two quantities have appeared in various studies by Fuller [3, 20, 29]. The derivation is recalled here for completeness.

3.4.1 Power flow in the fluid field

The pressure in the fluid field for one particular circumferential mode n is first expressed as a series

$$p = \sum_{s=1}^{S_n} P_{ns} \cos(n\theta) J_n(k_s^r r) e^{i(k_{ns} x - \omega t)}. \tag{3.18}$$
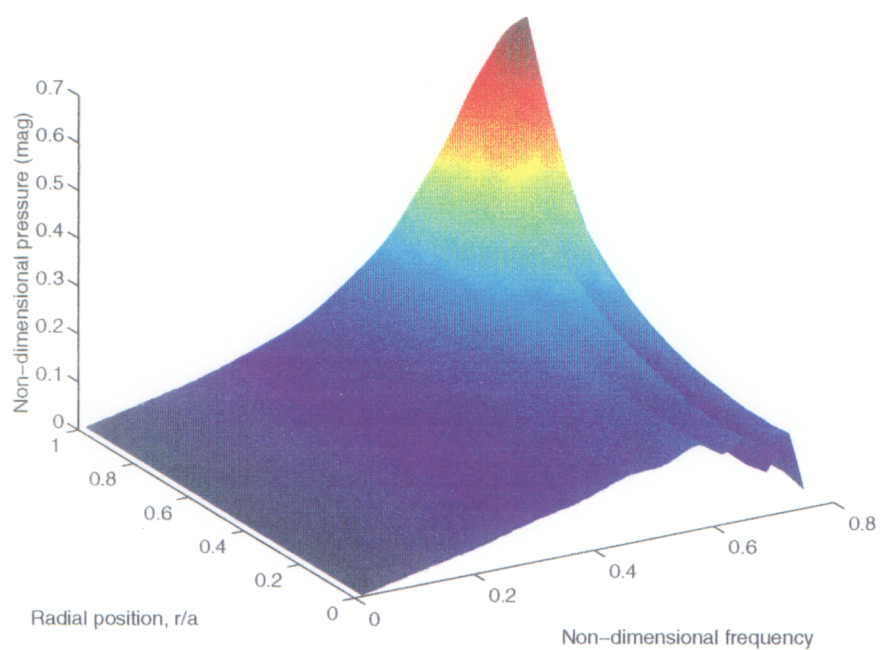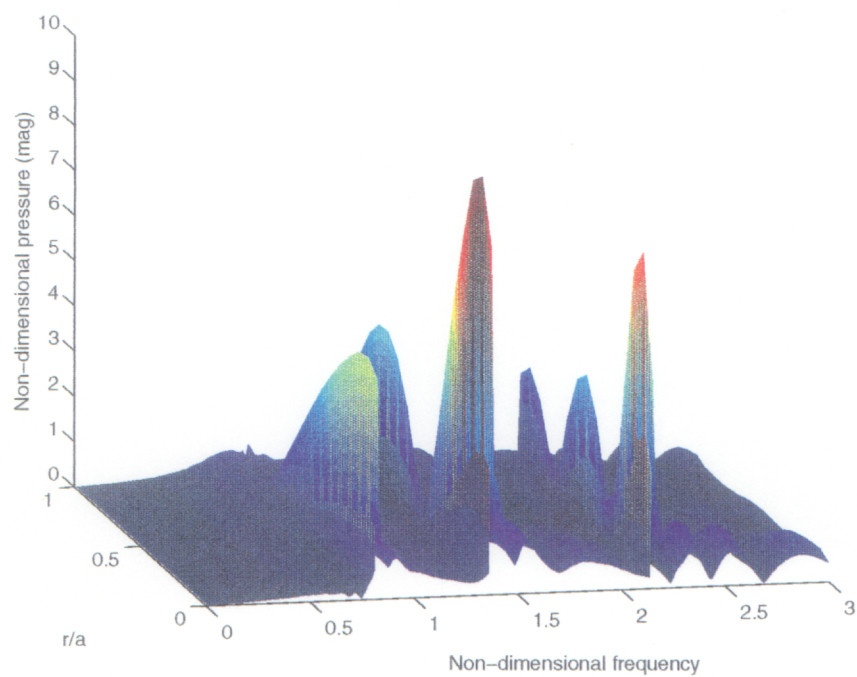
Figure 3.4: Theoretical pressure field in a water-filled steel shell ten radii from an axisymmetric radial line force.
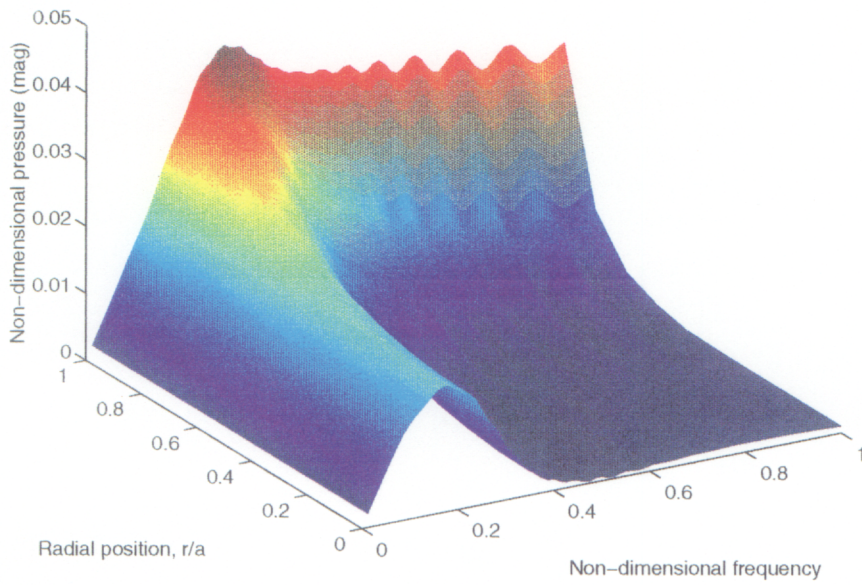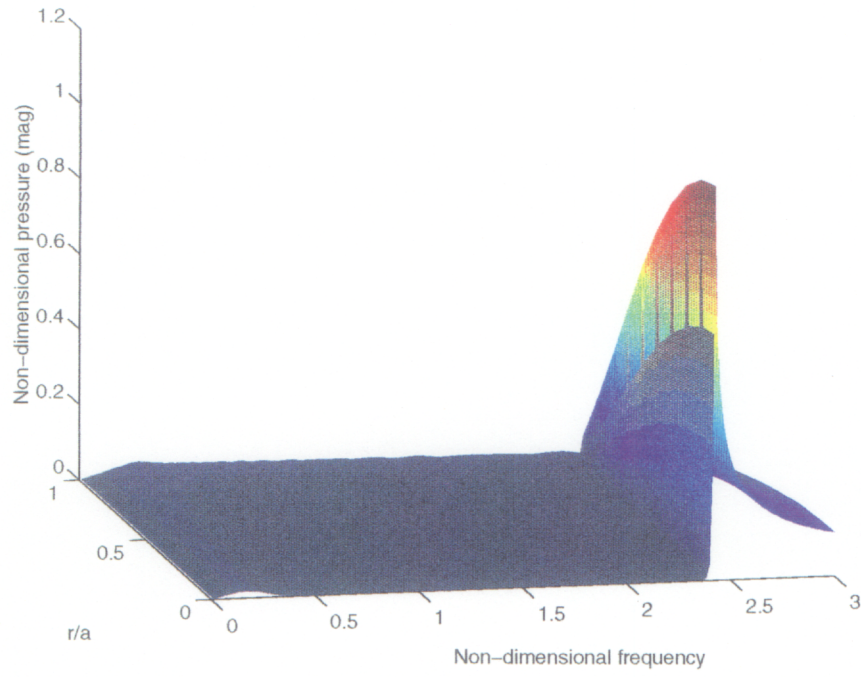
Figure 3.5: Theoretical pressure field in a water-filled plexiglass shell ten radii from the axisymmetric radial line force.

Using the usual Euler equation,

$$-\frac{\partial p}{\partial x} = \rho_f \frac{\partial v_x}{\partial t}, \tag{3.19}$$

one can obtain the axial component of the particle velocity written as follows

$$v_x = \sum_{s=1}^{S_n} (k_{ns}/\rho_f \omega) P_{ns} \cos(n\theta) J_n(k_s^r r) e^{i(k_{ns}x - \omega t)}. \tag{3.20}$$

The axial component of the time-averaged acoustic intensity is then given by

$$I_x^f(r, \theta) = \frac{1}{2} Re(p v_x^*), \tag{3.21}$$

where $*$ denotes the complex conjugate. Substituting the Equations (3.18) and (3.20) into (3.21) yields

$$I_x^f(r, \theta) = Re\left[\sum_{s=1}^{S_n}\sum_{j=1}^{S_n}(1/2\rho_f\omega)P_{ns}P_{nj}^* k_{nj}^* \cos^2(n\theta) J_n(k_s^r r) J_n^*(k_j^r r) e^{i(k_{ns} - k_{nj}^*)x}\right]. \tag{3.22}$$

The power flow in the fluid field is finally obtained by integrating I_x^f over the cross-section area as follows

$$\Pi_f = \int_0^{2\pi} \int_0^a I_x^f(r, \theta) r \, d\theta \, dr. \tag{3.23}$$

Using the relation between the modal pressure and displacement amplitudes (Eq. 2.11), the solution for the total power flow in the fluid can be written as

$$\Pi_f = Re\left[\frac{\pi}{2} c_L^3 \Omega^3 \rho_f \varepsilon_n \sum_{s=0}^{S_n}\sum_{j=0}^{S_n} W_{ns} W_{nj}^* e^{i(k_{ns} - k_{nj}^*)x} F_{sjn}\right], \tag{3.24}$$

where $\varepsilon_0 = 2$ and $\varepsilon_n = 1$ for $n \geq 1$. The fluid power factor F_{sjn} is given by

$$F_{sjn} = \frac{1}{a^2}\left[\frac{1}{k_s^r a J_n'(k_s^r a)}\right]\left[\frac{k_{nj} a}{k_j^r a J_n'(k_j^r a)}\right]^* \int_0^a J_n(k_s^r r) J_n^*(k_j^r r) r \, dr. \tag{3.25}$$

61

The solution of the integral in Equation (3.25) can be written as [46]

$$\int_0^a J_n(k_s^r r) J_n^*(k_j^r r) r\, dr = \frac{a^2}{(k_s^r a)^2 - (k_j^{r*} a)^2} \left[(k_s^r a)^2 J_n(k_s^r a) J_{n+1}^*(k_j^r a) \right. \qquad (3.26)$$
$$\left. - (k_j^{r*} a)^2 J_n^*(k_j^r a) J_{n+1}(k_s^r a) \right]$$

It should be noted that two different modes s, associated with the same circumferential distribution n, are not orthogonal [26]. Consequently, the cross terms in Expression (3.24) carry appreciable power and must be retained for a correct evaluation of the fluid power flow.

3.4.2 Power flow in the shell wall

The first expression for the power flow in thin cylindrical elastic shells was presented by Fuller [3]. The derivation was based on the integration around the shell circumference of the structural intensity which was made of four terms. More recent investigations by Romano [47] and Williams [48] have shown that a more exact expression of the axial component of the instantaneous structural intensity in a thin cylindrical shell is actually a sum of five terms,

$$I_x^s = N_x \dot{u} + N_{x\theta} \dot{v} + Q_x \dot{w} + M_x \dot{w}_x + M_{x\theta} \dot{w}_\theta, \qquad (3.27)$$

representing, respectively, the extensional power flow, the in-plane shear power flow, the out-of-plane shear power flow, the work of the bending moment M_x against the angular rotation $\dot{w}_x$ of the shell element in the x-direction and the work of the twisting moment $M_{x\theta}$ against the angular rotation $\dot{w}_\theta$ of the shell element about the x axis. This last term had been omitted by Fuller in his derivation of the shell power flow. It will be shown that this term is small for low circumferential mode orders.

62

In Equation (3.27), N_x, $N_{x\theta}$ and Q_x are the axial force, the in-plane shear force and the transverse shear force resultants; $\dot{}$ indicates a differentiation with respect to time.

The total time-averaged axial power flow in the shell wall is thus given by

$$\Pi_s = \frac{1}{2} Re \left(\int_0^{2\pi} N_x \dot{u}^* + N_{x\theta} \dot{v}^* + Q_x \dot{w}^* + M_x \dot{w}_x^* + M_{x\theta} \dot{w}_\theta^* \; a d\theta \right). \qquad (3.28)$$

If the shell is thin enough, as in the present analysis, a good approximation of the elastic law is given by the simplified Flügge equations [49]:

$$N_x \;\; = \;\; D \left[\frac{\partial u}{\partial x} + \frac{\nu}{a} \left(\frac{\partial v}{\partial \theta} + w \right) \right], \qquad (3.29)$$

$$N_{x\theta} \;\; = \;\; \frac{D(1-\nu)}{2} \left(\frac{\partial u}{a \partial \theta} + \frac{\partial v}{\partial x} \right), \qquad (3.30)$$

$$M_x \;\; = \;\; K \left(\frac{\partial^2 w}{\partial x^2} + \frac{\nu}{a^2} \frac{\partial^2 w}{\partial \theta^2} \right), \qquad (3.31)$$

$$M_{x\theta} \;\; = \;\; \frac{K(1-\nu)}{2} \frac{\partial^2 w}{\partial x \partial \theta}, \qquad (3.32)$$

$$Q_x \;\; = \;\; \frac{\partial M_x}{\partial x} + \frac{\partial M_{x\theta}}{a \partial \theta}, \qquad (3.33)$$

where, in Equations (3.29) to (3.33), the membrane stiffness is $D = Eh/(1-\nu^2)$ and the bending stiffness is $K = Eh^3/12(1-\nu^2)$.

The shell displacements for a particular circumferential mode n are expressed

as series,

$$u = \sum_{s=0}^{S_n} U_{ns} cos(n\theta) e^{i(k_{ns}x - \omega t - i\pi/2)}, \qquad (3.34)$$

$$v = \sum_{s=0}^{S_n} V_{ns} sin(n\theta) e^{i(k_{ns}x - \omega t)}, \qquad (3.35)$$

$$w = \sum_{s=0}^{S_n} W_{ns} cos(n\theta) e^{i(k_{ns}x - \omega t)}. \qquad (3.36)$$

Introducing the expressions (3.29) to (3.33) and (3.35) to (3.36) into Equation (3.28), one obtains the following solution for the structural power flow in the shell wall:

$$\Pi_s = Re \left[\pi \rho_s c_L^3 \Omega \sum_{s=1}^{S_n} \sum_{j=1}^{S_n} W_{ns} W_{nj}^* e^{i(k_{ns} - k_{nj}^*)x} S_{sjn} \right], \qquad (3.37)$$

where the shell factor S_{sjn} is given by

$$\begin{aligned}
S_{sjn} &= \left[(h/a)^3/12 \right] \left[(k_{ns}a)^3 + (k_{ns}a)^2(k_{nj}^*a) \right] \\
&+ (h/a) \left[(k_{ns}a)R_{as}R_{aj}^* + \nu R_{aj}^* \right], \qquad n = 0, \qquad (3.38)
\end{aligned}$$

$$\begin{aligned}
S_{sjn} &= \left[(h/a)^3/24 \right] \left[(k_{ns}a)^3 + (k_{ns}a)^2(k_{nj}^*a) + n^2(k_{ns}a) + \nu n^2(k_{nj}^*a) \right. \\
&+ \left. (k_{ns}a)(n^2 - n^2\nu + nR_{tj}^* - n\nu R_{tj}^*) \right] \\
&+ \left[(h/a)/2 \right] \left[(k_{ns}a)R_{as}R_{aj}^* + n\nu R_{ts}R_{aj}^* + \nu R_{aj}^* \right] \\
&+ \left[(h/a)(1-\nu)/4 \right] \left[nR_{as}R_{tj}^* + k_{ns}aR_{ts}R_{tj}^* \right], \qquad n \geq 1. \qquad (3.39)
\end{aligned}$$

In Equations (3.38) and (3.39), R_{as}, R_{ts}, R_{aj} and R_{tj} are the ratios of axial and torsional to radial amplitudes of vibration obtained by re-substituting the derived axial wavenumber k_{ns} or k_{nj} into the equations of motion (2.13) of the free vibrating system [3].

64

As for the fluid power flow, Equation (3.37) includes cross interaction terms that must be retained for a correct evaluation of the shell power flow.

3.4.3 Total power flow in the coupled shell system

The total power flow in the shell system is defined as the sum of the power flows in each of the two coupled media,

$$\Pi_t \; = \; \Pi_s \; + \; \Pi_f. \tag{3.40}$$

As seen from Equations (3.24) and (3.37), the power flow in either of the coupled media can vary from one axial position to another due to interferences, represented by cross interaction terms in the equations, between the various propagating waves. This phenomenon results in an exchange of energy between the fluid and the shell as the waves propagate [33]. The total power flow in the shell system is not subject to these oscillations. Nevertheless, the hysteretic damping in the shell material yields a slight decay of the total power flow as the various waves propagate.

3.5 Linear quadratic optimal control theory

The second case of control approach on Figure 3.1, with two control forces/two minimization points is considered (the first case, one control force/one minimization point, being a simplified case). Note that two error points are needed to avoid an overdetermined system, i.e. more than one solution for the control forces. The total radial displacement of the shell at the error locations x_e^1 and x_e^2

can be expressed in matrix form as

$$\mathbf{w^t} = (\mathbf{d}W_{ns}^d + \mathbf{C}\mathbf{f_c})\cos(n\theta) \tag{3.41}$$

where the vectors and matrices are given by

$$\mathbf{d} = \left[\ e^{i(k_{ns}^d x_e^1)} \quad e^{i(k_{ns}^d x_e^2)}\ \right]^T, \tag{3.42}$$

$$\mathbf{C} = \frac{1}{2\pi \rho_s c_L^2 h/a} \left[\begin{array}{cc} \int_{-\infty}^{+\infty} I_{33} e^{ik_n(x_e^1 - x_c^1)} dk_n a & \int_{-\infty}^{+\infty} I_{33} e^{ik_n(x_e^1 - x_c^2)} dk_n a \\ \int_{-\infty}^{+\infty} I_{33} e^{ik_n(x_e^2 - x_c^1)} dk_n a & \int_{-\infty}^{+\infty} I_{33} e^{ik_n(x_e^2 - x_c^2)} dk_n a \end{array}\right], \tag{3.43}$$

$$\mathbf{f_c} = \left[F_c^1 \ F_c^2\right]^T, \tag{3.44}$$

$$\mathbf{w^t} = \left[w^t(x_e^1, \theta) \ w^t(x_e^2, \theta)\right]^T. \tag{3.45}$$

The superscript "T" denotes the matrix transpose operator.

In order to minimize the radial displacement at the axial positions x_e^1 and x_e^2 along the circumference of the shell, the following cost function is defined

$$J = \sum_{i=1}^{2} \int_0^{2\pi} \left|w^t(x_e^i, \theta)\right|^2 d\theta. \tag{3.46}$$

This cost function is a real quadratic function of the strength of the control inputs. For a given magnitude of the incident propagating wave, J has a unique minimum value associated with an optimal set of control forces. This cost function can be written in matrix form as

$$\begin{aligned} J &= \pi \varepsilon_n \left[\mathbf{w^t}\right]^H \left[\mathbf{w^t}\right] \tag{3.47}\\ &= \pi \varepsilon_n \left[\mathbf{d}W_{ns}^d + \mathbf{C}\mathbf{f_c}\right]^H \left[\mathbf{d}W_{ns}^d + \mathbf{C}\mathbf{f_c}\right] \end{aligned}$$

$$= \pi \varepsilon_n \left\{ W_{ns}^d [\mathbf{d}^H \mathbf{d}] W_{ns}^d + \mathbf{f_c}^H [\mathbf{C}^H \mathbf{d}] W_{ns}^d + W_{ns}^d [\mathbf{d}^H \mathbf{C}] \mathbf{f_c} \right.$$
$$\left. + \mathbf{f_c}^H [\mathbf{C}^H \mathbf{C}] \mathbf{f_c} \right\} \tag{3.48}$$

where the superscript "H" denotes the Hermitian operator.

A general solution for this type of optimization problem has been developed by Nelson et al. [45]. The condition for the global minimum of the cost function J is

$$\frac{\partial J}{\partial \mathbf{f_c^r}} + i \frac{\partial J}{\partial \mathbf{f_c^i}} = 0 \ , \tag{3.49}$$

where $\mathbf{f_c^r}$ and $\mathbf{f_c^i}$ represent the real and imaginary part of the control vector $\mathbf{f_c}$ respectively. If L control inputs are considered to minimize the chosen acoustic field, the function J is dependent on $2L$ variables constituting the real and imaginary parts of the control input vector. This type of cost function can then be seen as a 'bowl shaped' hypersurface with a unique global minimum. Thus, taking the derivatives of the cost function J with respect to the real and imaginary part of the control vector leads to the optimal solution for the complex control forces

$$\mathbf{f_c^{opt}} = -[\mathbf{C}^H \mathbf{C}]^{-1} [\mathbf{C}^H \mathbf{d}] W_{ns}^d. \tag{3.50}$$

3.6 Control performance

The performance of the discontinuity created on the shell system by the active control forces is evaluated by comparing the total power flow in the system beyond the minimization points after control to the total power flow due to the incident wave alone at the same position. This approach differs from that previ-

ously used by Brévart and Fuller [50] who compared the power flow beyond the minimization points to the power flow of the incident wave just before it reached the discontinuity. Using this last approach, the passive power loss due to a decay of the disturbance amplitude, as the wave propagates through the discontinuity, is included in the performance parameter. This power loss can be important for large values of the shell hysteretic damping. The present approach gives more pertinent results as far as the control performance is concerned. The control performance parameter is thus defined as follows

$$I_\pi = \frac{(\Pi_t)_{x>x_e^2}^{after\ control}}{(\Pi_t)_{x>x_e^2}^{before\ control}}.$$

(3.51)

The power insertion loss, in decibels, due to the active control approach is then given by

$$IL = 10\ \log_{10}(I_\pi).$$

(3.52)

3.7 Results

In this section, the performance of the two control configurations described in Section 3.1 is computed considering various shell systems. The results are analyzed and explained in physical terms. For all the cases, the amplitude of the incident wave, in Equation (3.1), is assumed to be $W_{ns}^d = 1$ at $x = 0$. The first control force is applied at $x_c = 2a$. When considering the second case of control configuration, the two forces are closely spaced a distance $\Delta x_c = 0.1a$ apart in order to introduce a line moment component into the shell system. Note that this spacing is about ten times smaller than the minimum wavelength at the highest frequency of interest,

$\Omega = 3$. The spacing between the error points is $\Delta x_e = 0.2a$. The distance between the control forces and the minimization points is approximately 5 radii. This ensures that near field waves do not affect the error signals. The total power flow in the system is evaluated one diameter beyond the minimization points.

3.7.1 Axisymmetric wave motion (n=0)

We first consider axisymmetric disturbances and control forces. If a steel or plexiglass shell is *in vacuo*, it has been seen in Chapter 2 that there exist two waves, denoted as s=1 and s=2, which are real (with a relatively small imaginary part due to hysteretic damping), and therefore propagating at all frequencies. These two waves can thus be regarded as potential incident disturbances on the shell system. As the torsional shear wave s=2 is uncoupled from the radial motion of the shell, it can not be controlled by radial line forces. Hence, it will not be considered in the present analysis. When the shell is filled with water, it has been seen in Chapter 2 that two waves denoted as s=1 and s=2, in addition to the torsional shear wave s=0, can propagate at all frequencies. Both of these waves will be considered as disturbances.

Figure 3.6 shows the shell power loss IL considering an *in vacuo* steel shell. The reader is refered to Table 2.1 for shell material properties and geometrical characteristics. The branch s=1 of the dispersion curves, as seen in Figure 2.5, was used as an incident disturbance wave corresponding to a structural source. At low frequencies ($\Omega \leq 0.95$), even though the incident wave is extensional in nature, it is possible to reduce the downstream power flow because of Poisson's coupling effect. As the s=1 wave is the only propagating wave within this frequency range, one

69
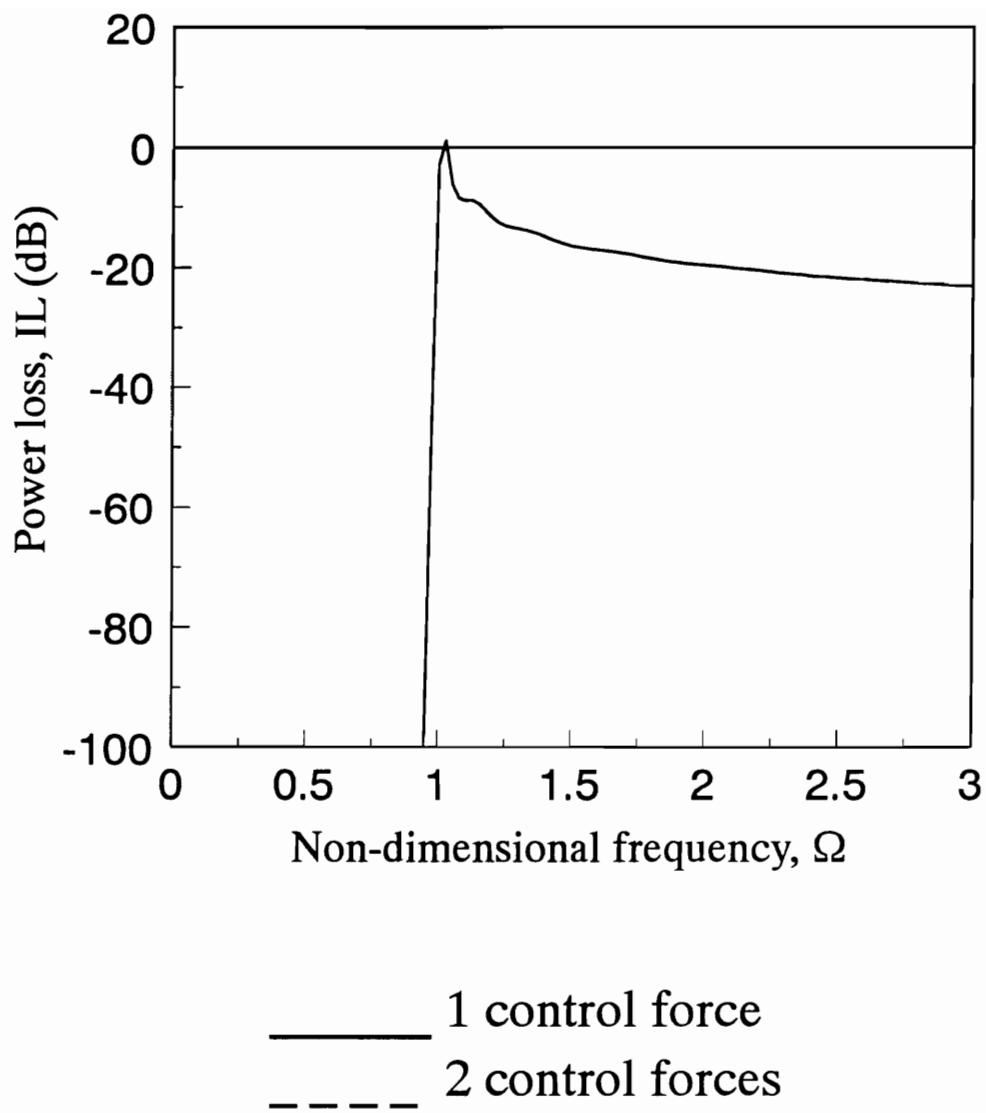
Figure 3.6: Power insertion loss, *in vacuo* steel shell, n=0, branch s=1 incident.

control force provides total control of the shell power flow (< -100 dB). At the ring frequency $\Omega = 1$, the shell strongly resonates and the one radial force/one error point control configuration does not yield any reduction of the shell power flow. Using two control forces and two minimization points, it is possible to keep the shell element from both translating and rotating. Total control of the shell power flow is thus obtained. Above the ring frequency, the incident wave changes in nature towards a purely flexural wave. One control force yields 10 to 20 dB of attenuation. Using two control forces, total control of the shell power flow is achieved as only two waves propagate in the system.

Figure 3.7 shows the total power loss due to active vibration control on a water-filled steel shell when the incident wave is the branch s=2. This branch behaves like a structural wave at low frequencies. For the case of one control force, even though the radial displacement is perfectly controlled at the error point (see in Figure 3.8 for example the magnitude of the radial displacement through the control discontinuity at $\Omega = 0.5$ and $\Omega = 3$), the active input appears to be very ineffective in controlling the total power flow. Increases of the total power flow in the system occur at various frequencies. The reason for this behavior is that part of the energy introduced in the system by the control input is diverted from the shell to the fluid field at the error point. Using two control forces yields very large attenuations of the total power flow at low frequencies. Around $\Omega = 0.85$, the control performance drops dramatically as the coupled system, subjected to a coincidence phenomenon, strongly resonates. In the frequency range $\Omega \in [0.9; 1.35]$, attenuations from 10 to 40 dB are seen to occur. At higher frequencies, the incident wave becomes a dominantly fluid type wave and most of the energy propagates via the fluid path; the attenuations achieved are thus negligible.

71

Figure 3.7: Power insertion loss, water-filled steel shell, n=0, branch s=2 incident.

72

Figure 3.8: Magnitude of the shell radial displacement, one control force/one error point, water-filled steel shell, n=0, branch s=2 incident.

Figure 3.9 shows the variations of the control performance with frequency when the incident disturbance on the water-filled steel shell is the s=1 wave. This wave predominantly has fluid wave type characteristics. As explained in Chapter 2, the s=1 wave is subsonic in the fluid field and consists of a pressure near field at the shell wall. Furthermore, Fuller and Fahy [20] demonstrated that below the ring frequency $\Omega = 1$, the power flow of the s=1 branch is dominant in the fluid field. Performing the control with only one force, the total power flow is seen to be reduced nearly across the entire frequency range. Good attenuations of 15 dB are obtained at low frequencies and an average 6 dB attenuation is obtained above the frequency $\Omega = 0.8$. Because of resonances of the coupled system associated with cut-on of high order duct modes, an increase of the power flow in the system is seen to occur at a few discrete frequencies such as $\Omega = 0.85$. When two control forces are used, more noticeable attenuations of the total power flow are observed, reaching total control (< -100 dB) at low frequencies and varying from 10 to 60 dB above $\Omega = 0.8$. The explanation for this unexpected high control performance is associated with the particular nature of the incident wave s=1. The pressure near field acts like a mass loading on the shell and is thus strongly affected by structural radial forces.

Figure 3.10 shows the total power loss IL considering an *in vacuo* plexiglass shell. The reader is refered to Table 2.1 for shell material properties and geometrical characteristics. The branch s=1 of the dispersion curves in Figure 2.9 was used as a disturbance. The results are very similar to those obtained for the *in vacuo* steel shell. However, using one control force and one error sensor results in spillover or poor control performances in a frequency range extending from $\Omega \simeq 0.9$ to $\Omega \simeq 1.25$. This has only appeared at the ring frequency $\Omega = 1$ for the steel shell. This
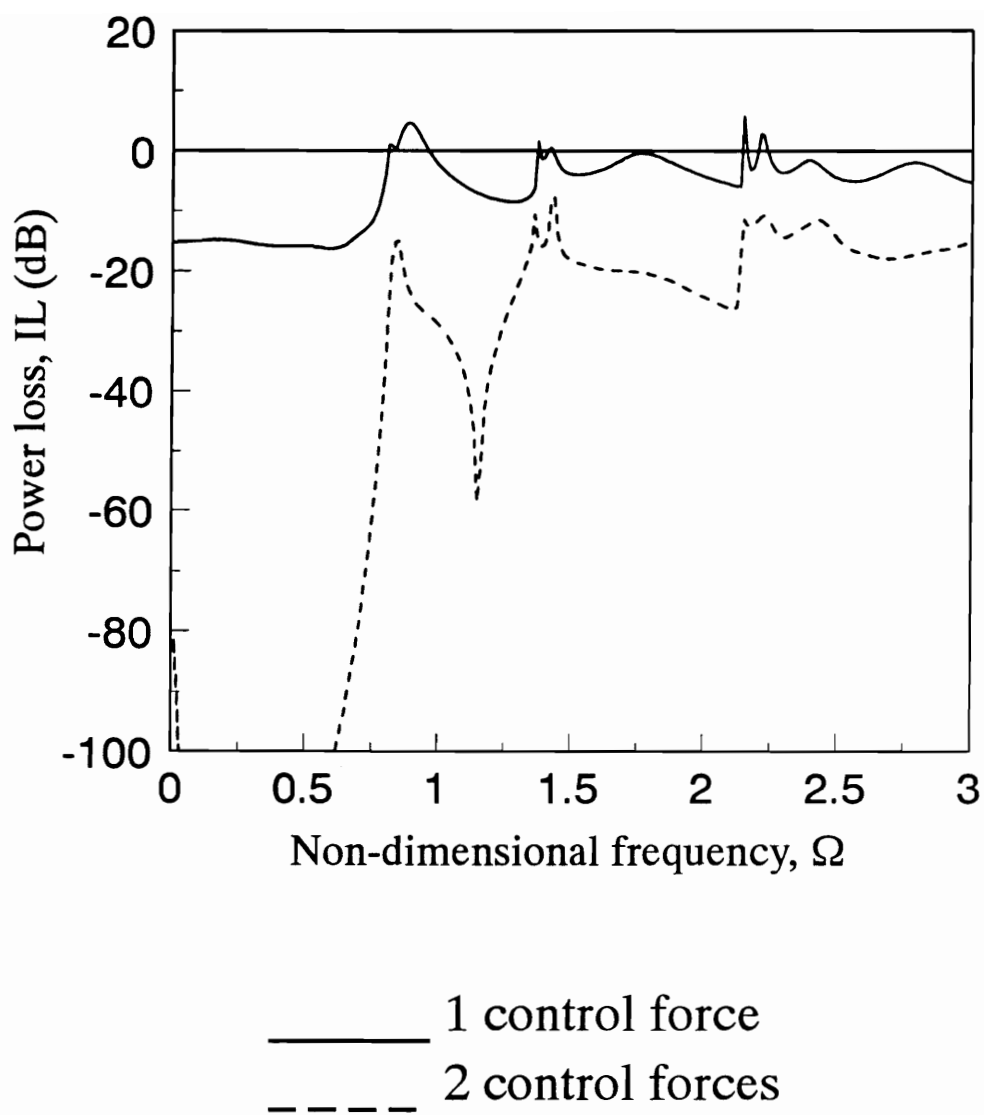
Figure 3.9: Power insertion loss, water-filled steel shell, n=0, branch s=1 incident.

behaviour may be due to the contribution of the extensional wave s=3 to the radial motion near cut on being larger in plexiglass than in steel; Poisson's ratio is larger in plexiglass and so is the damping effect on the s=1 wave. As for the steel shell, the use of two forces and two error sensors yields total control of the shell power flow.

Figure 3.11 shows the total power loss due to active vibration control on a water-filled plexiglass shell when the incident wave is the branch s=2, which behaves like an extensional shell wave across the entire frequency range $\Omega \in [0;3]$. As for the steel shell, no control of the total power flow is achieved using one control force. Using two control forces, a maximum of 1.5 dB attenuation of the power flow appears at low frequencies, despite the fact that the radial displacement is perfectly controlled at the error sensors (see in Figure 3.12 for example the radial displacement through the control discontinuity at $\Omega = 1.5$). This is due to the radial motion associated with the extensional wave s=2 being much smaller than that of the waves excited by the radial line forces, i.e. the s=1 wave and even the evanescent s=3 wave, whose energy is predominantly in the fluid field. As a result, the power flow initially in the shell wall is diverted to the fluid at the error sensor location. Part of the energy in the fluid is transferred back to the shell beyond the error sensors due to the interferences between the propagating waves.

Figure 3.13 shows the control performance parameter when the incident disturbance considered is the s=1 wave. This wave is subsonic in the fluid field and consists of a pressure near field at the shell wall. This near field acts on the shell like an added mass and the wave motion is thus strongly affected by structural radial forces. Using one control force, total power attenuations varying from 50 to 70 dB

Figure 3.10: Power insertion loss, *in vacuo* plexiglass shell, n=0, branch s=1 incident.
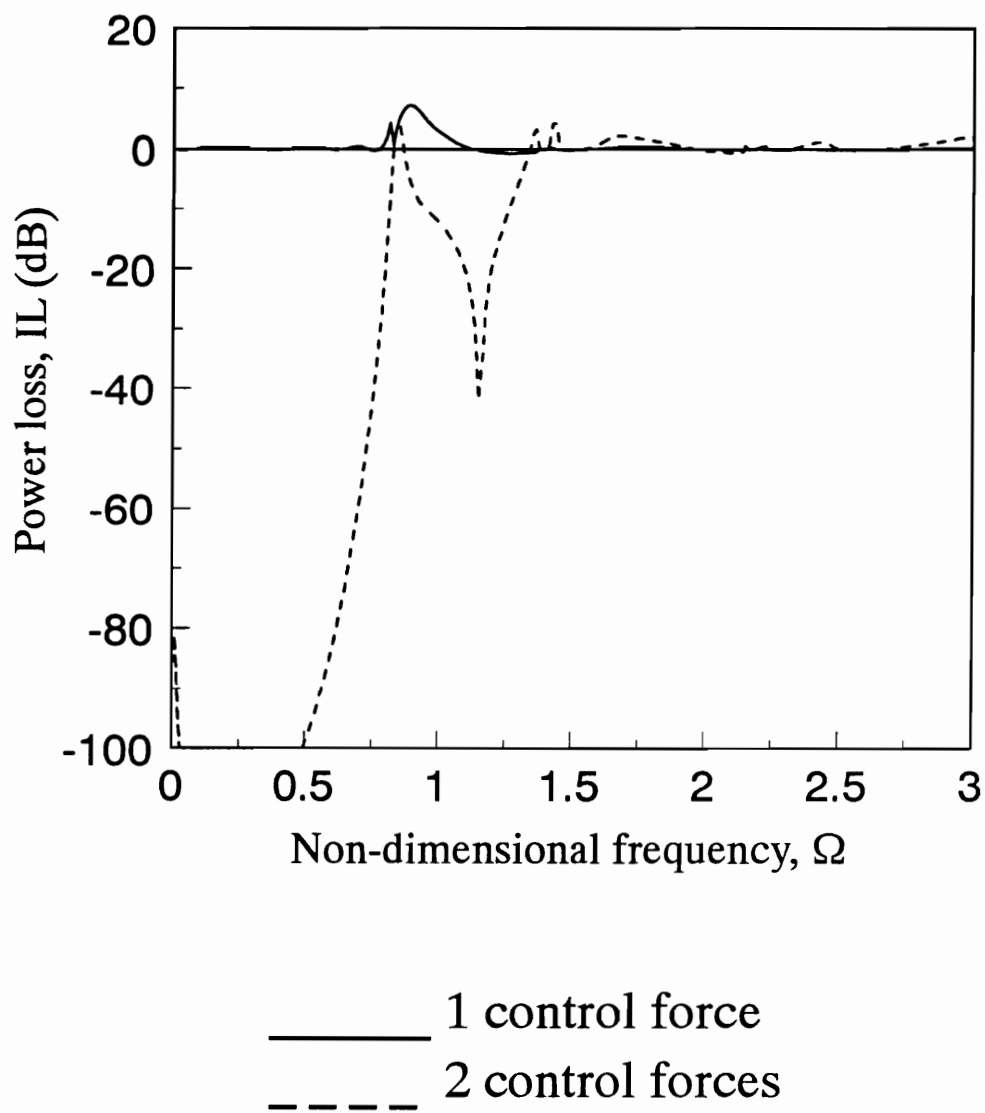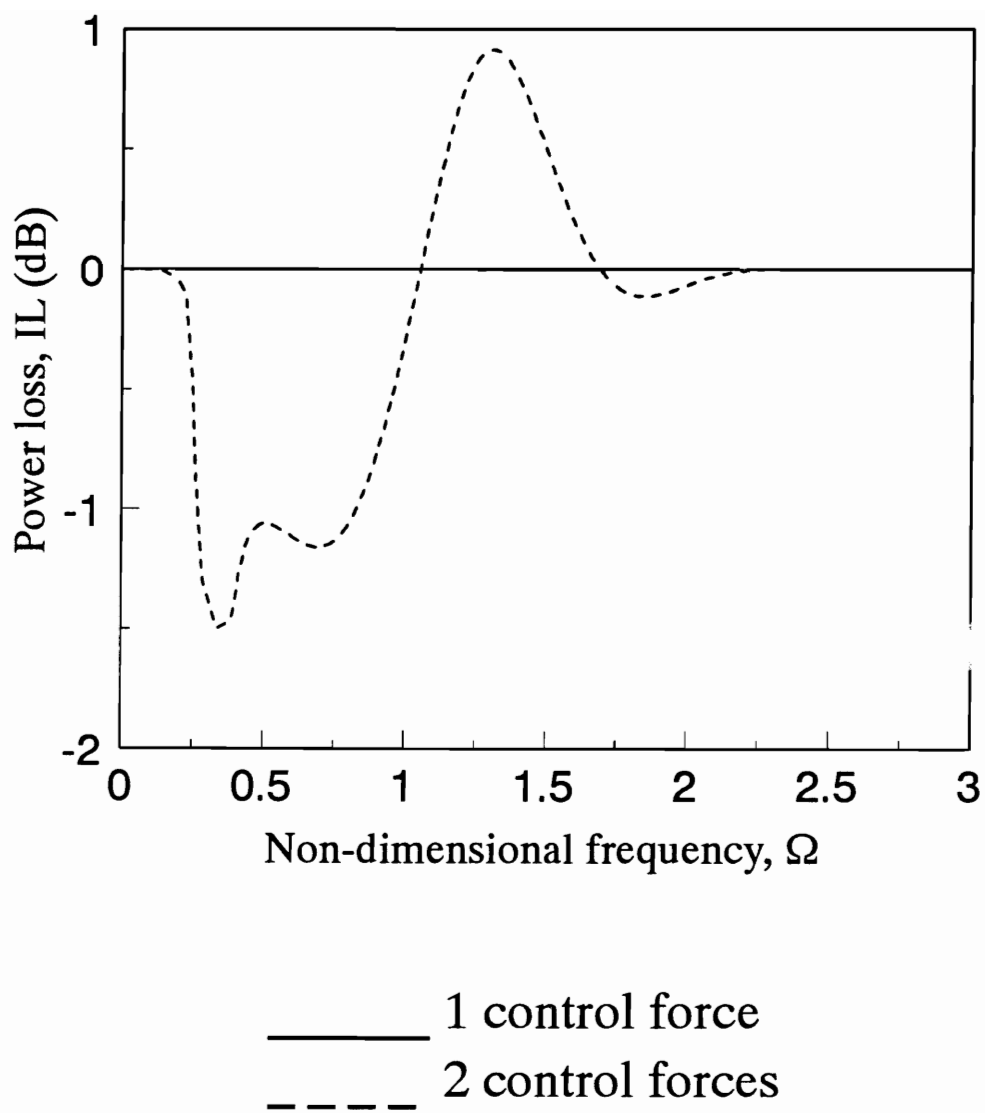
Figure 3.11: Power insertion loss, water-filled plexiglass shell, n=0, branch s=2 incident.
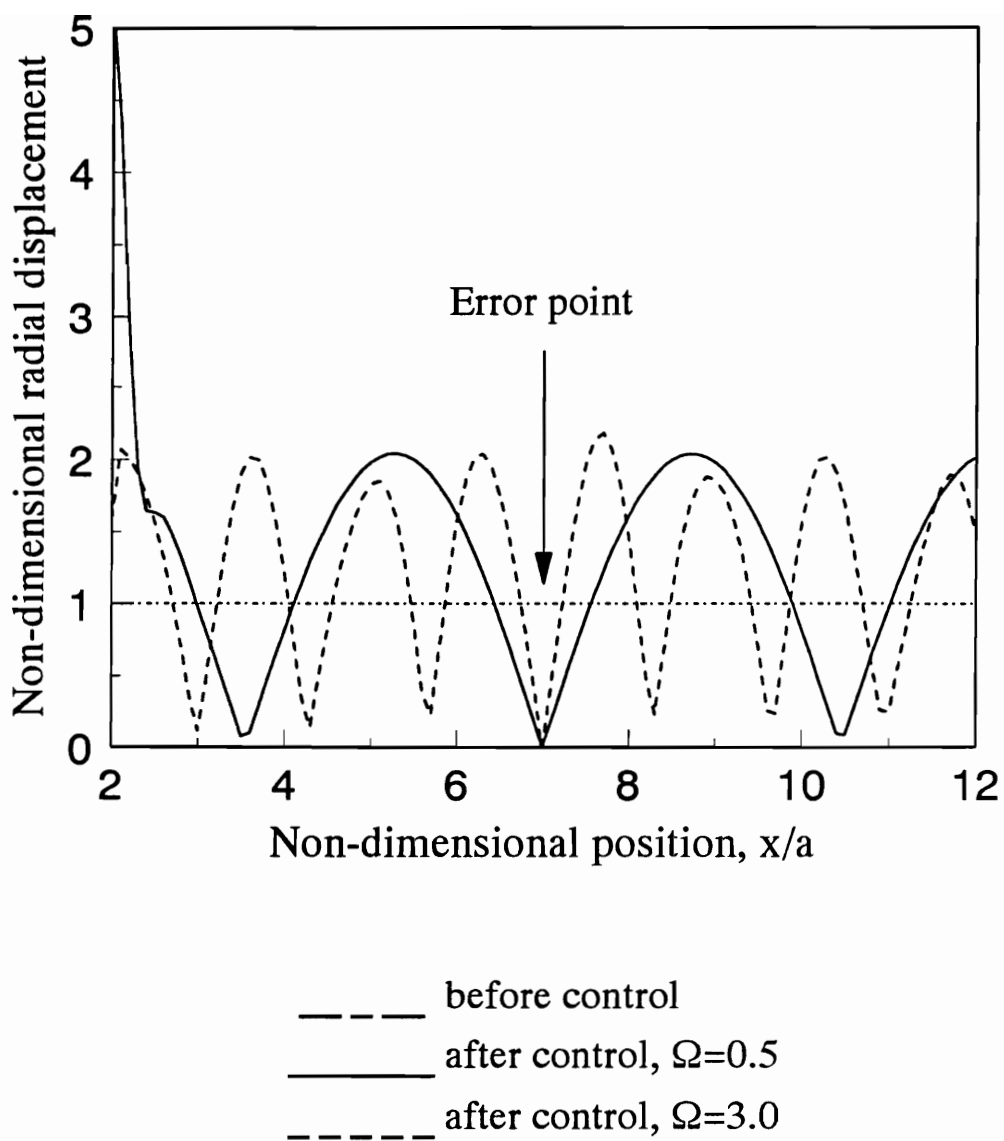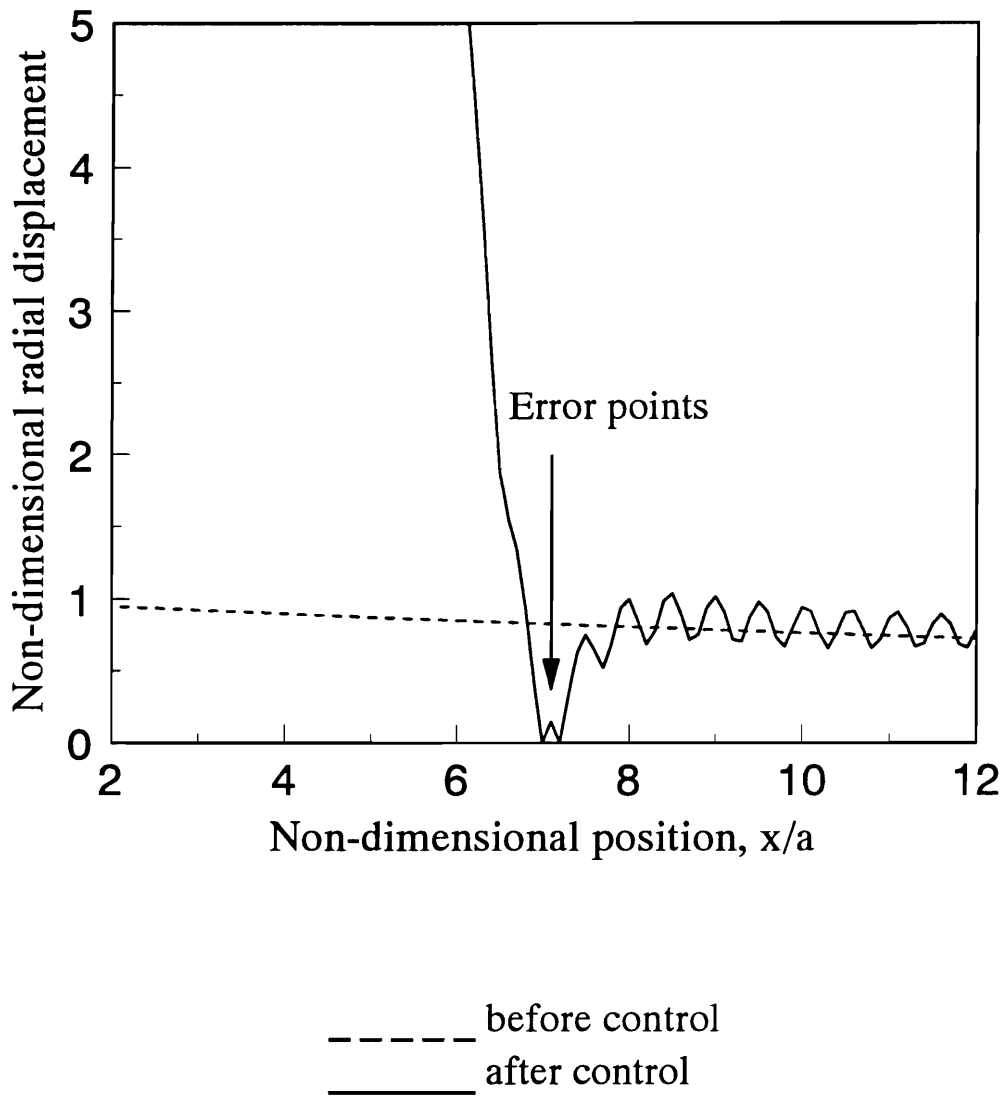
Figure 3.12: Magnitude of the shell radial displacement, one control force/one error point, water-filled plexiglass shell, n=0, branch s=2 incident.

are observed at frequencies below $\Omega = 2.3$. Near $\Omega = 2.4$, the control performance drops dramatically as the s=3 wave, approaching the first pressure release duct mode, cuts on. When two control forces are used, the total power flow is reduced by about 70 dB across the whole frequency range.

3.7.2 Beam type wave motion (n=1)

We now consider beam-type disturbances and control line forces (n=1). Chapter 2 revealed that, whether the shell (made of steel or plexiglass) is *in vacuo* or filled with water, there is only one wave, denoted as s=1, which is real (with a relatively small imaginary part), i.e. propagating, at low frequencies. Therefore, for each of the shell systems considered, only the s=1 wave will be regarded as a potential disturbance.

Figure 3.14 shows the shell power loss IL obtained by means of radial control line forces considering an *in vacuo* steel shell vibrating in the circumferential mode n=1. As explained in Chapter 2, the nature of this incident wave at low frequencies causes the shell to vibrate as a long, slender rod. Therefore, performing the control with only one line force provides good attenuations, varying from 10 to 30 dB, of the total power flow. At higher frequencies, the incident wave becomes mostly flexural and remains largely affected by a single structural line force; power flow reductions varying from 10 to 20 dB are observed, except around the non-dimensional frequency $\Omega = 1.4$ at which the extensional shell wave cuts on. Increasing the number of control forces to two leads to a significantly better control performance. At low frequencies, virtually total control of the disturbance is achieved. Above $\Omega = 1.4$, an average 30 dB of attenuation is observed.
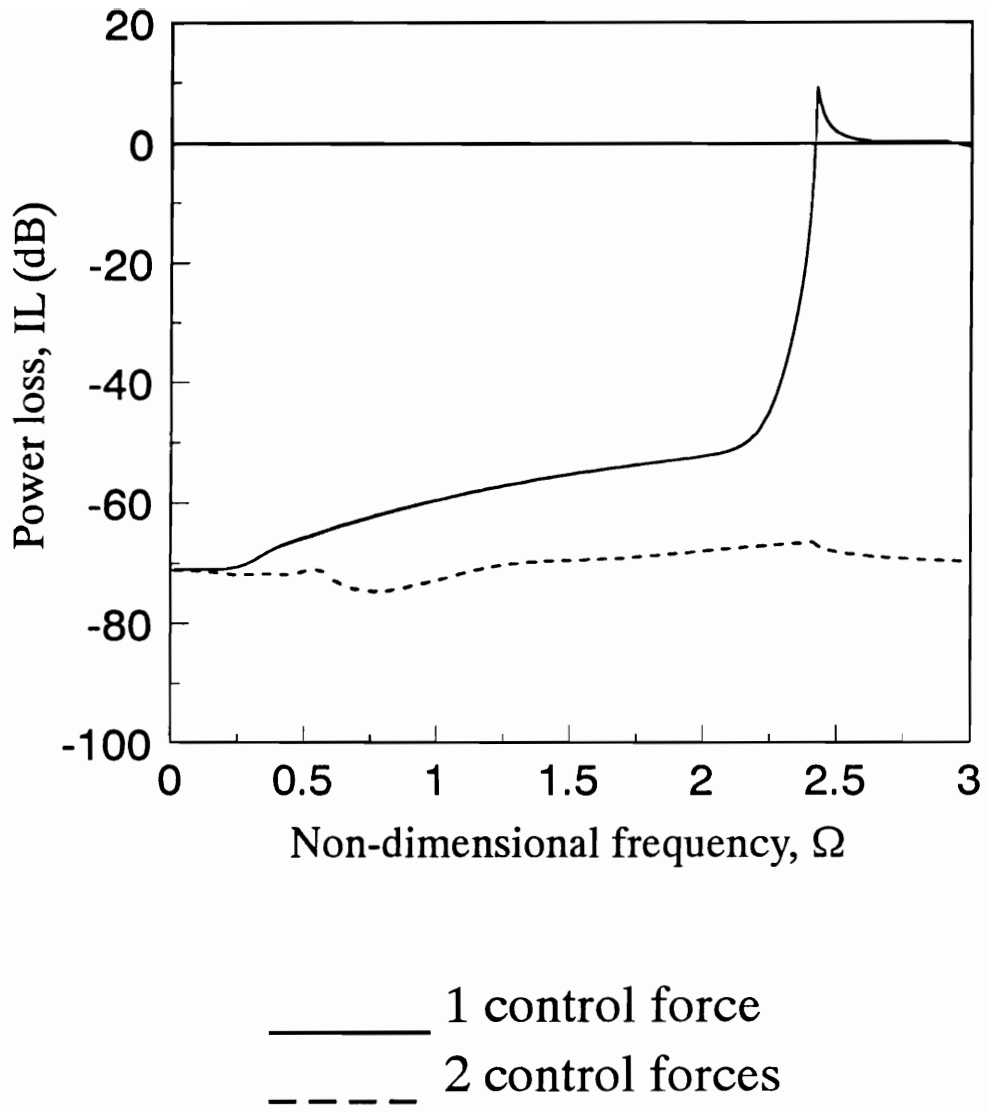
Figure 3.13: Control performance parameter, water-filled plexiglass shell, n=0, branch s=1 incident.
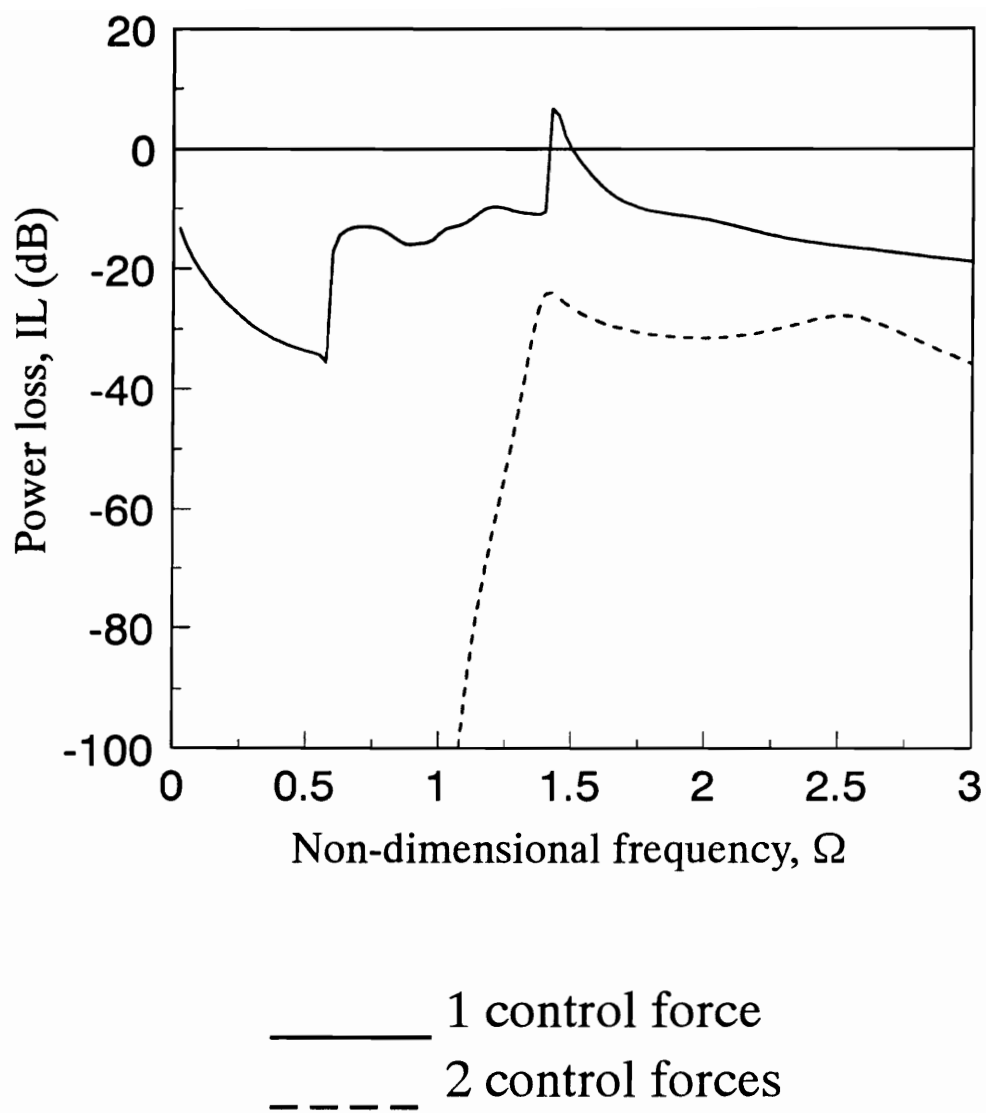
Figure 3.14: Power insertion loss, *in vacuo* steel shell, n=1, branch s=1 incident.

When the steel shell is filled with water (Figure 3.15), two important phenomena affect the control performance. At low frequencies, below the first acoustic cutoff frequency near $\Omega=0.55$, the control effectiveness is increased. Up to 70 dB of attenuation is obtained with only one control force. In this frequency range, the fluid simply acts as an added mass decreasing the fluid-filled pipe compliance [51]. However, above $\Omega \simeq 0.55$, as higher order acoustic modes propagate, the control performance is severely decreased. Less than 5 dB of attenuation is obtained with one force and a maximum of 25 dB is achieved with two forces. In this frequency range, an increased amount of the propagating energy is carried by the fluid medium and is thus weakly affected by structural forces.

The results considering an *in vacuo* plexiglass cylindrical shell (Figure 3.16) are very similar to those obtained for the *in vacuo* steel shell. However, using one control force, very poor performance is obtained in the frequency range $\Omega \in [0.9; 1.6]$ due to a stronger Poisson's coupling between extensional and radial shell motion.

When the plexiglass shell is filled with water (Figure 3.17), the control performance is increased across the entire frequency range due to the fluid acting like an added mass. Below $\Omega \simeq 0.55$ at which the torsional shear wave cuts on, attenuations of the total power flow varying from 20 to 80 dB are observed using one control force. Above this frequency, the power flow is reduced by 25 to 35 dB with one force and by 40 to 50 dB with a pair of control forces. Since the fluid has a high impedance relative to the shell wall, there is no acoustic mode of circumferential order n=1 cutting on below $\Omega = 3$. This explains why the results for the water-filled plexiglass shell largely differ from those obtained for the water-filled steel shell.
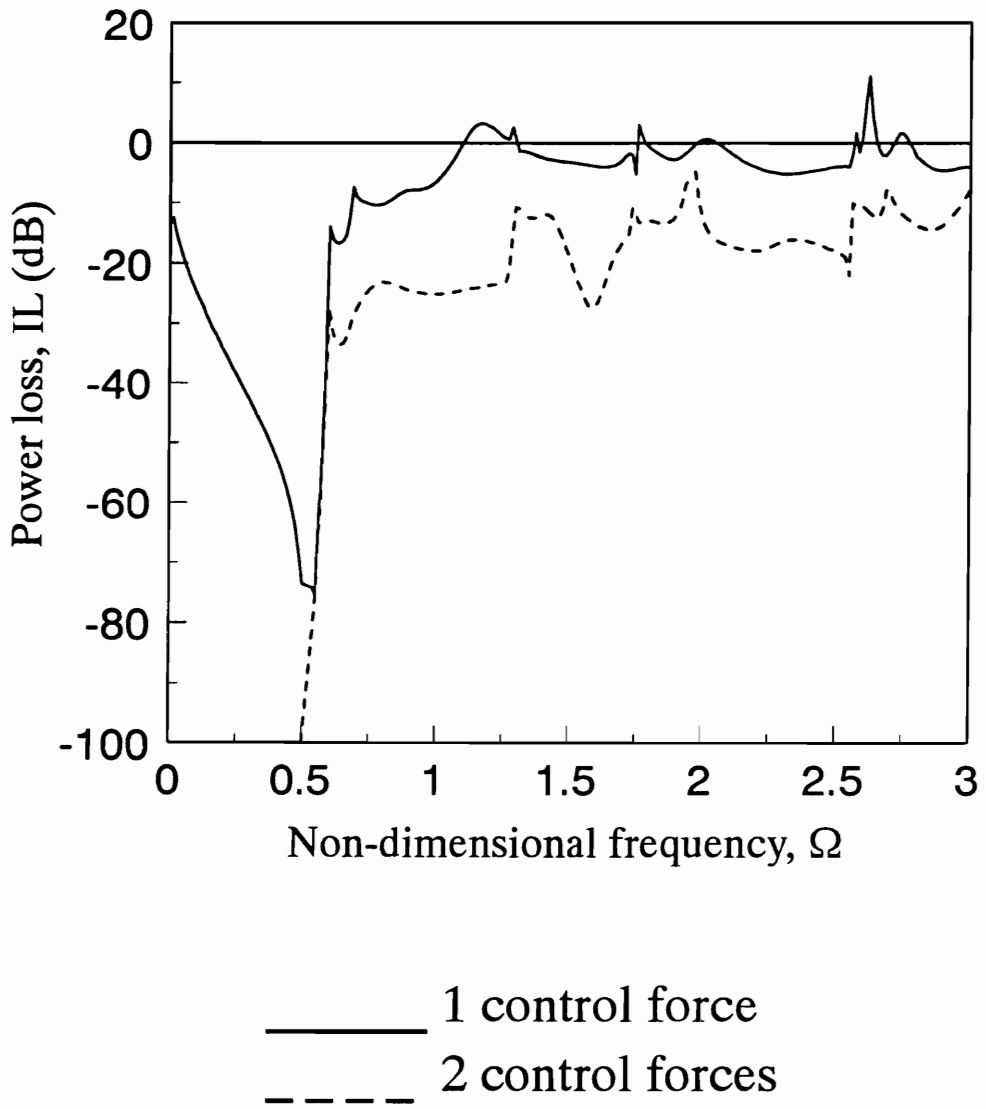
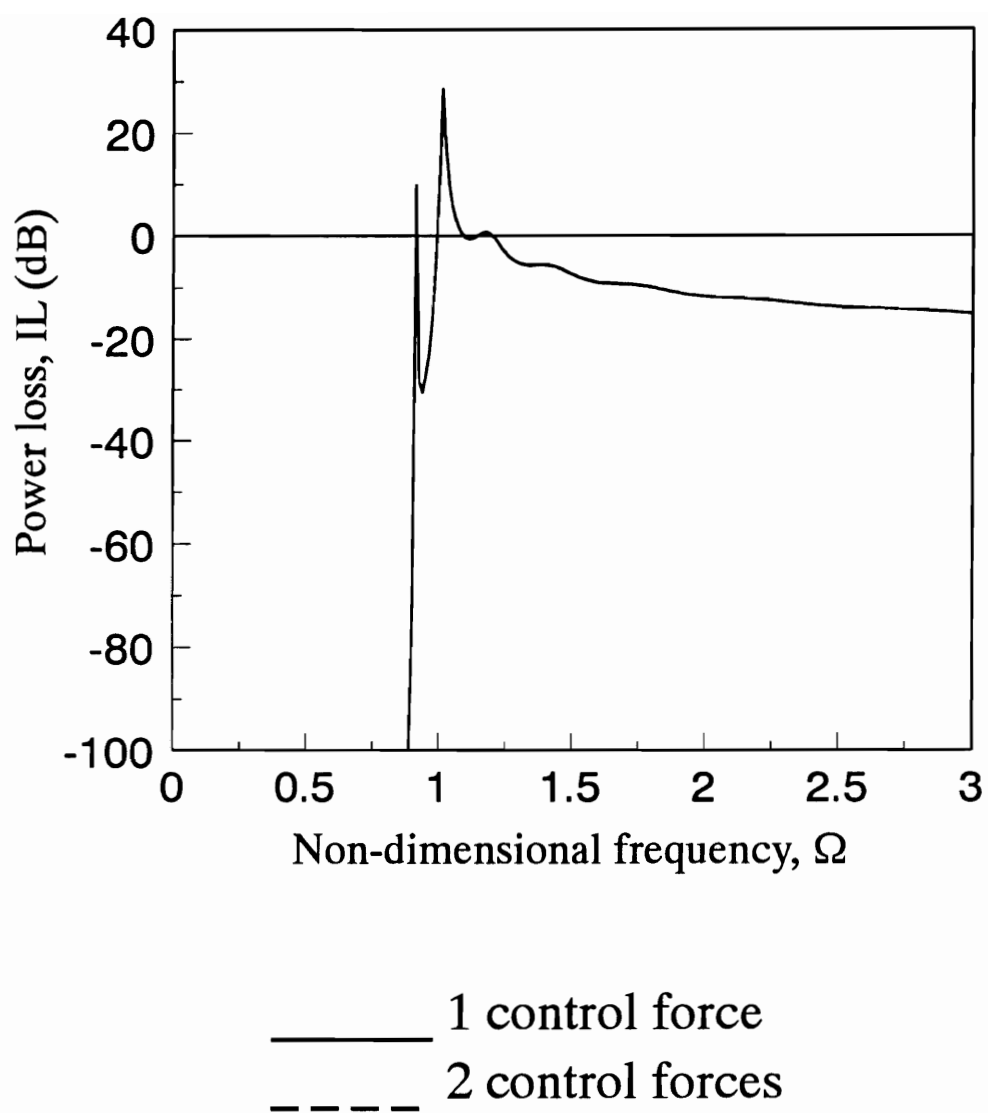Figure 3.15: Power insertion loss, water-filled steel shell, n=1, branch s=1 incident.
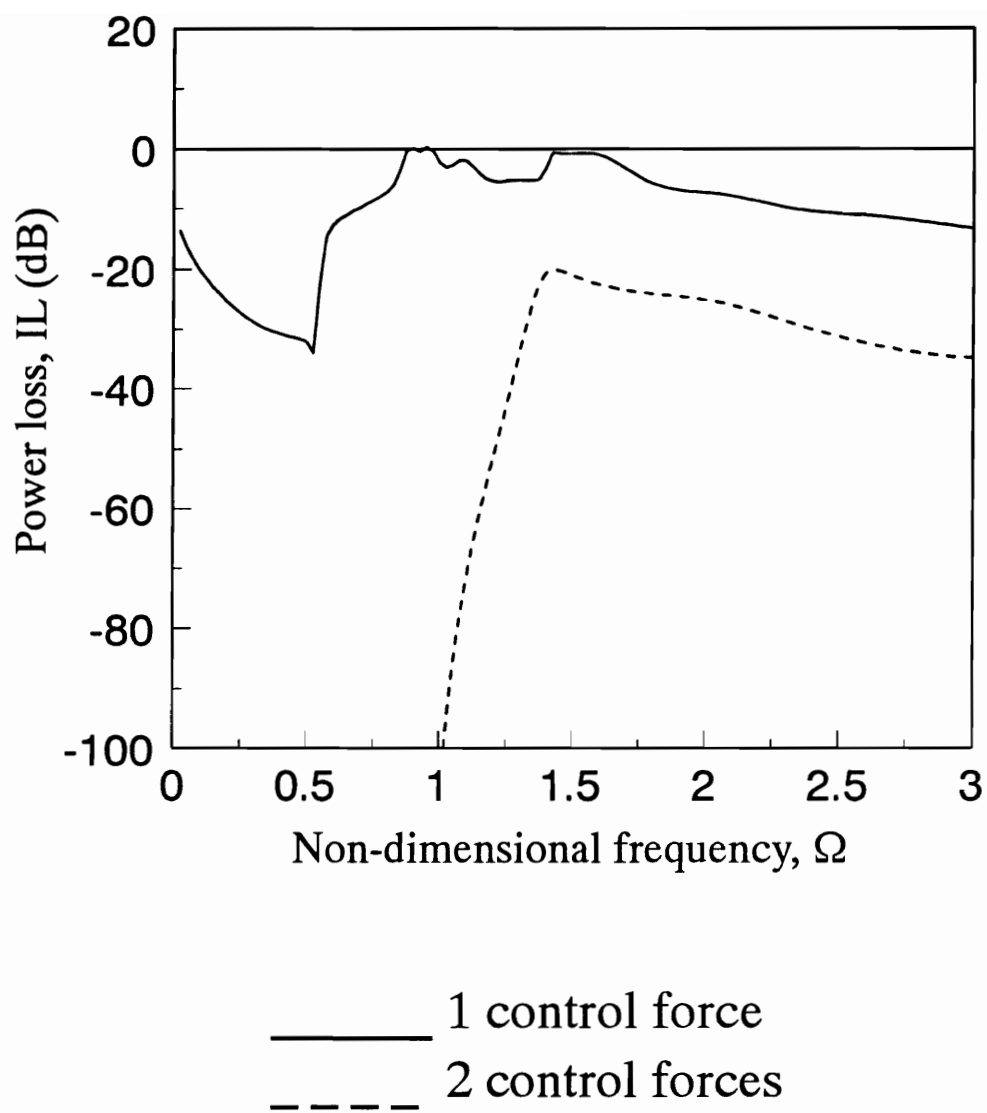
Figure 3.16: Power insertion loss, *in vacuo* plexiglass shell, n=1, branch s=1 incident.
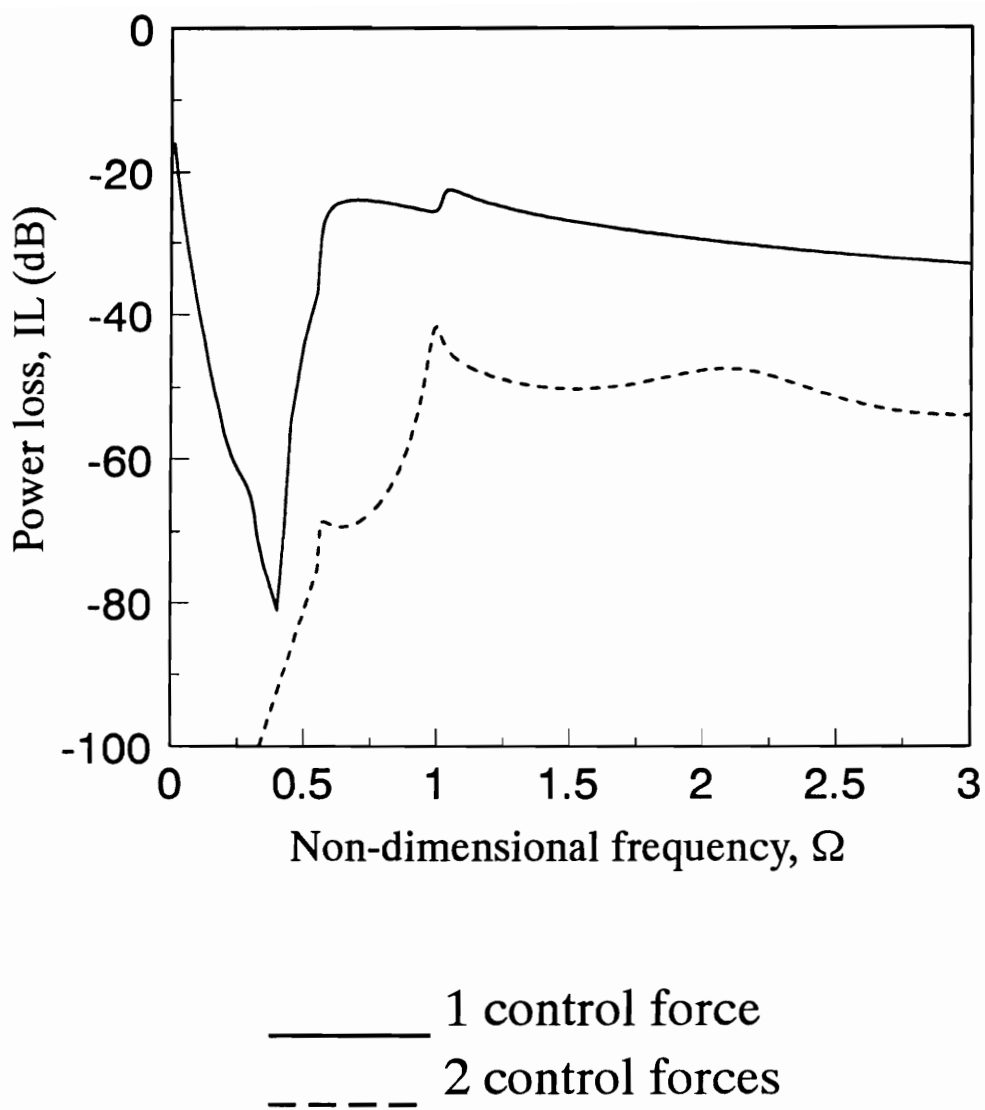
Figure 3.17: Power insertion loss, water-filled plexiglass shell, n=1, branch s=1 incident.

Chapter 4

Active Control of Pipe Vibrations due to Realistic Disturbances

The potential for active control of total energy flow in fluid-filled piping systems when considering the simplest disturbance that may appear in the system, i.e. a single propagating free wave of circumferential order n and radial indice s, was demonstrated in the previous chapter. In most cases, the results at low frequencies have revealed that one or two radial line forces with the same azimuthal distribution as the incident wave were sufficient to achieve considerable reductions of the total power flow. As only a few circumferential modes propagate at low frequencies, most harmonic disturbances in the low frequency range should be controllable with a small number of control inputs. In this Chapter, an active control approach to minimize the total power flow generated by a point force or an internal monopole source at low frequencies is investigated. The point force disturbance addresses the problem of mechanical excitation of the piping system whereas the internal monopole source directs the attention towards the acoustic excitation of the system. Once again, one prefers to use structural control inputs such as radial point forces and ring

forces, which are not obtrusive in the fluid field. The distribution of energy in the coupled system before and after control is evaluated and analyzed. The rationale is to determine whether structural control inputs can efficiently reduce the power flow in the system when it is dominant in the fluid field.

4.1 Point force disturbance

The first disturbance considered is an external radial point force. The point force disturbance is representative of various realistic structural sources piping systems are subjected to, such as forcing loads induced by pumps and compressors for example [51]. The frequency of excitation is assumed to be smaller than the cut-on frequency of the circumferential mode n=3 (see Chapter 2) so that only three circumferential modes (n=0, 1 and 2) contribute to the system response in the far-field. Figure 4.1 illustrates the arrangement of the active control approach investigated. The point force disturbance is located at $x = 0$, $\theta = 0°$. The control inputs, denoted as F_c^0, F_c^1 and F_c^2, are two radial point forces located at $\theta = 0°$, $x = x_c^1, x_c^2$, and one axisymmetric ring force located at $x = x_c^0$. A set of three sensors provides the error information. A first sensor, at $x = x_e^0$, is intended to observe the axisymmetric radial displacement of the shell. A second sensor, at $x = x_e^1$, observes the beam type radial displacement of the shell associated with the circumferential mode n=1. Finally, a third sensor, at $x = x_e^2$, observes the ovalling radial displacement of the shell associated with the circumferential mode n=2. The actual design and implementation of these modal error sensors will be considered in Chapter 5. The amplitude of the control forces minimizing these modal quantities is determined by applying the linear quadratic optimal control theory. The difference of total power

flow in the system before and after control is then used to evaluate the performance of the discontinuity created on the shell by the active vibration control.

The solution for the response of the system to a ring force has been presented in Chapter 3. In this section, the response of the system to a point force excitation is derived. Then, the optimal control forces are determined. The solution for the total power flow in the system, including terms associated with waves of various circumferential mode orders, is presented. The results of the investigation are discussed and analyzed for various configurations of the shell system.

4.1.1 Response of a fluid-filled cylindrical shell to an external radial point force

A radial point force applied at $\theta = 0°$ and $x = x_0$ can be written in terms of external pressure loading on the shell wall as

$$
\mathbf{p_0} = \begin{pmatrix} p_0^x \\ p_0^\theta \\ p_0^r \end{pmatrix} = \begin{pmatrix} 0 \\ 0 \\ F_0 \delta(\theta) \delta(x - x_0) \end{pmatrix} \tag{4.1}
$$

where F_0 has the unit of force per unit length, i.e. $a F_0$ has the unit of force.

The radial pressure p_0^r is then expressed as a Fourier expansion in the circumferential direction [5]:

$$
p_0^r = \sum_{n=0}^{\infty} f_0^n \cos(n\theta) \delta(x - x_0), \tag{4.2}
$$

where

$$
f_0^n = \frac{\epsilon_n}{\pi} \int_0^\pi F_0 \delta(\theta') \cos(n\theta') \, d\theta'. \tag{4.3}
$$

89
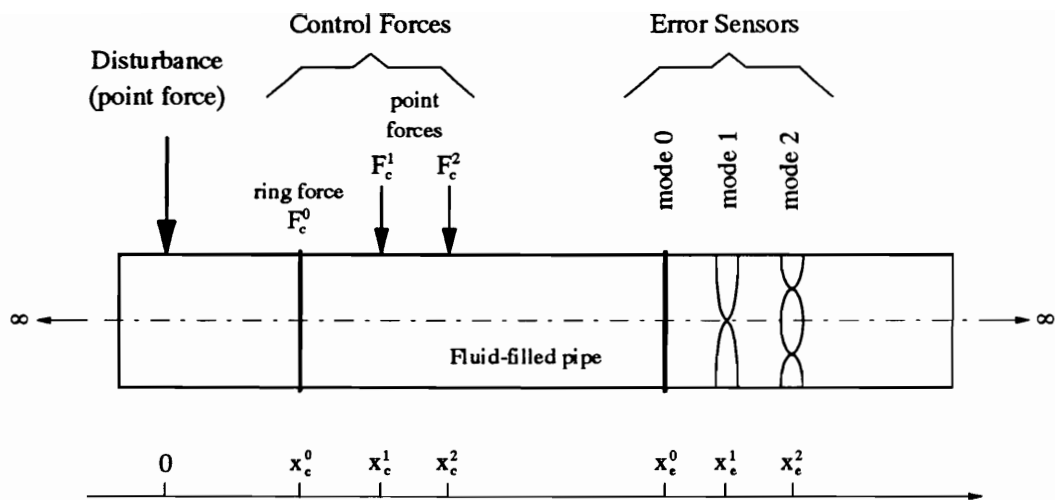
Figure 4.1: Active control arrangement for a point force disturbance at low frequency.

Solving the integral in Equation (4.3) yields

$$p_0^r = \sum_{n=0}^{\infty} \frac{F_0 \epsilon_n}{2\pi} \cos(n\theta) \delta(x - x_0), \tag{4.4}$$

where $\epsilon_0 = 1$ and $\epsilon_n = 2$ for $n \geq 1$.

Equation (4.4) shows that the point force is modelled as an infinite sum of radial line forces whose response has been previously derived in Section 3.3. In terms of shell radial displacement, the system response to a point force can thus be written as follows

$$w(x, \theta) = \frac{F_0}{4\pi^2 \rho_s c_L^2 h/a} \sum_{n=0}^{\infty} \epsilon_n \cos(n\theta) \int_{-\infty}^{+\infty} I_{33} e^{ik_n(x-x_0)} dk_n a \tag{4.5}$$

$$= \frac{iF_0}{2\pi \rho_s c_L^2 h/a} \sum_{n=0}^{\infty} \epsilon_n \cos(n\theta) \sum_{s=1}^{\infty} Res_n(s), \tag{4.6}$$

where the terms I_{33} and $Res_n(s)$ are given by Equations (3.12) and (3.15). As explained in Section 3.3, the number of residues taken into account to evaluate the shell response to a line force can be truncated to a finite value S_n. In the far-field, the number of circumferential modes included in the point force response can also be truncated to a finite value N since high order circumferential modes do not propagate below a certain frequency (the cut-on frequency), as explained in Chapter 2.

Equation (4.6) can be rewritten as follows:

$$w(x, \theta) = \sum_{n=0}^{N} w_n(x, \theta), \tag{4.7}$$

where

$$w_n(x, \theta) = \frac{F_0 \epsilon_n}{4\pi^2 \rho_s c_L^2 h/a} \cos(n\theta) \int_{-\infty}^{+\infty} I_{33} e^{ik_n(x-x_0)} dk_n a. \tag{4.8}$$

The function $w_n(x, \theta)$ represents the contribution of the circumferential mode n to the radial displacement of the shell at a given location $M(x, \theta)$. In the next section, it is referred to as the *modal radial displacement* of the shell system, associated with the circumferential mode n.

4.1.2 Linear quadratic optimal control

The modal radial displacements of the controlled shell system, corresponding to the circumferential modes n=0, n=1 and n=2, at the error locations x_e^0, x_e^1 and x_e^2 respectively, result from the superposition of the displacement field due the point force disturbance and the displacement fields due to the control inputs. They are expressed as

$$
\begin{aligned}
w_0^t(x_e^0, \theta) &= \frac{1}{2A} \left(F_d \int_{-\infty}^{+\infty} I_{33} e^{ik_0 x_e^0} dk_0 a + F_c^0 \int_{-\infty}^{+\infty} I_{33} e^{ik_0(x_e^0 - x_c^0)} dk_0 a \right. \\
&\quad + \left. F_c^1 \int_{-\infty}^{+\infty} I_{33} e^{ik_0(x_e^0 - x_c^1)} dk_0 a + F_c^2 \int_{-\infty}^{+\infty} I_{33} e^{ik_0(x_e^0 - x_c^2)} dk_0 a \right), \quad (4.9)
\end{aligned}
$$

$$
\begin{aligned}
w_1^t(x_e^1, \theta) &= \frac{1}{A} \left(F_d \cos \theta \int_{-\infty}^{+\infty} I_{33} e^{ik_1 x_e^1} dk_1 a + F_c^1 \cos \theta \int_{-\infty}^{+\infty} I_{33} e^{ik_1(x_e^1 - x_c^1)} dk_1 a \right. \\
&\quad + \left. F_c^2 \cos \theta \int_{-\infty}^{+\infty} I_{33} e^{ik_1(x_e^1 - x_c^2)} dk_1 a \right), \quad (4.10)
\end{aligned}
$$

$$
\begin{aligned}
w_2^t(x_e^2, \theta) &= \frac{1}{A} \left(F_d \cos 2\theta \int_{-\infty}^{+\infty} I_{33} e^{ik_2 x_e^2} dk_2 a + F_c^1 \cos 2\theta \int_{-\infty}^{+\infty} I_{33} e^{ik_2(x_e^2 - x_c^1)} dk_2 a \right. \\
&\quad + \left. F_c^2 \cos 2\theta \int_{-\infty}^{+\infty} I_{33} e^{ik_2(x_e^2 - x_c^2)} dk_2 a \right), \quad (4.11)
\end{aligned}
$$

where F_d is the amplitude of the point force disturbance and A is a constant term equal to $(2\pi^2 \rho_s c_L^2 h/a)$.

It appears from Equations (4.11) and (4.11) that the modal radial displacements of the shell, associated with the modes n=1 and n=2, are independent of the

control ring force F_c^0. Therefore, they can be expressed in the following matrix form

$$\mathbf{w^t} = \mathbf{d}F_d + \mathbf{C}\mathbf{f_c}, \qquad (4.12)$$

where the vectors and matrices are given by

$$\mathbf{d} = \frac{1}{A} \left[\cos\theta \int_{-\infty}^{+\infty} I_{33} e^{ik_1 x_e^1} dk_1 a \quad \cos 2\theta \int_{-\infty}^{+\infty} I_{33} e^{ik_2 x_e^2} dk_2 a \right]^T \qquad (4.13)$$

$$\mathbf{C} = \frac{1}{A} \left[\begin{array}{cc} \cos\theta \int_{-\infty}^{+\infty} I_{33} e^{ik_1(x_e^1 - x_c^1)} dk_1 a & \cos\theta \int_{-\infty}^{+\infty} I_{33} e^{ik_1(x_e^1 - x_c^2)} dk_1 a \\ \cos 2\theta \int_{-\infty}^{+\infty} I_{33} e^{ik_2(x_e^2 - x_c^1)} dk_2 a & \cos 2\theta \int_{-\infty}^{+\infty} I_{33} e^{ik_2(x_e^2 - x_c^2)} dk_2 a \end{array} \right] \qquad (4.14)$$

$$\mathbf{f_c} = \left[F_c^1 \quad F_c^2 \right]^T \qquad (4.15)$$

$$\mathbf{w^t} = \left[w_1^t(x_e^1, \theta) \quad w_2^t(x_e^2, \theta) \right]^T \qquad (4.16)$$

In order to minimize the modal radial displacements of the shell at the axial positions x_e^1 and x_e^2 around the circumference, the following cost function is defined

$$J = \sum_{i=1}^{2} \int_0^{2\pi} \left| w_i^t(x_e^i, \theta) \right|^2 d\theta. \qquad (4.17)$$

As seen in Chapter 3, the optimal vector of control forces to minimize the quadratic cost function J is given by

$$\mathbf{f_c^{opt}} = -[\mathbf{C}^H \mathbf{C}]^{-1} [\mathbf{C}^H \mathbf{d}] F_d. \qquad (4.18)$$

Equation (4.10) yields the third optimal control force, F_c^0, minimizing the

axisymmetric radial displacement at x_e^0,

$$
\begin{aligned}
F_c^0 &= \frac{-1}{\int_{-\infty}^{+\infty} I_{33} e^{ik_0(x_e^0 - x_c^0)} dk_0 a} \left(F_d \int_{-\infty}^{+\infty} I_{33} e^{ik_0 x_e^0} dk_0 a \right. \\
&\quad + \left. F_c^1 \int_{-\infty}^{+\infty} I_{33} e^{ik_0(x_e^0 - x_c^1)} dk_0 a + F_c^2 \int_{-\infty}^{+\infty} I_{33} e^{ik_0(x_e^0 - x_c^2)} dk_0 a \right) .
\end{aligned} \tag{4.19}
$$

4.1.3 Evaluation of the control performance

The performance of the discontinuity created on the shell system by the active control forces is evaluated by means of the power insertion loss IL, defined by Equation (3.52) and (3.51). However, the expressions (3.24), (3.37) and (3.40) for the fluid power flow, the shell power flow and the total power flow have to be revised to include various circumferential modes n.

To derive the total power flow in the system, the pressure in t... fluid ar the shell displacements are now expressed as the following series

$$
p = \sum_{n=0}^{N} \cos(n\theta) \sum_{s=1}^{S_n} P_{ns} J_n(k_s^r r) e^{i(k_{ns}x - \omega t)}, \tag{4.20}
$$

$$
u = \sum_{n=0}^{N} \cos(n\theta) \sum_{s=0}^{S_n} U_{ns} e^{i(k_{ns}x - \omega t - i\pi/2)}, \tag{4.21}
$$

$$
v = \sum_{n=0}^{N} \sin(n\theta) \sum_{s=0}^{S_n} V_{ns} e^{i(k_{ns}x - \omega t)}, \tag{4.22}
$$

$$
w = \sum_{n=0}^{N} \cos(n\theta) \sum_{s=0}^{S_n} W_{ns} e^{i(k_{ns}x - \omega t)}. \tag{4.23}
$$

Following the same steps as in Section 3.4 and applying the orthogonality principle between different circumferential modes,

$$
\frac{\epsilon_n}{2\pi} \int_{-\pi}^{\pi} \cos m\phi \cos n\phi = \delta_{mn}, \tag{4.24}
$$

94

where δ_{mn} is the Kronecker delta function, one obtains the expressions for the fluid power flow, the shell power flow and the total power flow in the system as

$$\Pi_f = Re\left[\frac{\pi}{2}c_L^3\Omega^3\rho_f\sum_{n=0}^{N}\varepsilon_n\sum_{s=0}^{S_n}\sum_{j=0}^{S_n}W_{ns}W_{nj}^*e^{i(k_{ns}-k_{nj}^*)x}F_{sjn}^f\right], \qquad (4.25)$$

$$\Pi_s = Re\left[\pi\rho_s c_L^3\Omega\sum_{n=0}^{N}\sum_{s=1}^{S_n}\sum_{j=1}^{S_n}W_{ns}W_{nj}^*e^{i(k_{ns}-k_{nj}^*)x}S_{sjn}^f\right], \qquad (4.26)$$

$$\Pi_t = \Pi_s + \Pi_f = \sum_{n=0}^{N}\Pi_t^n. \qquad (4.27)$$

Note that Π_t^n in Equation (4.27) denotes the total power flow due to a single circumferential mode n. This decomposition is possible because two modes (n, s) and (m, j) are orthogonal for $n \neq m$.

4.1.4   Results

In this section, the performance of the control configuration described above is presented. Various frequencies of excitation are considered. The point force disturbance is applied at $x = 0$ and its amplitude was arbitrarily chosen to be $F_d = 100N/m$. The axisymmetric control force is applied at $x_c^0 = 3a$. The control point forces are applied at $x_c^1 = 4a$ and $x_c^2 = 5a$. The spacing between the control forces has very little influence on the performance of the control approach and was primarily chosen such that it could be implemented experimentally. The modal error sensors, associated with the breathing mode n=0, the beam bending mode $n = 1$ and the ovalling mode $n = 2$, are located at $x_e^0 = 7a$, $x_e^1 = 7.5a$ and $x_e^2 = 8a$, respectively. One diameter spacing between the last control force and the first error sensor ensures a complete decay of the near field waves in the frequency range of concern ($\Omega < 0.3$). The power flow in the shell system before and after control is

evaluated at $x = 10a$.

For any excitation frequency of the disturbance, considering *in vacuo* and water-filled steel or plexiglass shells, the control approach yields a total attenuation of the modal radial displacements of the shell associated with the circumferential modes n=0,1 and 2, at the error sensor locations. Of interest is the effect of this control on the total power flow in the system.

Figure 4.2 shows the modal decomposition of the total power flow in an *in vacuo* steel shell before and after control for a frequency of excitation $\Omega = 0.05$. This frequency is about twice smaller than the cut-on frequency of the circumferential mode n=3. As shown is Figure 4.2, the response of the system at this frequency is dominated by the beam bending and the ovalling types of motion. When control is applied, the power conveyed by both of these modes is reduced by 16 dB and the power transmitted by the breathing mode n=0 is reduced by 27 dB. When the frequency is increased above $\Omega = 0.11$, at which the mode n=3 cuts on, the performance of the control approach is severely reduced. At $\Omega = 2$ (Figure 4.3), the total power insertion loss due to the active control is only 1.1 dB. The power transmitted by the circumferential modes 0, 1 and 2 is reduced by more than 10 dB but the control causes the power flow conveyed by the mode n=3 to increase. This phenomenon is usually called *spillover*. Spillover here occurs because none of the error sensors is designed to observe the shell motion associated with the mode n=3. Consequently, the actuators can easily add energy into higher order modes without affecting the control calculation. At $\Omega = 3$ (Figure 4.4), spillover in the modes n=3 and n=4 becomes very important and control yields an increase of the total power flow in the system (IL=-5.6 dB). At this frequency, a higher number of control

Figure 4.2: Modal decomposition of the total power flow in an *in vacuo* steel shell excited by a point force at $\Omega = 0.05$.

channels is needed to achieve good reductions of the total power flow. This example illustrates a drawback of active control. Unlike passive control, active approaches can lead to an increase of power in the system since they act by introducing energy. Results for the *in vacuo* plexiglass shell are very similar to those for the *in vacuo* steel shell; therefore, they are not presented.

Figure 4.5(a) shows the modal decomposition of the total power flow in a water-filled steel shell before and after control for a frequency of excitation $\Omega = 0.05$. The results before and after control are very similar to those obtained for the *vacuo shell*. The fluid loading has a very little influence on the response of the steel shell system at this frequency. Figure 4.5(b) shows that the point force disturbance at this frequency creates a flow of energy that is largely carried by the shell wall. According to the investigation on the free wave propagation in fluid-filled pipes (see Chapter 2), the effect of the fluid loading is expected to be more noticeable on the response of the plexiglass shell. In particular, it has be shown that the cut on frequencies of the circumferential modes $n > 1$ for the water-filled plexiglass shell are two to three times lower than those for the *in vacuo* shell. At $\Omega = 0.05$ for example (Figure 4.6), before control, the circumferential mode n=3 propagates and convey a large amount of the energy in the water-filled plexiglass shell. Even though none of the error sensors is designed to observe the propagating waves of circumferential order n=3, the power conveyed by the mode is reduced by 12 dB after control. This unexpected good performance is due to the waves of circumferential order n=2 and n=3 having nearly identical phase speeds at this frequency. The shell radial displacements associated with these two modes, induced by the point force disturbance, are thus in phase at the error sensor location x_e^2. By minimizing the ovalling shell motion at x_e^2, the control point forces inevitably minimized the

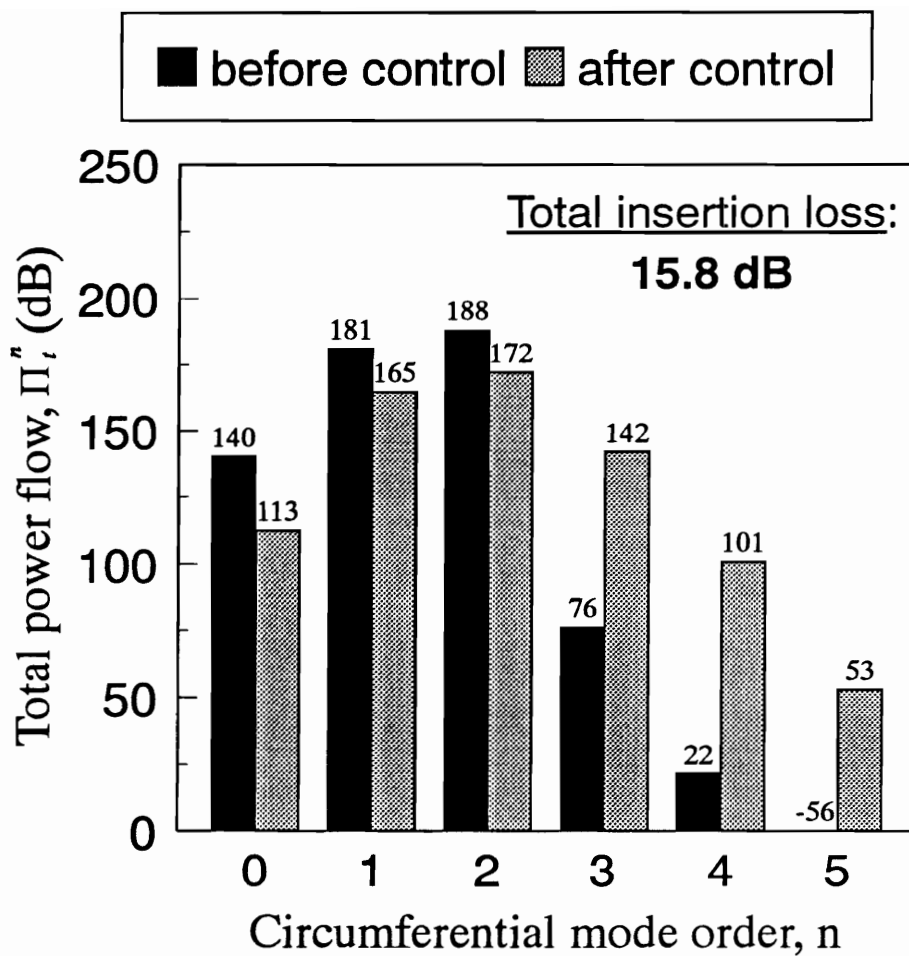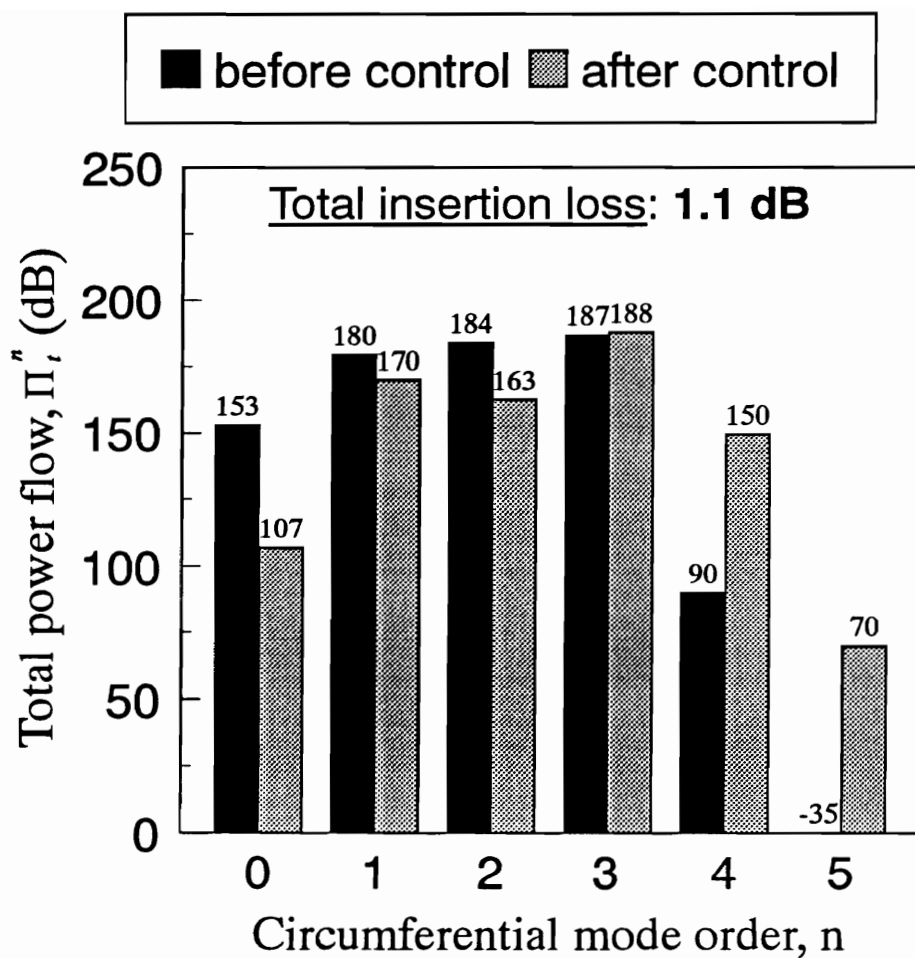Figure 4.3: Modal decomposition of the total power flow in an *in vacuo* steel shell excited by a point force at $\Omega = 0.2$.
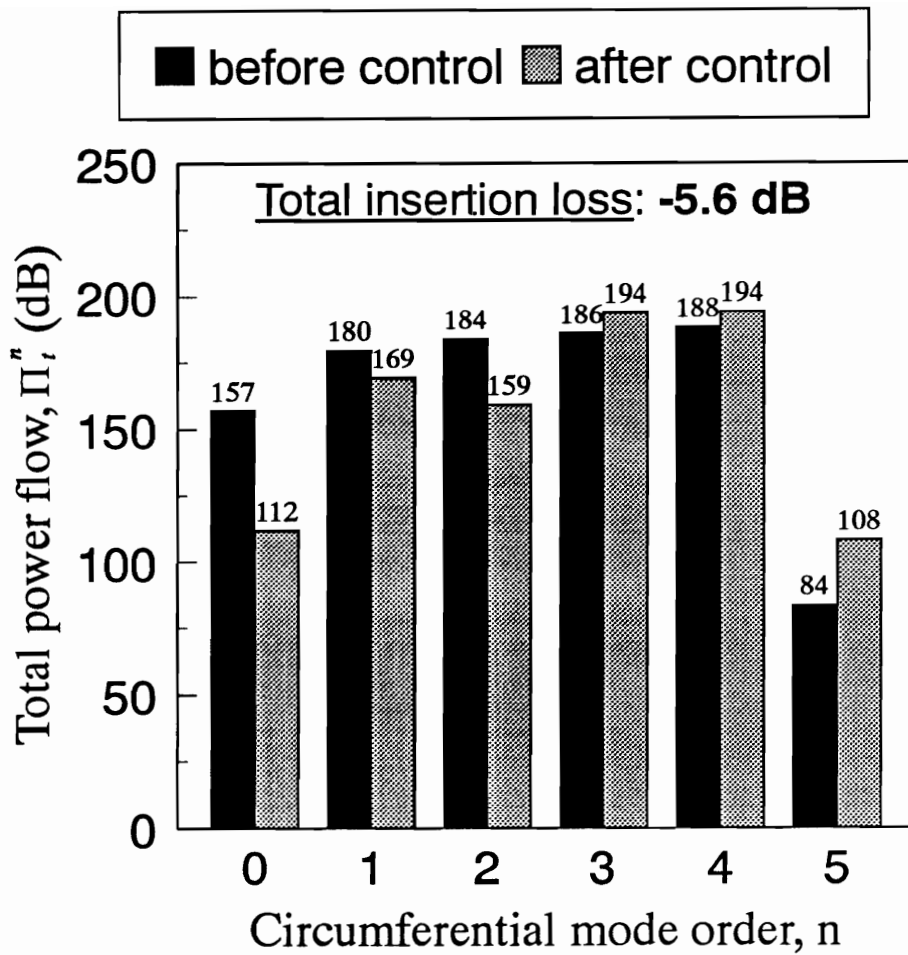
Figure 4.4: Modal decomposition of the total power flow in an *in vacuo* steel shell excited by a point force at $\Omega = 0.3$.
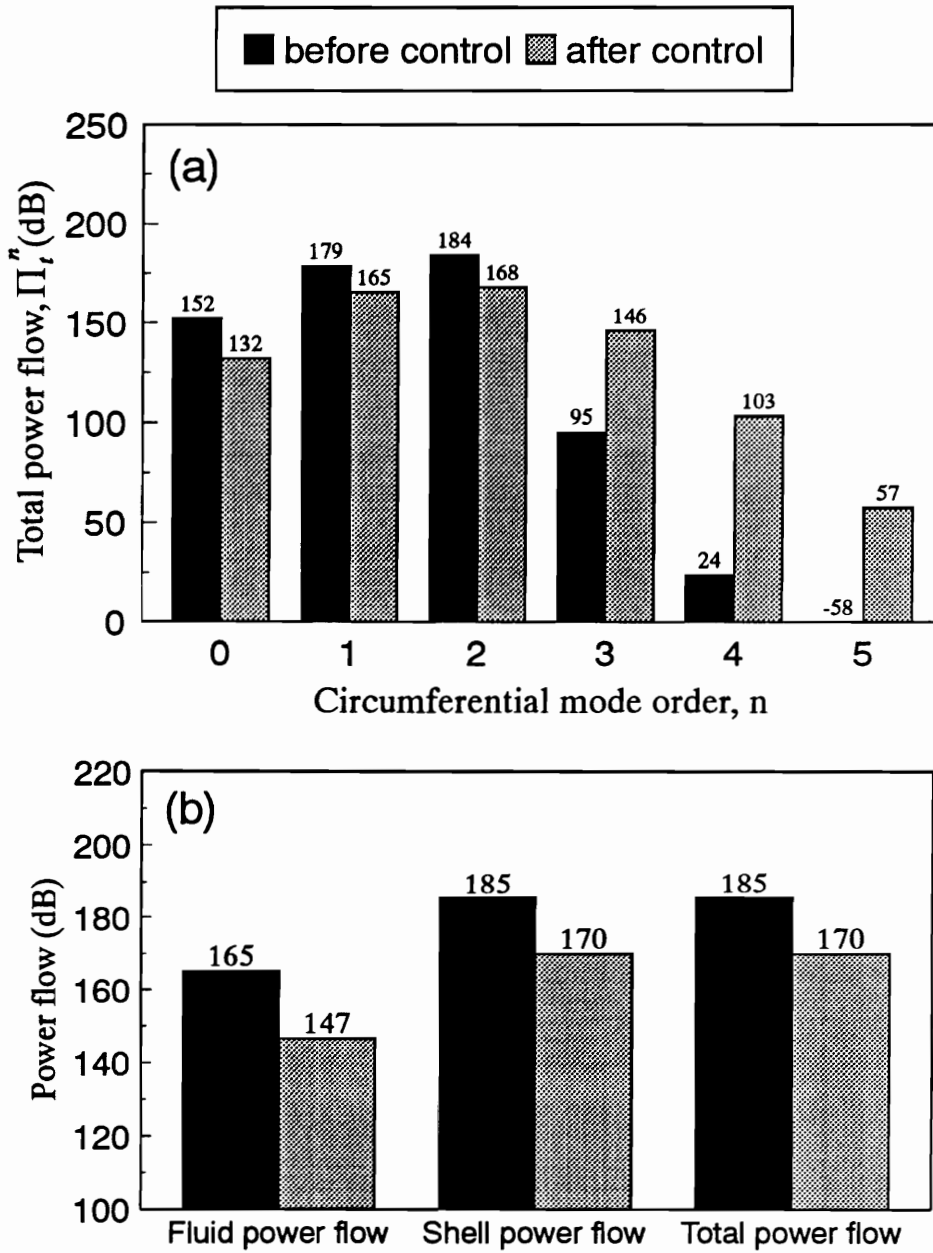
Figure 4.5: Total power flow in a water-filled steel shell excited by a point force at $\Omega = 0.05$; (a) modal decomposition, (b) distribution in the system.

shell motion associated with the mode n=3. This phenomenon would not appear if the disturbance was further away from the control forces. The slight mismatch between the two phase speeds would induce larger phase shifts between the modal displacements. At $\Omega = 0.1$ however (Figure 4.7), poor performance of the control approach is obtained because of spillover. No attenuation of the total power flow is achieved.

As similar control performances are obtained for water-filled steel and plexiglass shells at $\Omega = 0.05$, it is interesting to compare the control effort associated with each case. The control effort is here defined as follows

$$E_c = \sqrt{\sum_{n=0}^{2} \left| \frac{F_c^n}{F_d} \right|^2}. \tag{4.28}$$

It appears from Table 4.1 that the control efforts associated with these two cases are comparable. The amplitude of the radial control point forces is larger than the control ring force because the axisymmetric shell motion is not much excited by the point force disturbance.

4.2   Monopole disturbance

The second type of disturbance that has been studied is the monopole source inside a fluid-filled shell. This study is representative of common situations in which the cylindrical shell is excited by internal acoustic waves. This acoustic excitation may be due to local turbulence created by the presence of a discontinuity in the pipe flow, such as a valve or a bend for example [51]. The control approach is the same as the one used for the radial point force disturbance and is illustrated in Figure 4.8.
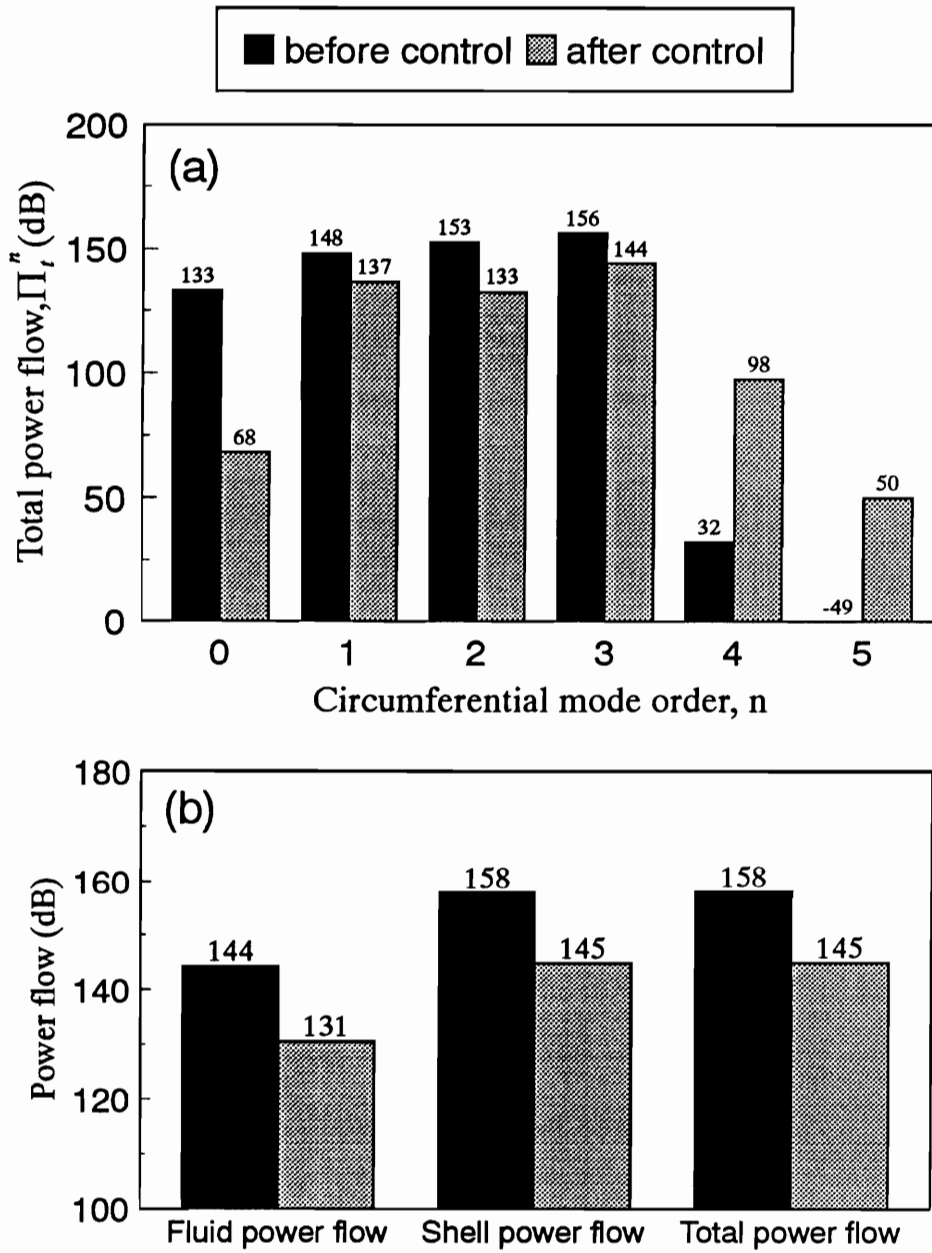
Figure 4.6: Total power flow in a water-filled plexiglass shell excited by a point force at $\Omega = 0.05$; (a) modal decomposition, (b) distribution in the system.
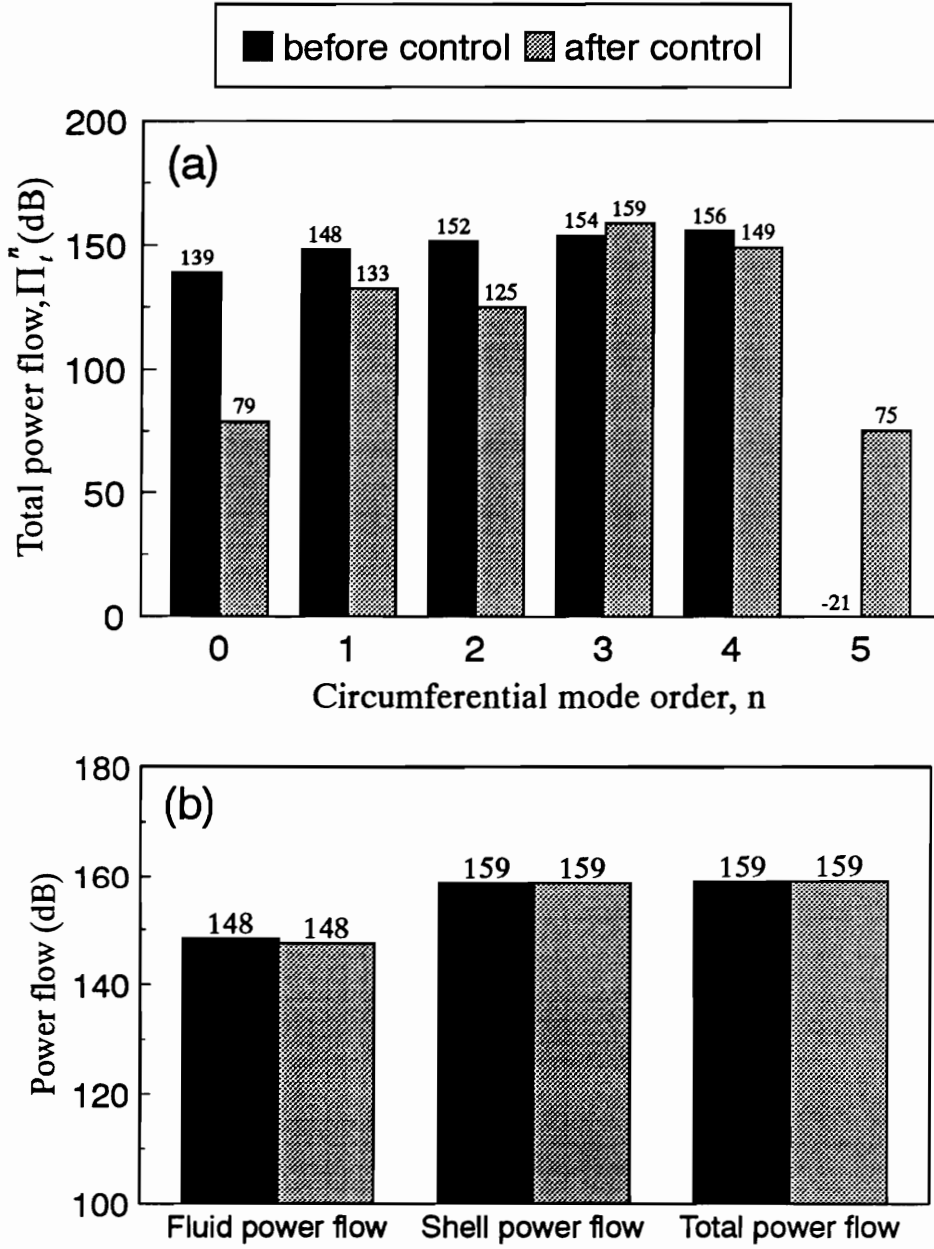
Figure 4.7: Total power flow in a water-filled plexiglass shell excited by a point force at $\Omega = 0.1$; (a) modal decomposition, (b) distribution in the system.

Table 4.1: Control effort for water-filled steel and plexiglass shells excited by a point force at the frequency $\Omega = 0.05$.

	Water-filled steel shell	Water-filled plexiglass shell
$|F_c^0/F_d|$	0.36	0.99
$|F_c^1/F_d|$	3.84	3.45
$|F_c^2/F_d|$	2.93	2.63
E_c	4.84	4.45

The monopole source is located at $x = 0$, $r = r_p$ and $\theta = 0°$. The control inputs are the same as in the previous section, i.e. two radial point forces located at $\theta = 0°$, $x = x_c^1, x_c^2$, and one axisymmetric ring force located at $x = x_c^0$. The modal radial displacement of the shell wall, associated with the circumferential modes n=0, n=1 and n=2, is minimized at $x = x_e^0$, $x = x_e^1$ and $x = x_e^2$ respectively, using linear quadratic optimal control theory.

The response of a fluid-filled cylindrical shell to an internal monopole source is derived next. The derivation of the optimal control forces is then briefly stated. Finally, the performance of the control approach is evaluated and analyzed for various system configurations.

4.2.1 Response of a fluid-filled cylindrical shell to an internal monopole source

The response of an infinite fluid-filled cylindrical elastic shell to an internal monopole source has been previously investigated by James [27] and Fuller [30]. The derivation is briefly recalled here for completeness.

We consider a monopole source located in the fluid at $r = r_p$, $\theta = 0°$ and $x = 0$, having a free field pressure equal to

$$p_p^f(r, \theta, x) = \frac{p_m}{R_0} e^{ik_f R_0},\tag{4.29}$$

where R_0 is the distance from the source to the observation point.

The shell displacements are expressed as inverse wavenumber transforms and

106
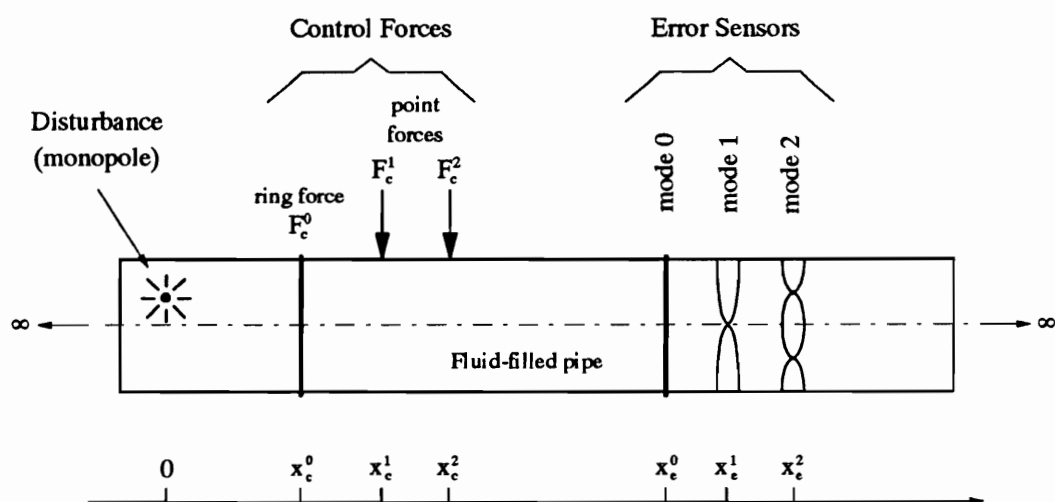
Figure 4.8: Active control configuration for an internal monopole disturbance at low frequency.

Fourier series in the circumferential direction,

$$u = \frac{1}{2\pi} \sum_{n=0}^{\infty} \cos(n\theta) \int_{-\infty}^{+\infty} \bar{U}_n e^{i(k_n x - \pi/2)} dk_n, \qquad (4.30)$$

$$v = \frac{1}{2\pi} \sum_{n=0}^{\infty} \sin(n\theta) \int_{-\infty}^{+\infty} \bar{V}_n e^{ik_n x} dk_n, \qquad (4.31)$$

$$w = \frac{1}{2\pi} \sum_{n=0}^{\infty} \cos(n\theta) \int_{-\infty}^{+\infty} \bar{W}_n e^{ik_n x} dk_n. \qquad (4.32)$$

$$(4.33)$$

As only the harmonic response is considered, the time variation $e^{-i\omega t}$ in Equations (4.29), (4.31), (4.32) and (4.33) has been omitted.

The pressure field at the shell wall associated with a monopole source has been derived by James [27] and is expressed in a spectral form for a given circumferential mode n as

$$\bar{p}_a(k_n, \theta) = 2 p_m \epsilon_n J_n(k^r r_p) \left[k^r a J_n'(k^r a) \right]^{-1} + \rho_f \omega^2 \bar{W}_n J_n(k^r a) \left[k^r a J_n'(k^r a) \right]^{-1} \quad (4.34)$$

Substituting Equations (4.31) thru (4.34) into the Kennard shell equations (2.1), (2.2) and (2.3) yields the spectral equations of motion of the forced response of the system to a monopole source for a given circumferential mode n,

$$\begin{bmatrix} L_{11} & L_{12} & L_{13} \\ L_{21} & L_{22} & L_{23} \\ L_{31} & L_{32} & L_{33} \end{bmatrix} \begin{bmatrix} \bar{U}_n \\ \bar{V}_n \\ \bar{W}_n \end{bmatrix} = \begin{bmatrix} 0 \\ 0 \\ T_3 \end{bmatrix}, \qquad (4.35)$$

where the terms of the matrix $\mathbf{L}$ are given by Equation (2.13) and T_3 is defined as

$$T_3 = \frac{2 a p_m \epsilon_n J_n(k^r r_p)}{\rho_s c_L^2 h / a k^r a J_n'(k^r a)}. \qquad (4.36)$$

Solving for $\bar{W}_n$ and taking the inverse Fourier transform give the radial dis-

placement w as

$$w(x, \theta) = \frac{p_m}{\pi \rho_s c_L^2 h/a} \sum_{n=0}^{\infty} \epsilon_n \cos(n\theta) \int_{-\infty}^{+\infty} \frac{J_n(k^r r_p)}{k^r a J_n'(k^r a)} I_{33} e^{ik_n x} dk_n a. \tag{4.37}$$

Using the theorem of residues to compute the integral in Equation (4.37) [30], the radial displacement can be written as

$$w(x, \theta) = \frac{2\imath p_m}{\rho_s c_L^2 h/a} \sum_{n=0}^{N} \epsilon_n \cos(n\theta) \sum_{s=1}^{S_n} Res_n^m(s), \tag{4.38}$$

$$Res_n^m(s) = \left. \frac{J_n(k^r r_p)(L_{11}L_{22} - L_{12}L_{21})}{(k^r a J_n'(k^r a)|L|)^\diamond} e^{ik_n x} \right|_{k_n = k_{ns}}. \tag{4.39}$$

4.2.2 Linear quadratic optimal control

The modal radial displacements of the controlled shell system, corresponding to the circumferential modes n=0, n=1 and n=2, at the error locations x_e^0, x_e^1 and x_e^2 respectively, result from the superposition of the displacement field due the monopole disturbance and the displacement fields due to the control inputs. They are expressed as

$$
\begin{aligned}
w_0^t(x_e^0, \theta) = \quad & \frac{1}{2A} \left(4\pi p_m \int_{-\infty}^{+\infty} \frac{J_0(k^r r_p)}{k^r a J_0'(k^r a)} I_{33} e^{ik_0 x_e^0} dk_0 a \right. \\
& + F_c^0 \int_{-\infty}^{+\infty} I_{33} e^{ik_0(x_e^0 - x_c^0)} dk_0 a + F_c^1 \int_{-\infty}^{+\infty} I_{33} e^{ik_0(x_e^0 - x_c^1)} dk_0 a \\
& + \left. F_c^2 \int_{-\infty}^{+\infty} I_{33} e^{ik_0(x_e^0 - x_c^2)} dk_0 a \right), \tag{4.40} \\
w_1^t(x_e^1, \theta) = \quad & \frac{1}{A} \left(4\pi p_m \cos\theta \int_{-\infty}^{+\infty} \frac{J_1(k^r r_p)}{k^r a J_1'(k^r a)} I_{33} e^{ik_1 x_e^1} dk_1 a \right. \\
& + F_c^1 \cos\theta \int_{-\infty}^{+\infty} I_{33} e^{ik_1(x_e^1 - x_c^1)} dk_1 a \\
& + \left. F_c^2 \cos\theta \int_{-\infty}^{+\infty} I_{33} e^{ik_1(x_e^1 - x_c^2)} dk_1 a \right), \tag{4.41}
\end{aligned}
$$

$$w_2^t(x_e^2, \theta) = \frac{1}{A}\left(4\pi p_m \cos 2\theta \int_{-\infty}^{+\infty} \frac{J_2(k^r r_p)}{k^r a J_2'(k^r a)} I_{33} e^{ik_2 x_e^2} dk_2 a\right.$$
$$+ F_c^1 \cos 2\theta \int_{-\infty}^{+\infty} I_{33} e^{ik_2(x_e^2 - x_c^1)} dk_2 a$$
$$\left. + F_c^2 \cos 2\theta \int_{-\infty}^{+\infty} I_{33} e^{ik_2(x_e^2 - x_c^2)} dk_2 a\right), \qquad (4.42)$$

where p_m is the amplitude of the internal monopole source.

The theory used to derive the optimal control forces is the same as in Section 4.1.2. The optimal vector of control point forces is thus given by

$$\mathbf{f}_c^{\text{opt}} = -[\mathbf{C}^H \mathbf{C}]^{-1} [\mathbf{C}^H \mathbf{d}] p_m, \qquad (4.43)$$

where

$$\mathbf{d} = \frac{4\pi}{A}\left[\begin{array}{c} \cos \theta \int_{-\infty}^{+\infty} \frac{J_1(k^r r_p)}{k^r a J_1'(k^r a)} I_{33} e^{ik_1 x_e^1} dk_1 a \\[2ex] \cos 2\theta \int_{-\infty}^{+\infty} \frac{J_2(k^r r_p)}{k^r a J_2'(k^r a)} I_{33} e^{ik_2 x_e^2} dk_2 a \end{array}\right] \qquad (4.44)$$

and the matrix $\mathbf{C}$ is the same as in Equation (4.14).

Equation (4.41) yields the third optimal control force, F_c^0, minimizing the axisymmetric radial displacement at x_e^0,

$$F_c^0 = \frac{-1}{\int_{-\infty}^{+\infty} I_{33} e^{ik_0(x_e^0 - x_c^0)} dk_0 a}\left(4\pi p_m \int_{-\infty}^{+\infty} \frac{J_0(k^r r_p)}{k^r a J_0'(k^r a)} I_{33} e^{ik_0 x_e^0} dk_0 a\right.$$
$$\left. + F_c^1 \int_{-\infty}^{+\infty} I_{33} e^{ik_0(x_e^0 - x_c^1)} dk_0 a + F_c^2 \int_{-\infty}^{+\infty} I_{33} e^{ik_0(x_e^0 - x_c^2)} dk_0 a\right). \qquad (4.45)$$

4.2.3 Results

The monopole source is located at $\theta = 0$, $x = 0$. Its radial position can vary from $r_p = 0$ to $r_p = a$ and its free field amplitude was arbitrarily chosen to be

110

$p_m = 100$Pa.m. The position of the control forces and the error sensors is unchanged from Section 4.1.3 so that the performances of the control arrangement for point force and monopole disturbances can be compared. The total power flow in the system at $x = 10a$, before and after control, is used to evaluate the performance of the active control approach.

Figure 4.9(a) shows the modal decomposition of the total power flow in a water-filled steel shell excited by a monopole source pulsating at $\Omega = 0.05$. The monopole is located near the axis of the shell, at $r_p = 0.1a$. Before control, the system response is dominated by the breathing mode and most of the energy propagates in the fluid field (see Figure 4.9(b)). When control is applied, the power conveyed by the breathing mode and the beam bending mode are respectively reduced by 12 and 7 dB whereas the power flow associated with the ovalling mode n=2 is seen to increase by 15 dB. The increase in ovalling shell motion is due to a large rotation of the shell element at the error sensor location x_e^2. Two closely spaced modal sensors would be necessary to keep the shell element from both translating and rotating at x_e^2. As Figure 4.9(b) reveals, the control approach results in a 25 dB attenuation of the power flow in the fluid field, part of which is compensated by an increase (8 dB) of the power flow in the shell wall. The net insertion loss of total power flow is 12 dB.

As the monopole source is moved toward the shell wall, the contribution of the circumferential modes $n \geq 1$ to the total power flow becomes more important; Figure 4.10 illustrates the case $r_p = 0.9a$. The system response remains dominated by the breathing mode and the energy is largely transmitted through the fluid field. The control performance is equal to that obtained for the case $r_p = 0.1a$.

Figure 4.9: Total power flow in a water-filled steel shell excited by an internal monopole source at $\Omega = 0.05$, $r_p = 0.1a$; (a) modal decomposition, (b) distribution in the system.
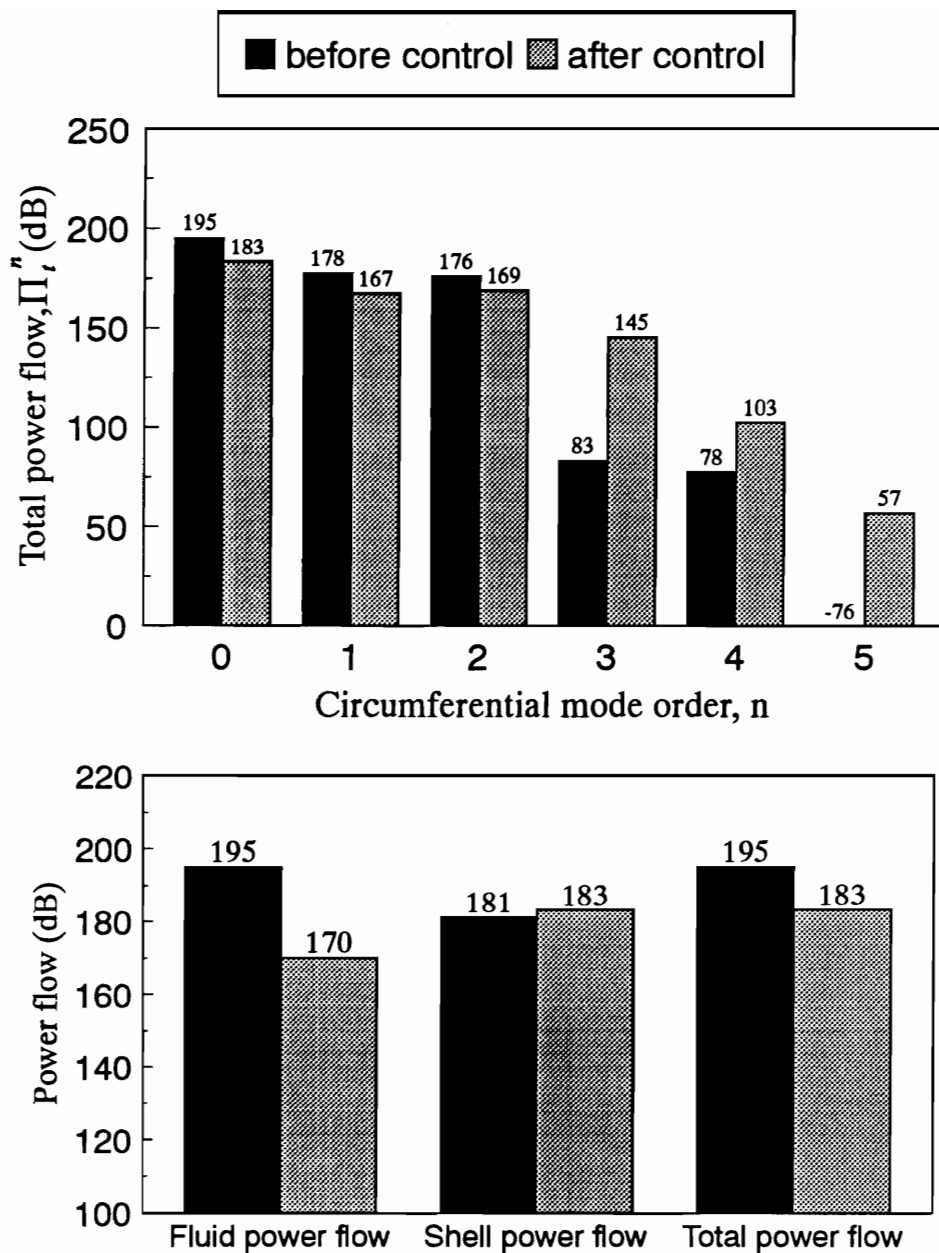
Figure 4.10: Total power flow in a water-filled steel shell excited by an internal monopole source at $\Omega = 0.05$, $r_p = 0.9a$; (a) modal decomposition, (b) distribution in the system.
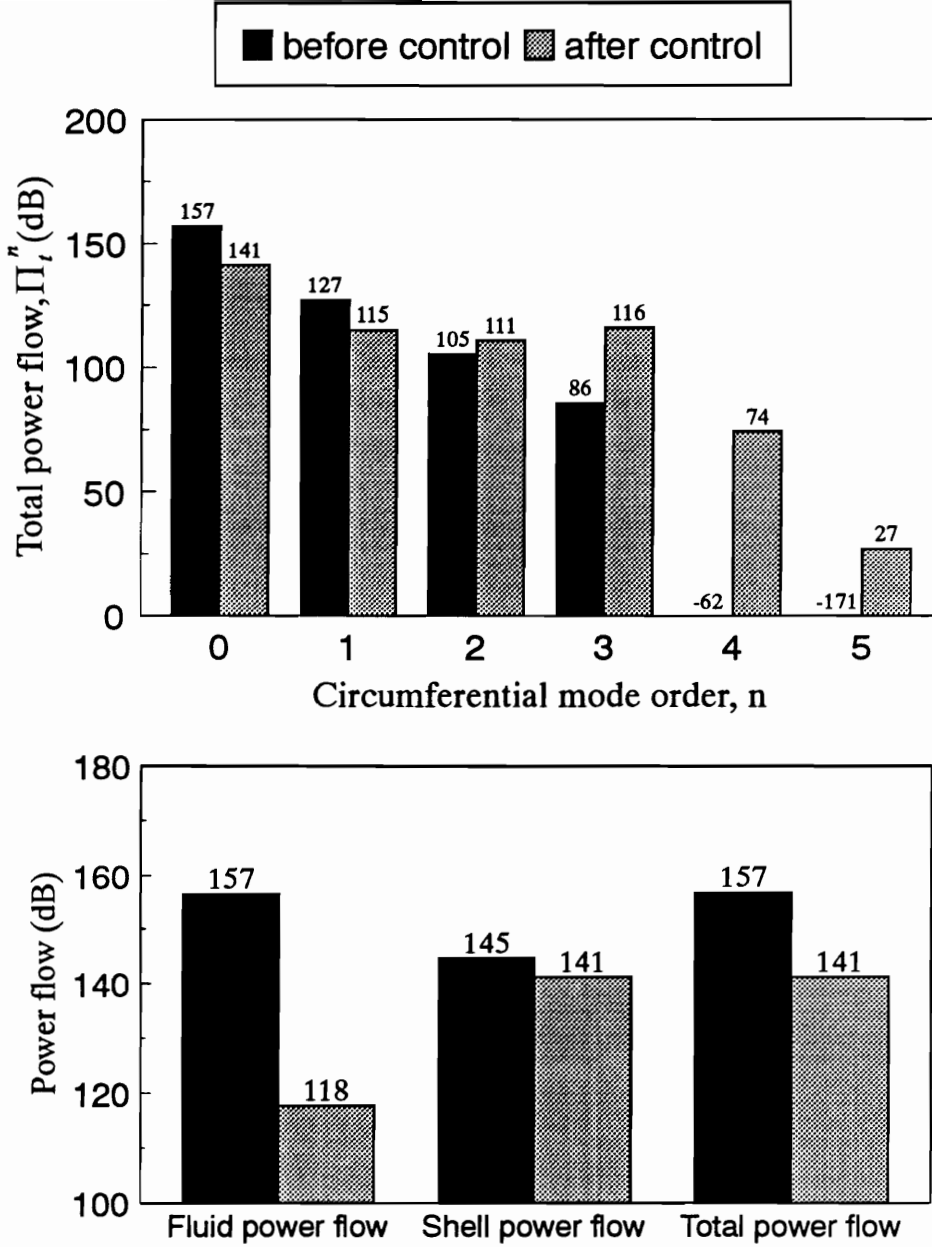
Figure 4.11: Total power flow in a water-filled plexiglass shell excited by an internal monopole source at $\Omega = 0.05$, $r_p = 0.1a$; (a) modal decomposition, (b) distribution in the system.

Considering a water-filled plexiglass shell and a monopole source near the axis (Figure 4.11), the insertion loss due to the active vibration control approach reaches 16 dB. Not only is the power flow in the fluid field reduced by 39 dB but the power flow in the shell wall is also attenuated (-4 dB). This high performance of the control is due to the low compliance of the shell yielding good coupling between the fluid and the shell and large effects of the structural radial forces on the fluid field. Figure 4.12 shows the results when the monopole is located close to the shell wall. Spillover in the circumferential mode n=3 is seen to limit the attenuation of the power flow in the shell wall and the resulting insertion loss is 12 dB. As the frequency is increased, this behaviour is likely to cause increases of the total power flow in the system after control. At $\Omega = 0.1$ (Figure 4.13), for a position of the monopole near the axis of the shell, the response of the uncontrolled system is largely dominated by the breathing mode and the energy is mainly conveyed in the fluid. After control, the power flow in the fluid is attenuated by 32 dB but the power flow in the shell wall is increased by 8 dB because of spillover in the circumferential modes n=3 and n=4. The resulting attenuation of the total power flow is 14 dB. As the disturbance is moved next to the shell wall (Figure 4.14), the contribution of the asymmetric circumferential modes ($n > 0$) to the response of the uncontrolled system becomes important. Before control, there are similar amounts of energy propagating in the fluid and in the shell wall. After control, the power flow in the fluid is reduced by 10 dB but the power flow in the shell wall is simultaneously increased by 4 dB. As a result of this redistribution of the energy in the coupled system, no attenuation of the total power flow is achieved.

Similar control performances are obtained for water-filled steel and plexiglass shells at $\Omega = 0.05$. It is thus interesting to compare the control effort required by
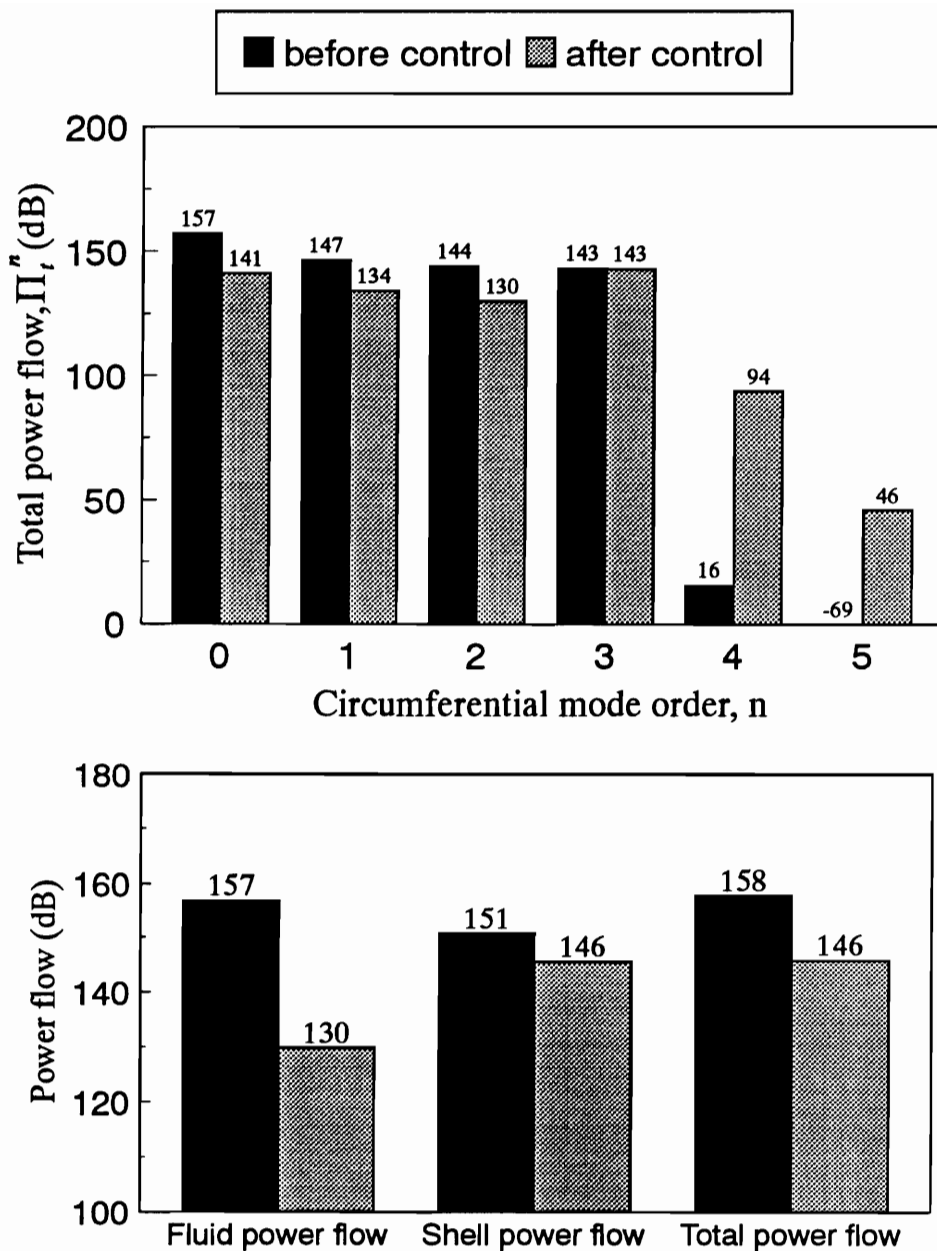
Figure 4.12: Total power flow in a water-filled plexiglass shell excited by an internal monopole source at $\Omega = 0.05$, $r_p = 0.9a$; (a) modal decomposition, (b) distribution in the system.
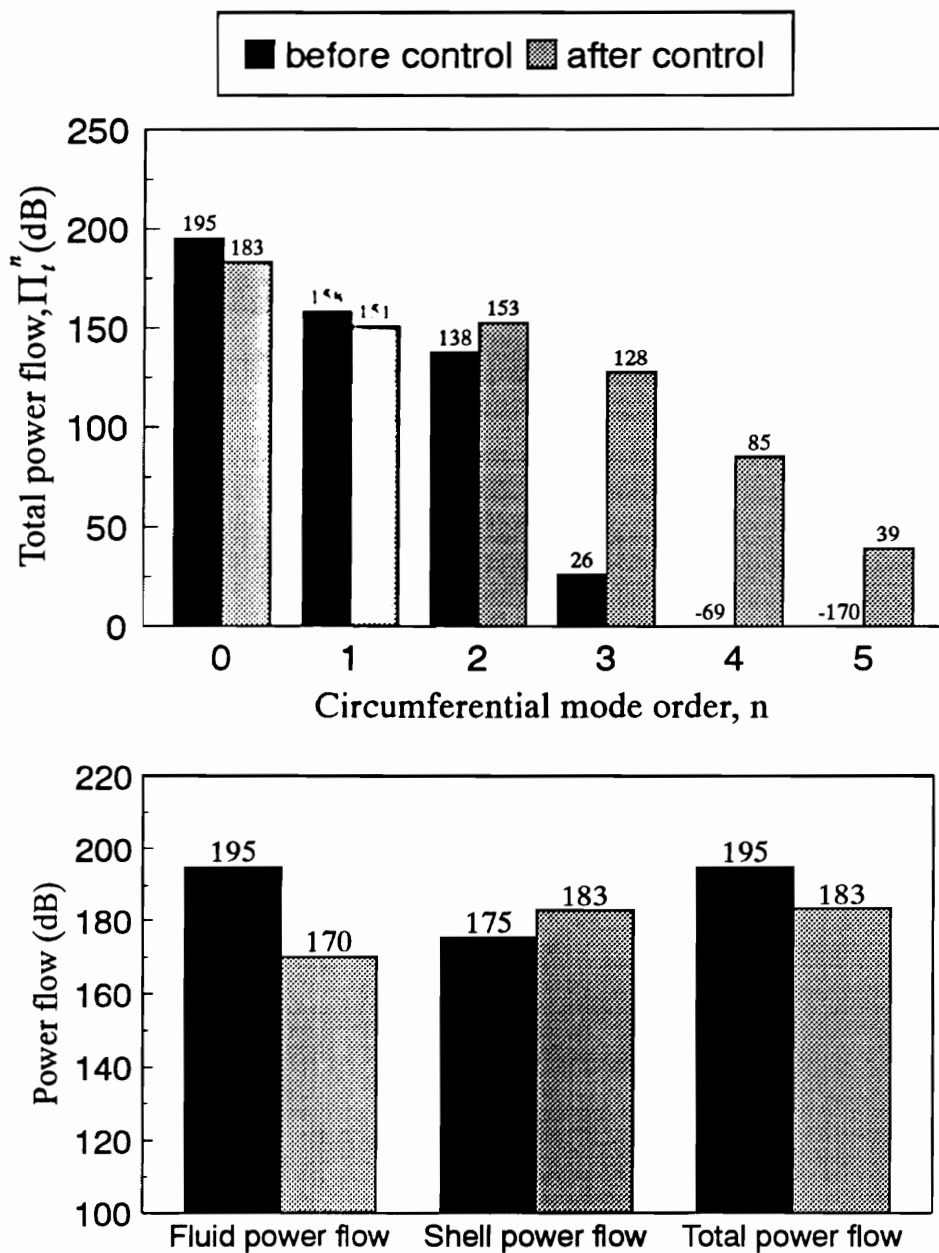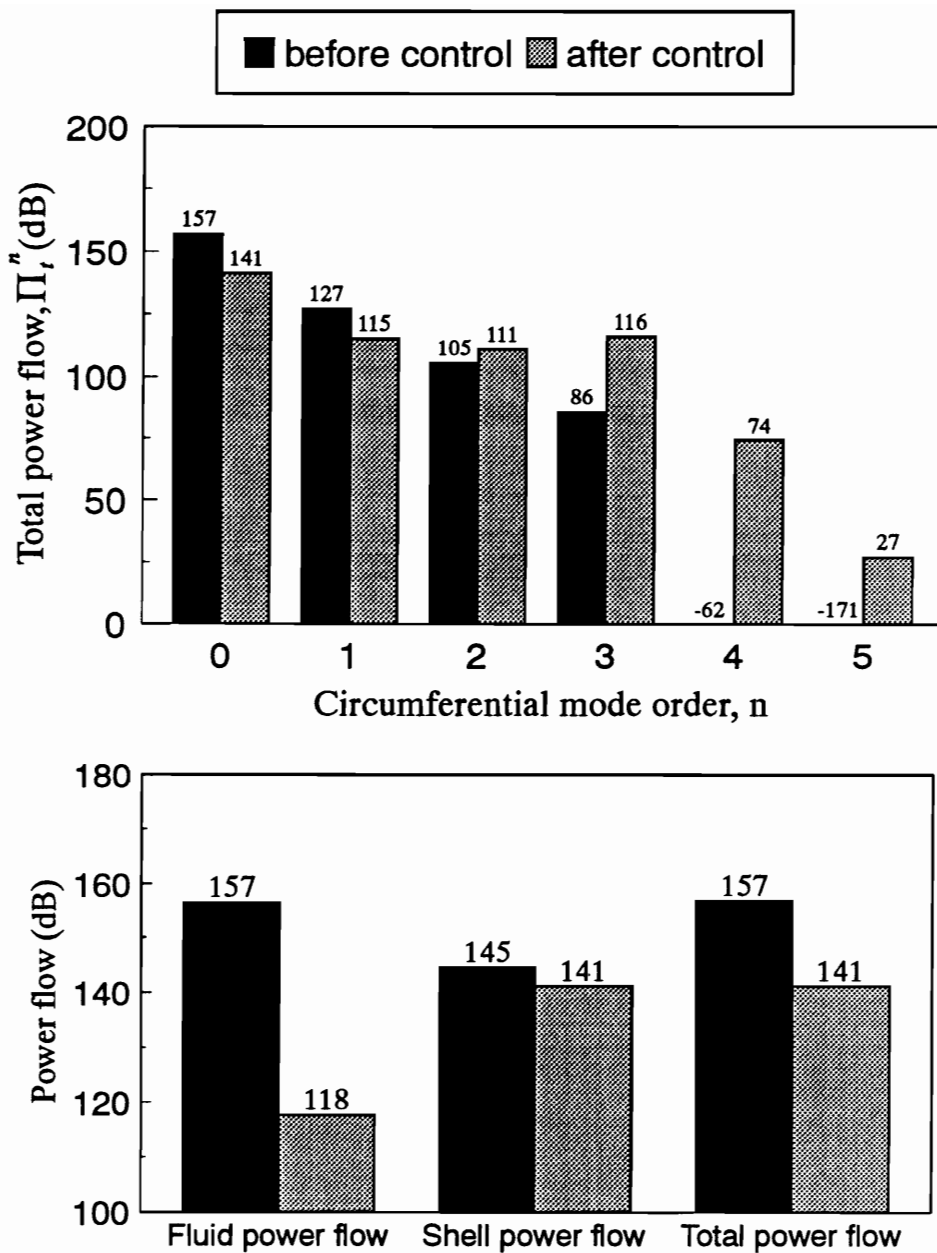
Figure 4.13: Total power flow in a water-filled plexiglass shell excited by an internal monopole source at $\Omega = 0.1$, $r_p = 0.1a$; (a) modal decomposition, (b) distribution in the system.

117

both configurations. Tables 4.2 and 4.3 show that, considering the monopole source near the axis of the shell or close to the wall, the control effort associated with the steel shell case is extremely large and about ten times higher than the control effort associated with the plexiglass shell system. For both cases, the control ring force is much larger than the control point forces because the monopole source at this frequency, whether it is located near the shell axis or close to the shell wall, predominantly excites the breathing mode n=0.

It has been demonstrated that the present active control approach on steel piping systems would require a large amount of control power when the disturbance is an internal acoustic source. The implementation of hard rubber inserts in steel piping systems would certainly provide a good solution to the transmission problem of vibrations in fluid-filled piping systems. Fuller [3] demonstrated that such discontinuities could create high passive transmission losses of the flexural waves propagating along *in vacuo* cylindrical shell. The combination of this passive effect with an active control approach on the insert, as presented here, would provide an effective means to reduce the total power flow in the piping system. However, because of the low cut-on frequencies of the high order circumferential modes in hard rubber shells filled with fluid, the frequency range in which these "smart" inserts could be used will be directly limited by the number of control channels. At least one control channel per propagating circumferential mode is necessary.
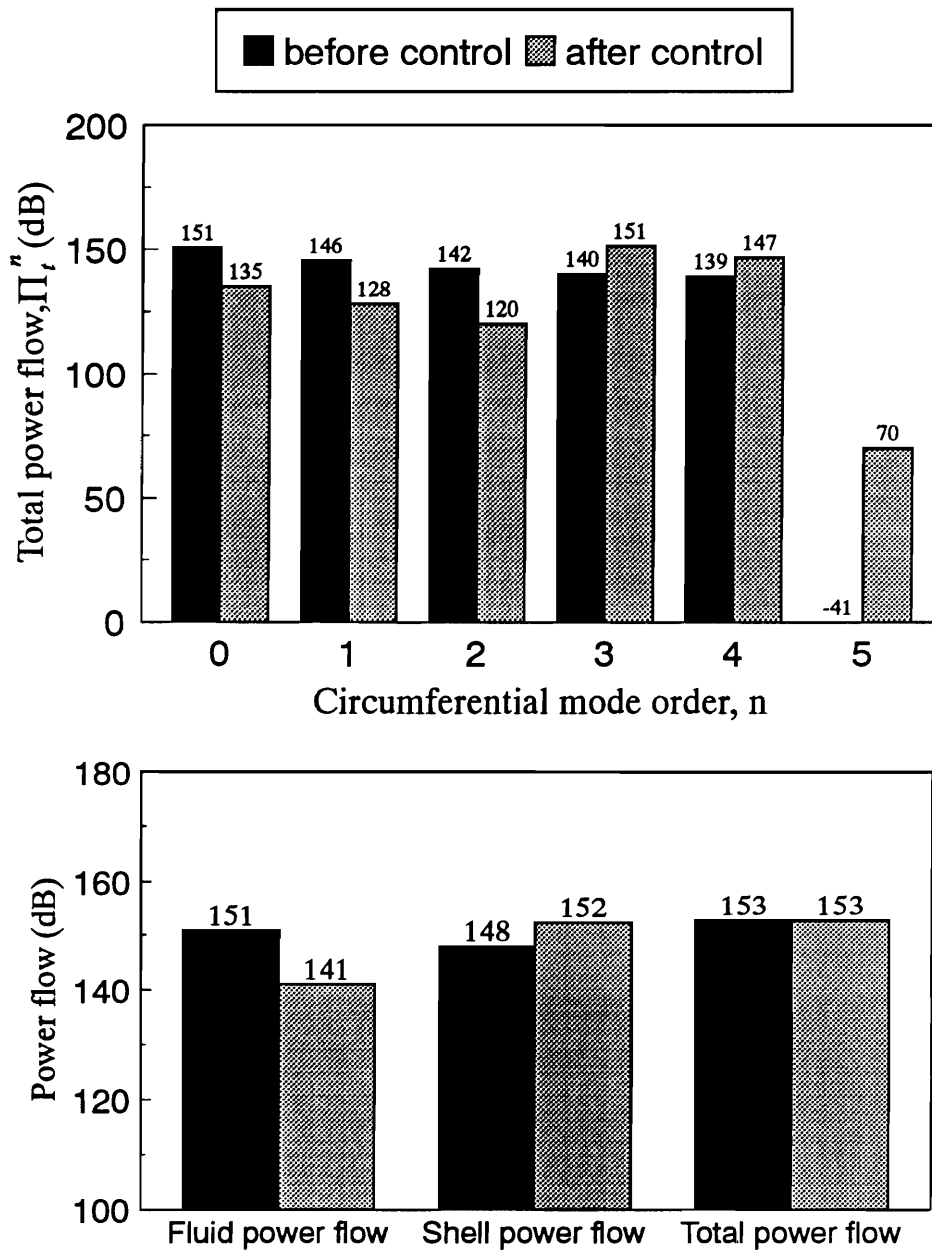
Figure 4.14: Total power flow in a water-filled plexiglass shell excited by an internal monopole source at $\Omega = 0.1$, $r_p = 0.9a$; (a) modal decomposition, (b) distribution in the system.

Table 4.2: Control effort for water-filled steel and plexiglass shells excited by a internal monopole source near the axis of the shell ($r_p = 0.1a$) at the frequency $\Omega = 0.05$.

	Water-filled steel shell	Water-filled plexiglass shell
$\|F_c^0/F_d\|$	137	14.9
$\|F_c^1/F_d\|$	0.34	0.19
$\|F_c^2/F_d\|$	0.32	0.18
E_c	137	14.9

Table 4.3: Control effort for water-filled steel and plexiglass shells excited by an internal monopole source near the shell wall ($r_p = 0.9a$) at the frequency $\Omega = 0.05$.

	Water-filled steel shell	Water-filled plexiglass shell
$|F_c^0/F_d|$	135	14.8
$|F_c^1/F_d|$	2.82	2.09
$|F_c^2/F_d|$	2.29	1.68
E_c	135	15

Chapter 5

Arrangement and Characterization of the Experimental Apparatus

A broad experimental study has been carried out in order to verify some of the analytical results presented in the previous chapters. Two sets of control experiments were performed. The first one was related to the work of Chapter 3 and focussed on the axisymmetric shell motion. The objective of the experiments was to show that the propagation of axisymmetric waves in infinite fluid-filled pipes can be effectively controlled by active means applied to the pipe wall in a large frequency range. The second set of experiments was related to the work of Chapter 4 and concerned the active control of the shell-fluid vibrations induced by a point force disturbance at low frequencies.

Before presenting the results of these experiments (which will be reviewed in Chapter 6), the experimental apparatus is discussed in detail in this chapter. The test structure is described along with a discussion on the achievement of the desired

boundary conditions. Preliminary experiments that were carried out in order to determine the shell material properties are presented. The results of other experiments assessing the validity of the theory developed in Chapter 2 and Chapter 3 are also included in this chapter. Among these results are the cut-on frequencies of the high order circumferential modes ($n > 1$) for the test shell in air and filled with water. These frequencies are compared to the calculated ones. The measured pressure field inside the shell filled with water, for an axisymmetric broadband excitation, is also presented and analyzed by comparison to the corresponding analytical computation. Upon completing this overview of the test structure, the control actuators and sensors are described and their implementation is discussed. Finally, the controller implementing the multi-channel version of the filtered-x adaptive LMS algorithm is presented.

5.1   Description and characterization of the test structure

In this section, the experimental shell system is described. The results of preliminary experiments that were performed in order to characterize the test structure are also included in this section. The experimental data is analyzed by comparison to numerical results presented in Chapter 2 and Chapter 3.

5.1.1   Description of the experimental shell system

Figure 5.1 shows a schematic of the experimental shell system investigated and Figure 5.2 shows a photograph of the arrangement. The cylindrical shell studied

123
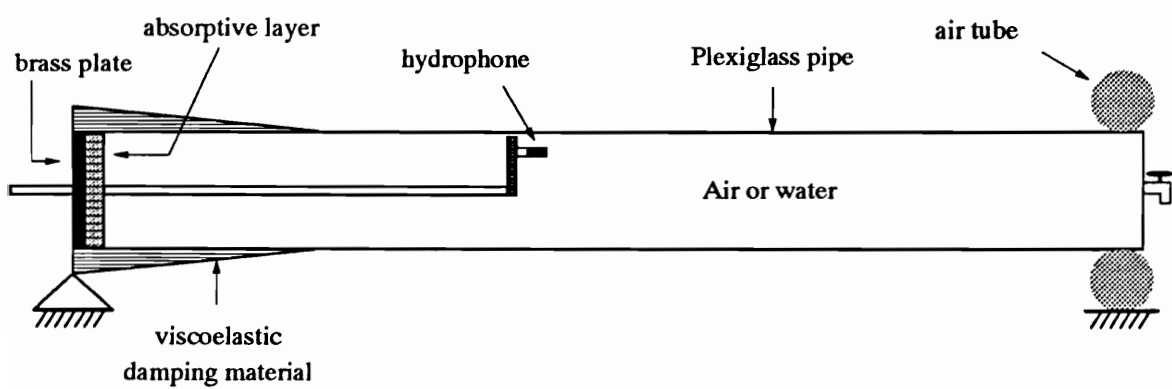
Figure 5.1: Schematic of the experimental setup.
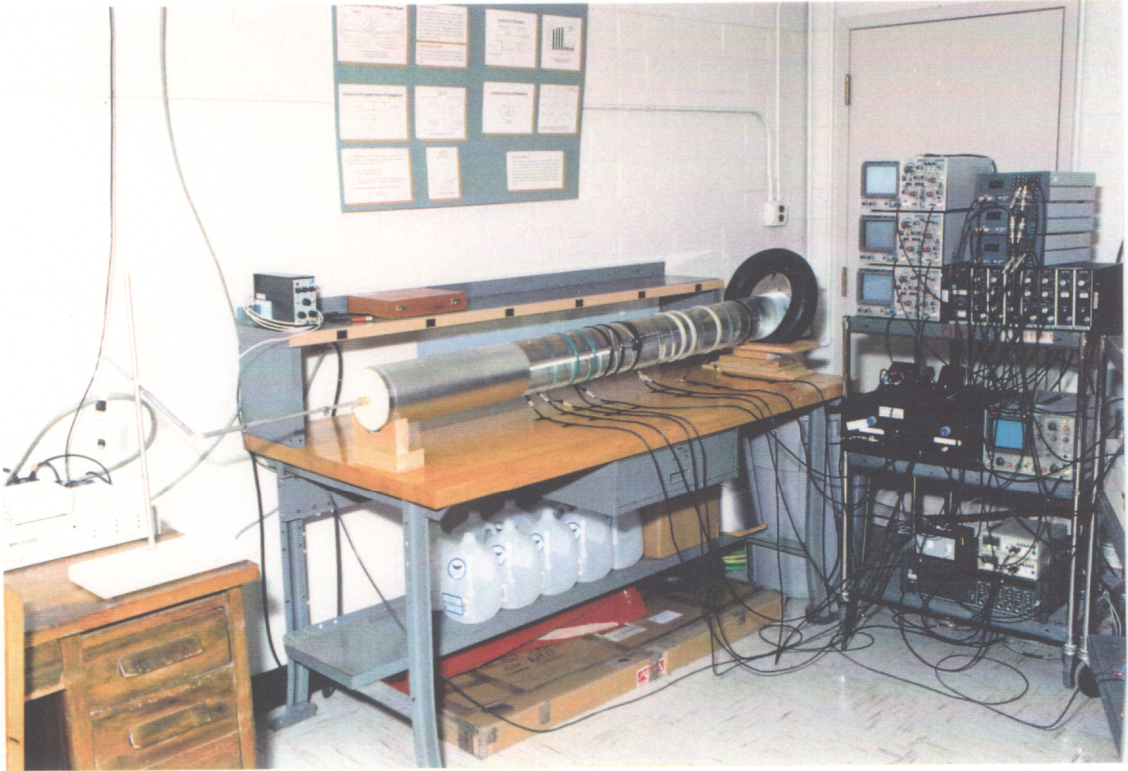
Figure 5.2: Photograph of the experimental arrangement.

was made of plexiglass. It had a length of 1.83 m, an outside diameter of 15.2 cm and a wall thickness of 3.17mm. The use of a plexiglass shell to conduct the experiments was justified by various aspects of the investigation, as listed below

- It was desired to study the active control of the axisymmetric wave propagation in a range of non-dimensional frequencies varying from 0 to 3 ($\Omega = 2\pi f a/c_L$). As the 3I3O controller used for experiments (based on the Texas Instruments TMS 320C30 microprocessor) was limited to frequencies of the disturbance below 10 kHz, it was preferable to use a material with a small extensional phase speed, such as plexiglass. The actual frequency range corresponding to $\Omega \in [0,3]$ for the present plexiglass shell was 0-9183 Hz. The frequency corresponding to $\Omega = 3$, for a shell with the same geometry but made of steel for example, would have been around 33000 Hz.

- A major concern for the shell system was to minimize the wave reflections at one end of the pipe, i.e. to build an anechoic termination. If reflections do not occur at either end of the pipe, the shell system appear infinite to the waves propagating toward that end. It is then possible to relate the experimental results to the theory developed for infinite shell systems in the previous chapters. Building an anechoic termination for the second set of control experiments conducted was impossible because the pipe length was too small compared to the wavelength of the propagating waves in the frequency range of concern ($\Omega < 0.3$). For this set of experiments, wave reflections at the ends of the pipe will thus be accounted for in the interpretation of the results. However, building an anechoic termination for the first set of experiments, associated with the axisymmetric wave propagation, appeared more feasible.

126

As the next section will reveal, plexiglass is a highly damped material. Based on the measured value of hysteretic damping in the present plexiglass shell, the attenuation of the axisymmetric wave amplitudes, as propagation occurs, has been determined in Chapter 2. According to the values of the imaginary part of the waves indicated in Figure 2.13, the attenuation of the *in vacuo* extensional and flexural waves is larger than 6 dB per meter for non-dimensional frequencies between 0.5 and 3. Above the ring frequency, this attenuation is about 23 dB per meter for the flexural wave and 12 dB per meter for the extensional wave. According to the results in Figure 2.14, when the shell is filled with water, the attenuation of the axisymmetric fluid-type wave, (s=1) is larger than 15 dB per meter above $\Omega = 0.5$ and that of the extensional shell wave is larger than 6 dB per meter in the same frequency range. Thus, considering a vibration source located near one end of the plexiglass pipe, the reflected axisymmetric waves at the other end of the pipe will be highly attenuated by natural propagation alone for excitation frequencies above 1500 Hz ($\Omega \simeq 0.5$).

- Finally, plexiglass is a transparent material. It is thus possible to check for the presence of unwanted bubbles in the fluid and at the interface between the two media. Gas bubbles modify the boundary condition at the shell-fluid interface.They also affect the properties of the fluid medium: the speed of sound is altered and the sound waves are damped [53]. In opaque pipes, the presence of bubbles or rust can not be noticed. This matter has been used by some authors to explain discrepancies in their experimental results [54, 55].

The plexiglass pipe was closed at both ends and could be filled with liquid. In order to increase the amount of damping in the system near the end of the pipe away from the disturbance, thin stripes of light viscoelastic damping material were wrapped around the shell. In addition, an absorptive layer (Saper D acoustic tile [52]) was bonded on the inner side of the brass end cap used to seal the pipe. According to the manufacturer BFGoodrich, the layer can provide up to 10 dB attenuation of the reflected acoustic pressure field in the fluid at frequencies above 2000 Hz. No particular treatment was applied to the other end of the pipe, implying that wave reflections at this end did occur. The shell was supported by an air tube whose resonance frequency and stiffness were so low that it did not significantly affect the pipe dynamics. The tube also minimized the transmission of noise from the bench to the test structure.

In order to measure the pressure field in the fluid, before and after control, the pipe was equipped with an internal traverse carrying a miniature Bruel and Kjaer hydrophone (model 8103). The hydrophone was 4 cm long and had a diameter of 9.5 mm. A close-up of the hydrophone on the traverse head is shown in Figure 5.3. The traversing system was designed to provide three dimensional movement of the hydrophone inside the shell. The basis of the traverse was a rigid stainless steel tube positioned on the axis of the pipe. This tube was supported by the brass end cap of the anechoic termination. It could move axially and circumferentially relative to the cap. The traverse head is shown in Figure 5.4 for two different radial positions of the hydrophone . Radial traversing, from r=0 to r=0.9a, was obtained by pulling nylon strings attached to a small sliding piece carrying the hydrophone. The signal cable of the hydrophone and the nylon positioning strings were routed through the steel tube.
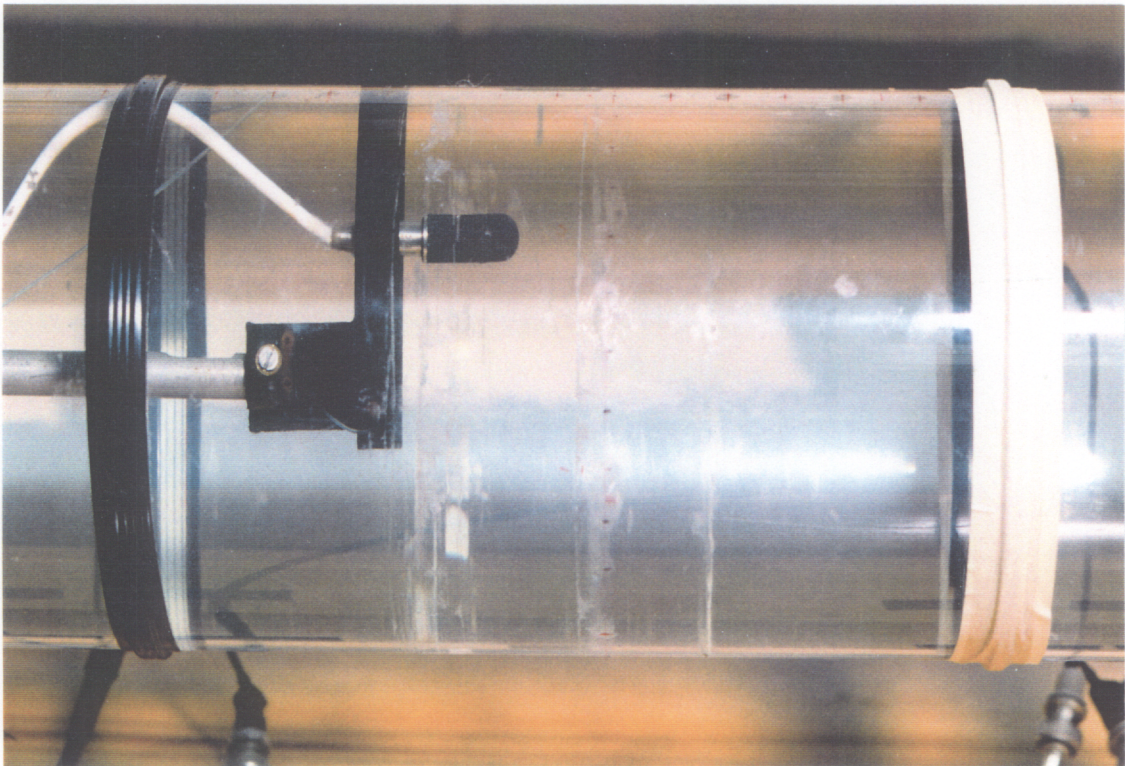
Figure 5.3: Photograph of the hydrophone inside the plexiglass shell.
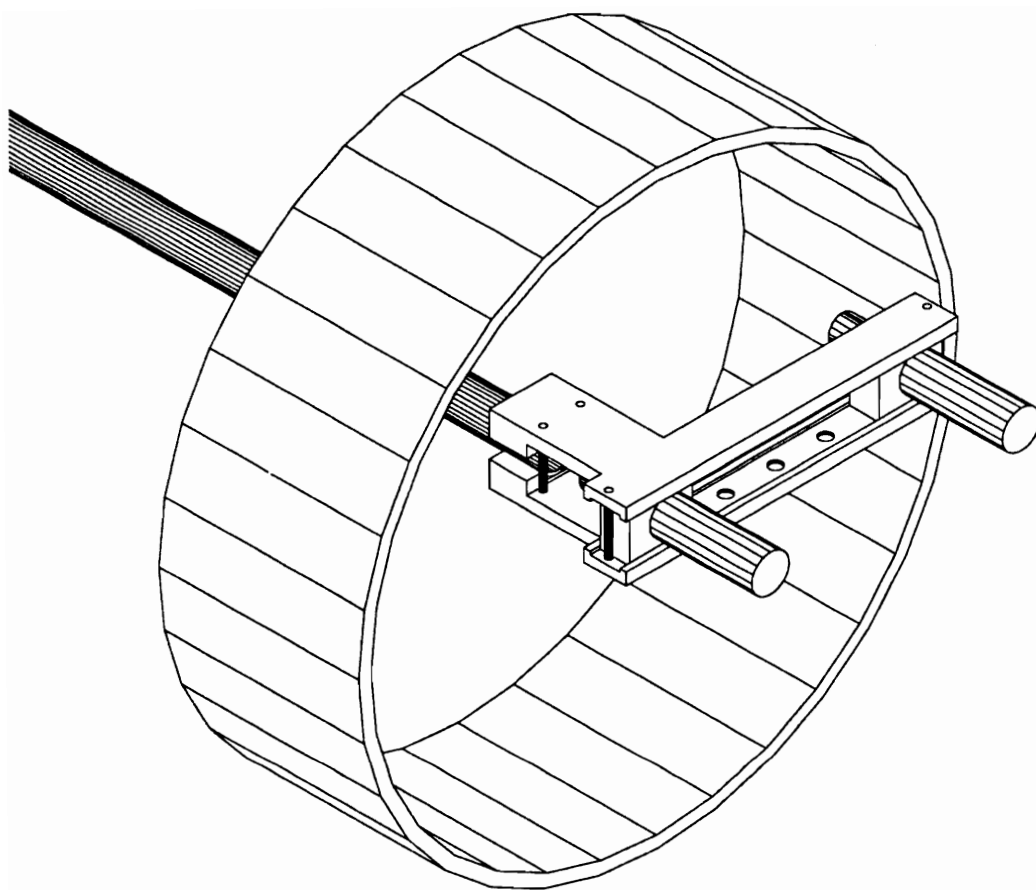
Figure 5.4: Sketch of the traverse head carrying the hydrophone.

5.1.2 Properties of the shell material

Preliminary experiments were carried out in order to determine the ring frequency, the extensional phase speed, c_L, and the hysteretic damping, η, of the plexiglass cylindrical shell. The shell hysteretic damping was used in the previous chapters to present analytical results for *in vacuo* and water-filled plexiglass shells. The ring frequency and the extensional phase speed had to be determined in order to find the relation between the non-dimensional frequencies used in the previous chapters and the actual frequencies they correspond to for the actual shell system. It is recalled that the frequency, in Hz, corresponding to a non-dimensional frequency Ω, is given by

$$f = f_r \times \Omega, \tag{5.1}$$

where f_r is the ring frequency, corresponding to $\Omega = 1$, which is defined as

$$f_r = \frac{c_L}{2\pi a}. \tag{5.2}$$

The non-dimensional cut-on frequencies of the high order circumferential modes ($n > 1$) for the shell *in vacuo* have been determined in Chapter 2. By measuring the actual frequencies they correspond to, the ring frequency can be obtained, using Equation (5.1). To this purpose, the following experiment was performed. The shell, without end caps, was hung in the air with soft bungee cords. This arrangement corresponds to free-free boundary conditions of the shell. The shell was driven by an electromechanical shaker which was attached to the structure 30 cm from one end using a stinger and a bolt glued to the shell. At the same angular position, 60 cm from the other end of the shell, the radial response of the shell was mea-

131

sured by a Bruel & Kjaer mini accelerometer, weighting 0.65 gram. A band limited whitenoise signal (0-800 Hz) issued from the signal generator of a Bruel & Kjaer spectrum analyzer (model 2032) was amplified and fed to the shaker. The transfer function between the input signal and the amplified output of the accelerometer was processed by the B&K spectrum analyzer. The magnitude of the transfer function is shown in Figure 5.5. It is characterized by various peaks corresponding to the resonances of the two-dimensional cylinder modes (n,m). To isolate the resonant peaks due to circumferential modes cutting on, i.e. the modes (2,1), (3,1), (4,1),..., the above measurement was repeated for different boundary conditions of the shell. Indeed, it has been shown in Chapter 2 that the cut-on frequency of a circumferential mode is only a function of the shell geometry. The resonances of the shell associated with these cut-on frequencies are thus independent of the shell boundary conditions. For the second measurement, the shell was arranged as indicated in Figure 5.1. The resonant frequencies which were unchanged from one measurement to the other were the cut-on frequencies of circumferential modes $n > 1$. These frequencies, for the circumferential modes n=2, n=3 and n=4, are indicated in Figure 5.5. By comparing these three frequencies to the non-dimensional cut-on frequencies calculated in Chapter 2 (see Table 2.4), one obtains three values of ring frequency. The average of the results gives $f_r = 3061$ Hz. The corresponding extensional phase speed in the plexiglass shell wall is $c_L = 1435$ m/s.

A common method to determine the hysteretic damping in the shell material is the "half-power bandwidth" [43]. For a single degree of freedom system, the method consists in measuring the frequency bandwidth between points on the response curve for which the response is $1/\sqrt{2}$ times the response at the resonance. It can be shown that a good evaluation of the damping is given by the ratio of
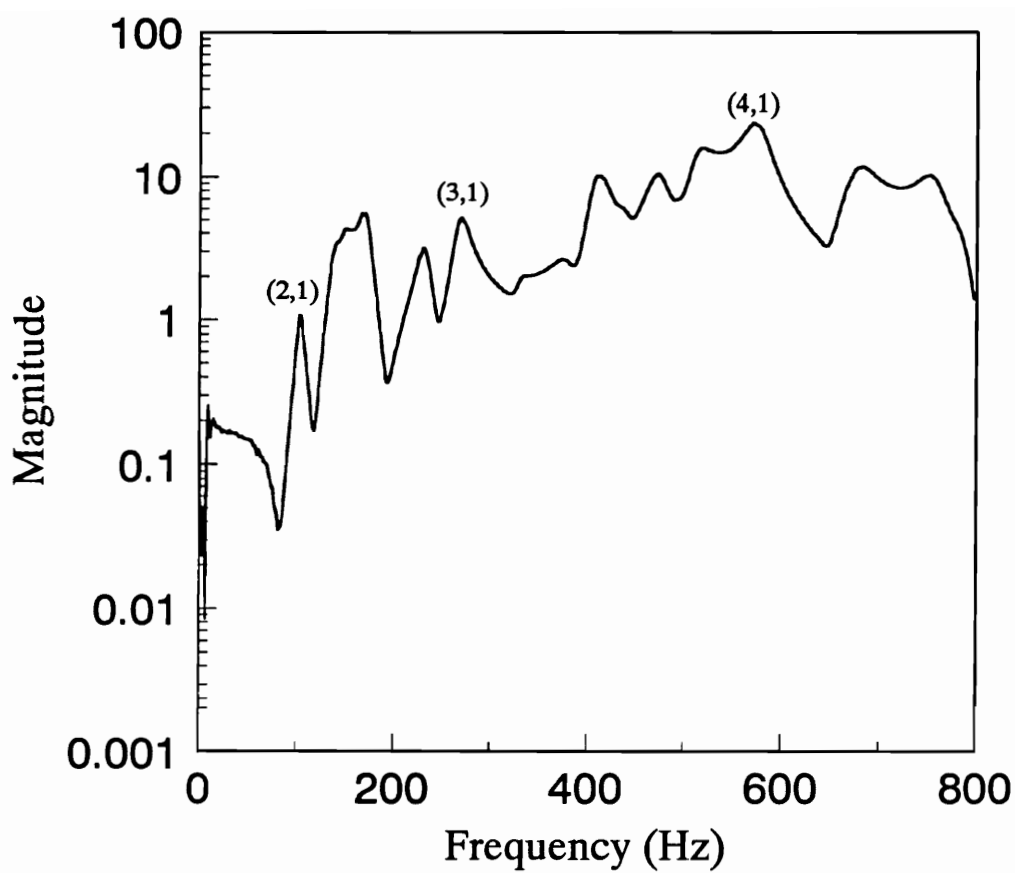
Figure 5.5: Frequency response of the *in vacuo* plexiglass shell with free ends to a radial point force (shaker).

133
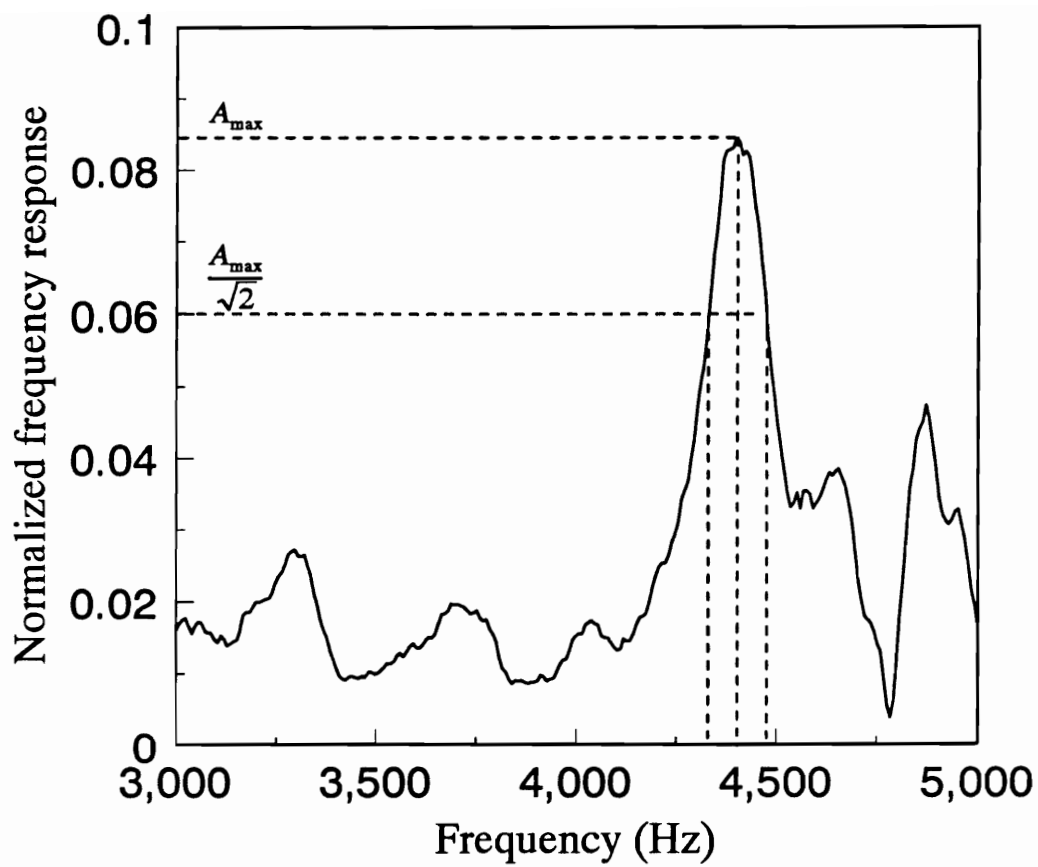
Figure 5.6: Frequency response of the *in vacuo* plexiglass shell with free ends to a ring force.

the frequency bandwidth divided by the resonant frequency. For free-free boundary conditions, the plexiglass shell was driven by a ring force in order to minimize the number of cylinder modes in the response. The implementation of the axisymmetric excitation, using a PVDF cable, will be addressed in Section 5.2.1. The ring force was applied 30 cm from one end of the shell and the response of the shell was measured 60 cm from the other end by a B&K mini accelerometer. Figure 5.6 shows the magnitude of the transfer function between the input signal (band limited whitenoise 0-6400 Hz) and the amplified output of the accelerometer, for frequencies between 3000 and 6000 Hz. The value of hysteretic damping in the shell was obtained from the response near the resonance at 4400 Hz:

$$\eta = \frac{\Delta f}{f_{res}} = \frac{160}{4400} = 0.036 \ . \tag{5.3}$$

This value of hysteretic damping in the plexiglass shell was assumed to be constant below 9183 Hz ($\Omega = 3$).

5.1.3   Cut-on frequencies of the shell system

Using the average value of ring frequency determined in the previous section, one can now compare in Table 5.1 the values of cut-on frequencies calculated from Table 2.4 to those obtained experimentally for the shell *in vacuo*. The discrepancies are seen to be small, the largest error being equal to 3.9% (mode n=3).

The cut-on frequencies of the circumferential modes n=2, n=3 and n=4 for the shell filled with water were also determined. The shell was arranged as indicated in Figure 5.1 and was filled with water. It was driven by an electromechanical shaker 30 cm from the end of the pipe supported by the air tube and the radial

135

Table 5.1: Comparison of theoretical and experimental cut-on frequencies of the circumferential modes n=2,3 and 4, *in vacuo* shell

Mode order	Calculated cut-on frequency (Hz)	Measured cut-on frequency (Hz)
2	101	101.5
3	285.2	274
4	546.7	564

response of the shell at the same angular position, 60 cm from the other end of the shell, was measured by a Bruel & Kjaer mini accelerometer. A band limited whitenoise signal (0-400 Hz) was amplified and fed to the shaker. Figure 5.7 shows the magnitude of the transfer function between the whitenoise signal and the output of the accelerometer in the frequency range 0-300 Hz. Again, the resonances due to circumferential modes cutting on were determined by changing the boundary conditions. The air tube in Figure 5.1 was removed and the measurement was repeated. The cut-on frequencies of the circumferential modes n=2, n=3 and n=4 for the shell filled with water are shown in Table 5.2 and compared to the theoretical values determined in Chapter 2. Measured and calculated values are once again very consistent.

These results suggest that the cut-on frequencies of a cylindrical shell, whether it is *in vacuo* or filled with liquid, are accurately determined by using the characteristic equation (2.16), derived in Chapter 2.

5.1.4   Axisymmetric broadband pressure field in the fluid

The pressure field in an infinite cylindrical shell filled with fluid, due to an axisymmetric radial line force, has been analytically derived in Chapter 3. Results for the plexiglass shell in the frequency range $\Omega \in [0; 3]$ are shown in Figure 3.5.

The experimental data corresponding to this computation is shown in Figure 5.8. The implementation of the axisymmetric excitation, using a PVDF cable, will be addressed in the next section. To obtain the experimental data, a band limited whitenoise signal (0-12800 Hz) was amplified and fed to the PVDF cable.
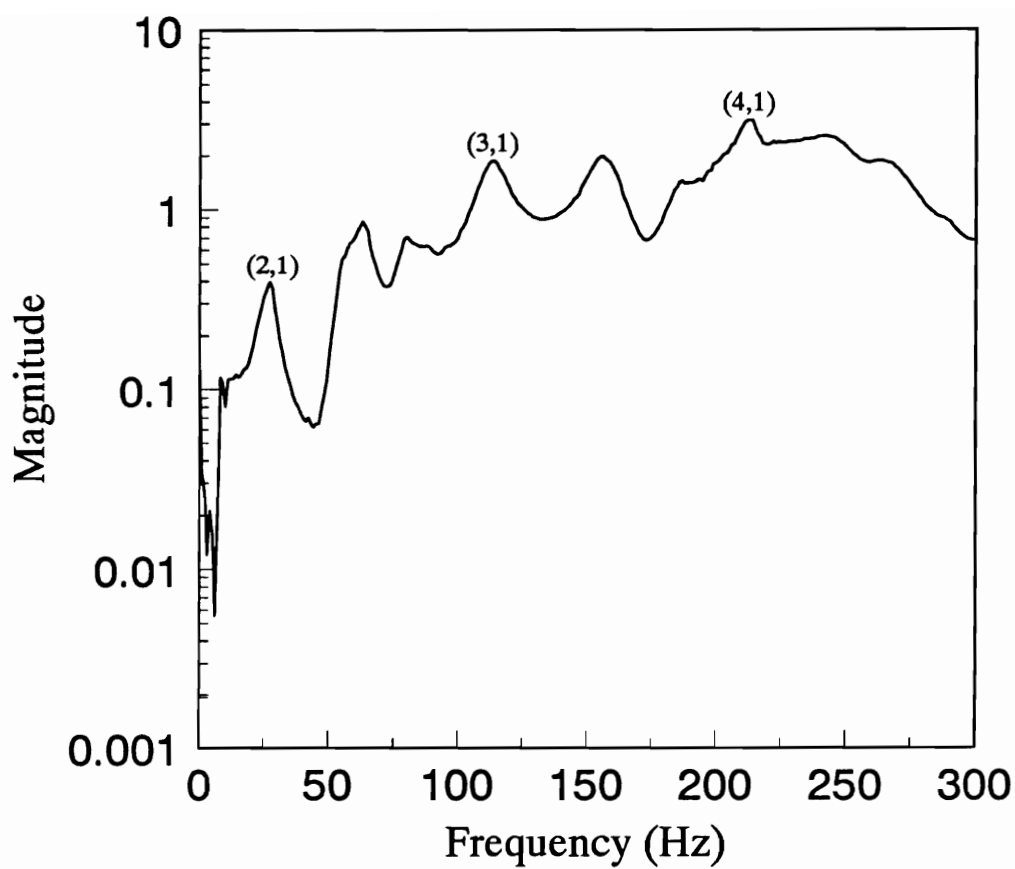
Figure 5.7: Frequency response of the plexiglass shell filled with water to a radial point force (shaker).

Table 5.2: Comparison of theoretical and experimental cut-on frequencies of the circumferential modes n=2,3 and 4, water-filled shell

Mode order	Calculated cut-on frequency (Hz)	Measured cut-on frequency (Hz)
2	33.7	28
3	110.2	114
4	226.5	213

The hydrophone was located ten radii from the ring force. The transfer function between the input signal and the amplified output of the hydrophone was processed for 72 positions of the hydrophone in the pipe cross section (one measurement every 30° around the shell for 6 radial positions between r=0 and r=0.9a). For each radial position, Figure 5.8 shows the average of the pressure measured around the shell interior, associated with the breathing mode n=0. The measured response at high frequency is very consistent with the numerical computation. At low frequency (< 3200 Hz), the trend is verified but substantial discrepancies are observed. The coherence of the measurements in this frequency range was very low. This could be due by the very low level of the pressure in this frequency range. More importantly, the excitation by the PVDF cable in this frequency range was non-linear (this will be discussed in more detail in the next section). The pressure in the fluid at one frequency thus resulted from various frequencies of excitation. This is the main explanation for the low coherence of the measurements. The numerical computation has also revealed that the pressure was dominant near the shell wall at low frequencies. However, this behaviour could not be assessed as the measurements of the pressure field in the fluid were restricted to radial position $r \leq 0.9a$.

5.2 Control actuators and sensors

The experimental study on axisymmetric shell motion investigates the use of KYNAR piezoelectric polymer wires [56] as actuators and sensors. The implementation of the PVDF wires is discussed in this section.

The actuators used in the second set of control experiments were two elec-
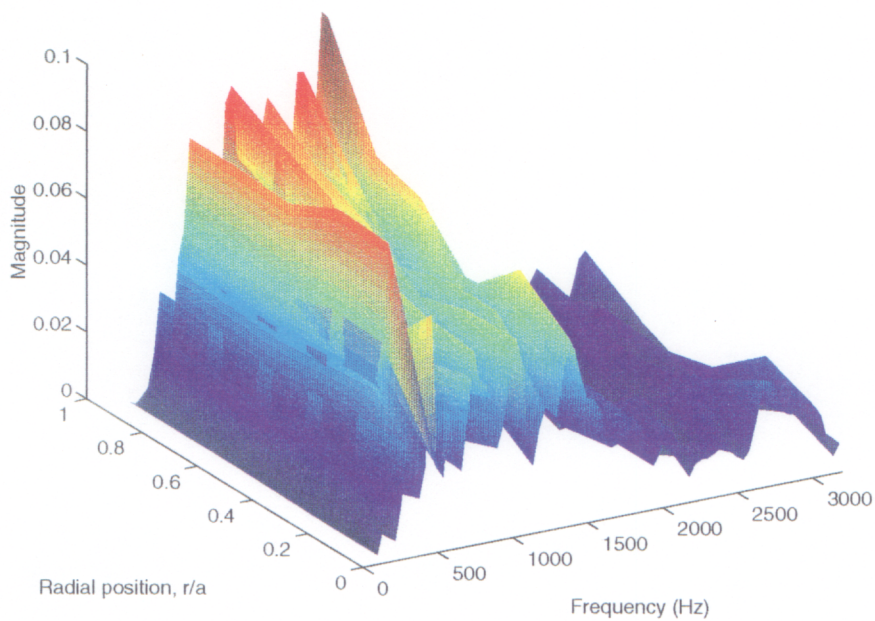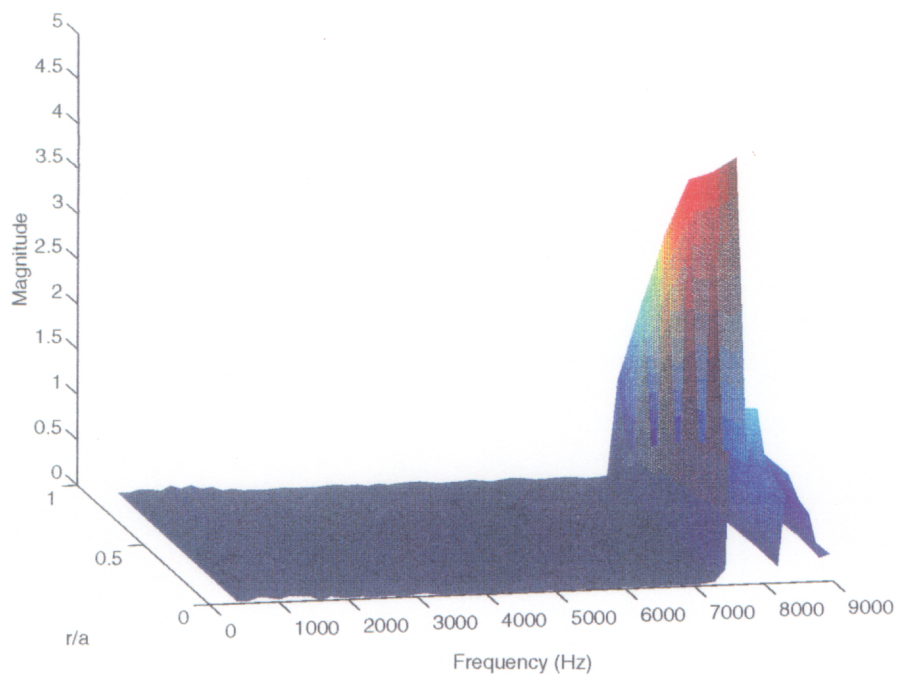
Figure 5.8: Measured pressure field ten radii from the excitation (PVDF cable).

tromechanical shakers and a PVDF wire. Shakers applied to the shell as radial point forces largely excite the flexural waves of circumferential order $n > 0$ but are rather ineffective at driving the axisymmetric shell motion. On the other hand, a PVDF cable wrapped around the wall can only excite the shell breathing mode. The combination of these two types of actuators was thus necessary to control the propagation of the circumferential modes in the system. Regarding sensors, the axisymmetric shell displacement was observed by a PVDF cable. The radial displacement of the shell associated with the circumferential modes n=1 and n=2 was observed by modal error sensors made of PVDF film. Design and implementation of these modal sensors are reviewed in this section.

5.2.1 PVDF wires

The KYNAR PVDF cable is illustrated in Figure 5.9. It has the appearance of a standard coaxial cable but is constructed with a piezoelectric polymer insulation layer between the copper braided inner conductor and the outer shield. It is protected by a rugged polyurethane jacket. Typical properties of the cable are indicated in Table 5.3.

The PVDF cable can be used as a sensor. Its electrical response, in terms of charge collected at the electrodes, is proportional to the strain induced within the volume of piezoelectric polymer. As strain can be applied radially and longitudinally, the cable is sensitive to stretch but can also monitor radial impacts [56].

The PVDF cable was demonstrated to be a good transducer for axisymmetric wave motion in cylindrical shells by Pinnington and Briscoe [58]. The sensor imple-

copper spiral
shield

black
polyurethane

silver plated
copper

insulation
copolymer
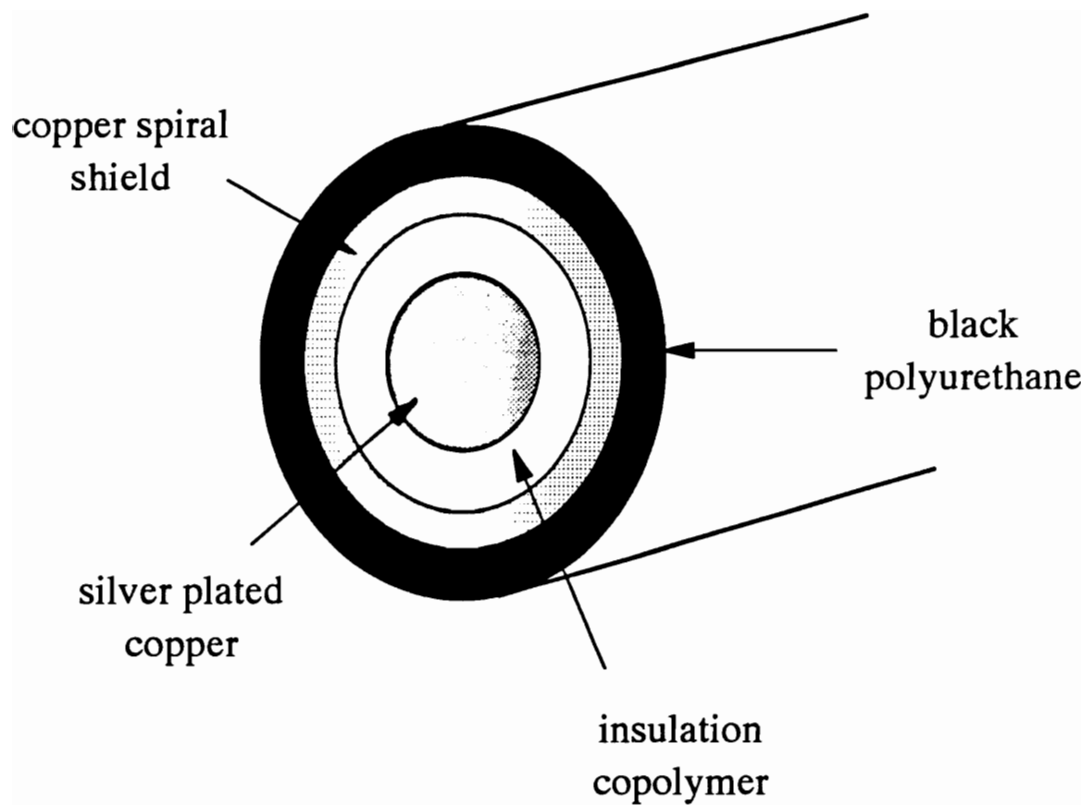
Figure 5.9: Schematic of the KYNAR PVDF wire.

Table 5.3: Typical properties of KYNAR Piezo Cable.

Properties	Value	Units
Tensile Strength	240	MPa
Young's Modulus	2.3	GPa
Density	1890	Kg/m^3
Hydrostatic Piezo Coefficient	15	pC/N
Longitudinal Piezo Coefficient	250×10^{-3}	Vm/N
Energy Output	10	$mJ/Strain(\%)$
Voltage Output	5	$kV/Strain(\%)$

mentation described by Pinnington *et al.* consists in firmly attaching the cable to the pipe surface so that the longitudinal strain in the cable equals the surface strain of the shell. A single layer of double sided self-adhesive tape is wrapped around the pipe. The PVDF cable is then wrapped an exact number of turns around the circumference of pipe on top of the tape. Finally, an electric tape is firmly wrapped around the cable to totally eliminate any flapping of the wire.

Assuming perfect bonding between the cable and the shell, the net extension Δl of the wire, arising from the radial displacement of the shell wall w at the sensor position x_s, is given by

$$\Delta l \;=\; N_t \left(\int_0^{2\pi} (a+w)d\theta \;-\; 2\pi a \right), \tag{5.4}$$

where N_t is the number of cable loops.

Using Equation (4.23) to describe the radial shell motion yields

$$\Delta l \;=\; N_t \left(\int_0^{2\pi} (a + \sum_{n=0}^{N} \cos(n\theta) \sum_{s=0}^{S_n} W_{ns}e^{ik_{ns}x_s})d\theta \;-\; 2\pi a \right) \tag{5.5}$$

$$= \; 0 \qquad\qquad if \; n \neq 0 \tag{5.6}$$

$$= \; 2\pi N_t \sum_{s=0}^{S_0} W_{0s}e^{ik_{0s}x_s} \qquad if \; n = 0. \tag{5.7}$$

This results proves that, ideally, i.e. if the cable is perfectly bonded to the shell wall, the transducer is only sensitive to the axisymmetric waves which involve a net extension of the pipe circumference.

A schematic of the electrical circuit modeling the PVDF sensor is depicted in Figure 5.10. The sensor can be seen as a charge generator, q_s, with a capacitor, C_s, and a resitor, R_s, in parallel. The resistivity of the sensor is very high ($\simeq 1.5 \times 10^{12}$

ohm-m) and can be ignored. It appears from the electrical circuit that the output voltage of the sensor is not only determined by the charge source but also by the capacitance and, above all, by the input impedance of the device the sensor is connected to. For the sensor to provide strain measurement, care must thus be taken in choosing the voltage amplifier used to increase the electrical response of the sensor. Due to the high output impedance of the sensor, an operational amplifier with a high input impedance ($> 10^8$ ohms) is required to eliminate impedance mismatch and loading of the circuit [57].

Like any other piezoelectric material, the PVDF wire can be used as an induced strain actuator. If a voltage is applied to the cable, a charge will be created at the electrodes and the cable will stretch. The PVDF cable is carefully wrapped an even number of turns around the pipe, as described previously. If it was perfectly bonded to the shell, the cable would only generate axisymmetric waves, as demonstrated above. However, the attachment of the cable to the shell is not perfect. The compliance of the cable is high and the plexiglass shell thus appears very stiff to the actuator. Therefore, during a period of vibration, part of the cable may not always be in contact with the shell. For example, the cable may be able to constrict the shell circumference but may not be able to outstretch it. This behaviour results in non-linearities of the system response. These non-linearities may be observed on the frequency response which exhibits contents at other frequencies than the excitation frequency. If the cable is not uniformly bonded to the shell around the circumference, higher order circumferential modes (n=1,2,...) may also be excited by the PVDF cable.

For the cases studied, good excitation of the axisymmetric shell motion was

146
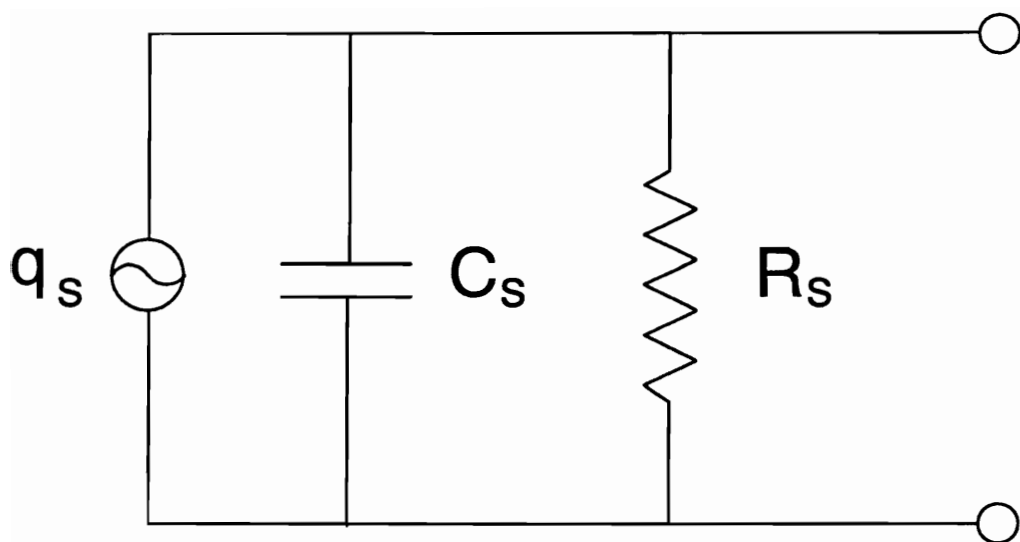
Figure 5.10: Schematic diagram of PVDF electrical circuit.

obtained with 4 loops of cable at frequencies above 1500 Hz ($\Omega \simeq 0.5$). Below 1500 Hz, the input mobility of the shell (n=0) is very low (see Chapter 3) and the excitation of the pipe by the PVDF cable was highly non-linear. The best results appeared above the ring frequency (near 3060 Hz) as the shell motion was largely flexural in nature. The input mobility of the shell (n=0) in this frequency range is high, i.e. small inputs induce large radial motion of the shell wall.

5.2.2 Shaped PVDF film sensors

The modal error sensors used in the second set of experiments were made of Kynar PVDF film [61]. The thickness of the film was $28\mu m$. The electrical response of the PVDF film is proportional to the integral of the strain induced within the volume of the sensor. The three directions in which strain can be applied are indicated in Figure 5.11. Associated with the θ, z and r-direction of the material are the piezo strain constants d_{31}, d_{32} and d_{33} respectively. Values for each of these constants as well as properties of polyvinylidene fluoride appear in Table 5.4. The film is bonded to the shell material such that the circumferential direction corresponds to the piezo strain constant d_{31}. As d_{31} is much larger than the other piezo constants, the charge generated by the film is mainly due to the strain in the θ-direction. If the shell vibrations are highly dominated by flexural modes, the response of the film in units of charge can be expressed as

$$q = Y d_{31} \frac{h}{2} \int_A F(x,\theta) \frac{\partial w(\theta)}{a^2 \partial \theta^2} a d\theta dx, \qquad (5.8)$$

where $F(x,\theta)$ represents the effective surface of the sensor electrodes.

The radial displacement of the shell at the sensor location x_s may be written

148
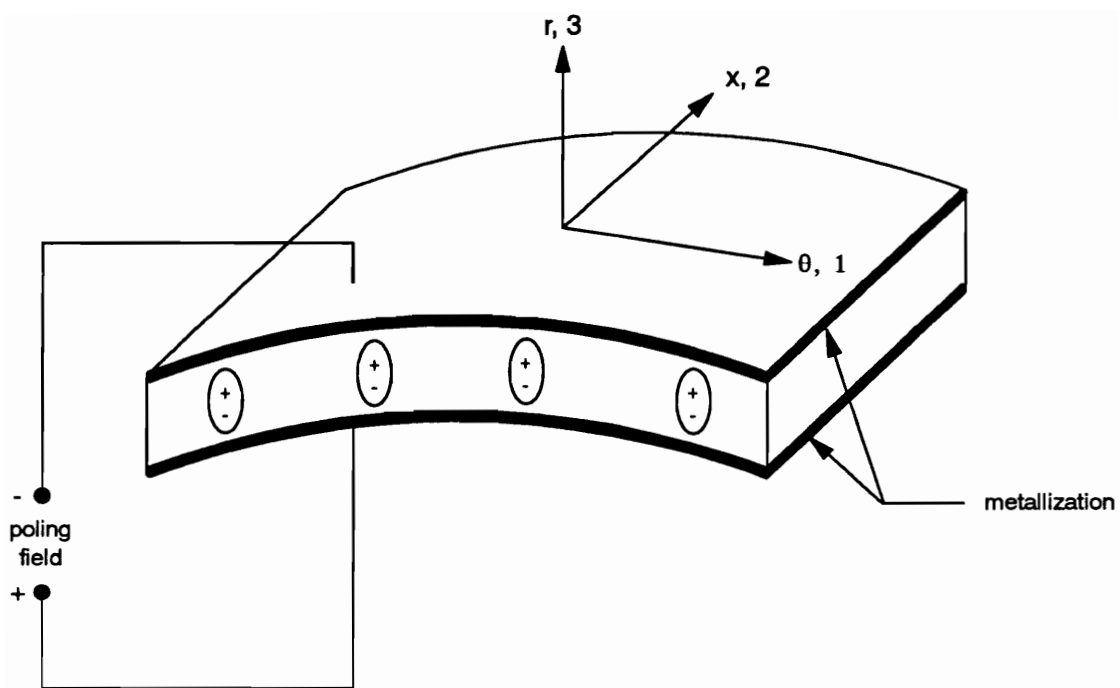
Figure 5.11: Schematic of PVDF coordinate system.

Table 5.4: Typical properties of KYNAR Piezo Film.

Properties	Symbol	Value	Units
Piezo Strain Constants	d_{31}	23×10^{12}	$(C/m^2)/(N/m^2)$
	d_{32}	3×10^{12}	$(C/m^2)/(N/m^2)$
	d_{33}	-33×10^{12}	$(C/m^2)/(N/m^2)$
Young's Modulus	Y	2×10^9	N/m^2
Permitivity	ε	106×10^{-12}	F/m
Capacitance	C_s	379×10^{-12}	F/cm^2
Density	ρ	1780	kg/m^3

in its more general form as

$$w = \sum_{n=0}^{N} \sum_{s=0}^{S_n} W_{ns} \cos(n(\theta - \theta_n)) e^{ik_{ns}x_s}. \tag{5.9}$$

For a given circumferential mode shape n, θ_n in Equation (5.9) defines the angular position of the closest antinode to the $\theta = 0$ axis. In the following discussion as well as in Chapter 6, θ_n is referred to as *the polarization angle* of the circumferential mode n.

Using Equation (5.9) and assuming that the width, b, of the sensor is much smaller than the length of the propagating waves in the system, Equation (5.8) becomes

$$q = -Y d_{31} \frac{bh}{2a} \sum_{n=0}^{N} \sum_{s=0}^{S_n} W_{ns} e^{ik_{ns}x_s} \int_0^{2\pi} G(\theta) \cos(n(\theta - \theta_n)) d\theta, \tag{5.10}$$

where $G(\theta)$ represents the variation of the electrode profile in the circumferential direction.

First, it is assumed that the polarization angle, θ_m, of a given circumferential mode m is known. $G(\theta)$ is then chosen to be

$$G(\theta) = \cos(m(\theta - \theta_m)). \tag{5.11}$$

Applying the orthogonality principle (4.24), Equation (5.10) becomes

$$q = -Y d_{31} \frac{bh\pi}{2a} \sum_{s=0}^{S_m} W_{ms} e^{ik_{ms}x_s}. \tag{5.12}$$

For the chosen variation $G(\theta)$ of the electrode profile, the above equation shows that the charge collected is proportional to the modal radial displacement of the shell associated with the circumferential mode of order m. The resulting sensor (mode

151

m) can thus be made of 2m pieces of PVDF film etched as half sine waves which are attached around the shell and wired with alternating polarities. The sensor is illustrated in Figure 5.12 for m=2. Care must be taken to amplify the sensor output using an amplifier with a high input impedance, as explained in the previous section.

Practically, the exact angular position of the various circumferential modes propagating in the system is often unknown. Consequently, if the sensor is shaped as a cosine function $(G(\theta) = \cos m\theta)$ and the circumferential mode m is polarized at $\theta_m = 90°$, i.e. distributed as a sine function with respect to $\theta = 0$, the output of the sensor, given by Equation (5.10), will be zero. One way to avoid the problem is to use two closely spaced modal sensors, one shaped as a cosine function $(G(\theta) = \cos m\theta)$ and the other shaped as a sine function $(G(\theta) = \sin m\theta)$. Using Equation (5.10), the outputs of the two sensors may be written as

$$q_1 = q \cos m\theta_m, \qquad q_2 = q \sin m\theta_m, \qquad (5.13)$$

where the expression for the charge q is given by Equation (5.12). Both of the sensor outputs are proportional to the modal radial displacement of the shell associated with the circumferential mode m. For any value of θ_m, at least one of the sensor output will not be zero. Therefore, minimizing the output of both sensors ensures a minimization of the shell modal displacement (mode m) at the sensor location. Note that two control channels are required in order to implement this strategy.

In cases where the application of the control forces has little influence on the polarization of the circumferential modes, minimization of the shell modal displacements can be achieved by using a single control channel per propagating mode. The amplified outputs of the two sensors are added together using a multiplexer with
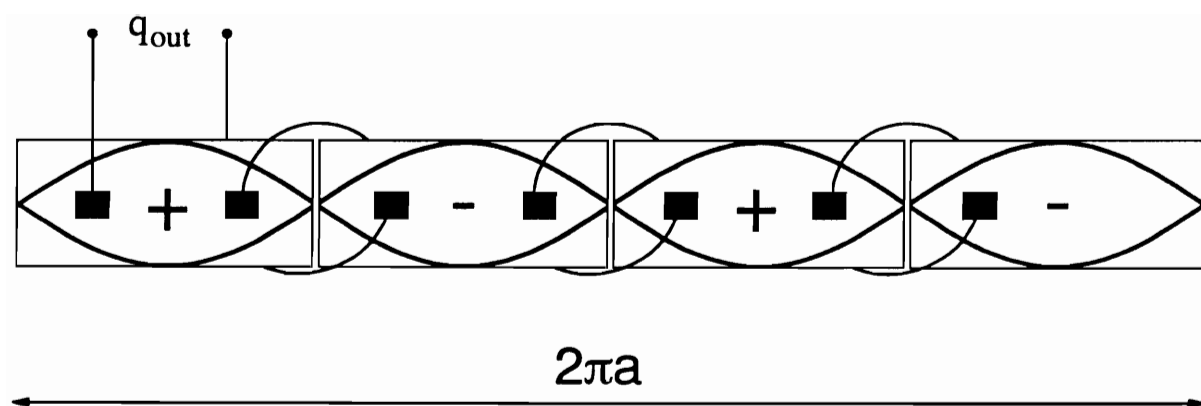
Figure 5.12: Schematic of unwrapped modal sensor (n=2).

variable input gains. The output voltage of the multiplexer may be written as

$$V = q\,C\,(A\cos m\theta_m + B\sin m\theta_m), \qquad (5.14)$$

where C is a constant gain, A and B are the input gains of the multiplexer. For any value of θ_m, there always exists a pair of gains A and B such that the voltage V is not zero. The output of the multiplexer is proportional to the modal radial displacement of the shell associated with the circumferential mode m and may thus be used as the error signal.

The pairs of modal sensors (n=1,2) used in the experiments are shown in the photograph of Figure 5.13.

5.2.3 The controller

The minimization of the error signals in the control experiments was achieved by using a feedforward adaptive controller with three inputs, i.e. the error signals, and three outputs driving the control actuators. A schematic diagram of the controller is shown in Figure 5.14. The control system uses the adaptive MIMO Filtered-x LMS algorithm to adapt the coefficients of FIR control filters based upon a reference signal and the error signals. This technique is now well known in the field of adaptive control and the reader is referred to books by Widrow and Stearns [59] or Nelson and Elliot [60] for detailed information. The control algorithm was implemented on a TMS 320C30 signal processing chip programmable in assembly language. The digital signal processing board (DSP) was manufactured by Spectrum. It was resident in an IBM-compatible host computer which was used to execute the controller. The control program was written by Jeff Vipperman, a former gradu-

154
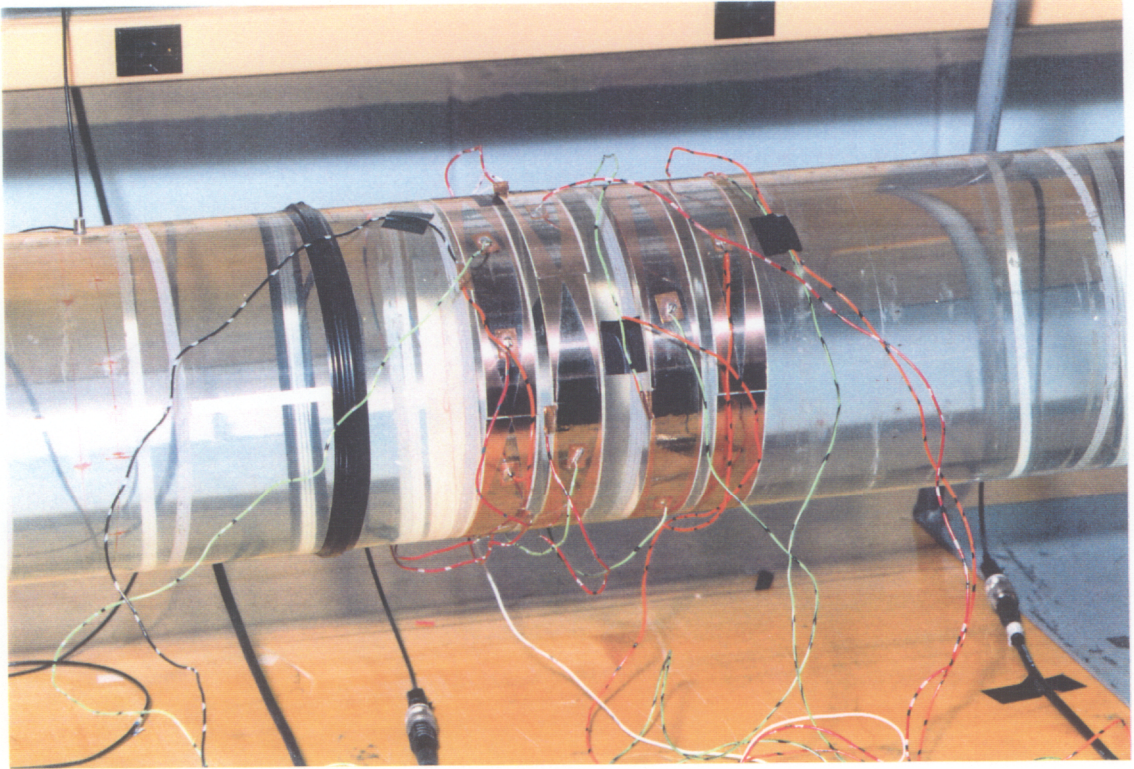
Figure 5.13: Close-up photograph of the error sensors.

ate student in the Vibration and Acoustics Laboratories, Mechanical Engineering Department at Virginia Polytechnic Institute and State University.

In implementing the control, several filters and amplifiers were required to condition the input and output signals. The sampling frequency of the DSP board was typically chosen a factor of 5 greater than the frequency to be controlled. To prevent aliasing problems, the error signals were conditioned by programmable low pass filters manufactured by Frequency Devices. The cut-off frequency of the filters was usually chosen 100 Hz larger than the excitation frequency. In order to optimize the dynamic range of the DSP, the error signals were also amplified to reach the input level of ± 1.0 volt. For this purpose, Ithaco amplifiers with variable gain adjustment were used. In addition to conditioning the inputs, the control outputs were also filtered and amplified. Since the analog outputs of the controller are based upon a digital to analog conversion, the electrical signal had to be filtered in order to eliminate the high frequency chirp created by the zero order hold of the digital-to-analog converter. Again, this task was accomplished by using low pass filters from Frequency Devices. The output signals were limited to ± 2.0 volts. To drive PVDF cables, the output signals were passed through a high power amplifier built in the Vibration and Acoustics Laboratories. To drive electromechanical shakers, a NEC power amplifier was used. The harmonic input used to provide the reference signal to the controller as well as drive the disturbance was issued from a signal generator resident in a B&K spectrum analyzer (model 2032).
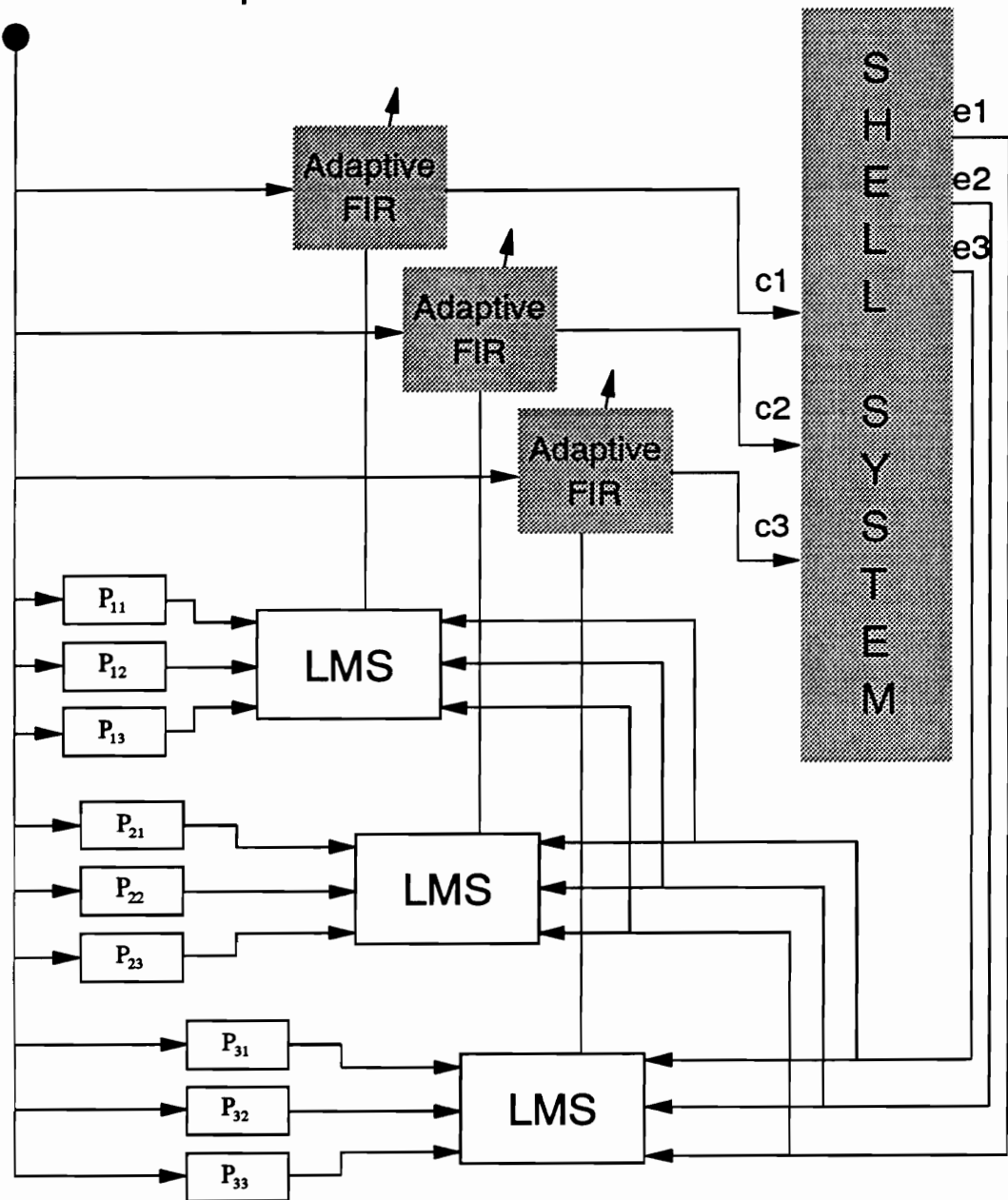
Figure 5.14: Block diagram for 3I3O feedforward adaptive controller.

Chapter 6

Experimental Results

The experimental apparatus has been extensively described and characterized in Chapter 5. In this chapter, the results of two sets of control experiments are presented and analyzed. Each set is associated with a particular disturbance type. The first set of experiments deals with the control of the axisymmetric wave propagation in a semi-infinite plexiglass shell containing either air or water. The exterior medium in both cases is air. The use of PVDF cables to implement axisymmetric actuators and sensors is investigated. The second set of experiments concerns the control of the shell vibrations induced by a radial point force disturbance applied to the shell wall at low frequencies. It will be shown that controlling the propagation of waves of circumferential order n=1 and n=2 is possible, using two point force actuators (shakers) and spatially distributed error sensors made of PVDF film. Again, both air-filled and water-filled shells will be considered.

6.1 Active control of an axisymmetric radial line force disturbance

The results of an experimental investigation to minimize the axisymmetric wave propagation in a semi-infinite plexiglass shell in air or filled with water are presented in this section. The shell was primarily driven by a PVDF cable at frequencies varying from 1500 Hz to 9000 Hz. In this frequency range, the excitation by the PVDF cable may be reasonably modelled by an axisymmetric radial line force.

6.1.1 Experimental arrangement

It has been shown in Chapter 2 that a maximum of three axisymmetric waves can propagate in the plexiglass shell (in air or filled with water) in the frequency range $\Omega \in [0; 3]$, i.e. for f between 0 and 9183 Hz. Consequently, total control of the power flow in this frequency range is theoretically achievable using 3 axisymmetric actuators and 3 sensors (see Chapter 3).

Figure 6.1 shows a schematic of the control arrangement and a photograph of the actual setup is shown in Figure 6.2. The disturbance is a PVDF cable covered with black electric tape on the right end side of the pipe. The three actuators and the three sensors are also PVDF cables, covered with white and black electric tape respectively. The implementation of the PVDF cable as an axisymmetric actuator or a modal sensor (n=0) has been described in Chapter 5. The distance between the actuators/sensors and the disturbance is indicated in Table 6.1.
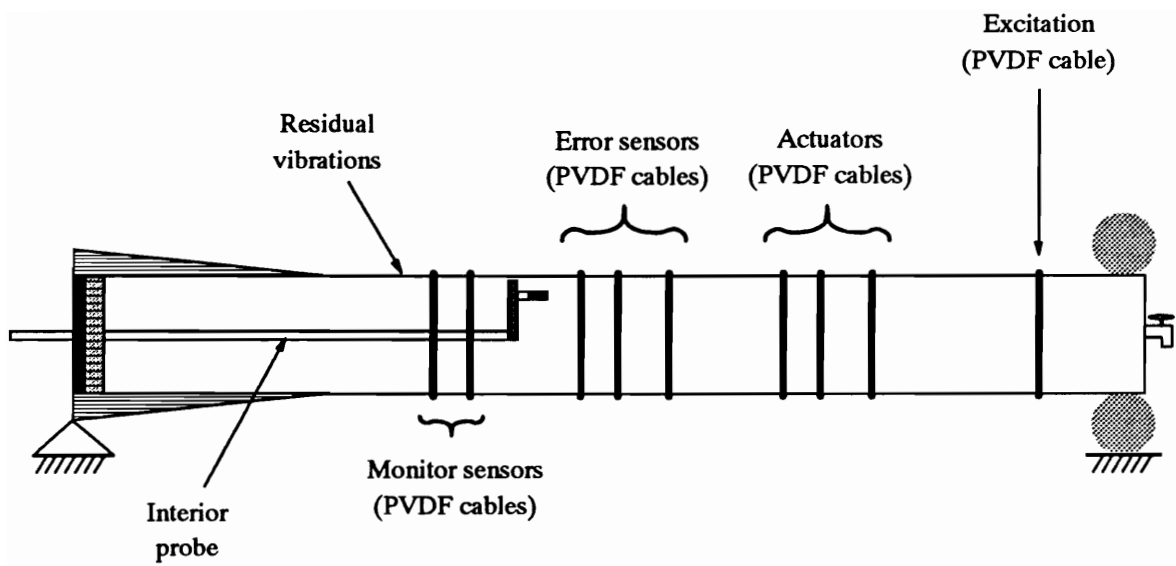
Figure 6.1: Schematic of the control arrangement.
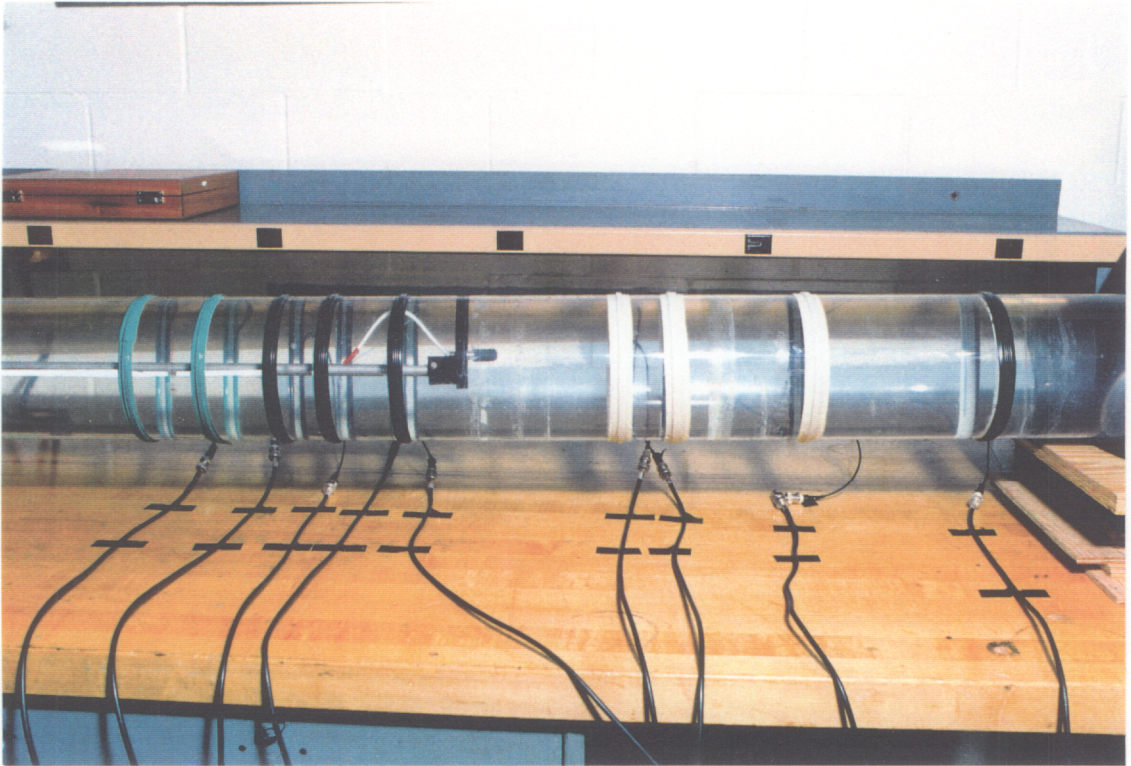
Figure 6.2: Photograph of the control arrangement.

Table 6.1: Spacing between control actuators/sensors and the axisymmetric disturbance (PVDF cable)

	Distance from the disturbance (mm)
Actuator 1	190
Actuator 2	331
Actuator 3	385
Sensor 1	609
Sensor 2	683
Sensor 3	736

6.1.2 Control layout

All the experiments were performed at single frequencies and, thus, the signal fed to the disturbance source was a pure tone sinusoid. The excitation frequency varied from 1500 Hz to 9000 Hz. At each frequency, the minimization of the error signals was achieved by using a feedforward adaptive controller with three inputs, i.e. the error signals, and three outputs driving the control actuators. The reader is referred to Chapter 5 for information on the controller and the control implementation.

The performance of the control approach was evaluated from the residual axisymmetric radial displacement of the shell measured by two PVDF cables termed the monitor sensors in Figure 6.1, one radius and two radii beyond the last error sensor. The monitor sensors are covered with the green electric tape in Figure 6.2.

It has been shown in Chapter 2 that only two axisymmetric waves can propagate in the air-filled shell (the torsional shear wave is omitted as it is uncoupled from the radial shell motion). When the shell is filled with water, there exists only two propagating axisymmetric waves at frequencies below 7350 Hz ($\Omega < 2.4$). Ideally, if only two waves (s=1 and s=2) propagate in the system, two measurements of the radial shell displacement are sufficient to determine the amplitude of each propagating wave. Let w_p and w_q be the shell radial displacement measured at x_p and $x_p + a$ for example; then, providing that the wavenumbers k_1 and k_2 are exactly known, the solution for the wave amplitudes W_1 and W_2 at x_p is given by:

$$\begin{bmatrix} W_1 \\ W_2 \end{bmatrix} = \begin{bmatrix} 1 & 1 \\ e^{ik_1 a} & e^{ik_2 a} \end{bmatrix}^{-1} \begin{bmatrix} w_p \\ w_q \end{bmatrix}. \tag{6.1}$$

Note from Equation (6.1) that there exists a solution for W_1 and W_2 only if

$$k_1 - k_2 \neq \pm(2m + 1)\frac{\pi}{a}, \qquad m = 0, 1, 2, ... \qquad (6.2)$$

The wave amplitudes directly yield information on the total power flow through the use of Equations (3.24), (3.37) and (3.40).

In the present case, however, none of the required elements for the above wave decomposition is precisely available. First, the attachment procedure of the PVDF cables is such that the sensors are very likely to have different sensitivities. In addition, the width of the PVDF sensors (about 8mm) yields an uncertainty on their actual position. Finally, small errors on the wavenumbers, due to the approximate evaluation of the shell material properties, yield large errors in the wave decomposition at the frequencies of concern.

At frequencies below 7350 Hz, whether the shell is empty or filled with water, the shell response to an axisymmetric radial line force is largely due to the wave denoted as s=1 in previous chapters. Assuming that only one wave is propagating, the attenuation of the shell power flow may be roughly given by the attenuation of the shell radial displacement at either of the monitor sensor locations. However, as the two propagating waves (s=1 and s=2) may have similar amplitudes after control, a sensor located near a destructive interference of the two waves will give an overestimated value of the insertion loss. It can be shown that the spacing between two destructive interferences of these waves is given by

$$\Delta x_i^d = \frac{2\pi}{k_1 - k_2}. \qquad (6.3)$$

By measuring the attenuation of the radial displacement at two closely spaced loca-

tions, i.e. using two monitor sensors, overestimated values of the insertion loss may be avoided. Let I_W^p and I_W^q be the attenuations (in dB) of the shell axisymmetric radial displacement, w_0, at the monitor sensor locations, i.e. at x_p and $x_p + a$,

$$I_W^p = 20 \log_{10} \left(\frac{w_0(x_p)^{after\ control}}{w_0(x_p)^{before\ control}} \right), \quad I_W^q = 20 \log_{10} \left(\frac{w_0(x_p + a)^{after\ control}}{w_0(x_p + a)^{before\ control}} \right). (6.4)$$

The insertion loss is then defined as the minimum attenuation of the shell axisymmetric radial displacement at either of the two monitor sensor locations. It is thus given by

$$IL = \max (I_W^p , I_W^q). \tag{6.5}$$

When the pipe is filled with water, the internal pressure field provides an indication on the amount of power conveyed by the fluid medium. If the pressure in the fluid is largely due to a single propagating wave, the axial component of the time-averaged acoustic intensity in the fluid, given by Equation (3.21), may be rewritten as

$$I_x^f(r, \theta) = \frac{k_{0s}}{2\rho_f \omega} pp^*, \tag{6.6}$$

where k_{0s} is the axial wavenumber of the axisymmetric propagating wave. Therefore, the power flow in the fluid is proportional to the integral of the pressure square over the fluid cross section.

6.1.3 Results and discussion

First, the shell was empty, i.e. filled with air. When control was applied, the attenuations of the three error signals varied from 30 to 60 dB, depending on
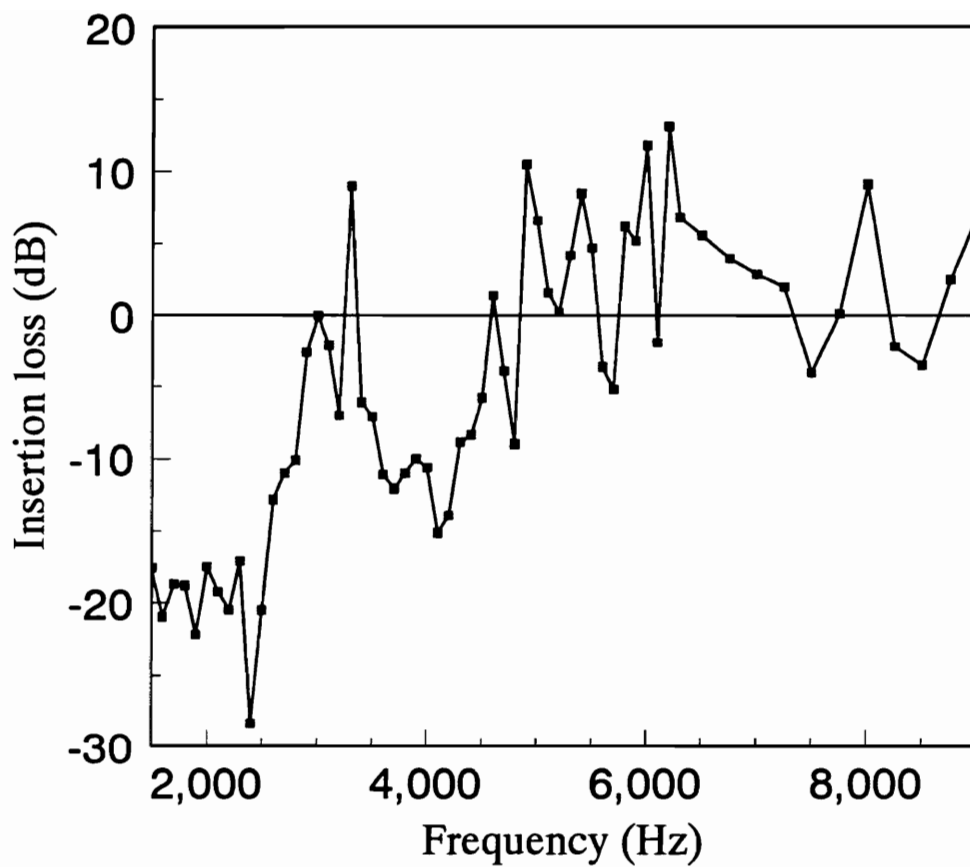
165

Figure 6.3: Insertion loss due to active control of the axisymmetric wave propagation in the air-filled shell.

the frequency of excitation. The axisymmetric radial displacement of the shell at the two monitor sensor locations was measured before and after control. Figure 6.3 shows the resulting insertion loss, as defined by Equation (6.5), at each frequency.

At low frequencies for this configuration, between 1500 Hz and 2700 Hz, only the extensional shell wave is propagating. In this frequency range, good attenuations of the shell radial displacement, varying from 18 to 28 dB, were obtained, as shown in Figure 6.3. As previously demonstrated by Pinnington *et al.* [58], the PVDF cable can monitor the axial strain in an empty pipe as the axial strain is simply related to the circumferential strain by the Poisson's ratio. In this frequency range (1500-2700 Hz), the attenuation of the structural power flow equals the attenuation of the shell radial displacement.

Between 2700 Hz and 2900 Hz, as the propagating wave changes from extensional to flexural in nature, the performance of the control approach decreased severely until no attenuation of the radial shell displacement was achieved near the ring frequency, at 3000 Hz. Then, as the wave s=2 cut on near 3300 Hz, a large increase (+7 dB) of the shell radial motion was seen to occur. These poor performances of the control arrangement are associated with the extreme behaviour of the shell system near coincidence and cut-on frequencies. As the system was resonating, the shell mobility in the frequency range $f \in [2800; 3400]$ was extremely large. The wave s=2, near cut on, had an extremely long wavelength, approaching infinity (at cut-on) according to the shell theory. The sensors may thus have created discontinuities on the shell and caused the propagating waves to be partially reflected. It is also believed that the sensors were sensitive to higher order circumferential modes in this frequency range. Between 3400 Hz and 4600 Hz, the system response was largely governed by the flexural wave and the insertion loss due to active control

varied from 10 to 15 dB. For frequencies of excitation above 4600 Hz, no attenuation of the power flow could be achieved; the wavelength of the flexural wave was too small relative to the width of the PVDF sensors and yielded erroneous error signals. The sensors might also have been sensitive to higher order circumferential modes.

When the shell was filled with water, the attenuations of the error signals achieved by the 3I3O controller varied from 30 to 70 dB, depending on the frequency of excitation. Figure 6.4 shows the resulting insertion loss at each frequency.

In a large frequency range, spreading from 1500 Hz to 7600 Hz, the axisymmetric radial displacement of the shell beyond the error sensors was reduced; the attenuations varied from 7 to 22 dB. As explained in Chapter 3, the internal pressure field due to axisymmetric motion in the frequency range 1500-7400 Hz ($\Omega \in [0.5; 2.4]$) is characterized by a near field closely hugging the shell wall. Because the hydrophone could not be moved very close to the shell wall, the attenuation of the pressure field in this frequency range could not be determined. As the particle velocity in the fluid equals the radial velocity of the shell at the interface between the two medium, it is believed that the pressure near field experienced attenuations comparable to that of the shell radial displacement. Above 7400 Hz, as the fluid behaviour approached the pressure release duct solution, the meaningful pressures in the fluid before and after control could be measured and compared. The transfer function between the reference signal and the amplified output of the hydrophone was processed for 72 positions of the hydrophone in the pipe cross section (one measurement every 30° around the shell for 6 radial positions between r=0 and r=0.9a). Figure 6.5 shows the real part of the pressure field at 7600 Hz at the axial position of the third error sensor, before and after control. A non-zero pressure field at this particular position denotes an energy flow crossing the discontinuity created by the
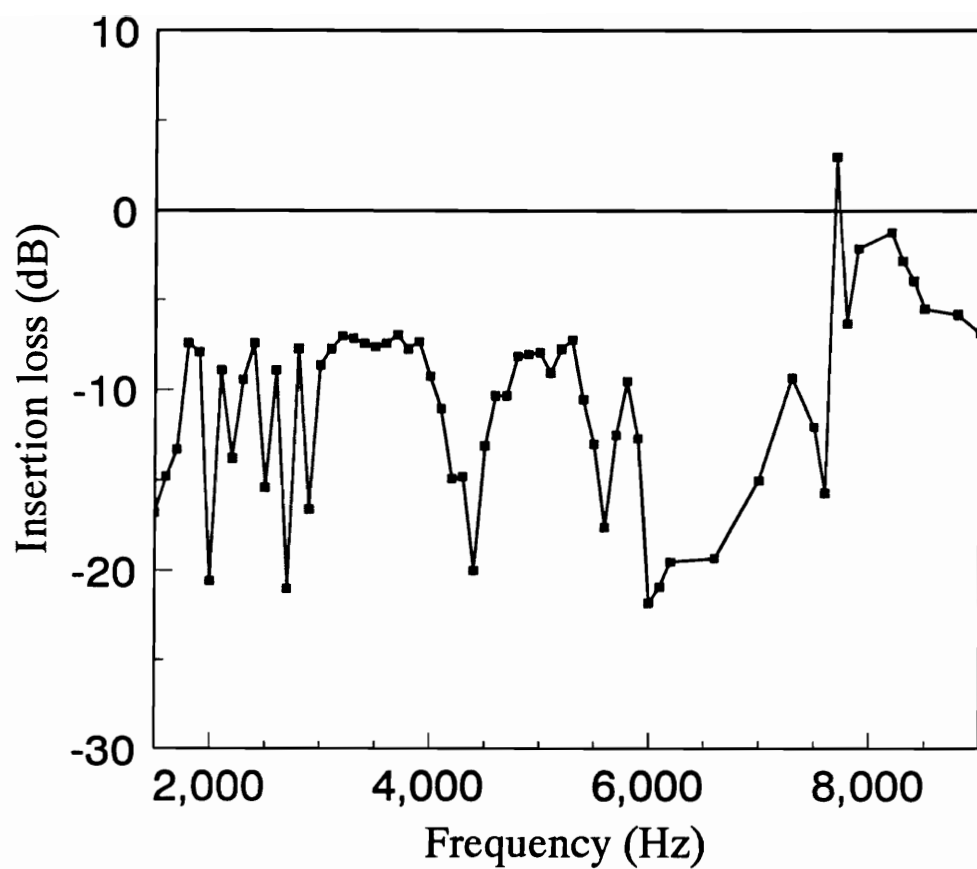
Figure 6.4: Insertion loss due to active control of the axisymmetric wave propagation in the water-filled shell.

active control arrangement on the pipe. Figure 6.5 reveals bowl shaped distributions of the pressure in the fluid (with a maximum pressure on the axis of the pipe) before and after control, due to the wave (s=3) approaching the pressure release duct solution. The attenuation of the pressure field is indicated in Figure 6.6. An average 15 dB reduction of the pressure field is obtained, similar to that of the shell radial displacement beyond the error sensors. As the fluid field at this frequency was largely governed by one wave, i.e. the pressure release duct mode (s=3) approaching cut-on, the attenuation of the pressure field denotes a large attenuation of the power flow in the fluid. Thus, at 7600 Hz, the total power flow in the system was actually reduced by about 15 dB.

For a frequency of excitation of 7700 Hz ($\Omega = 2.5$), at which the pressure release duct mode precisely cuts on, no attenuation of the shell radial motion beyond the sensors could be achieved. This behaviour was due to the shell and fluid motions being quasi uncoupled at this particular frequency; even though the radial displacement of the shell was highly attenuated at the third error sensor location, Figure 6.8 shows that the pressure field at this position was barely affected by the control approach. The energy flow in the shell was flanked into the fluid at the error sensor locations and transferred back to the shell beyond the error sensors because of wave interferences.

6.2 Active control of a radial point force disturbance

In this section, we summarize the results of the experiments carried out to validate the theory developed in Chapter 4 for the active control of a point

Figure 6.5: Measured pressure field in the fluid at the third error sensor location sensors, ring force excitation (PVDF cable) at 7600 Hz; (a) before control, (b) after control.

Figure 6.6: Pressure reduction in the fluid field at the third error sensor location, f=7600 Hz.
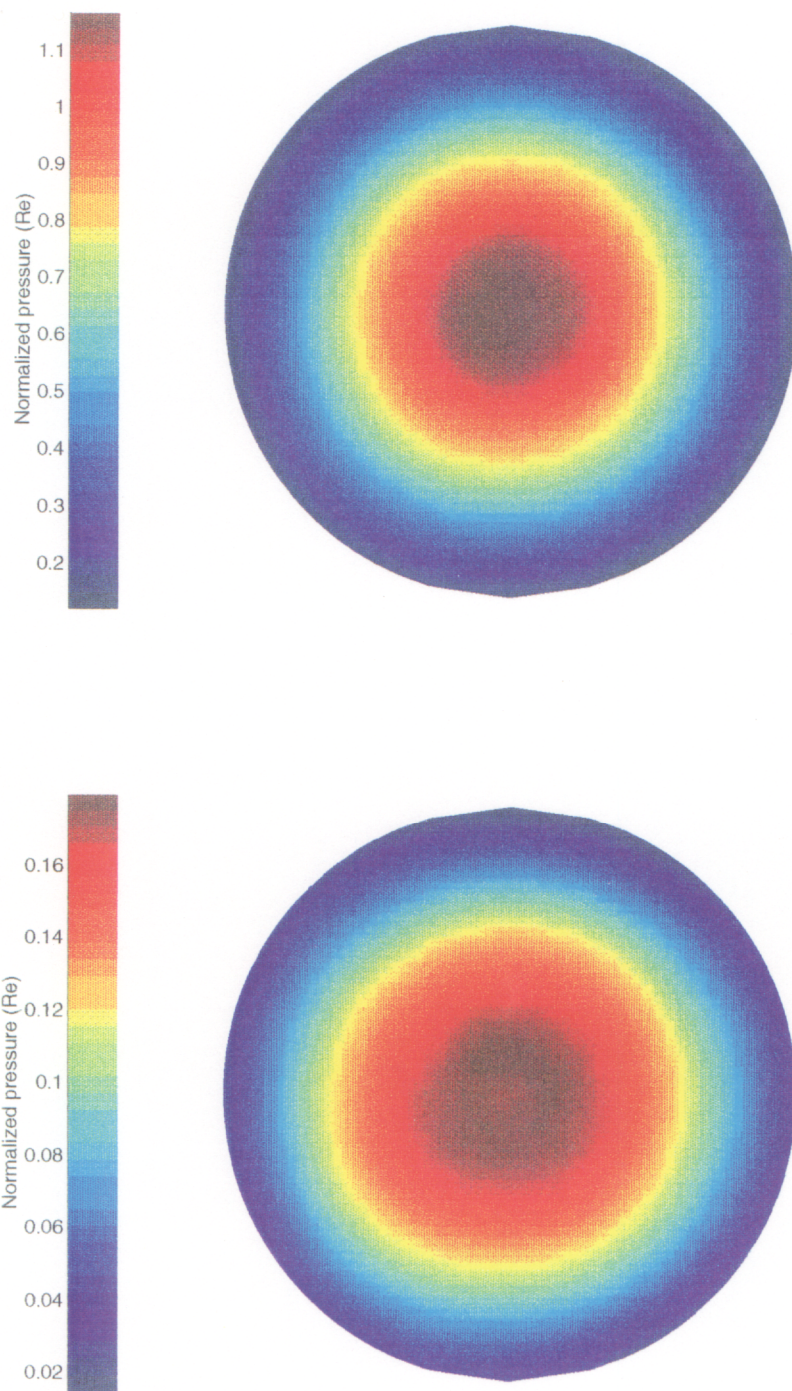
Figure 6.7: Measured pressure field in the fluid at the third error sensor location sensors, ring force excitation (PVDF cable) at 7700 Hz; (a) before control, (b) after control.
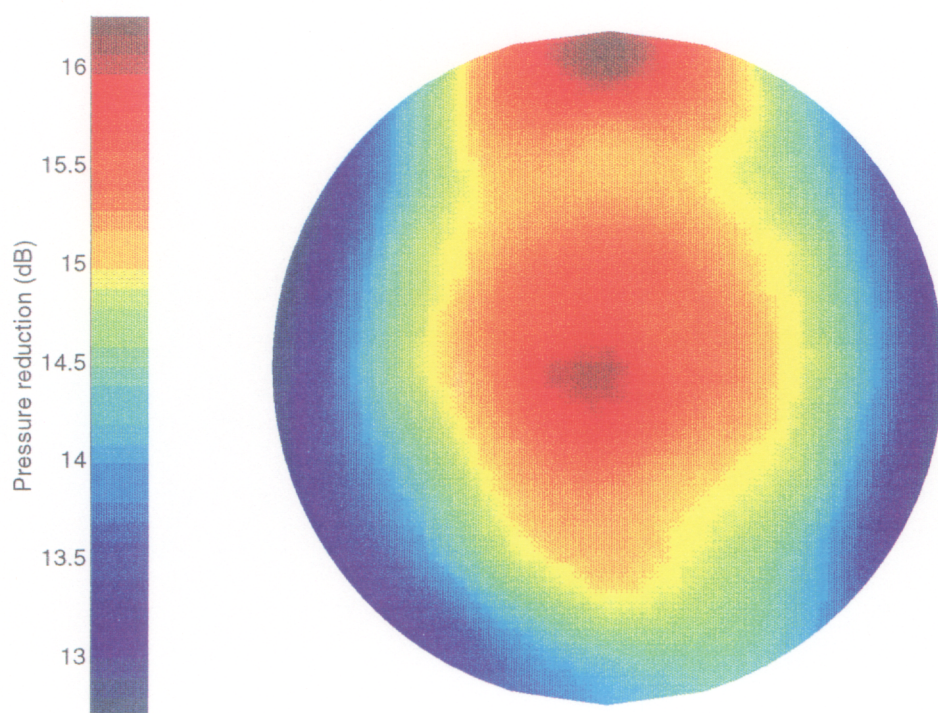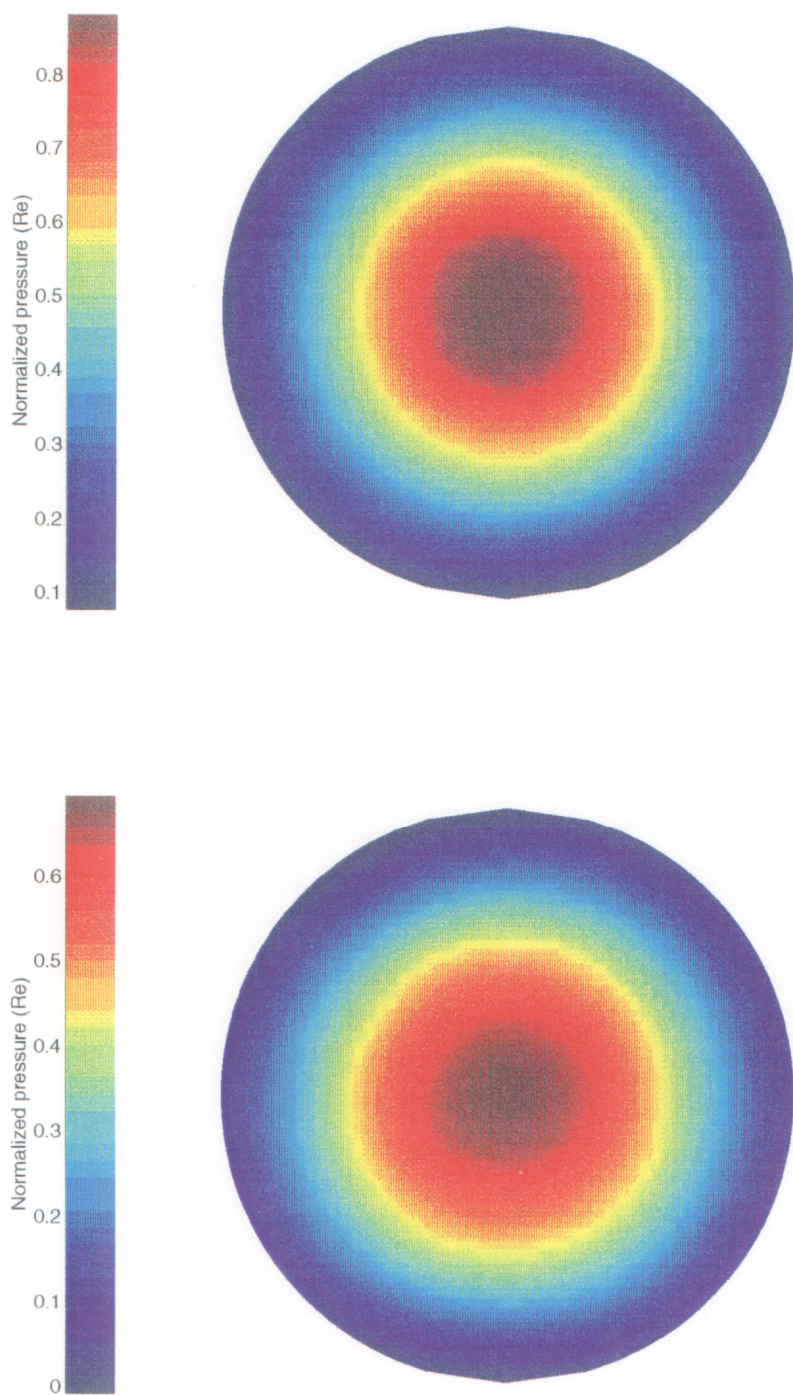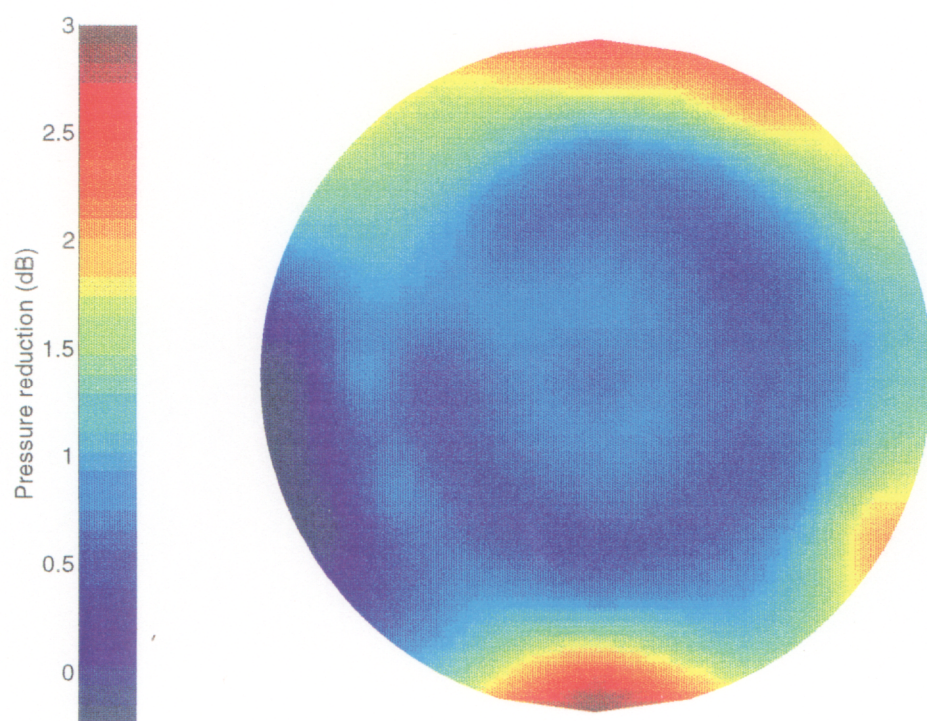
Figure 6.8: Pressure reduction in the fluid field at the third error sensor location, f=7700 Hz.

force disturbance at low frequencies. The control arrangement is described. The performance of the approach for air and water-filled shells is presented and discussed in physical terms.

6.2.1 Experimental arrangement

Figure 6.9 shows a schematic of the control arrangement and a photograph of the actual setup is shown in Figure 6.10. The primary vibration source is an electromechanical shaker hung vertically, on the right end side of the pipe. The shaker was fastened to the shell using a stinger screwed on a bolt which was itself glued to the shell. This arrangement of the disturbance can be reasonably modelled by a point force excitation at low frequencies. The angular position of the shaker is defined as $\theta = 0°$. As mentioned in Chapter 5, two types of control actuators were used simultaneously for this situation: two shakers at the same angular position as the disturbance and a PVDF cable wrapped around the shell. The axisymmetric shell displacement was observed by a PVDF cable. The radial displacement of the shell associated with the circumferential modes n=1 and n=2 was observed by modal error sensors constructed from PVDF film. The reader is referred to Chapter 5 for details on the design and the implementation of the sensors. The distance between the actuators/sensors and the disturbance is indicated in Table 6.2.

As mentioned in Chapter 5, in the frequency range of concern for these experiments (≤ 700 Hz), the length of the propagating waves is such that the termination was ineffective at absorbing vibrational energy. Thus, reflections at the end of the pipe and the resulting axial mode shapes will have to be accounted for in the interpretation of the results.

Figure 6.9: Schematic of the control arrangement.

Figure 6.10: Photograph of the experimental arrangement.
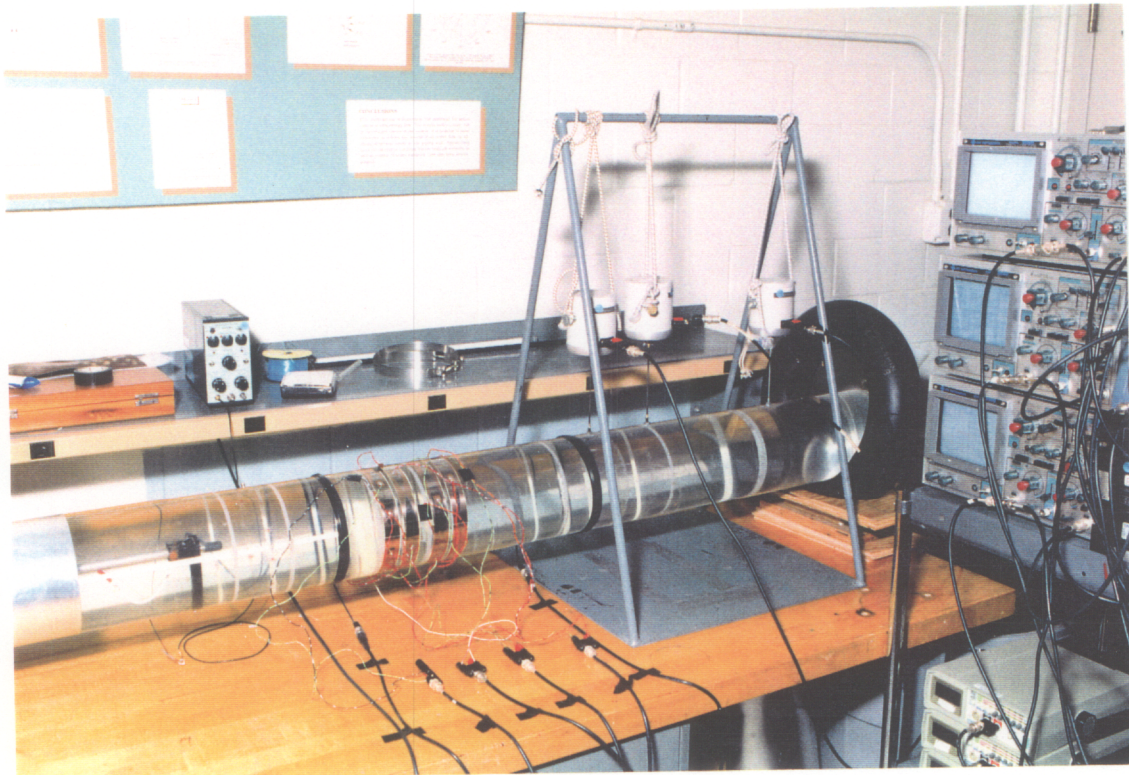
Table 6.2: Spacing between control actuators/sensors and the point force distur-
bance (shaker)

	Distance from the disturbance (mm)
Actuator 1	255
Actuator 2	365
Actuator 3	400
Sensor 1 (part 1) Sensor 1 (part 2)	630 660
Sensor 2 (part 1) Sensor 2 (part 2)	705 735
Sensor 3	805

6.2.2 Control layout

The experiments were again performed at single frequencies and, thus, the signal fed to the disturbance source was a pure tone sinusoid. Similar excitation frequencies to those considered in Chapter 4 were investigated, i.e. frequencies below and just above the cut-on frequency of the circumferential mode n=3 which is not observed. At each frequency, the minimization of the radial displacement of the shell associated with the first three circumferential modes was achieved by using a feedforward adaptive controller with three inputs, i.e. the error signals issued from the modal sensors, and three outputs driving the control actuators. As all the point forces in the system are applied at the same angular position, the control had little influence on the angular position of the circumferential modes. As a result, the minimization of the shell modal displacements associated with the circumferential modes n=1 and n=2 could be achieved by using a single control channel per mode. The procedure has been described in Chapter 5.

The radial amplitude of the circumferential modes n=0,1,2,3,4 and 5 one radius beyond the error sensors was determined before and after control as follows. The modal decomposition of the shell motion at the designated axial position was achieved by measuring the radial acceleration of the shell at 11 different locations around the circumference of the pipe with a small B&K accelerometer (0.65 gram). For frequencies well below the cut-on frequency of the circumferential mode n=6, the radial displacement of the shell at the axial position of concern can be modelled as

$$w(\theta) \;=\; A_0 \;+\; \sum_{n=1}^{5} A_n \cos(n(\theta - \theta_n)) \tag{6.7}$$

$$= A_0 + \sum_{n=1}^{5} A_n \left(\cos(n\theta) \cos(n\theta_n) + \sin(n\theta) \sin(n\theta_n) \right) \tag{6.8}$$

$$= A_0 + \sum_{n=1}^{5} a_n \cos(n\theta) + b_n \sin(n\theta). \tag{6.9}$$

For a given circumferential mode shape n, θ_n in Equations (6.7) and (6.8) defines the angular position of the closest antinode to the $\theta = 0$ axis. In the following discussion, θ_n is referred to as *the polarization angle* of the circumferential mode n.

The radial displacement at the 11 angular positions, θ^i, around the pipe is expressed in a matrix form as

$$
\begin{bmatrix}
w(\theta^1) \\
w(\theta^2) \\
\cdot \\
\cdot \\
\cdot \\
\cdot \\
\cdot \\
w(\theta^{11})
\end{bmatrix}
=
\begin{bmatrix}
1 & \cos(\theta^1) & \sin(\theta^1) & . & . & \cos(5\theta^1) & \sin(5\theta^1) \\
1 & \cos(2\theta^2) & \sin(\theta^2) & . & . & \cos(5\theta^2) & \sin(5\theta^2) \\
\cdot & \cdot & \cdot & . & . & \cdot & \cdot \\
\cdot & \cdot & \cdot & . & . & \cdot & \cdot \\
\cdot & \cdot & \cdot & . & . & \cdot & \cdot \\
\cdot & \cdot & \cdot & . & . & \cdot & \cdot \\
\cdot & \cdot & \cdot & . & . & \cdot & \cdot \\
1 & \cos(\theta^{11}) & \sin(\theta^{11}) & . & . & \cos(5\theta^{11}) & \sin(5\theta^{11})
\end{bmatrix}
\begin{bmatrix}
A_0 \\
a_1 \\
b_1 \\
\cdot \\
\cdot \\
\cdot \\
a_5 \\
b_5
\end{bmatrix}
\tag{6.10}
$$

The above system of equations yields the 11 unknowns A_0, a_1, b_1, a_2, b_2, a_3, b_3, a_4, b_4, a_5 and b_5 describing the 6 circumferential mode shapes. The magnitude and the angular position of each mode are then given by

$$A_n = \sqrt{a_n^2 + b_n^2} \quad n = 1, 2, 3, 4, 5, \tag{6.11}$$

$$\tan(n\theta_n) = b_n/a_n, \quad n = 1, 2, 3, 4, 5. \tag{6.12}$$

Note that, as a_n and b_n are complex, $n\theta_n$ does not always have a real solution. It can be shown a complex $n\theta_n$ yields a time domain rotation of the circumferential mode n; this mode is said to be spinning. More details on the origin and characteristics of spinning modes are given in Appendix B.

In the frequency range of concern, each circumferential mode is mainly gov-

erned by the propagation of a single wave type. If this wave is reflected at the end of the pipe, the amplitude of the mode at a given axial position x_p may be written as

$$A_n = A_n^i e^{ik_n x_p} + A_n^r e^{-ik_n x_p}, \tag{6.13}$$

where k_n is the wavenumber associated with the circumferential mode n and A_n^r and A_n^i are the amplitudes of the incident and reflected waves respectively. We now assume that the amplitude of the mode n at x_p and at another axial position x_q is zero,

$$\begin{cases} A_n^i e^{ik_n x_p} + A_n^r e^{-ik_n x_p} = 0 \\ A_n^i e^{ik_n x_q} + A_n^r e^{-ik_n x_q} = 0 \end{cases} \tag{6.14}$$

There exists an non-trivial solution ($A_n^i \neq A_n^r \neq 0$) to the system of equations (6.14) only if

$$\begin{vmatrix} e^{ik_n x_p} & e^{-ik_n x_p} \\ e^{ik_n x_q} & e^{-ik_n x_q} \end{vmatrix} = 0, \tag{6.15}$$

i.e. only if

$$\sin k_n(x_p - x_q) = 0 \tag{6.16}$$

or

$$k_n(x_p - x_q) = (2m + 1)\frac{\pi}{2}, \qquad m = 0, 1, 2, \ldots \tag{6.17}$$

As a result, if the distance $x_p - x_q$ is smaller than $\lambda_n/2$, A_n^i and A_n^i must be zero. Therefore, large attenuations of the modal amplitudes, A_n, at the error sensor locations and one radius beyond the error sensors reveal a global attenuation of the mode propagation.

6.2.3 Results and discussion

For various excitation frequencies of the disturbance, the performance of the active control approach investigated is discussed in this section. Both air-filled and water-filled shells are considered.

The active control approach was first applied to the air-filled shell. At 150 Hz ($\Omega \simeq 0.05$), the attenuation of the error signals achieved by using the 3I3O feedforward controller were 23.3 dB for the mode n=0, 23 dB for the mode n=1 and 39.6 dB for the mode n=2. Figure 6.11 shows the modal decomposition, before and after control, of the transfer function between the shell radial acceleration one diameter beyond the error sensors and the input signal to the disturbance source. Before control, the response of the shell was dominated by the ovalling mode (n=2). This mode was attenuated by 19 dB after control at the axial position of the monitor accelerometer. Due to the extreme length of the propagating waves at this frequency, the attenuation of the mode at two different axial positions (including the error sensor location) spaced 4 radii apart reveals a global attenuation of the mode propagation. This result has been demonstrated in the previous section. The mode n=1 was attenuated by 8 dB. The other circumferential modes had very small amplitudes before and after control. The results at this frequency are very consistent with those obtained in Chapter 4.

At 300 Hz ($\Omega \simeq 0.1$), the first wave of circumferential order n=3 was propagating. The measured cut-on frequency of the mode is 274 Hz (see Chapter 5). Had the shell been infinite, it has been shown in Chapter 4 that the mode n=3 would have dominated the response. However, Figure 6.11 shows that the response of the shell at the monitor location was dominated by the circumferential mode n=2. This

Figure 6.11: Modal decomposition of the radial acceleration of the shell one diameter beyond the error sensors, *in vacuo* shell excited by a point force at 150 Hz.

behaviour is associated with the wave reflections at the ends of the shell inducing a standing wave pattern of the shell vibrations in the axial direction. After control, the mode n=2 was attenuated by 31 dB beyond the error sensors. As the waves of circumferential order n=2 and n=3 have nearly identical phase speeds at this frequency, the mode n=3 was seen to experience a 19 dB reduction. This type of behaviour has been discussed in Chapter 4. The modes n=0 and n=1 were both attenuated by 12 dB.

For a frequency of excitation equal to 700 Hz ($\Omega \simeq 2.2$), three modes (n=1,2 and 3) largely contributed to the shell response before control. After control, the error signals were attenuated by 22 dB (n=0), 31 dB (n=1) and 39 dB (n=2). Beyond the sensors however, the radial acceleration of the shell wall associated with the beam mode had increased by 6 dB. This surprising result is associated with a standing wave pattern of the beam mode (n=1) in the axial direction that presented a node of vibration in the proximity of the modal sensor (n=1). As the circumferential mode n=1 was not observed, the control point forces yielded an increase of the beam like shell motion. Such behaviour is more likely to happen at higher frequencies.

As expected from the analytical work of Chapter 4, the performance of the control approach on the water-filled shell was quite different. At 80 Hz ($\Omega = 0.026$), Figure 6.14 shows that the response at the monitor position before control was mainly dictated by the circumferential modes n=1 and n=2, polarized at $-58.8°$ and 3.5° angles respectively. Note that the angular position of the circumferential mode n=1 ($-58.8°$) at this frequency justifies the need of having modal error sensors made of both sine and cosine shaped PVDF films, as explained in Chapter 5. The dominance of the circumferential modes n=1 and n=2 before control is also apparent
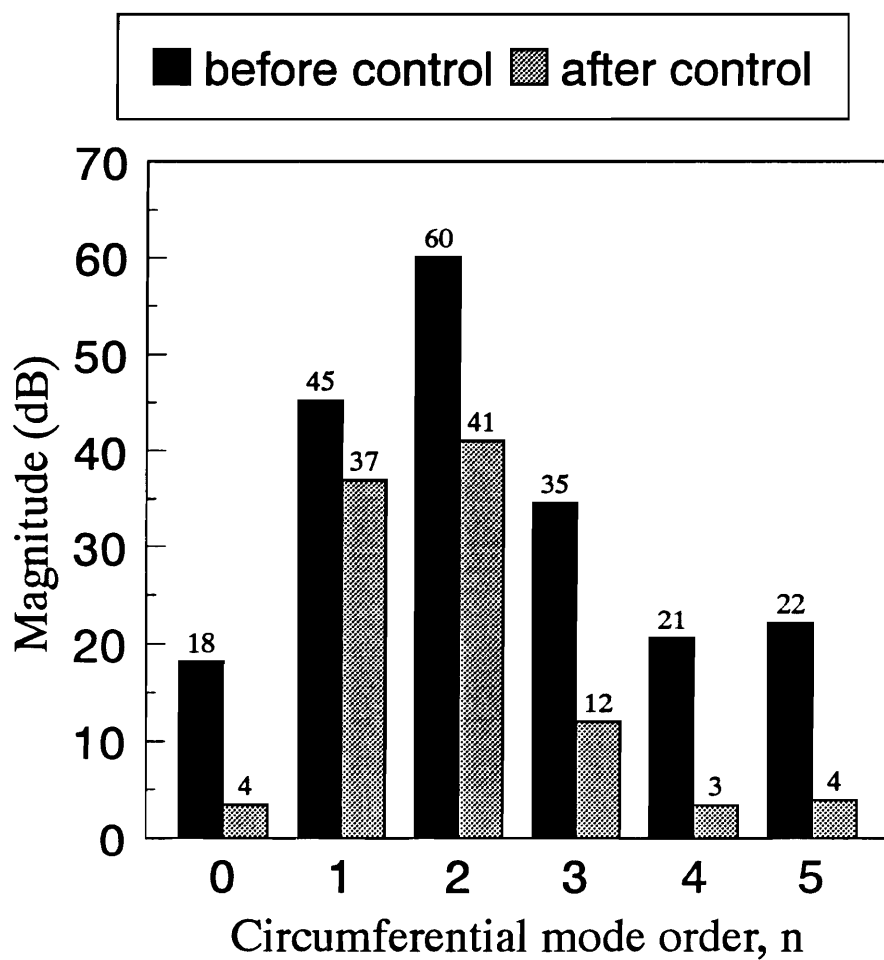
Figure 6.12: Modal decomposition of the radial acceleration of the shell one diameter beyond the error sensors, *in vacuo* shell excited by a point force at 300 Hz.
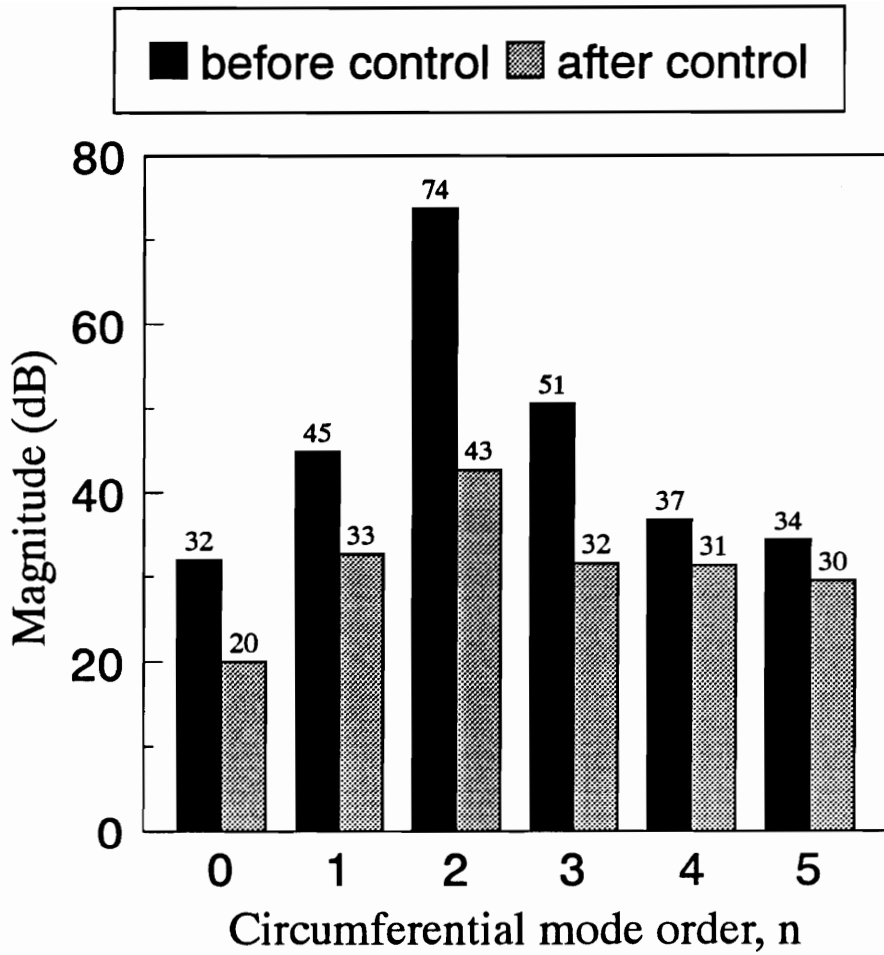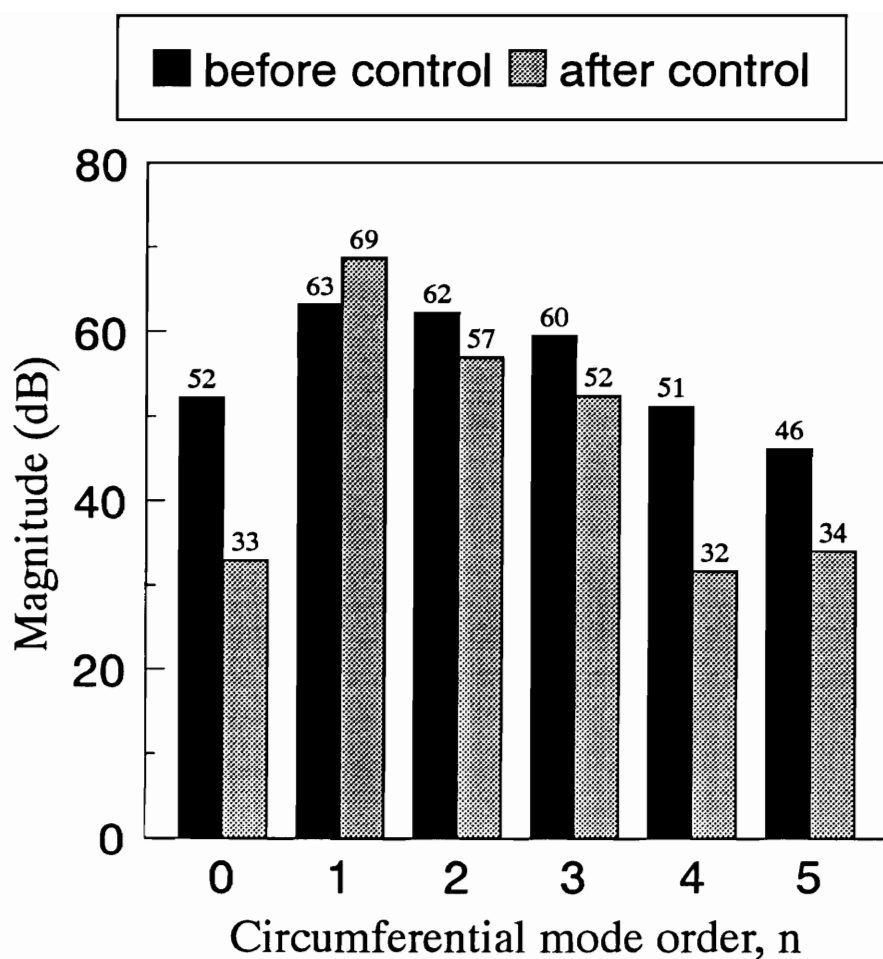
Figure 6.13: Modal decomposition of the radial acceleration of the shell one diameter beyond the error sensors, *in vacuo* shell excited by a point force at 700 Hz.

on the pressure field in the fluid measured with the internal probe one diameter beyond the error sensors (Figure 6.15(a)). When control was applied, the error signals generated by the modal sensors were attenuated by 40 dB (n=0), 36 dB (n=1) and 28 dB (n=2). The attenuation of the circumferential mode n=2 beyond the error sensors, at the monitor accelerometer position, was nearly identical to that at the modal sensor location (26 dB). However, the insertion loss of the beam type (n=1) radial motion was only 7 dB. Figure 6.15(b) shows the imaginary part of the pressure field in the fluid after control. As a result of the relatively small attenuation of the beam type motion, the pressure distribution looks like the first acoustic duct mode of circumferential order n=1. The attenuation of the pressure field in the fluid is shown in Figure 6.16; the levels are seen to vary from 5 to 40 dB, indicating a net reduction of the power flow conveyed by the fluid.

At 150 Hz ($\Omega \simeq 0.05$), the first wave of circumferential order n=3 is propagating. The measured cut-on frequency of the mode is 114 Hz (see Chapter 5). The mode (n=3) would predominate the shell response if the system was infinite (see Chapter 4). Because of the axial standing wave pattern associated with the wave reflections at the ends of the shell, it appeared that the magnitude of the ovalling mode (n=2) was much larger than that of the mode n=3 at the monitor accelerometer location (see Figure 6.17). When control was applied, the modes n=2 and n=3 were attenuated by 15 dB and 11 dB respectively beyond the sensors. As Figures 6.18 and 6.19 reveal, reductions of the pressure in the fluid field are seen to vary from 0 to 20 dB.

As the frequency of excitation is further increased, higher order circumferential modes cut on. As these circumferential modes (n=3,4,...) are not observed by

187

Figure 6.14: Modal decomposition of the radial acceleration of the shell one diameter beyond the error sensors, water-filled shell excited by a point force at 80 Hz.

Figure 6.15: Measured pressure field in the fluid one diameter beyond the error sensors, point force excitation at 80 Hz; (a) before control, (b) after control.

Figure 6.16: Pressure reduction one diameter beyond error sensors, f=80 Hz.

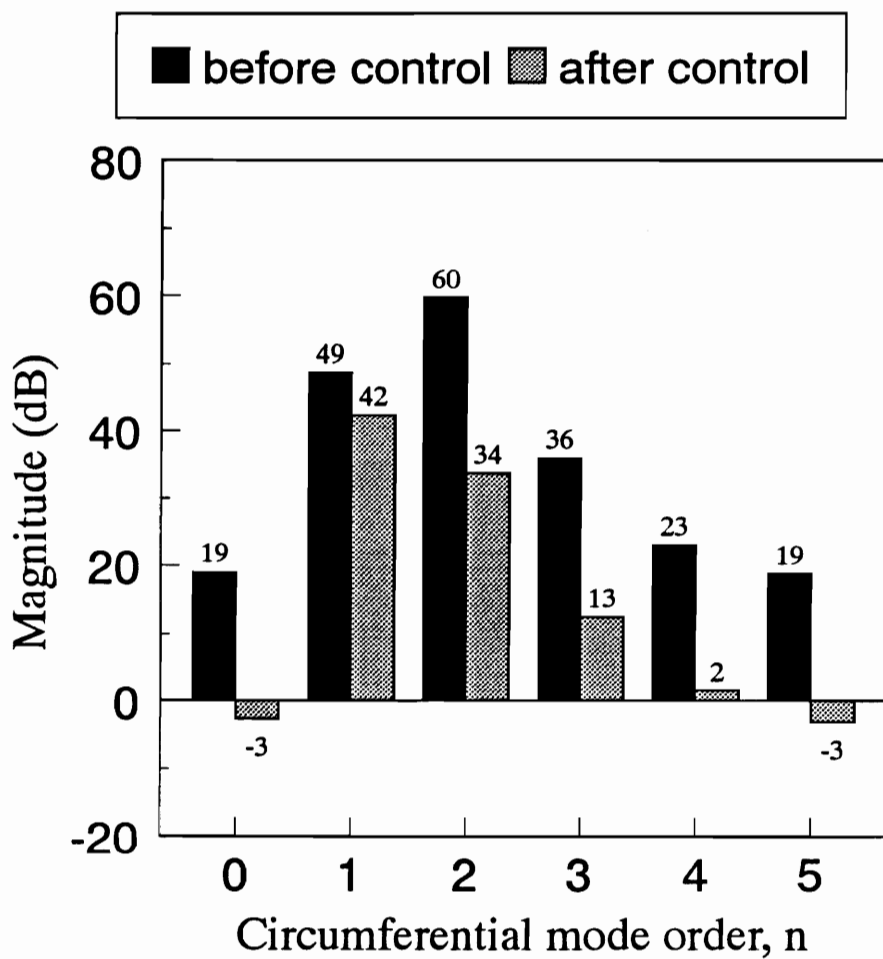Figure 6.17: Modal decomposition of the radial acceleration of the shell one diameter beyond the error sensors, water-filled shell excited by a point force at 150 Hz.
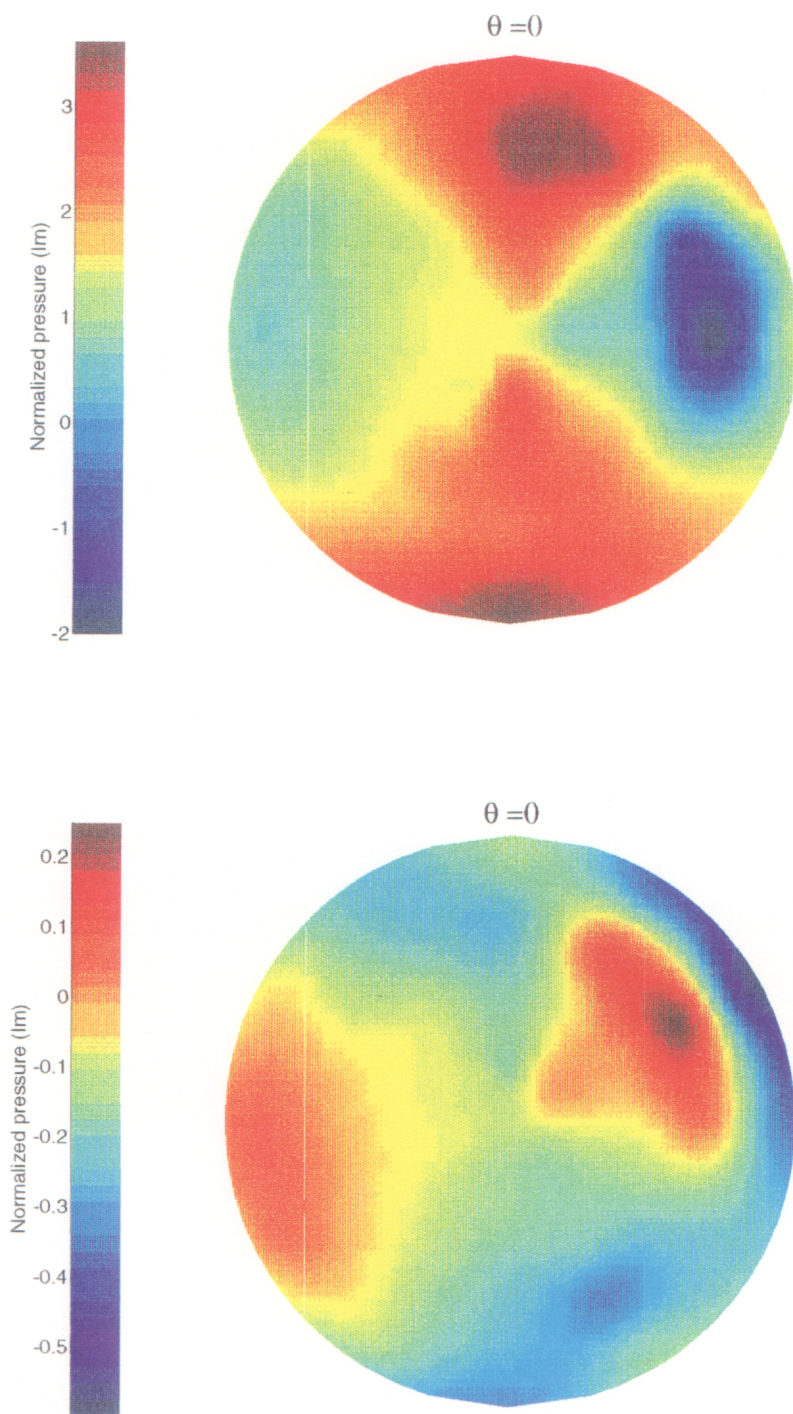
Figure 6.18: Measured pressure field in the fluid one diameter beyond the error sensors, point force excitation at 150 Hz; (a) before control, (b) after control.
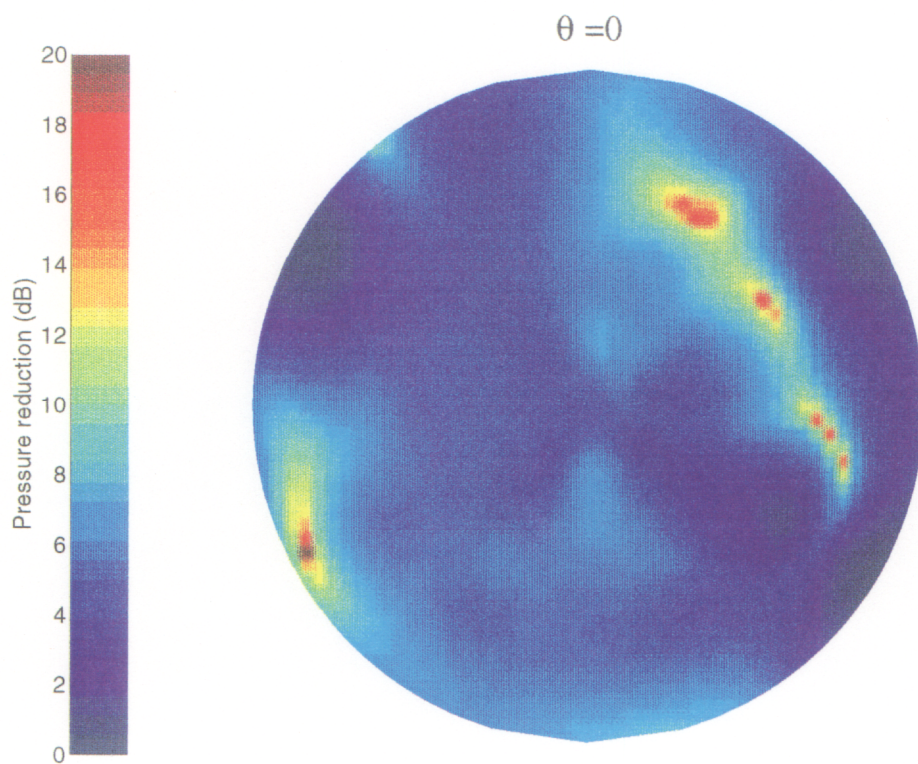
Figure 6.19: Pressure reduction one diameter beyond error sensors, f=150 Hz.

modal error sensors, spillover is expected to happen. Because of the wave reflections at the ends of the shell, spillover in the circumferential modes n=0, n=1 and n=2 is also likely to occur if any of the three modal sensor is located near a circumferential nodal line. At 250 Hz (Figure 6.20), control of the modes n=2 and n=3 was achieved but spillover appeared in the mode n=1. At 350 Hz (Figure 6.20), spillover occurred in every circumferential mode for $n > 0$. At this frequency, an increased number of control channels is thus necessary to achieve a reduction of the total power flow in the system. As demonstrated by Gibbs [35] in beams, two identical modal sensors on the pipe would allow more control of both incident and reflected waves of a given circumferential mode order. Higher order modal sensors are also needed because the contribution of the higher order circumferential modes is significant.

The experimental results presented in this section support the conclusions obtained from the analytical model in Chapter 4. At low frequencies, it is possible to actively control the total power flow in cylindrical elastic shells filled with air or liquid. The results successfully demonstrate that the radial motion of the shell may be observed by modal error sensors made of shaped PVDF film attached to the shell wall. It has been demonstrated that the use of two control channels per circumferential mode $(n > 0)$ may not be necessary if the angular position of the circumferential modes varies little during control. Using two modal sensors (sine and cosine shaped) for each circumferential mode is however recommended. Finally, a wave filtering technique requiring two sets of modal sensors per circumferential mode would ensure the control of both incident and reflected waves in pipes of finite length.
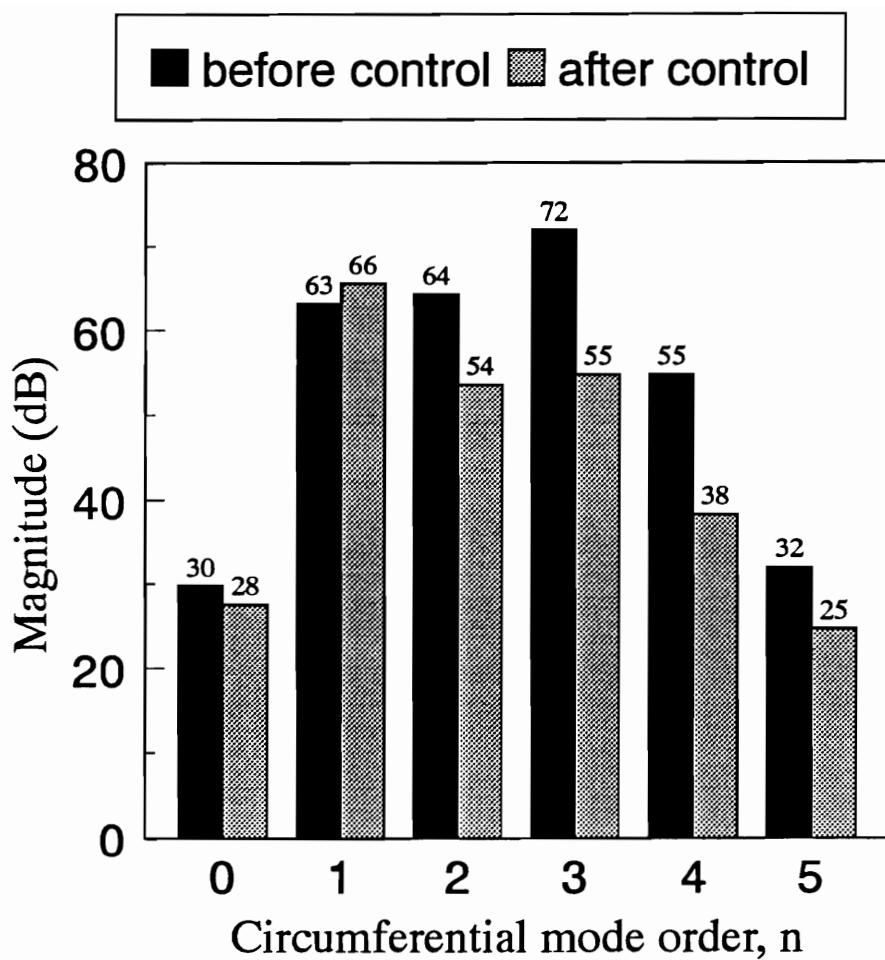
Figure 6.20: Modal decomposition of the radial acceleration of the shell one diameter beyond the error sensors, water-filled shell excited by a point force at 250 Hz.
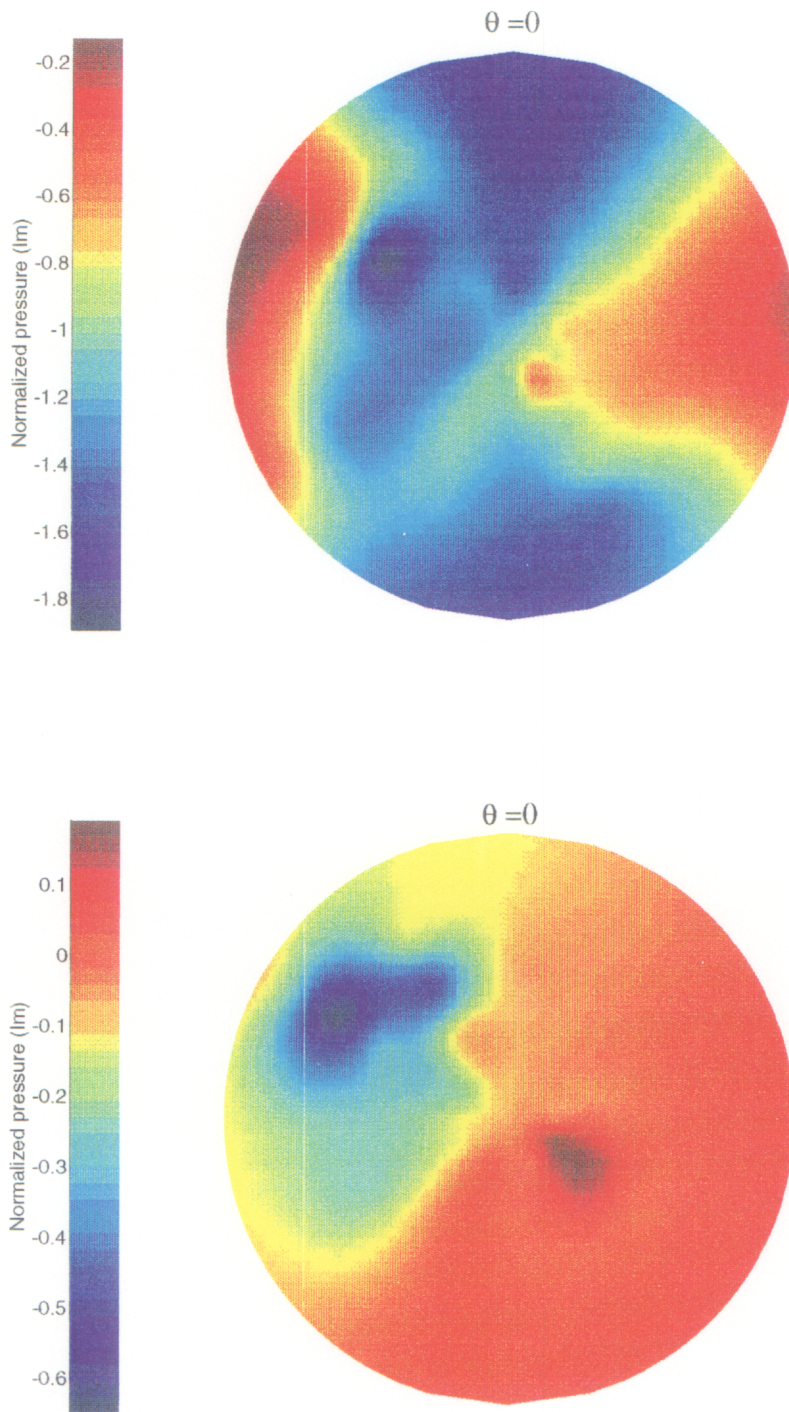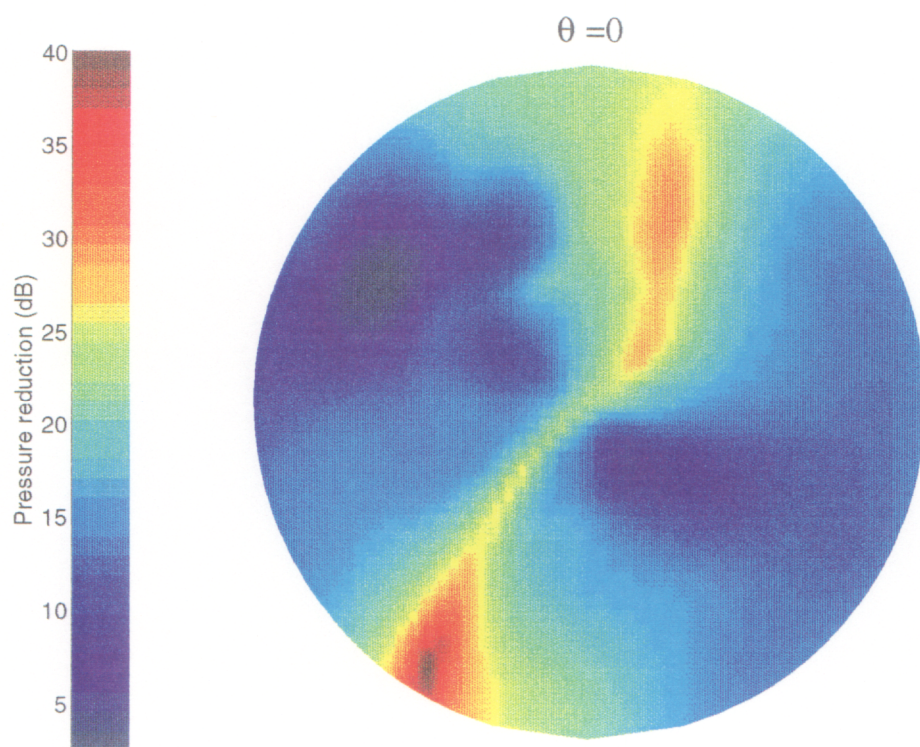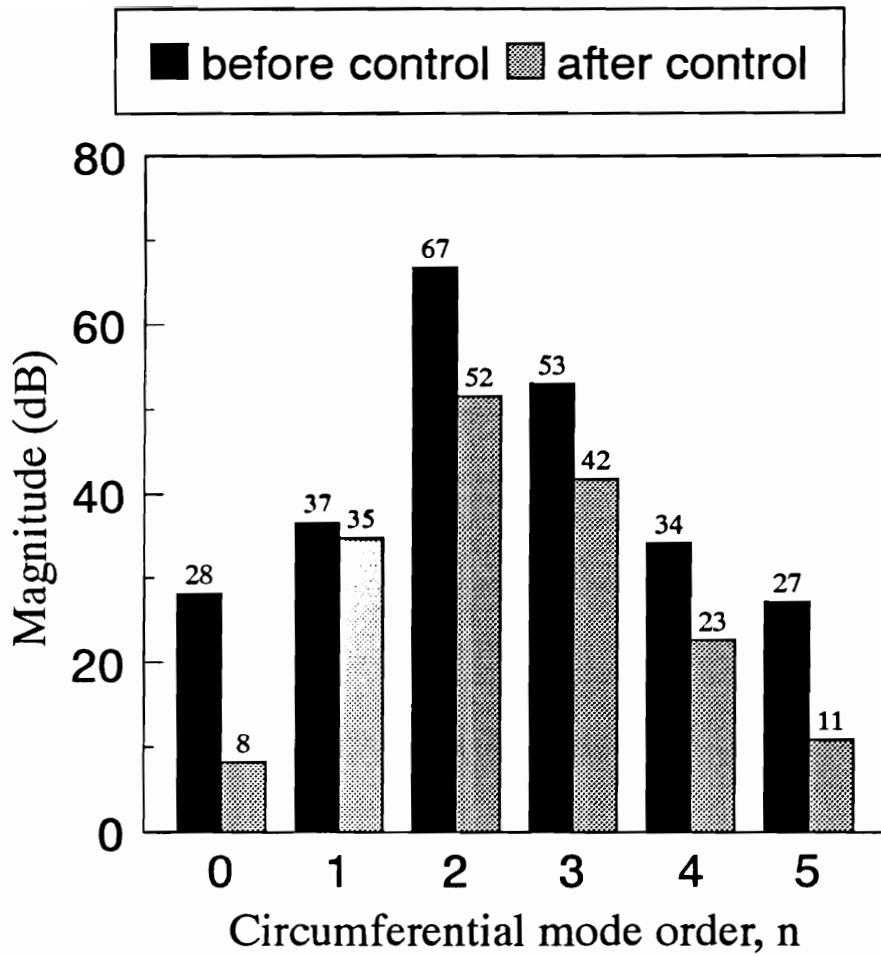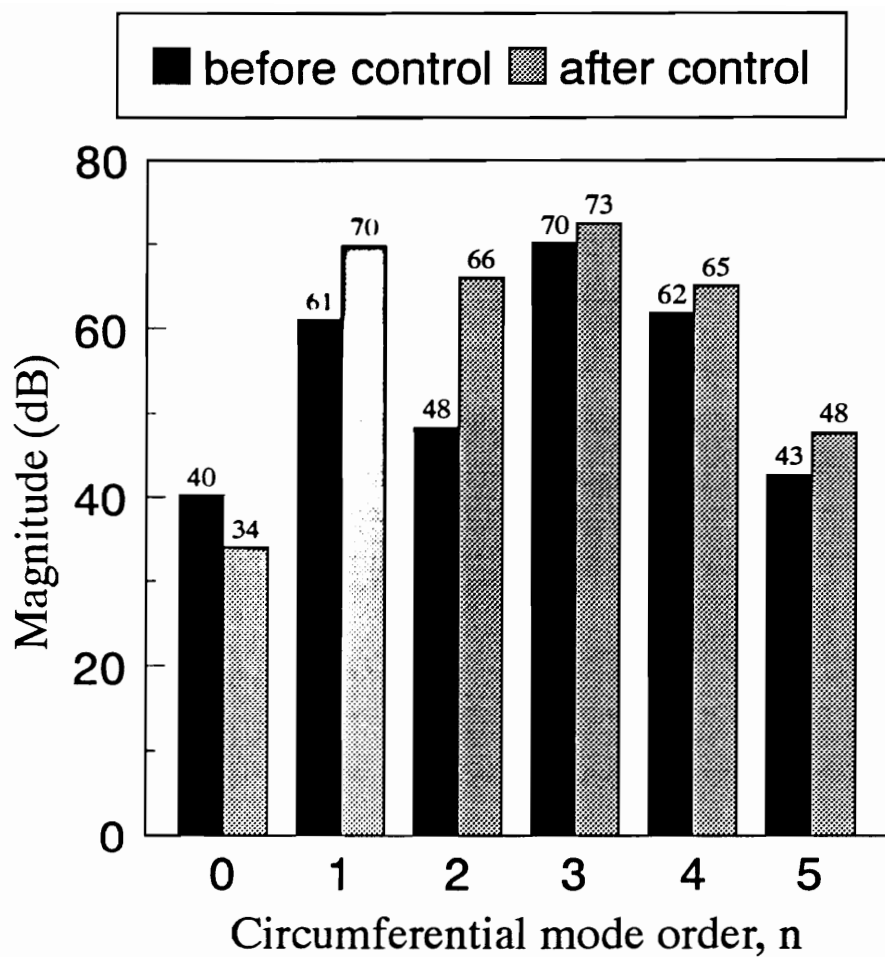
Figure 6.21: Modal decomposition of the radial acceleration of the shell one diameter beyond the error sensors, water-filled shell excited by a point force at 350 Hz.

Chapter 7

Conclusions and Recommendations

The main goal of this work was to show that reduction of the total power flow in fluid-filled cylindrical elastic shells can be achieved by using an active control approach based on structural control inputs and error sensors. Because of the coupling between the shell and the internal fluid medium, structural control inputs are likely to affect the power flow in the shell wall as well as the power flow in the fluid field.

By considering different infinite shell systems and various types of disturbance in these systems, a broad analytical study has revealed the odds and limitations of the active control approach:

- Single propagating free waves of circumferential order n=0 or n=1 were the first disturbances considered. The objective was to demonstrate the capability of radial line control forces to reduce the total power flow associated with these waves. In the axisymmetric case, it was found easier to reduce the total power

197

flow propagating along the coupled system when the disturbance was a fluid-type incident wave. This behaviour was associated with the particular nature of the wave, i.e. pressure near field close to the shell wall. For structural wave type propagation, the fluid severely decreased the control performance. In the n=1 case, it was noticed that the fluid increased the control performance below the first acoustic cutoff frequency. Above this frequency, good control of the power flow using structural line forces was difficult to achieve as more energy was carried by the fluid medium.

- Control of the total power flow induced by more complex disturbances, such as point forces or internal monopole sources, was shown to be feasible. The control strategy relied on individually sensing the shell motion associated with each circumferential mode propagating energy in the system. Since the number of propagating circumferential modes increased with frequency, the performance of the control approach was frequency limited by the number of control channels. With respect to that matter, it was proved that the non-dimensional cut-on frequencies of *in vacuo* shell systems are independent of the shell material properties. Therefore, given a number of control channels, the higher the extensional phase speed of the shell material the broader the actual frequency range over which the control system has authority.

Considering fluid-filled shells, the results have shown that the power flow induced by a point force disturbance was mainly conveyed by the shell wall; structural control inputs were thus very effective at reducing the power flow in the system. The internal fluid loading had the effect of lowering the system cut-on frequencies, more markedly when the shell wall was highly compliant. Therefore, the frequency range yielding good performances of the control ar-

rangement for fluid-filled shells was narrower than the one for *in vacuo* shells. The results also demonstrated that the power flow induced by an internal monopole source was predominantly conveyed by the fluid medium. Because of the coupling between the two media, good attenuations of the power flow in the system could be obtained. However, considering a fluid-filled steel shell, i.e. a shell system with a low compliance, the control was a difficult task to achieve since very large control forces were required. Considering a more compliant shell system, the fluid field was more efficiently affected by radial forces and the control effort needed was much smaller.

The results of various experiments conducted on a semi-infinite plexiglass shell system have been presented:

- The cut-on frequencies of the investigated shell system were evaluated and compared to the calculated ones. The axisymmetric pressure field in the fluid, induced by a broadband ring force, was measured with an hydrophone and compared to the pressure computed analytically. These preliminary results corroborated the accuracy of the general theory developed for fluid-filled shells.

- The active control of an harmonic axisymmetric radial disturbance in the frequency range 1500-9000 Hz was implemented and the consistency of the control performance achieved was assessed. Regarding the air-filled shell, the control arrangement did not have any authority on the shell power flow above 4600 Hz and near the ring frequency ($\simeq$ 3060 Hz). When the shell was filled with water, the insertion loss (in terms of shell radial displacement) varied from 7 to 22 dB between 1500 Hz and 7600 Hz, indicating a net reduction of

the total power flow in the shell.

In conducting this study, new actuators and sensors made of PVDF cable were experimentally tested.

- The active approach to control the power flow induced by the disturbance of an electromechanical shaker was experimentally tested. The shaker was assumed to generate a radial point force. Modal error sensors (n=0,1,2), constructed from shaped PVDF film and cable attached to the shell, were used. Regarding the air-filled shell, good attenuations of the power flow beyond the error sensors were achieved for excitation frequencies below approximately 600 Hz. At higher frequencies, spillover in the circumferential mode n=1 was seen to occur because of wave reflections at the ends of the shell which created axial standing wave patterns sometimes yielding poor modal observability. When the shell was filled with water, large reductions of the power flow in the shell and in the fluid could only be achieved at frequencies below 250 Hz. At higher frequencies, the propagation of circumferential modes n>2 as well as wave axial reflections resulted in spillover.

The preceding analysis demonstrates the potential for active control of total energy flow in fluid-filled piping systems. The results indicate that, due to the coupled nature of the system, it is possible in some situations to control the interior fluid power flow by applying structural inputs to the piping wall. Future research work should be devoted to the following topics:

1. Additional experiments dealing with the active control of the total power flow induced by fluid type disturbances should be conducted.

2. The scope of the experimental work presented in the dissertation was limited to harmonic disturbances. Real systems, however, are often subjected to broadband frequency disturbances. It would thus be of interest to extend the work to a broadband frequency excitation.

3. Wave vector filtering, i.e. real time separation of the waves travelling in positive and negative directions, has been used to control the total power flow in thin beams [35]. An implementation of the technique on finite shell systems at low frequencies could be attempted.

4. It is believed that embedded PVDF cables could provide good control actuators for real piping systems. This remains to be proven.

5. As performed by Fuller [3] for *in vacuo* shell systems, it would be interesting to analytically investigate the effect of a finite length discontinuity of the shell material on the wave propagation in *fluid-filled* shell systems. Actuators and sensors could then be added to the insert to achieve a combined active/passive attenuation effect of the discontinuity on the total power flow in the system.

6. There is enough material in the literature [23, 24] to conduct an analytical study on the effect of fluid convection on the performance of the active control approaches presented in this dissertation.

List of References

[1] H. Kraus 1967 *Thin Elastic Shells*. New York: Wiley.

[2] A.W. Leissa 1973 *Vibration of Shells*. NASA SP-288, National Aeronautics and Space Administration, Washington, D.C.

[3] C.R. Fuller 1981 *Journal of Sound and Vibration* 75, pp.207-228. The effects of wall discontinuities on the propagation of flexural waves in cylindrical shells.

[4] M. Heckl 1962 *The Journal of the Acoustical Society of America* 34, pp.1553-1557. Vibrations of point-driven shells.

[5] M.C. Junger and D. Feit 1986 *Sound, Structures, and Their Interaction*. Cambridge: MIT Press, Second Edition.

[6] G. Hermann and I. Mirsky 1956 *Journal of Applied Mechanics* 23, pp.563. Three-dimensional and shell theory analysis of axially symmetric motions of cylinders.

[7] I. Mirsky and G. Hermann 1957 *The Journal of the Acoustical Society of America* 29, pp.1116. Nonaxially symmetric motions of thick cylindrical shells.

[8] I. Mirsky and G. Hermann 1958 *Journal of Applied Mechanics* 25, pp.97. Axially symmetric motions of thick cylindrical shells.

[9] D.C. Gazis 1959 *The Journal of the Acoustical Society of America* 31, pp.568. Three-dimensional investigation of the propagation of waves in hollow circular cylinders - Analytical foundation.

[10] J.E. Greenspon 1960 *Journal of Aero-Space Science* 27, pp.37. Flexural vibrations of a thick-walled circular cylinder according to exact theory of elasticity.

[11] J.F. Bird, R.W. Hart and F.T. McClure 1960 *The Journal of the Acoustical Society of America* 32, pp.1404. Vibrations of thick-walled hollow cylinders - Exact numerical solutions.

[12] A.E. Armenakas, D.C. Gazis and G. Hermann 1969 *Free Vibrations of Circular Cylindrical Shells*. New York: Pergamon Press.

[13] G.V. Borgiotti and E.M. Rosen 1992 *The Journal of the Acoustical Society of America* 91(2), pp.911-925. The state vector approach to the wave and power flow analysis of the forced vibrations of a cylindrical shell. Part I: Infinite cylinders in vacuum.

[14] G.V. Borgiotti and E.M. Rosen 1993 *The Journal of the Acoustical Society of America* 93(2), pp.864-874. The state vector approach to the wave analysis of the forced vibrations of a cylindrical shell. Part II: Finite cylinders in vacuum.

[15] R. Kumar 1966 *Acustica* 17, pp.218. Axially symmetric vibrations of a thin cylindrical elastic shell, filled with non-viscous fluid.

[16] R. Kumar 1971 *Acustica* 24, pp.137. Flexural vibrations of fluid-filled circular cylindrical shells.

[17] V.A. Del Grosso and R.E. McGill 1968 *Acustica* 20, pp.313. Remarks on "Axially symmetric vibrations of a thin cylindrical elastic shell filled with nonviscous compressible fluid".

[18] V.A. Del Grosso 1971 *Acustica* 24, pp.1073. Analysis of multimode acoustic propagation in liquid cylinders with realistic boundary conditions - Application to sound speed and absorption measurements.

[19] R. Kumar 1972 *Acustica* 27, pp.317-329. Dispersion of axially symmetric waves in empty and fluid-filled cylindrical shells.

[20] C.R. Fuller and F.J. Fahy 1982 *Journal of Sound and Vibration* 81(4), pp.501-518. Characteristics of wave propagation and energy distributions in cylindrical elastic shells filled with fluid.

[21] P. Esparcieux 1986 *Ph.D. Dissertation, Institute of Sound and Vibration Research, University of Southampton, UK.* Measurements of vibrational wave characteristics of beams and pipes with and without discontinuities.

[22] T.J. Plona, B.K. Sinha, S. Kostek and S.-K. Chang 1992 *The Journal of the Acoustical Society of America* 92(2), pp.1144-1155. Axisymmetric wave propagation in fluid-loaded cylindrical shells. II: Theory versus experiment.

[23] G.F. Leyrat 1990 *Ph.D. Dissertation, Florida Atlantic University, Boca Raton, Florida.* Effects of an internal flow on the vibration of thin cylindrical shells.

[24] B.J. Brévart and C.R. Fuller 1993 *Journal of Sound and Vibration* 167(1) pp.149-163. Effect of an internal flow on the distribution of vibrational energy in an infinite fluid-filled thin cylindrical elastic shell.

[25] V.N. Merkulov, V.Y. Prikhod'ko and V.V. Tyutekin 1979 *Soviet Physics - Acoustics* 25, pp.51-54. Normal modes in a thin cylindrical elastic shell filled with fluid and driven by forces specified on its surface.

[26] V.N. Merkulov, V.Y. Prikhod'ko and V.V. Tyutekin 1978 *Soviet Physics - Acoustics* 24, pp.405-409. Excitation and propagation of normal modes in a thin cylindrical elastic shell filled with fluid.

[27] J.H. James 1981 *Admiralty Marine Technology Establishement Technical Memorandum TM* 81048. Sound radiation from fluid-filled pipes.

[28] J.H. James 1982 *Admiralty Marine Technology Establishement Technical Memorandum TM* 82036. Computation of acoustic power, vibration response and acoustic pressures of fluid-filled pipes.

[29] C.R. Fuller 1983 *Journal of Sound and Vibration* 87, pp.409-427. The input mobility of an infinite circular cylindrical elastic shell filled with fluid.

[30] C.R. Fuller 1984 *Journal of Sound and Vibration* 96(1), pp.101-110. Monopole excitation of vibrations in an infinite cylindrical shell filled with fluid.

[31] B.J. Brévart, C. Journeau and C.R. Fuller 1994 *To appear in Journal of Sound and Vibration*. High frequency response of a fluid-filled cylindrical shell with an internal column of gas bubbles [Application to active acoustic gas leak detection].

[32] B.J. Brévart and C.R. Fuller 1993 *Accepted for publication in Journal of Sound and Vibration*. Radial impulsive excitation of infinite fluid-filled elastic cylindrical shells.

[33] B.J. Brévart and C.R. Fuller 1994 *Accepted for publication in Journal of Sound and Vibration.* Energy exchange between the coupled media of impulsively excited, fluid-filled, elastic cylinders.

[34] M. Möser, M. Heckl and K.-H. Ginters 1986 *Acustica* 60, pp.34-44. Zur Schallausbreitung in Flüssigkeitsgefüllten kreiszylindrischen Rohren (On wave propagation in fluid-filled circular cylindrical tubes).

[35] G.P. Gibbs 1993 *Ph.D. Dissertation, Virginia Polytechnic Institute and State University, Blacksburg, Virginia.* Simultaneous active control of flexural and extensional power flow in thin beams.

[36] G. Pavić 1992 *Journal of Sound and Vibration* 154(3), pp.411-429. Vibroacoustical energy flow though straight pipes.

[37] C. de Jong 1994 *Analysis of pulsations and vibrations in fluid-filled pipe systems.* Delft, Netherlands: TNO Institute of Applied Physics Press.

[38] C.N. Corrado and M.A. Clifton 1994 *Proceedings of NOISE-CON 94*, pp.923-928. Array processing requirements for the measurement of structure and fluid borne propagation of flow noise in pipes.

[39] C.R. Fuller 1986 *Journal of Sound and Vibration* 109(2), pp.259-275. Radiation of sound from an infinite cylindrical elastic shell excited by an internal monopole source.

[40] E.H. Kennard 1953 *Journal of Applied Mechanics* 20, pp.33-40. The new approach to shell theory: Circular cylinders.

[41] P.M. Morse and K. U. Ingard 1968 *Theoretical Acoustics.* Princeton: Princeton University Press.

[42] *User's manual: IMSL Math/Library,* 1989. Version 1.1.

[43] A.D. Nashif, D.I.G. Jones and J.P. Henderson 1992 *Vibration Damping.* New York: Wiley.

[44] L.L. Beranek and I.L. Vér 1992 *Noise and Vibration Control Engineering.* New York: Wiley.

[45] P.A. Nelson, A.R.D. Curtis, S.J. Elliott, A.J. Bullmore 1987 *Journal of Sound and Vibration* 116(3), pp.397-414. The minimum power output of free field point sources and the active control of sound.

[46] M. Abramowitz and I.A. Stegun 1965 *Handbook of Mathematical Functions.* New York: Dover.

[47] A.J. Romano, P.B. Abraham and E.G. Williams 1990 *The Journal of the Acoustical Society of America* 87(3), pp.1166-1175. A Poynting vector formulation for thin shells and plates, and its application to structural intensity analysis and source localization. Part I: Theory.

[48] E.G. Williams 1991 *The Journal of the Acoustical Society of America* 89(4), pp.1615-1622. Structural intensity in thin cylindrical shells.

[49] W. Flugge 1973 *Stresses in Shells.* New York: Springer-Verlag, Second Edition.

[50] B.J. Brévart and C.R. Fuller 1993 *The Journal of the Acoustical Society of America* 94(3), pp.1467-1475. Active control of coupled wave propagation in fluid-filled elastic cylindrical shells.

[51] P.H. White and R.J. Sawley 1972 *Trans ASME, Journal of Engineering for Industry* 94, pp.746-751. Energy transmission in piping systems and its relation to noise control.

[52] BFGoodrich Aerospace, Engineered Polymer Products, Jacksonville, FL.

[53] E. Silberman 1957 *The Journal of the Acoustical Society of America* 29, pp.925-933. Sound velocity and attenuation in bubbly mixtures measured in standing wave tubes.

[54] L. Feng 1992 *Submitted to Journal of Sound and Vibration.* Experimental studies on acoustic properties of a finite elastic pipe filled with air/water.

[55] L. Feng 1992 *Submitted to Journal of Sound and Vibration.* Noise and vibration of a fluid filled elastic pipe coated with an absorptive layer on the inner side of the wall.

[56] *Product Data Sheet 56.* AMP Incorporated, Flexible Film Products, Valley Forge, PA.

[57] C.K. Lee and T.C. O'Sullivan 1991 *The Journal of the Acoustical Society of America* 90(2), pp.945-953. Piezoelectric Strain Rate Gages.

[58] R.J. Pinnington and A.R. Briscoe 1994 *Journal of Sound and Vibration* 173(4), pp.503-516. External applied sensor for axisymmetric waves in a fluid-filled pipe.

[59] B. Widrow and S.D. Stearns 1985 *Adaptive Signal Processing.* Englewood Cliffs, NJ: Prentice-Hall.

[60] P.A. Nelson and S.J. Elliot 1992 *Active Control of Sound*. London: Academic Press.

[61] *KYNAR Piezo Film Technical Manual*, 1987. Valley Forge, PA: Pennwalt Corporation.

Appendix A

Closed Form Derivative of the Characteristic Function

In order to compute the residues yielding the response of the fluid filled shell to a line force or a monopole source, the derivative of the characteristic function with respect to $k_n a$ must be evaluated.

The characteristic function is first written as

$$
|\mathbf{L}| = \begin{vmatrix} A_{110} + A_{112}x^2 & A_{121}x & A_{131}x \\ A_{121}x & A_{220} + A_{222}x^2 & A_{230}x \\ A_{311}x & A_{320} & A_{330} + A_{332}x^2 + A_{334}x^4 - FL \end{vmatrix} \quad (A.1)
$$

$$
= |\mathbf{L}|_{FL=0} - FL \times \begin{vmatrix} A_{110} + A_{112}x^2 & A_{121}x \\ A_{121}x & A_{220} + A_{222}x^2 \end{vmatrix} \quad (A.2)
$$

where $|\mathbf{L}|_{FL=0}$ denotes the characteristic function of the *in vacuo* system and

$$
\begin{aligned}
&x = k_n a \\
&A_{110} = -\Omega^2 + \tfrac{1}{2}(1-\nu)n^2 && A_{112} = 1 \\
&A_{121} = \tfrac{1}{2}(1+\nu)n && A_{131} = \nu \\
&A_{211} = A_{121} && A_{220} = -\Omega^2 + n^2 \\
&A_{222} = \tfrac{1}{2}(1-\nu) && A_{230} = n - \tfrac{h^2}{8a^2}\tfrac{\nu}{1-\nu}n(n^2-1) \quad (A.3)\\
&A_{311} = A_{131} && A_{320} = n \\
&A_{330} = -\Omega^2 + 1 + \beta^2\left[n^4 - \tfrac{4-\nu}{2(1-\nu)}n^2 + \tfrac{2+\nu}{2(1-\nu)}\right] \\
&A_{332} = 2\beta^2 n^2 && A_{334} = \beta^2
\end{aligned}
$$

The characteristic function of the *in vacuo* system is an eighth order polynomial which can be written as

$$
|\mathbf{L}|_{FL=0} = \sum_{k=0}^{8} B_k x^k, \tag{A.4}
$$

where the coefficients B_k are given by

$$
B_1 \;=\; B_3 \;=\; B_5 \;=\; B_7 \;=\; 0 \tag{A.5}
$$

$$
B_0 \;=\; A_{330}A_{110}A_{220} - A_{320}A_{230}A_{110} \tag{A.6}
$$

$$
B_2 \;=\; -A_{131}^2 A_{220} - A_{112}A_{230}A_{320} - A_{330}A_{121}^2 + A_{230}A_{131}A_{121}
$$
$$
+\; A_{320}A_{131}A_{121} + A_{332}A_{110}A_{220} + A_{330}A_{112}A_{220} + A_{330}A_{110}A_{222} \tag{A.7}
$$

$$
B_4 \;=\; A_{330}A_{112}A_{222} + A_{332}A_{112}A_{220} + A_{332}A_{110}A_{220} + A_{334}A_{110}A_{220}
$$
$$
-\; A_{332}A_{121}^2 - A_{222}A_{131}^2 \tag{A.8}
$$

$$
B_6 \;=\; A_{334}A_{112}A_{220} + A_{334}A_{110}A_{222} + A_{112}A_{222}A_{332} - A_{334}A_{121}^2 \tag{A.9}
$$

$$
B_8 \;=\; A_{334}A_{112}A_{222} \tag{A.10}
$$

The fluid loading term is expressed in a concise manner as

$$
FL = P\frac{J_n(y)}{yJ_n'(y)}, \tag{A.11}
$$

where $y = k_s^r a$ and $P = \Omega^2 \frac{\rho_f}{\rho_s}(\frac{h}{a})^{-1}$.

The derivative of FL is

$$\frac{\partial FL}{\partial x} = P\left\{\frac{y'}{y} - \frac{y' J_n(y)}{[yJ_n'(y)]^2}\left[J_n'(y) + yJ_n''(y)\right]\right\},\qquad\text{(A.12)}$$

where $y' = -x/y$.

The first derivative of the characteristic function is finally given by

$$
\begin{aligned}
\frac{\partial}{\partial x}|\mathbf{L}| = \ &- \ FL\left[2(A_{220}A_{112} + A_{222}A_{110} - A_{121}^2)x + 4A_{112}A_{222}x^3\right]\\
&- \frac{\partial FL}{\partial x}\left[A_{110}A_{220} + (A_{220}A_{112} + A_{222}A_{110} - A_{121}^2)x^2 + A_{112}A_{222}x^4\right]\\
&+ \sum_{k=0}^{8} kB_k x^{k-1}.\qquad\text{(A.13)}
\end{aligned}
$$

Appendix B

Spinning Circumferential Modes

Spinning modes are commonly seen to occur in real cylindrical shell systems as well as in circular acoustic ducts. The origin of the phenomenon can be very complex. In most cases however, the appearance of spinning modes is due to the presence of various coherent sources in the same system. In order to describe and explain the phenomenon, we consider here the excitation of the same infinite cylindrical shell system by several harmonic radial disturbances.

Any harmonic radial disturbance d_i can be written as follows

$$d_i = D_i X_i(x) T_i(\theta) R_i(r) \cos(\omega t), \qquad (B.1)$$

where D_i, $X_i(x)$, $T_i(\theta)$ and $R_i(r)$ are the amplitude and distributions of the disturbance in the x, θ and r directions respectively.

If $T_i(\theta)$ is a function presenting a symmetry with respect to the angle θ_i, it can be expressed as a Fourier series

$$T_i(\theta) = \sum_{n=0}^{\infty} t_i^n \cos(n(\theta - \theta_i)). \qquad (B.2)$$

213

In this case, it can be shown that the complex solution of the response y_i of the shell system to this single source at a given location M, in terms of shell displacement, shell velocity, shell acceleration or fluid pressure, can be written as

$$y_i = \sum_{n=0}^{\infty} A_i^n \cos(n(\theta - \theta_i))e^{i\omega t}. \tag{B.3}$$

This implies that all the circumferential modes propagating in the system are polarized at $\theta = \theta_i$.

Now, if P coherent sources are present in the system, using the superposition theorem yields the total response,

$$y = \sum_{i=1}^{P} y_i \tag{B.4}$$

$$= \sum_{i=1}^{P} \sum_{n=0}^{\infty} A_i^n \cos(n(\theta - \theta_i))e^{i\omega t}. \tag{B.5}$$

By commuting the two summations in Equation (B.5), one obtains the real time domain solution for the total modal response y^n as

$$y^n = Re\left(\sum_{i=1}^{P} A_i^n \cos(n(\theta - \theta_i))e^{i\omega t}\right) \tag{B.6}$$

$$= Re\left(\sum_{i=1}^{P} A_i^n \cos(n\theta_i)\ \cos(n\theta)\ e^{i\omega t} + \sum_{i=1}^{P} A_i^n \sin(n\theta_i)\ \sin(n\theta)\ e^{i\omega t}\right). \tag{B.7}$$

Thus, at any time t, the polarization angle of the circumferential mode n is given by

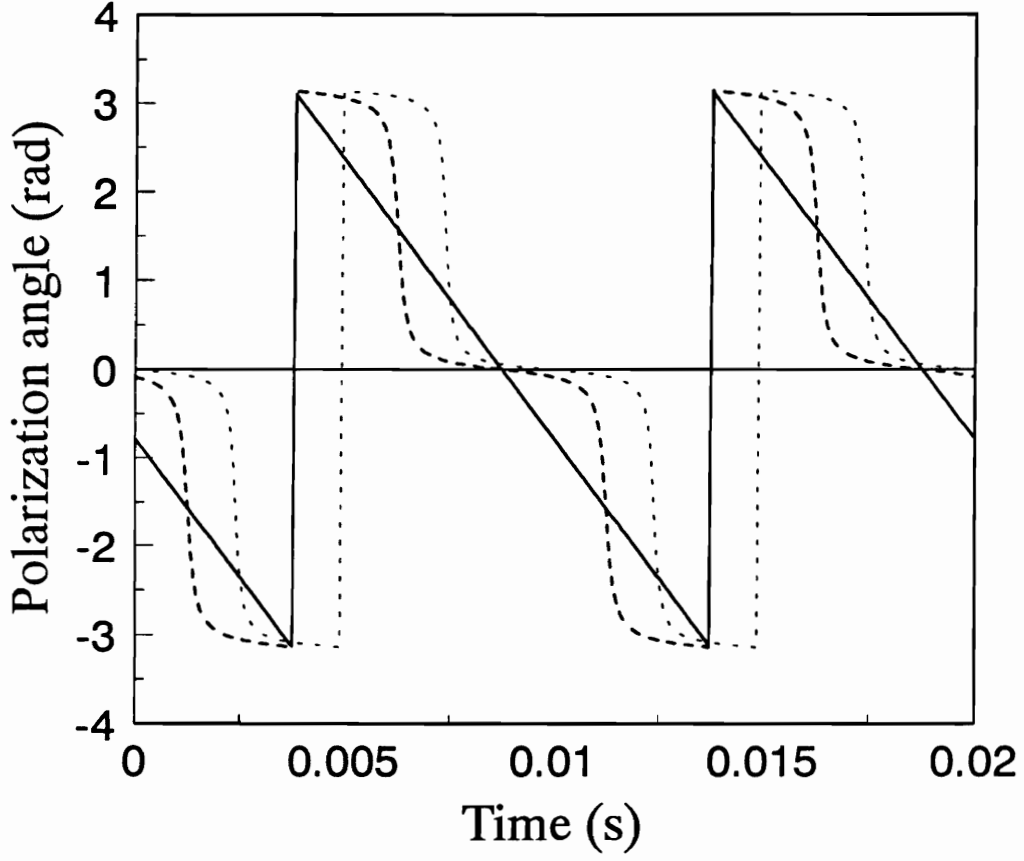$$tg(n\theta^n) = \frac{Re\left(\sum_{i=1}^{P} A_i^n \sin(n\theta_i)\ e^{i\omega t}\right)}{Re\left(\sum_{i=1}^{P} A_i^n \cos(n\theta_i)\ e^{i\omega t}\right)}. \tag{B.8}$$

Because A_i^n's are complex values, Expression (B.8) reveals that only three special configurations of the disturbances yield time invariant values of θ^n:

- there is only one disturbance

- all the modal amplitudes A_i^n are in phase or out of phase

- the disturbances are polarized at the same angle.

These two arrangements excepted, the mode has a time variant polarization angle: it is said to be *spinning*.

This phenomenon is illustrated by looking at the case of two disturbances (P=2). Figure B.1 shows the time variation of θ^1 (n=1), given by Equation (B.8), at 100 Hz. For $A_1^1 = 1$, $A_2^1 = exp(i\pi/2)$, $\theta_1 = -45°$ and $\theta_1 = 45°$, the mode n=1 is seen to spin at constant speed $w = 2\pi f$. For two close angular positions of the disturbances ($-5°$ and $5°$), the polarization angle of the mode is most of the time (relative to a period) confined between θ_1 and θ_2. Similar behaviour is obtained when the phase lag between the modal amplitudes A_1^1 and A_2^1 is small. In this case, the polarization angle varies little from $(\theta_1 + \theta_2)/2$.

Figure B.1: Polarization angle of the circumferential mode n=1, two radial disturbances - Spinning mode.

The legend entries read:

——— $\theta_1 = -45°$, $\theta_2 = 45°$, $A_1^1 = 1$, $A_2^1 = e^{i\pi/2}$

– – – – $\theta_1 = -5°$, $\theta_2 = 5°$, $A_1^1 = 1$, $A_2^1 = e^{i\pi/2}$

············ $\theta_1 = -45°$, $\theta_2 = 45°$, $A_1^1 = 1$, $A_2^1 = e^{i\pi/24}$

Vita

Bertrand Brévart was born on April 11, 1968 in Migennes, France, and was raised in the peaceful town of Offranville, in Normandy. After graduating from Pablo Neruda high school, Dieppe, France, in 1986, he enrolled in the University of Technology of Compiègne (UTC), France. In 1988, he joined the Acoustics and Vibration branch of the Mechanical Engineering Department. He received his Engineer Diploma from UTC in October 1991. A year before, in August, he left his homeland for the United States of America and enrolled in graduate school at Virginia Polytechnic Institute and State University. He worked on a Ph.D. in the Vibration and Acoustics Laboratories directed by Chris R. Fuller and completed his degree in December 1994. In January 1995, he will start working for Alcatel-Alsthom Recherche in Marcoussis, France.